Dipl.-Ing. Stefan Kleindel

The Opportunities and Limits of Injection Molding Simulation Applied to Parts with Complex 3D Geometry

Dissertation

to achieve the university degree of
Doctor of Engineering Sciences

submitted to
Graz University of Technology
Faculty of Mechanical Engineering and Economical Sciences

Supervisor
Univ.-Prof. Dipl.-Ing. Dr.techn. Christoph Hochenauer

second Supervisor
Univ.-Prof. Dipl-Ing. Dr.mont. Walter Friesenbichler

Vienna, September 2016

Statutory Declaration

I declare that I have authored this thesis independently, that I have not used other than the declared sources/resources, and that I have explicitly marked all material which has been quoted either literally or by content from the used sources.

Vienna, _____   _____

              Date   Signature

Eidesstattliche Erklärung[1]

Ich erkläre an Eides statt, dass ich die vorliegende Arbeit selbstständig verfasst, andere als die angegebenen Quellen/Hilfsmittel nicht benutzt, und die den benutzten Quellen wörtlich und inhaltlich entnommenen Stellen als solche kenntlich gemacht habe.

Wien, am _____   _____

              Datum   Unterschrift

---

[1]Beschluss der Curricula-Kommission für Bachelor-, Master- und Diplomstudien vom 10.11.2008; Genehmigung des Senates am 1.12.2008

Abstract

This thesis deals with injection molding simulation applied to complex, "chunky" parts. Such parts are characterized by thick walls in relation to their width in both the flow and transverse direction. They are used for applications with high demands on mechanical strength and stiffness. The primary aim of this thesis is to investigate the capability, of state-of-the-art simulation software, to predict warpage of chunky, injection molded parts. An accurate prediction of warpage enables corrective action before the mold is built, and thus, to avoid the time-consuming and costly re-working of the mold.

Predicting warpage of an injection molded part is a highly challenging task and still an active field of research. The models and methods used in the field of injection molding simulation were initially developed and verified for parts having a thin-shell structure. Research work considering chunky parts and the involved 3D effects is hardly available. The ability of accurately predicting the warpage of chunky parts was not yet demonstrated.

The commercial software Autodesk Moldflow Insight was used to simulate the injection molding process of chunky parts. Numerous case studies were performed on different plastic parts which were already in production. All of them were of complex and chunky shapes. The simulations were always supported by molding trials and the results compared to measurements. The impact of all relevant aspects of injection molding simulation (such as modeling, material data, process settings and boundary conditions, solver settings, sub-models, etc.) on the solution accuracy was investigated. The findings were then used to refine the numerical models by considering all dominating contributors to warpage. In all cases, the simulation results were in good agreement with the experiments. The prediction of warpage succeded with reasonable accuracy. The deviations to the molded and measured parts were in the order of 10% to 30%. Some of the case studies required a higher modeling effort to capture specific effects in order to obtain accurate results. In one case, it was necessary to add a detailed model of the hot runner nozzle to simulate the heat flux into the mold (which is usually neglected) and thus accurately predict the temperature distribution around the cavity. One way to take the hot runner nozzle into account is outlined in this thesis.

The knowledge attained from these studies was then used to predict and compensate for the warpage of a distinctly complex part before the mold was actually built. Initial molding trials produced parts without warpage. Hence, the suitability of modern 3D injection molding simulation software for chunky parts was demonstrated.

One case study, however, indicated a weakness in the simulation model. It failed to predict the warpage of a part even qualitatively. A thorough experimental and numerical investigation was conducted to narrow down possible reasons. X-ray computed tomography (µCT) was used to scan and gain insight into the inner structure of molded parts. This nondestructive technology allows to obtain a 3D representation of the density distribution in the whole scanned volume with a spatial resolution in the µm range. Thus, objects like glass fibers or voids can be distinguished from the polymer matrix by their deviating density. CT scans of the moldings were performed to quantify voids and obtain experimental fiber orientation data. It was found that a smaller void volume correlates to lower warpage. The simulation model does not reflect this relationship. The fiber data was used to calculate fiber orientation distribution and fiber length distribution. A comparison with the predicted fiber orientation revealed a limited ability of the fiber models to predict the orientation in thick walls. A good accordance was observed in the shell layer. The size of the core zone and the fiber orientation within was only in qualitative agreement.

A simple U-shaped part with thick walls in the corners was designed to further investigate the influence of voids and fiber orientation on warpage predictions. The numerical model was closely validated by measurements of cavity pressure and mold temperature. The experimental results for POM again showed a correlation between warpage and void volume. Warpage predictions were in good agreement with measurements on parts with low void volume and severely deviated in all other cases. The warpage of fiber reinforced polymer grades was essentially dominated by the fiber orientation. In contrast to the other studies, warpage was severely under-predicted by the numerical model, indicating flaws in fiber modeling.

These studies revealed two effects which may compromise the accuracy of warpage predictions for chunky parts. Both are only significant if the warpage originates from a thick-walled section of the molding. Firstly, poor packing efficiency causes high volumetric shrinkage in thick walls of the molding (which is characterized by the formation of voids). This contribution to warpage is not properly captured by the numerical model. Secondly, the limited accuracy of fiber orientation predictions in thick walls was identified as a potential source of error.

Kurzfassung

Die vorliegende Arbeit behandelt die Simulation des Spritzgiessprozesses von »klobigen« Kunststoffteilen mit komplexer Geometrie. Ein wesentliches Kennzeichnen solcher Teile ist eine große Wandstärke in Relation zur Fließweglänge. Klobige Kunststoffteile finden bei Anwendungen mit hohen Steifigkeits- und/oder Festigkeitsanforderungen an den Formteil Verwendung. Das Hauptziel dieser Arbeit war die Untersuchung von Anwendbarkeit und Grenzen moderner Simulationswerkzeuge zur Vorhersage des Verzuges klobiger, gespritzter Kunststoffteile. Eine genaue Verzugsvorhersage ermöglicht präventive Maßnahmen noch bevor der Bau des zugehörigen Spritzgiesswerkzeuges tatsächlich begonnen hat. Dadurch können zur Fehlerbehebung nötige, teure und zeitaufwändige Modifikationen am fertigen Werkzeug minimiert werden oder sogar entfallen.

Die Verzugsvorhersage eines gespritzten Kunststoffteils ist äußerst anspruchsvoll und noch immer Thema aktiver Forschung. Die aktuell bei der Spritzgiesssimulation verwendeten Modelle und Methoden wurden ursprünglich für dünnwandige Teile entwickelt und verifiziert. Kaum eine Forschungsarbeit beschäftigt sich mit der Anwendung der Simulation auf klobige Teile und den hier vorhandenen 3D-Effekten. Bisher wurde also nicht untersucht ob eine zuverlässige Vorhersage des Verzuges von klobigen Kunststoffteilen möglich ist.

Die kommerzielle Software Autodesk Moldflow Insight wurde in dieser Arbeit zur Simulation des Spritzgießprozess klobiger Teile verwendet. Es wurden zahlreiche, verschiedene Teile aus der Produktion im Rahmen von umfangreichen Fallstudien untersucht. Alle diese Teile weisen eine komplexe und klobige Gestalt auf. Die Simulationen wurden auf Basis experimenteller Bemusterungen durchgeführt und die Ergebnisse mit Messungen verglichen. Damit wurden alle relevanten Gesichtspunkte der Spritzgiesssimulation (wie Modellierung, Materialdaten, Prozessparameter, Randbedingungen, Solvereinstellungen, Sub-Modelle, ...) und deren Einfluss auf die Ergebnisgenauigkeit untersucht. Mit den daraus abgeleiteten Erkenntnissen wurde die Modellierung der einzelnen Fallstudien verbessert und somit alle dominanten Einflussfaktoren auf den Verzug berücksichtigt. In all diesen Fällen wurde eine gute Übereinstimmung von Simulation und Experiment erzielt. Auch die Vorhersage des Verzuges erfolgte mit akzeptabler bis hervorragender Genauigkeit. Die Abweichungen zum tatsächlichen, gemessenen Verzug lagen im Bereich von rund 10% bis

30%. In einigen Fällen konnte die hohe Ergebnisgenauigkeit nur durch aufwändige Modellierung zur Abbildung spezieller Effekte erreicht werden. Es musste beispielsweise ein detailliertes Modell der Heißkanaldüse erstellt werden. Damit konnte der Wärmeeintrag in das Werkzeug (normalerweise vernachlässigbar) realitätsnah abgebildet und die Temperaturverteilung um die Kavität wesentlich genauer berechnet werden. Ein möglicher Weg zur Modellierung der Heißkanaldüse wird in dieser Arbeit vorgestellt.

Mit den gewonnenen Erkenntnissen wurde dann der Verzug eines komplexen, klobigen Teils vorhergesagt und kompensiert bevor das Formwerkzeug tatsächlich gebaut wurde. Die Erstbemusterung lieferte bereits verzugsfreie Formteile. Somit wurde die Eignung der modernen 3D Spritzgiesssimulation auch für komplexe, klobige Teile erfolgreich demonstriert.

Eine Fallstudie ließ jedoch Schwachstellen in der numerischen Modellierung vermuten. Der Verzug des Formteils wurde weder quantitativ noch qualitativ richtig vorhergesagt. Es wurden umfangreiche Untersuchungen durchgeführt und die möglichen Ursachen für das Versagen der Simulation eingegrenzt. Gespritzte Formteile wurden mittels industrieller Computertomographie (μCT) gescannt um Informationen über die innere Struktur zu erhalten. Mit dieser zerstörungsfreien Methode erhält man eine dreidimensionale Beschreibung der Dichteverteilung innerhalb des gescannten Volumens mit einer Ortsauflösung im μm Bereich. Objekte wie etwa Glasfasern oder Lunker können anhand des Dichteunterschiedes zur Kunststoffmatrix charakterisiert werden. Mit den CT Messungen wurde das Lunkervolumen in den Formteilen quantifiziert und experimentelle Faserdaten gewonnen. Es zeigte sich, dass eine Reduktion des Lunkervolumens auch zur Reduktion des Formteilverzuges führte. Dieser Zusammenhang wird vom Simulationsmodell jedoch nicht abgebildet. Mit den experimentellen Faserdaten wurden die räumliche Verteilung des Faserorientierungstensors und der Faserlänge berechnet. Der Vergleich mit der simulierten Faserorientierung zeigte, dass die Vorhersage der Faserorientierung in dicken Wänden nur beschränkt funktioniert. Eine gute Übereinstimmung wurde dort nur in Wandnähe erzielt. Die Größe der Kernzone und die Faserorientierung in der Kernzone wurde nur qualitativ vorhergesagt.

Der Einfluss von Lunker und Faserorientierung auf den Verzug wurde anhand eines speziell dafür entworfenen, U-förmigen und in den Ecken dickwandigen Testteils genauer untersucht. Das Simulationsmodell wurde dabei sehr genau mit Messdaten des Forminnendruckes und der Werkzeugtemperatur validiert. Experimente mit POM zeigten wieder eine starke Korrelation von Lunkervolumen und Verzug. Die Verzugsvorhersage war in guter Übereinstimmung mit dem Experiment bei Teilen mit kleinem Lunkervolumen, aber deutlich zu niedrig in allen anderen Fällen. Bei der Verarbeitung von faserverstärktem Material wurde der Formteilverzug von der Faserorientierung dominiert. Im Gegensatz zu den übrigen Fallstudien wurde der

Formteilverzug hier immer massiv unterschätzt. Dies deutet erneut auf eine Schwäche der Fasermodelle und deren ungenaue Vorhersage der Orientierung in den dicken Wänden hin.

Diese Fallstudien brachten zwei Effekte zum Vorschein welche die Genauigkeit der Verzugsvorhersage von klobigen Teilen kompromittieren könnten. Beide sind nur dann von Bedeutung wenn der Verzug von dickwandigen Bereichen des Formteils auftritt. Erstens: Eine schlechte Nachdruckwirkung führt zu sehr hoher volumetrischer Schwindung in den dickwandigen Bereichen des Formteils (gekennzeichnet durch die Bildung von Lunkern). Dieser Beitrag zum Verzug wird von der Simulation nicht ausreichend abgebildet. Zweitens: Die beschränkte Genauigkeit der Faserorientierungsberechnung in dickwandigen Teilen stellt eine weitere potentielle Fehlerquelle dar.

Acknowledgments

Contents

Contents

Contents

Contents

List of Figures

List of Figures

List of Figures

List of Tables

List of Tables

1. Introduction

This section is intended to give a brief introduction to the benefits and challenges related to the injection molding process, to highlight the motivation and aims behind this thesis, and to provide an impression of the value of injection molding simulation tools. It is not intended to give deep insight into the theory or a review of research activities in the field of injection molding, both of which are covered in the following chapters.

Features of the injection molding process

Injection molding is a common process for the mass production of plastic parts with complex shapes, tight tolerances, and tailored properties. A tool life in the order of 10^6 molding cycles, in combination with low cycle times of usually less than 2 minutes, enable a low price per unit. Moldings made from high-performance polymers with glass or carbon fiber reinforcement are frequently used to replace metal parts. These applications often demand high stiffness and strength of the part, even at elevated temperatures. In contrast to die casted parts, a post-treatment, such as subsequent machining of the moldings, is usually not required and the tool life is much longer.

One downside of the injection molding process is the high cost of a mold. Although seemingly simple at the first glance, they are truly sophisticated tools. Injection molds for mass production commonly consist of two mold halves with mold inserts embedded in a massive mold base. A runner system is needed to guide the molten plastic from the machine nozzle to the cavity. Either hot or cold runners are used. A cold runner is ejected together with the part, while a hot runner is basically a heated channel to keep the polymer in a molten state. The mold can hold one or more cavities to produce several parts with each cycle. Depending on the complexity of the part, side cores, sleeves, or more sophisticated demolding features, such as folding cores, could be necessary to produce the required part shape. The mold needs a cooling system to remove the heat of the plastic melt and to maintain the desired mold temperature. An ejection system is necessary to push the parts out of the mold. The mold inserts must resist wear and are therefore commonly made from hardened tool steel. Inserts and mold base must withstand melt pressure and the clamping force of the injection molding machine with minimal deflection. Parting faces on the mold

inserts must be precision machined to tolerances in the order of 0.01 mm. The surface finish of cavity and core faces is transferred to the plastic part and must therefore match the requirements of the part designer. Hence, building injection molds is a challenging, time-consuming, and very costly task.

In practice, some process related issues may occur. Among many others, these include surface defects, short shots, and burn- or sink marks. The molded part may also have zones with poor mechanical strength properties. Another quite common but much more challenging problem is uneven (commonly called "differential") shrinkage, which is the root cause for warpage of the molded parts. Within the context of this thesis, shrinkage means that the molding does actually have the shape of the cavity, but that it is somewhat smaller. On the contrary, an out-of-plane deflection of the part, in other words, a shape change, is called warpage. Shrinkage is mostly caused by thermal contraction and morphology changes when the polymer cools from melt to ambient temperature. For practical mold design shrinkage is considered by simply scaling the cavity by an empirical factor[1]. This method is widely used and presents few problems.

Severe warpage of the molding may impair its functionality, complicate or hinder the assembly of parts, or simply infringe on aesthetic requirements. Reworking the mold is, in most cases, the only way to remove this defect. As already pointed out, this is a very expensive and time consuming task. The cost of the correction could even exceed the cost of the initial mold. Using numerical simulation to predict and compensate for warpage, before the mold is even built, is a promising method to overcome this problem. Modern injection molding simulation tools allow the simulation of the filling, packing and cooling stages of the molding process. Additionally, the final shape and dimensions of the cold product can be predicted. However, the injection molding process, with its underlying physics, is highly complex, and not all the involved phenomena are well understood. The prediction of the moving melt front, and hence, the formation of weld and meld lines, usually succeeds with high accuracy. The prediction of residual stresses, which are the basis for the warpage calculation, is still based on major simplifications in order to overcome limitations in material modeling.

Scope of thesis

Classic plastic parts have a thin-shell structure with a more or less constant wall thicknesses. Thus, experiments, measurements, and the validation of simulation models are commonly performed on parts with simple geometry, such as flat plates or center gated disks. This thesis focuses on industrial plastic parts, which do not

---

[1]depending on the polymer this factor is typically in the range of 1–1.03

have the classic thin-shell structure. All the parts considered in this thesis feature varying wall thicknesses ranging from around 1 mm to 10 mm, while their overall size does not exceed the size of a human fist. A 3D flow regime occurs at intersections of two or more walls, at rather sharp jumps in wall thickness, as well as in regions with thick walls relative to their width in the flow and transverse directions. Parts where such geometry features dominate the design are called "chunky" within this thesis. Chunky parts are used for applications which require high stiffness and mechanical strength. A high level of functional integration, the fusion of several simple parts to one complex part, and a sophisticated design for a pleasing appearance, are further requirements with gaining importance. Part designers may not be able to create components which are perfectly suited for injection molding.

Chunky parts do not have the level of flexibility of the classic thin-shell-like plastic parts. Even small out-of-plane deflections can hinder or even prevent the assembly of the molded part. Therefore, one important aim of this thesis is the accurate quantitative warpage prediction of chunky parts. This is a basic requirement to detect and eliminate warpage issues before the mold is built. The research question was: Is a commercial injection molding simulation software able to accurately predict warpage of chunky parts? And further: If yes, are there any limitations?

This thesis demonstrates the application of state-of-the-art injection molding simulation software to such complex, chunky parts. It reveals the opportunities provided by such software, as well as its limitations. To accomplish this objective, the commercial software Autodesk Moldflow Insight was used throughout this thesis.

Methods and research activities

This thesis was founded on several case studies which were investigated both numerically and experimentally. Most of them are based on "real" industrial parts[2] where molding trials and measurements enabled the validation of the simulation model. Furthermore, the factors (such as modeling, meshing, solver settings, material data, sub-models, model constants, etc.) which have an influence on the simulation results were determined to gain knowledge of modeling chunky parts. A detailed 3D model of a hot runner nozzle was introduced to consider its influence on the temperature distribution around the cavity and, consequently, on the part warpage . It was found that accurate warpage predictions are feasible if the suggestions on modeling outlined in this thesis are considered. In most cases, good to excellent agreement of prediction and measurement was achieved.

However, two case studies raised questions which called for further research. In one case, the predicted filling pattern of a long plate did not match the experimental result.

---

[2]The parts were designed for a specific application and not intended for research purposes.

1. Introduction

It was found that the elasticity of the mold (which is not considered in simulation) caused this discrepancy. Good accordance was achieved after the stiffness of the mold was improved. In the second case, the simulation failed to predict the warpage of a part correctly. A thorough investigation was conducted, involving several molding trials and numerical simulations. Measurements using μCT were performed to check the part for voids and to obtain experimental fiber orientation data. The experimental results showed that a reduction of the void volume causes a decrease in warpage. The simulation model does not show this relationship. Moreover, the experimental fiber orientation data was compared to the predicted orientation. A reasonably good agreement was achieved in the shell layer of the part. The size of the core zone and the fiber orientation within was only in qualitative agreement.

A simple U-shaped part with thick walls in the corner was designed to gain knowledge about the warpage of chunky parts. The mold was equipped with pressure and temperature sensors to closely verify the simulation results. Molding trials using POM, PA6 GF35 and PA6 GF45 were performed along with simulations. In the case of POM, a correlation of void volume and warpage was again observed. Warpage predictions were only in good agreement with the measurements of moldings with a low void volume. No such dependency was observed for the fiber filled materials. Warpage predictions were generally not as accurate as in other cases presented in this study. The simulation results indicated that improvements in warpage prediction of fiber reinforced moldings may require enhancements to the fiber models.

All of these investigations led to the conclusion that accurate warpage predictions are feasible as long as warpage does not originate at a thick-walled section of the part. It was shown that very high shrinkage in thick sections of the part (which is characterized by the formation of voids) may cause poor accordance between predicted and actual warpage. Moreover, the performance of recent fiber models in predicting fiber orientation in thick walls was evaluated. Hence, the limits of state-of-the-art injection molding simulation software were discovered and subjects for further research activities suggested.

Another problem related of the injection molding process are weld lines. The parts considered in this thesis are designed for applications with high demands for mechanical performance. For this reason, a special mold was built for dumbbell-shaped specimens. It allows the characterization of weld lines and the investigation of their significance on the strength properties of the specimen. An experimental study was conducted using POM and PA6 GF45. The experimental results were correlated to numerical predictions of the weld line shape. The study shows how weld lines affect strength, how to determine its significance by simulation, and also shows one method to improve the strength of weld lines.

2. Modeling the injection molding process

Modeling the injection molding process is an ongoing field of research. Early commercial packages to simulate the mold filling of simple parts became available in the early 1980s. Today it is possible to analyze complex 3D models coupled with the temperature field in the whole mold. This chapter provides a brief overview of commonly used modeling approaches in injection molding simulation.

2.1. The filling and packing stages

In the filling stage, the screw of the molding machine is forced forward by velocity control. The melt is pressed through the runner system and enters the cavity through the gate. Just before the cavity is completely filled, it is switched from velocity to pressure control, and the packing stage starts. The hot molten polymer shrinks as it cools while the packing pressure forces additional material into the cavity. Volumetric shrinkage is therefore partly compensated for as long as the gate is open. When the melt is forced through narrow channels (such as the gate), the high viscosity of the polymer melt causes high shear stresses, and therefore, high pressure loss and heat generation. Hence, shear heat delays the sealing of the gate. After the gate has sealed, the part is still kept in the closed mold to cool down until it is stiff enough for ejection.

The challenge is to simulate a non-isothermal, laminar flow of a compressible, viscous fluid with shear thinning behavior, the moving melt front and solidification. In the case of fiber reinforced polymers, the fiber orientation distribution must also be tracked throughout the filling and packing stages. There are of course even more challenges, such as modeling crystallization. Some notes on this will be given in subsequent chapters.

2.1.1. 2.5D-flow: The Hele-Shaw approximation

Classic plastic parts usually have a thin-shell like structure with a more or less constant wall thickness. Such a design allows for a major simplification of the governing equations. The flow in each wall is approximated by a Hele-Shaw-flow, meaning a flow in a small gap [1]. In this case, the z-component of the velocity vector (the flow component in thickness direction) is zero. A velocity profile over the thickness of the plate is calculated based on the viscosity model and the boundary conditions at the mold wall. The result is a 3D representation of the velocity field, whereby the z-component is always zero. Moreover, the pressure distribution in the fluid must only be solved in x and y direction. Since it is neither 2D nor fully 3D, this approach is commonly called 2.5D simulation. It is appropriate for parts with large thin-walled regions, such as housings for all kind of consumer products or interior parts in the automotive sector. An important requirement for accurate results using this approach is that the width of each section is many times larger than the local wall thickness [2].

The Hele-Shaw model is used in combination with midplane and dual domain models for the discretization of the computational domain. The midplane model requires a midplane representation of the part, which must be derived from the 3D CAD Model. Each surface is meshed with a shell mesh, and a thickness must be assigned to each face. [2] Despite its computational efficiency, this approach is rarely used anymore due to its higher modeling effort. Another drawback is that it does not allow the definition of varying wall thicknesses as are commonly present on ribs with a draft angle for the proper demolding of the part.

The dual domain approach was developed to overcome the geometry hurdle. It only requires a surface mesh of the 3D CAD model, whereas the triangular mesh elements on opposite sides of the wall need to be aligned. The local wall thickness is then calculated by the distance of each pair of opposing mesh elements. At locations where the placement of matching elements is not possible, as is the case in every corner, the implementation of this method becomes difficult [3]. The dual domain model combines the low computational effort of the midplane model with the ability to analyze parts with complex shapes with little meshing effort. [2]

The main advantage of 2.5D analysis is that a high resolution in thickness direction can be achieved with relatively little computational effort. Due to the high temperature and velocity gradients and the varying fiber orientation over the wall thickness, a fine discretization over the wall thickness is highly desirable. A detailed description is found in [4–6]. Because of the restriction to parts with thin-shell geometry, this method is not used in this thesis.

2.1.2. 3D flow: The Navier-Stokes equations

In the case of chunky parts, the assumption of a Hele-Shaw flow is not valid. A 3D simulation by solving the full Navier-Stokes equations is required.

The flow of the polymer melt is governed by the following conservation laws. The conservation of mass is given by:

$$\frac{\partial \rho}{\partial t} + \nabla \cdot \rho \boldsymbol{u} = 0 \qquad (2.1)$$

where $\rho = \rho\left(\boldsymbol{x}, t\right)$ is the density, $\boldsymbol{u} = \boldsymbol{u}\left(\boldsymbol{x}, t\right)$ is the velocity vector and t the time. The conservation of momentum may be written:

$$\frac{\partial \left(\rho \boldsymbol{u}\right)}{\partial t} + \nabla \cdot \rho \boldsymbol{u}\boldsymbol{u} = \nabla \cdot \boldsymbol{\sigma} + \rho \boldsymbol{g} \qquad (2.2)$$

with $\boldsymbol{\sigma}$ being the stress tensor and $\boldsymbol{g}$ being the vector of gravitational acceleration. A constitutive relationship between the extra stress tensor $\boldsymbol{\tau} = \boldsymbol{\sigma} + p\boldsymbol{I}$ and the rate of strain tensor $\dot{\boldsymbol{\epsilon}}$ is needed. The constitutive law for a compressible, generalized Newtonian fluid is widely used. It is given by

$$\boldsymbol{\sigma} = -p\boldsymbol{I} + 2\eta(\dot{\gamma})\dot{\boldsymbol{\epsilon}} \qquad (2.3)$$

where p is the pressure. The viscosity η of molten polymers is dependent on shear rate $\dot{\gamma}$ and temperature T. Commonly used viscosity functions $\eta(\dot{\gamma})$ are covered in Section 2.1.4. Inserting equation (2.3) in (2.2) results in the Navier-Stokes momentum equation for compressible, generalized Newtonian fluids:

$$\frac{\partial \left(\rho \boldsymbol{u}\right)}{\partial t} + \nabla \cdot \rho \boldsymbol{u}\boldsymbol{u} = -\nabla p + \eta(\dot{\gamma})\Delta \boldsymbol{u} + \rho \mathbf{g} \qquad (2.4)$$

The first term on the left side of this equation represents the rate of change of momentum in a fluid volume element and the second term the inertial forces. The terms on the right side are the frictional (2st term) and the volume forces (3rd term) acting on a fluid volume element. Due to the high viscosity of polymer melts, some simplifications of the Navier-Stokes equations may be considered without introducing significant errors. The gravitational volume force effect is usually not considered. In a normal mold filling process with a highly viscous polymer melt and a low flow velocity, the inertial forces are low compared to the viscous forces and may be neglected (Stokes flow). [6]

There are exceptions where the inertia terms must be considered. One is the prediction of jetting. A thorough investigation regarding this topic was performed by Costa *et al.* [7].

Finally the conservation of energy may be written:

$$\rho c_p \left(\frac{\partial T}{\partial t} + \boldsymbol{u} \cdot \nabla T \right) = \beta T \left(\frac{\partial p}{\partial T} + \boldsymbol{u} \cdot \nabla p \right) + p \nabla \cdot \boldsymbol{u} + \boldsymbol{\sigma} : \nabla \boldsymbol{u} + \nabla \cdot (k \nabla T) \qquad (2.5)$$

with the specific heat at constant pressure c_p, the temperature $T = T(\boldsymbol{x}, t)$, the polymer expansivity β and the thermal conductivity k. β is defined as

$$\beta = -\frac{1}{\rho} \frac{\delta p}{\delta T} \qquad (2.6)$$

[8] . The physical interpretation of the energy conservation equation is that the rate of change of the temperature is affected through terms of mechanical compression (1st term on the right hand side), flow work (2nd term on the right hand side), viscous dissipation (3rd term on the right hand side), and heat conduction (last term). [9]

The main drawback of a full 3D analysis is the high computational effort. In contrast to the 2.5D simulation, a volume mesh is needed for 3D simulation. The high gradients in thickness direction present in the injection molding process require a sufficiently fine discretization even in very thin walls [10]. Moreover, for accurate results, the aspect ratio of the elements must not be excessively large. This is especially true when a subsequent warpage analysis is performed on the same mesh. For a Moldflow 3D analysis, a maximum aspect ratio of the tetrahedral elements should not exceed 50:1 [11]. These requirements lead to high element counts and high computational costs. Nevertheless, this method is used throughout this work since all of the parts investigated are of complex and chunky shapes, and therefore demand a true 3D representation of the model.

2.1.3. Tracking the melt-air interface

In the mold filling analysis, it is necessary to track the moving melt front. This is important in order to investigate the flow behavior in the mold and the characteristics of the flow front, in particular, the formation of weld lines. The melt/air interface can be tracked by a Lagrangian or captured by a Eulerian algorithm [12]. One method to utilize the advantages of both methods, called Arbitrary Lagrangian-Eulerian has been discussed and applied to mold filling by Bajaj *et al.* [13], Gaston *et al.* [14], and Lewis *et al.* [15].

When using a Lagrangian algorithm, only the polymer domain is meshed and the melt/air interface is represented by the boundary of the mesh. Since the boundary of the mesh moves, the nodes inside the mesh must be shifted, or else remeshing must be applied, to maintain proper mesh quality. Due to the mesh distortion involved,

this method is restricted to relatively simple geometries, where the frequency of remeshing steps is low and the computational cost is acceptable. [16]

The Eulerian algorithm requires a mesh of the whole domain. A scalar field is solved to determine the position of the flow front. Commonly used methods are the Volume of Fluid Method (VOF) [17, 18] and the Level Set Method [19, 20]. The Level Set Method is used by Moldflow [21] and has some advantages over the VOF model [22]. It is a robust method which enables an accurate description of the interface even on coarse meshes and in case of complex topology. The level set equation is given by

$$\frac{\partial \phi}{\partial t} + \boldsymbol{u} \cdot \nabla \phi = 0 \tag{2.7}$$

where $\phi(\boldsymbol{x}, t)$ is the level set distance function, $\boldsymbol{x}$ a point in space, and t a point in time. ϕ could be any smooth function which gives the position of the interface at its zero level set. Usually, the signed distance function $\phi(\boldsymbol{x}, t) = \pm d$ is used, where d is the closest distance of point $\boldsymbol{x}$ to the interface. A positive sign means the point is inside the interface (the melt), and a negative sign is used when the point is outside of the interface. Hence, the surface of the interface is defined by all points where $\phi(\boldsymbol{x}, t) = 0$. After initialization, at the beginning of the calculation, the time evolution of the interface is given by equation (2.7). Reinitialization is required to ensure that $\phi(\boldsymbol{x}, t)$ satisfies the signed distance function throughout the simulation [22].

2.1.4. Modeling viscosity and compressibility

A viscosity model is needed to describe the viscosity as a function of temperature and shear rate $\eta\left(T, \dot{\gamma}\right)$. Polymer melts show a decrease in viscosity with rising temperature and increasing shear rate (shear thinning behavior). A plot of the viscosity over shear rate, for a typical thermoplastic grade, is depicted in Fig. 2.1.

At very low shear rates, the fluid exhibits Newtonian behavior. With increasing shear rate, the entanglement of the polymer chains is gradually reduced, and the viscosity declines. The decrease in viscosity levels out when the polymer chains are fully aligned. In practice, this limit is hardly reached since material degradation comes into play at very high shear rates. [23]

A number of viscosity functions were considered for the purpose of injection molding simulation. The simplest model is the power law model [24], proposed by de Waele in 1923 and Ostwald in 1925, which is valid in the shear thinning region, but not able to model the Newtonian region at low shear rates. More commonly used are the Carreau model [25] and the Cross model [26], which was used in this thesis. Both models accurately describe the Newtonian, transition and shear thinning regions. Additionally, the Carreau model captures the lower Newtonian region at ultrahigh
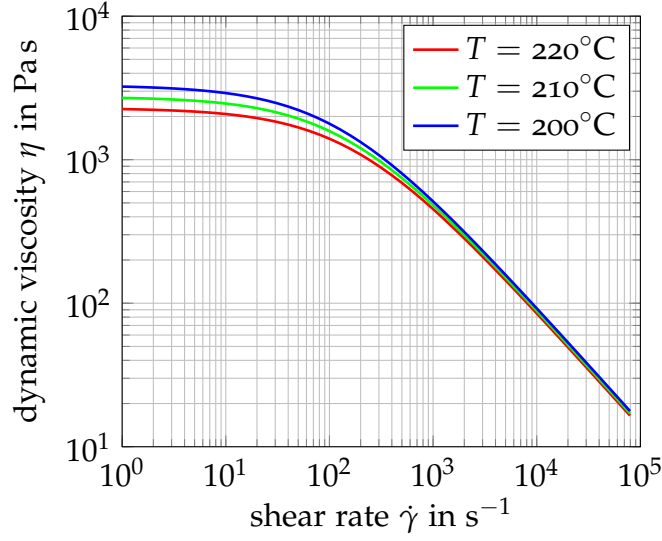
Figure 2.1.: Viscosity over shear rate plot for DuPont Derlrin 127UV at three different temperatures (see A.1.2).

shear rates, which is of little value in most cases. The dependency on temperature is usually modeled by the Arrhenius or WLF [27] equation. The Cross model, in conjunction with the WLF zero-shear viscosity model (often called Cross-WLF model), is widely used for injection molding simulation [28].

The Cross model is given by

$$\eta = \frac{\eta_0}{1 + \left(\frac{\eta_0 \dot{\gamma}}{\tau^*}\right)^{1-n}} \tag{2.8}$$

where $\dot{\gamma}$ stands for the shear rate, τ^* is the critical stress level at the transition to shear thinning, and n is the power law index in the high shear rate regime. The WLF zero shear viscosity model is given by:

$$\eta_0 = D_1 \exp\left[-\frac{A_1(T - T^*)}{A_2 + (T - T^*)}\right] \tag{2.9}$$

with the absolute temperature T, the glass transition temperature $T^* = D_2 + D_3 p$, the pressure p and the model parameters A_1, A_2, A_3, D_1, D_2 and D_3. A_2 is defined as $A_2 = A_3 + D_3 p$. At high pressure, the polymer chains are forced closer together, causing a decrease in mobility. Therefore, the viscosity increases with increasing pressure [23]. The model parameter D_3 takes the pressure dependency of the viscosity into account. The measurement of viscosity at elevated pressures is rather sophisticated, and therefore, rarely performed. Hence, rheological data considering pressure dependency is only available for a fraction of all material grades.

An equation of state $v = v(p, T)$ is needed to model the temperature and pressure dependency of the specific volume of the polymer. The accurate measurement and mathematical representation of the pvT relationship is essential for the prediction of shrinkage and warpage of the molding.

Fig. 2.2 shows a comparison of typical pvT diagrams of amorphous (2.2a) and semi-crystalline (2.2b) polymers. The thermal response is apparently quite different.
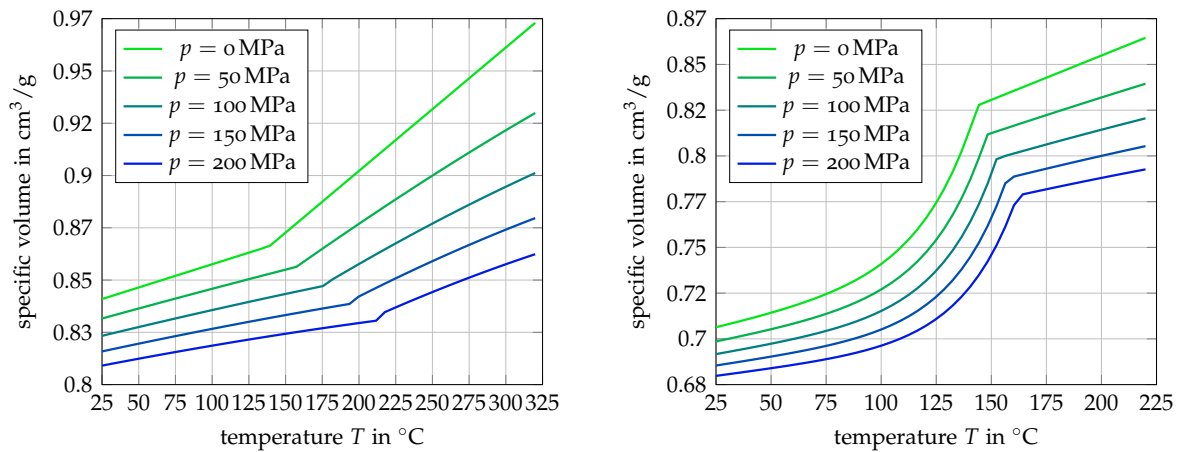
(a) Lexan LS1 from SABIC Innovative Plastics.

(b) Delrin 100 from DuPont at a cooling rate of -0.333 K/s.

Figure 2.2.: The characteristic pvT relationship of amorphous (a) and semi-crystalline polymers (b) the data was taken from the Moldflow Insight material database.

The specific volume of the amorphous polymer is approximately proportional to its temperature. At the glass transition temperature T_g, however, the slope changes abruptly. A phase change does not occur and there is no distinct melting point. With decreasing temperature, the viscosity of the polymer increases until the "glassy" or "frozen" state below T_g is reached. The semi-crystalline polymer shows a distinct change in specific volume at the transition temperature T_t. At this temperature, a phase change from amorphous liquid to crystalline solid takes place. As the name "semi-crystalline" implies, not the whole volume crystallizes. The crystals are embedded in a amorphous matrix. The packing of the polymer chains is denser in the crystalline phase, and its specific volume is therefore lower. A semi-crystalline polymer remains solid until the transition temperature is reached and it then turns liquid when most of the crystals are molten.

In both cases, the pvT relationship is affected by several factors, such as the cooling rate. This is especially true for semi-crystalline grades. The majority of the available material data, however, was measured at a cooling rate in the order of -20 K/min. This is much lower than in the injection molding process. A large amount of research

work was dedicated to the development of test devices, the determination of the pvT relationship under different conditions (such as high cooling rate), and the impact on the simulation results (see for instance [29–34]).

Due to the complexity of the material behavior, the pvT relationship is commonly described by an equation of state, which is fitted to the measured data. This modeling approach does not consider any additional influencing factors (besides pressure and temperature) on the pvT properties of the polymer. The most commonly used model is the 2-domain Tait pvT model [35–37]. It is suitable for amorphous and semi-crystalline polymer grades and given by

$$v(T,p) = v_0(T) \left[1 - C \ln \left(1 + \frac{p}{B(T)} \right) + v_t(T,p) \right] \tag{2.10}$$

where $v(T,p)$ is the specific volume at temperature and pressure, v_0 is the specific volume at zero gauge pressure, $v_t(T,p)$ is only for crystalline resins and applies only below the transition temperature, T is the absolute temperature, p is the pressure, C is a constant (0.0894) and $B(T)$ accounts for the pressure sensitivity of the material.

For ($T > T_t$):

$$v_0 = b_{1m} + b_{2m}(T - b_5) \tag{2.11}$$

$$B(T) = b_{3m} \exp\left[-b_{4m}(T - b_5)\right] \tag{2.12}$$

$$v_t(T,p) = 0 \tag{2.13}$$

and ($T < T_t$):

$$v_0 = b_{1s} + b_{2s}(T - b_5) \tag{2.14}$$

$$B(T) = b_{3s} \exp\left[-b_{4s}(T - b_5)\right] \tag{2.15}$$

$$v_t(T,p) = b_7 \exp\left[(b_8(T - b_5)) - (b_9 p)\right] \tag{2.16}$$

2.1.5. Fiber orientation

Predicting the fiber orientation distribution (FOD) is an important aspect of injection molding simulation. Stiffness and strength properties of an injection molded fiber reinforced part are anisotropic and depend on the fiber orientation. The fiber orientation itself is a result of the manufacturing process, and therefore not known in advance. The injection molding simulation is therefore the missing link between part design and structural analysis. Another aspect that must be considered is the influence of the fibers on warpage. The anisotropy causes differential shrinkage during the molding process, which may lead to excessive warpage of the part. Thus, fiber models are required to predict the fiber orientation state in the molding as well as the elastic and thermal properties of the composite. These orientation dependent properties

are then used for subsequent structural simulations such as warpage and service load analysis. A thorough overview of the basics of fiber orientation modeling can be found in [6].

Early attempts to model the orientation distribution of rigid fibers in a viscous fluid and the experimental validation were performed by Folgar & Tucker III [38]. They used the equation of Jeffery [39] to calculate the motion of ellipsoidal particles immersed in a viscous fluid, and added a rotary diffusion term in order to address the fiber-fiber interaction in concentrated suspensions. Advani & Tucker III [40] introduced the fiber orientation tensor in order to describe the FOD of suspensions containing rigid short fibers. This led to a drastic reduction in the computational effort to calculate the fiber orientation. Darlington & Smith [41] carried out experimental investigations on the FOD in different center-gated cavities by using different resins and varying processing conditions. Among other things, they observed the presence of fiber-free layers. Bay [42] performed measurements of the fiber orientation at different locations of center-gated disks and film-gated strips, and compared them to predictions of a finite difference simulation of the mold filling problem. He found that the model predicts the typical skin-core structure very well, but overpredicts the small out-of-plane fiber orientations and places the core-shell-transition too close to the midplane. Higher accuracy of the FOD prediction was achieved by introducing a new closure approximation. Bay & Tucker III [43] implemented a numerical scheme to consider the effect of the fountain flow on temperature and fiber orientation near the flow front. It was found that the outer skin layer is only predicted when the effect of the fountain flow is considered in the simulation. An experimental validation of the simulation results was presented in Bay & Tucker III [44]. Gupta & Wang [45] performed experimental and numerical investigations on the influence of processing conditions on the FOD of a rectangular thin plate, and derived mechanical material properties based on the predicted fiber orientation. Lee *et al.* [46] investigated the influence of compressibility on the fiber orientation distribution in injection molded products. Zheng *et al.* [47] combined a thermoviscoelastic formulation with an anisotropic rotary diffusion equation for the calculation of the flow induced fiber orientation to predict thermal and pressure induced residual stresses in the molding. The influence of fiber-fiber interactions and coupling between fiber orientation and polymer chain conformation on the rheological properties of the fiber suspension was investigated by Guo *et al.* [48]. They used experiments and numerical simulations to investigate suspensions with fiber volume fractions of up to 35% over a broad range of shear rates. A thorough comparison of measured and predicted FOD on a rectangular plaque with variable thickness was performed by Vincent *et al.* [49]. Polyarylamide with a content of 30 to 50% short glass fibers by weight was used. Wang *et al.* [50] developed an objective fiber orientation model which captures the slow orientation kinetics exhibited in short fiber suspensions. The new model was tested for a variety of flows, and showed an excellent fit to the shear stress transient in

a shear reversal experiment. A further improvement over the standard Folgar-Tucker model was made by Phelps & Tucker III [51], by incorporating an anisotropic rotary diffusion . The model also captures the slow orientation kinetics and has improved FOD prediction capabilities for injection molded long-fiber reinforced composites. Shokri & Bhatnagar [52] experimentally investigated the effect of the post-filling stage on the resulting FOD, while Oumer & Mamat [53] studied the influence of phase change on the numerical prediction accuracy of the FOD. A completely different approach to obtaining the FOD was presented by Yashiro *et al.* [54]. They used a moving particle semi-implicit method to track the motion of individual fibers through the domain. The results were quantitatively compared to x-ray CT data and showed good agreement. Agboola *et al.* [55] performed a numerical evaluation by combining the isotropic (Folgar and Tucker) and anisotropic rotary diffusion model (Phelps and Tucker) with different closure approximations, and by comparing FOD and resulting part stiffness. They found a significant difference in the predicted stiffness between the two rotary diffusion models. Mazahir *et al.* [56] performed measurements and numerical simulations of the FOD on a center-gated disk. They used the standard Folgar-Tucker model and its slip, and reduced strain closure versions, and subsequently found that both models predict the FOD in the steady shell layer very well, but fail to predict the evolution of the fiber orientation in all three layers. Phelps *et al.* [57] presented a model to predict the fiber length attrition during the processing by injection molding of long-fiber thermoplastic composites. The predicted fiber length distribution compared well to measurements on PP with glass fiber moldings.

Two different models used to predict the fiber orientation in the molding are presented below. The standard Folgar-Tucker (F-T) [38] model is widely used and implemented in most commercial molding simulation codes. However, some studies have indicated that the Folgar-Tucker model overpredicts the change of rate of the fiber orientation tensor [58]. Hence, the evolution of the fiber orientation to steady state is not captured accurately and an overprediction of the overall fiber alignment occurs [59]. The Folgar-Tucker model used for the fiber orientation calculation on 3D meshes is given by:

$$\frac{D\mathbf{A}}{Dt} = (\mathbf{W} \cdot \mathbf{A} - \mathbf{A} \cdot \mathbf{W}) + \xi(\mathbf{D} \cdot \mathbf{A} + \mathbf{A} \cdot \mathbf{D} - 2\mathbb{A} : \mathbf{D}) + 2C_I \dot{\gamma}(\mathbf{I} - 3\mathbf{A}) \qquad (2.17)$$

where $\mathbf{A}$ is the second-order orientation tensor, $\mathbf{W}$ is the vorticity tensor, $\mathbf{D}$ is the rate of deformation tensor, ξ is a particle shape factor, C_I is the fiber interaction coefficient and $\dot{\gamma}$ is the scalar magnitude of $\mathbf{D}$. $\mathbb{A}$ is the fourth-order orientation tensor which is not known. A closure approximation is necessary to express $\mathbb{A}$ as a function of components of $\mathbf{A}$ to close the set of evolution equations. Various closure approximations were developed and several were implemented in Moldflow Insight [60]. These include the hybrid closure [40] and four closures based on the family

of orthotropic closures proposed by Cintra & Tucker III [61], namely, the Moldflow Bi-linear model, orthotropic fitted, Moldflow Bi-quadratic model and orthotropic fitted for low C_I.

The fiber interaction coefficient C_I is basically a material property and depends on the volume fraction of the fibers and their aspect ratio. As its name implies, this parameter controls the fiber-fiber interaction, which prevents full alignment of the fibers. A higher C_I leads to a lower orientation magnitude in the first principal direction (it causes a higher degree of randomness). Several empirical relationships were proposed to determine the value of C_I. Based on experiments with different fiber concentrations in simple shear flow, Bay [42] suggested:

$$C_I = 0.0184 \exp(-0.7184 \phi a_r) \tag{2.18}$$

where ϕ stands for the volume fraction and a_r for the aspect ratio of the fibers. Phan-Thien *et al.* [62] performed direct simulations of the fiber suspension dynamics and proposed the following relationship:

$$C_I = 0.03[1 - \exp(-0.224 \phi a_r)] \tag{2.19}$$

Due to the known limitations of the well established F-T model, the Reduced Strain Closure model (RSC) [50, 51] is the second choice for this thesis. The model slows down the evolution of the orientation tensor by reducing the growth rates of the eigenvalues by a constant scalar factor while maintaining the rotation rates of the eigenvectors. The RSC model is given by:

$$\frac{D\mathbf{A}}{Dt} = (\mathbf{W} \cdot \mathbf{A} - \mathbf{A} \cdot \mathbf{W}) + \xi(\mathbf{D} \cdot \mathbf{A} + \mathbf{A} \cdot \mathbf{D}$$
$$- 2[\mathbb{A} + (1 - \kappa)(\mathbb{L} - \mathbb{M} : \mathbf{A})] : \mathbf{D}) + 2\kappa C_I \dot{\gamma}(\mathbf{I} - 3\mathbf{A}) \tag{2.20}$$

with $\mathbb{L}$ and $\mathbb{M}$ being forth-order tensors and functions of the eigenvalues λ_i and the eigenvectors $\mathbf{e}_i$ of the orientation tensor $\mathbf{A}$. They are defined as $\mathbb{L} = \sum_{i=1}^{3} \lambda_i \mathbf{e}_i \mathbf{e}_i \mathbf{e}_i \mathbf{e}_i$ and $\mathbb{M} = \sum_{i=1}^{3} \mathbf{e}_i \mathbf{e}_i \mathbf{e}_i \mathbf{e}_i$. κ is a scalar phenomenological parameter, which must be determined by fitting the fiber orientation to experimental data. [63]

A thorough investigation of the fiber orientation in a chunky part is presented in Chapter 6, where predictions and measurements are compared. The results of this case study confirm the superiority of the RSC over the F-T model.

2.2. The cooling stage

When the gate has finally frozen, the part is still kept in the closed mold until it is stiff enough for ejection. One of the mold's important tasks is the quick and uniform

cooling of the plastic part. The quicker the cooling, the shorter the cycle time, and the higher the productivity of the mold. This is achieved by means of a coolant which flows through cooling lines surrounding the cavity. The temperature of the coolant (in most cases water) is controlled by a temperature control unit. Engineering polymer grades such as PA or POM need elevated mold temperatures to ensure a high level of crystallization and a proper surface finish. There is a heat flux from the injected hot polymer through the mold into the cooling channels. The coolant heats up in areas close to the cavity and will release heat near the boundaries of the mold base, where a heat loss to ambient due to convection and radiation occurs.

Depending on the part shape, it is generally hardly possible to have the cooling lines closely follow the part topology. Conventional cooling lines are drilled into mold plates and inserts. Following a curved face with a straight cooling line is simply not feasible. Cores are often cooled with baffle, bubbler or cooling inserts, which are inserted in drilled holes. [64] Other methods to improve cooling conditions include the use of inserts with higher thermal conductivity, such as chopper alloys [65], or heat pipes. The higher thermal conductivity of the mold material leads to lower temperature gradients and less temperature variation between heat sources and sinks.

More sophisticated production methods like selective laser melting make it possible to build a high number of parallel fed conformal cooling channels with small diameters. These channels can be placed in close proximity to the cavity wall, with fewer restrictions in shape. Scientific research in field of conformal cooling channels in conjunction with additive manufacturing techniques has been conducted by [66–68] and many others. However, even when a constant distance between cavity wall and cooling channel is maintained, the uniform temperature of the cavity wall is not guaranteed. The heat flux density required to ensure a uniform cavity wall temperature is not constant all around the cavity. It depends on part geometry, local wall thickness, crystallization of the polymer, and other influencing factors [69]. Thus, varying cooling rates are present and these will cause an unbalanced stress distribution over the wall thickness of the part. This is one major reason for part warpage [70–73]. When the target simulation results are the necessary cycle time and/or warpage, the assumption of a uniform and constant wall temperature is only valid when the mold's cooling system is highly optimized.

The aim of the mold cooling simulation is to predict the temperature distribution in the mold. It is required in order to optimize the size, number, and location of the cooling lines to achieve cooling conditions over the whole part surface that are as uniform as possible. Moreover, the prediction of the cavity wall temperature distribution is used as boundary condition for the filling, packing and cooling stage of the injection molding process. And so, the impact of the mold cooling design on

cycle time and in-mold stresses is considered. Therefore, the impact of non-uniform cooling on warpage can be investigated.

2.2.1. Modeling mold cooling

The temperature field in all mold components is governed by

$$\frac{\partial T}{\partial t} = a_M \nabla^2 T \tag{2.21}$$

with the thermal diffusivity $a_M = \frac{k_M}{\rho_M c_M}$. k_M is the thermal conductivity, ρ_M the density, and c_M the specific heat of the mold material. There are at least three types of boundaries in every mold: the polymer–mold, the mold–cooling channel and the mold–ambient interfaces. The boundary condition at the melt–mold interface can be written

$$k_M \frac{\partial T}{\partial \boldsymbol{n}} = -q \tag{2.22}$$

with $\boldsymbol{n}$ being the normal vector at the interface and q being the heat flux across the interface. Since q is not known in advance, it must be determined by a coupled transient heat transfer calculation involving polymer, mold and cooling domains. [6]

Equation (2.22) is valid when perfect contact between polymer and mold is assumed. The work of Delaunay *et al.* [74] and Yu *et al.* [75] shows that the thermal contact resistance between polymer and mold is not negligible and a function of time. A perfect contact boundary condition is not feasible even during the filling and packing stages. The presence of thermal contact resistance, which is equal to the reciprocal of the HTC, does affect the growth of the frozen layer, and therefore also the filling pattern, pressure evolution and thermal stress development. According to Urquhart & Brown [76], the flow solution is only sensitive to very low values of HTC and/or for very thin walls, especially in the packing and cooling stages of the molding cycle. Dawson *et al.* [77] quantified the thermal contact resistance at steel-polymer interfaces, including the formation of air gaps. In the case of good contact (which is assumed at the filling stage), HTC values in the order of $10^3 - 10^4$ W/m^{2}K were measured. Calculations by Nylund & Meinander [78] show that HTC values above 2-3 kW/m^{2}K have little influence on the cooling time in the injection molding process. To address the non-perfect contact between mold and melt, equation (2.22) may be rewritten to

$$k_M \frac{\partial T}{\partial \boldsymbol{n}} = -h_c(T - T_m) \tag{2.23}$$

where h_c is the heat transfer coefficient (HTC) at the mold–melt interface and T_m is the bulk temperature of the polymer. Within this thesis, HTC values of 5000 and

$2500\,\mathrm{W/m^2K}$ are assumed at the mold-melt interface during the filling and packing stages, respectively, to address the non-perfect contact between polymer and mold. When the cavity pressure drops to ambient, the HTC value is further decreased to $1250\,\mathrm{W/m^2K}$.

At the mold–cooling channel interface, the boundary condition may be defined as

$$k_M \frac{\partial T}{\partial \boldsymbol{n}} = -h_c(T - T_b) \tag{2.24}$$

where h_c is the heat transfer coefficient (HTC) and T_b is the bulk temperature of the coolant. Due to its numerical efficiency, it is common practice to use a 1-D modeling approach for conventional cooling lines. h_c is then obtained by

$$h_c = \frac{k_c Nu}{d_c} \tag{2.25}$$

where k_c is the thermal conductivity of the coolant, d_c is the diameter of the cooling channel and Nu is the Nusselt number. Nu may be calculated with the Dittus-Boelter equation which is given by

$$Nu = 0.023 Re_{dc}^{0.8} Pr^{0.4} \tag{2.26}$$

with Re_{dc} being the Reynolds- and Pr the Prandtl number. [6] This explicit function is easy to solve and a good approximation for turbulent flows ($Re_{dc} > 10000$) and when the temperature difference between bulk fluid and channel wall is low. This is the case in a properly designed mold cooling system.

For curved 3D cooling channels close to the cavity where h_c will vary with the local coolant velocity, it may be necessary to solve pressure, velocity, temperature and turbulence in the coolant by 3D CFD.

At the mold boundary, a heat loss due to natural convection and radiation takes place. Moreover, conduction causes a heat loss from the mold into the platens of the molding machine. The heat loss to ambient is normally only of interest when high mold temperatures are required. Accurate calculation of the actual heat flux, considering natural convection and radiation, is possible by 3D CFD but extremely time-consuming. Moreover, the temperature distribution between cooling lines and cavity is hardly affected by the heat loss at the mold boundary. It is therefore more common to assume a HTC based on experience. In this case, the boundary condition is given by

$$k_M \frac{\partial T}{\partial \boldsymbol{n}} = -h_a(T - T_a) \tag{2.27}$$

where T_a is the ambient temperature and h_a is the HTC value, which is in the order of $10\,\mathrm{W/m^2K}$.

2.2.2. Solving the governing equations

Solving the temperature field in the mold is commonly done by using either the Boundary Element Method (BEM) [79] or the Finite Element Method (FEM) [80]. A detailed description of these methods is beyond the scope of this thesis and is found elsewhere [5]. In the following section, only the main pros and cons of each method are discussed.

Boundary Element Method

The basic idea of the boundary element method is the transformation of the governing equation (2.21) into an integral equation only dependent on boundary values. Therefore, only the domain boundaries require discretization and must be meshed. This is a major advantage since meshing the volume of the mold components requires considerable effort. However, this method is restricted to steady state temperature fields and is therefore only suitable to determine a cycle-averaged mold temperature field. [81]

Finite Element Method

Solving the temperature distribution in the mold using FEM requires a volume mesh. Therefore, the modeling effort for the cooling simulation is substantially higher. The main advantage of this approach is the ability to predict the transient temperature distribution in the mold. There are basically two ways to do this.

The more efficient (and in most cases sufficiently accurate way) is to assume that the cavity is instantly filled. This is normally a reasonable simplification since the injection time is usually very short compared to the cycle time. In this case, the filled cavity is treated as a solid body that has the melt temperature at the very start of the cycle. Then, only equation (2.21) must be solved over all domains to complete the cooling simulation and obtain the thermal boundary conditions at the cavity wall for use in the filling, and packing simulations. Either a cycle averaged, or a transient mold temperature distribution can be obtained with this method. One of its drawbacks is that additional heat introduced by shear in the polymer melt is not considered. [82] Due to the relatively low computational cost, this decoupled approach was used throughout this thesis with few exceptions.

A coupled simulation must be performed, if the effect of mold filling and viscous dissipation on the transient temperature field in the mold, has to be considered. In this case, the mold temperature is solved together with the polymer flow at each time step. To achieve a steady-state cyclic condition, several injection cycles must be

calculated. Hence, this method is extremely computationally demanding. [82] This method was used for the case study presented in Section 5.2, where the predicted mold temperature was compared to measured temperature profiles. Both methods are available in Moldflow Insight under the analysis step called "Cool (FEM)".

2.3. Modeling warpage

During the filling, packing and cooling stages of the injection molding process, stresses build up in the part constrained by the mold. As long as the part is in the mold, the integral of stresses over part thickness is always balanced with the external forces applied by the mold walls [6]. When the part is ejected, deformation of the part is no longer restricted and this results in shrinkage and warpage.

Shrinkage means that the part has the same shape as the cavity while its dimensions are smaller. Warpage, on the other hand, means that the part changes its shape (out-of-plane deflection). Shrinkage and warpage are closely related since warpage is caused by non-uniform shrinkage. [71]

The reliable prediction of the shrinkage and warpage of complex injection molded parts is still a major challenge. Due to the complexity of the thermoplastic material behavior and the simplifications and assumptions which are therefore necessary in the numerical model, there are numerous factors which affect the accuracy of the numerical warpage prediction. Among them are material properties, fiber orientation, crystallization, processing and cooling conditions, as well as modeling and numerical errors. All of these topics are an active field of research, and significant improvements in warpage prediction have been made already. Numerous research papers have been published which deal with the prediction of the warpage of injection molded products. Many of them focus on optimization methods and/or surrogate models to predict warpage and determine an optimal set of process parameters to minimize part warpage. Huang & Tai [83] used the injection molding simulation software C-Mold and design of experiments (DOE) to investigate the influence of the molding conditions on the warpage of the part. Subramanian *et al.* [84] showed a complex optimization method to minimize the warpage of an optical housing by modifying the mechanical design of the part, gate location, and process conditions based on C-Mold predictions. Kurtaran *et al.* [85] determined optimal processing conditions using Moldflow software in conjunction with DOE, an artificial neural network, and a genetic algorithm. Numerical warpage predictions were also validated with measurements of the molded parts. Ozcelik *et al.* performed an optimization for minimal warpage of a thin walled part considering the gate location as an additional design variable in [86] and added structural analysis in [87]. Chen *et al.* [88] also investigated the influence of processing conditions on the warpage of a thin-shell

plastic part. They found melt temperature and packing pressure to be the most significant factors. Ahn *et al.* [89] determined optimal processing conditions for minimal warpage considering the core shift effects in the mold. Deng *et al.* [90] integrated injection molding simulation with a global optimization algorithm in order to obtain the optimal process conditions for minimal part deflection in a computationally efficient manner. Guo *et al.* [91] developed a mathematical model based on design of experiments (DOE) and CAE to predict the warpage of a car housing trim for various processing conditions. Wang *et al.* [92] predicted sink marks and the warpage of parts produced by a rapid heat cycle molding process (RHCM) using Moldflow. They derived the optimal processing conditions for minimal warpage through DOE. Liu *et al.* [93] made an attempt to investigate the influence of process conditions on shrinkage and warpage separately. A simple box shaped part was molded under varying process conditions and measurements of both shrinkage and warpage were carried out. The experimental results were compared to numerical simulations. It was found that the response of shrinkage to process conditions is different to that of warpage.

Both amorphous as well as semi-crystalline polymers typically show a viscoelastic material response [94]. The mechanical behavior and its physical properties vary with temperature and time. A viscous-elastic [95–97] or viscoelastic model [98–101] can be used to calculate pressure-induced and thermal stresses. These stresses are applied as initial conditions to the FEM model of the unconstrained (demolded) plastic part. The equilibrium state of residual stresses and the deformation of the ejected and cold part is calculated.

A linear thermoviscoelastic model, with the assumption of thermorheological simplicity, is given by

$$\sigma_{ij} = \int_0^t C_{ijkl}\left(\xi(t) - \xi(t')\right)\left(\frac{\partial \epsilon_{kl}}{\partial t'} - \alpha_{kl}\left(\xi(t) - \xi(t')\right)\frac{\partial T}{\partial t'}\right)dt' \qquad (2.28)$$

where C_{ijkl} is the 4th order stiffness tensor, t and t' are time variables, T is temperature, α_{kl} is the tensor of thermal coefficients of expansion and $\xi(t)$ is the pseudo-time scale:

$$\xi(t) = \int_0^t \frac{dt'}{a_T} \qquad (2.29)$$

where a_T is the time temperature shift factor, which accounts for the temperature effect on the material response. [4]

Thermorheological simplicity is present when all relaxation mechanisms have the same temperature dependence, and therefore the change in linear viscoelastic behavior of the material, as a function of temperature, corresponds to shift in logarithmic

time scale [4, 102]. A large number of real materials are not thermorheologically simple and, therefore, the determination of the relaxation functions is not possible [103]. The main advantage of this constitutive relation is the ability to predict stress relaxation during the packing and cooling stages due to in-mold constraints.

A viscous-elastic, or thermo-elastic, model is commonly used to overcome the issue of viscoelastic material characterization. This model requires a transition or no-flow temperature T_t to distinguish between melt and solid states. Above this temperature, the material does not sustain stress, while below this temperature the material is assumed to be elastic. The model is given by

$$
\sigma_{ij} = \begin{cases} 0 & \text{for } T \geq T_t \\ \int\limits_0^t c_{ijkl}^e \left(\frac{\partial \epsilon_{kl}}{\partial t'} - \alpha_{kl}(t') \frac{\partial T}{\partial t'} \right) dt' & \text{for } T < T_t \end{cases}
\tag{2.30}
$$

Were σ_{ij} is the stress tensor, ϵ_{kl} the total strain tensor, c_{ijkl}^e the stiffness tensor, t' is the time and T the temperature.[4]

A major problem is the determination of T_t; since it is not a physically clearly defined material property, different methods have been suggested to determine T_t. A common way is to derive the transition temperature from DSC (differential scanning calorimetry) measurements of the polymer. [104] T_t will also depend on pressure, cooling rate, and even the thermo-mechanical history the polymer has experienced. This is especially true for semi-crystalline polymers [105].

The model provides significant simplification and the ability to give a good qualitative description of the stress state [106] and part warpage, as will be shown in this thesis.

To predict shrinkage and warpage of a fiber-filled polymer, it is necessary to model the anisotropic mechanical and thermal properties of the composite with respect to fiber orientation. The tensors c_{ijkl}^e and α_{kl} depend on the fiber orientation state and must be calculated by a micro-mechanics model and a thermal expansion coefficient model, respectively. Investigations performed by Tucker III & Liang [107] led to the conclusion that the Mori-Tanaka model [108] is the best model for injection molded composites. The Mori-Tanaka model and the Rosen-Hashin model [109] are used throughout this thesis to compute the properties of the composite from the properties of matrix and inclusions.

3. Case studies - prediction vs. measurement

A selection of case studies performed by the author is presented in this section. Each study focuses on different aspect of injection molding simulation. The numerical models are described in detail and the results are compared to measurements. Suggestions for proper modeling were derived and are summarized at the end of this chapter.

All of the parts investigated feature large variations in wall thickness in addition to complex geometry. Following the naming convention described in the introduction, they are "chunky". Therefore, none of these parts was suitable for a 2,5 D simulation as described in Section 2.1.1. Thus, a full 3D simulation was performed in all studies. POM and glass-fiber-reinforced PA6 with various fiber contents was used in those studies. With only one exception, all the simulations presented in this chapter deal with parts where molds already existed. Process settings and boundary conditions were therefore defined in accordance with the molding trials performed with each mold. All case studies presented in this chapter are based on "real" parts for "real products" (they were not intended to serve academic research) made with production molds. For this reason, the molds were not equipped with temperature or pressure sensors.

One important result of the injection molding simulation is the prediction of part warpage. In most of the cases, the primary target was to predict warpage as accurately as possible. Using parts with existing molds enabled the investigation of influencing factors like processing parameters, material properties, mesh and solver settings on the accuracy of the solution with experimental validation. The ultimate goal of injection molding simulation tools is the accurate prediction of the final part dimensions and shape (shrinkage and warpage). If this is could be achieved with reasonable accuracy, warpage could be detected and compensated for before the mold was built. Such a case is shown in Section 3.7. In this case, boundary conditions and processing settings for cooling, filling, packing and warpage analysis were estimated. The simulation results were then used to improve the part design, for the selection of a proper gate location, and finally to compensate for warpage. This was done by deforming the 3D CAD representation of the part (the target shape and dimensions of the molding) in the opposite direction of the warpage.

The chapter is also intended to highlight the sensitivity of the simulation results on process conditions, material data and modeling approach for different polymer grades. This knowledge is of great practical importance. It helps to estimate the error of the numerical results caused by estimated simulation settings.

3.1. Material data

The accurate description of the material behavior during the simulated molding process relies on accurate material data. All the material data used for the simulations presented in this thesis was taken from the Moldflow Insight Material Data Base and is also provided in Appendix A. This database also provides some information about the source of the material data and the measurement methods used. Additionally, a quality indicator is given for the analysis steps filling, packing and warpage. It is bronze, silver or gold[1] and reflect the quality of the material data provided. Using a material with gold status means using accurate data based on measurements of the specific grade. It is therefore a requirement for reliable and accurate simulation results. However, due to the abundance of different material grades, a complete set of measured material data is rarely available. Therefore, materials with silver status were also used in this thesis. Showing the impact of material data on the accuracy of the simulation results is one major aim of this thesis. For this reason, some of the case studies were performed with different material grades with different quality indicators.

3.2. Measurements

Several measuring techniques were used to gain experimental data for the validation of the numerical models. These will be briefly described in the following sections.

Temperature, pressure and volume flow rate of the coolant

The volume flow and the inlet and return temperatures of the cooling circuits were measured by a magnetic-inductive flow meter and PT100 temperature sensors, respectively. The measurements were used to obtain proper boundary conditions for the simulation model, but were not used for validation purposes.

---

[1]A bronze status means, for instance, that the material data provided is incomplete, or that it was derived from a similar grade. Gold status implies that all the critical material properties were actually measured.

Measurements of the cavity pressure were obtained by using Kistler pressure sensors with a measurement uncertainty of 1%. Temperature measurements in the mold (see Section 5.2.3) were carried out using type k thermocouples with a diameter of 1.5 mm. Their measurement uncertainty was ± 1 K.

Dimensions of molded parts

Validation of shrinkage and warpage results is a difficult task due to the complex geometry of the parts and their 3D deformation modes. An optical 3D-scanner of the type ATOS II 400 from GOM, Germany was used to capture the parts' surface geometry with high accuracy and speed. It generates a dense point cloud representation of the objects' surface, which is further processed to a polygon mesh. The accuracy of the system depends on the objects' size. All scanned parts presented in this thesis have approximately the dimension of a human fist. It was found that, in this case, the measuring uncertainty was less than 0.05 mm. Hence, the accuracy of the measurements is sufficient to validate the accuracy of the warpage predictions. The digital surface description of the real molding was then compared to the surface mesh of the virtually molded part (the part shape predicted by Moldflow). This 3D comparison was performed using the commercial software Geomagic Qualify:

> Geomagic® Control™ (formerly Geomagic Qualify®) enables manufacturers to perform fast, accurate graphical comparisons between digital reference models and the scans and probes of as-built parts for first-article inspection, production inspection and supplier quality management. [110]

A digital caliper was used to measure and compare certain dimensions where the geometry of the moldings allowed a measuring uncertainty of below 0.05 mm.

Voids and fiber orientation

Industrial computed tomography (CT) was used to gain insight into defects inside the moldings and to obtain experimental fiber orientation data.

The case study presented in Section 5.1 deals with the formation of voids and porous zones in chunky parts. A μCT device RayScan 250 XE was used to check the molded parts for such defects. The scans were performed using a voxel edge length of 65 μm. The μCT data was analyzed automatically using the software VG Studio MAX 2.2, applying the defect detection tool. The process is non-destructive and gives an accurate description of the actual void volume.

A common technique to obtain the 3D fiber orientation is the analysis of polished cross sections by either optical or scanning electron microscopy. A fiber with a certain

angle to the cutting plane will appear as an ellipse. Assuming that each fiber is a straight cylinder, the 3D orientation is reconstructed by measuring the length and angle of the semi-axes. However, this method has several drawbacks. The image processing must be able to remove fragments of broken fibers, fibers that are cut at the tip, and split touching fibers. A rotation of the fiber of π around the minor axis will give exactly the same ellipse. By using different cutting planes or by investigating two cross sections after successive polishing, this ambiguity can be cleared up. In the case of scanning electron microscopy, the fiber below the cross section appears as a shadow at one of the ellipses tips. This method was successfully used by Hine *et al.* [111] and Eberhardt *et al.* [112]. Chapter 6 deals with the measurement and prediction of the fiber orientation in a 3D geometry. A sub-µm device Nanotom (GE Phoenix x-ray, Germany) was used to experimentally determine the fiber orientation. In contrast to the classical methods mentioned above, the CT data makes it possible to analyze a volume rather than just cross sections. From the CT data, the start and end points of all fibers are extracted and used for the calculation of both fiber orientation distribution (FOD) and fiber length distribution (FLD). The necessary resolution depends on fiber diameter, fiber length and the difference in density between filler and matrix. The mean diameter of the glass fibers is in the order of 10 to 20 µm. For the determination of fiber length distribution, a voxel size of 2 µm was chosen, whereas a voxel size of 3 µm was chosen to determine fiber orientation. Previous studies by Salaberger *et al.* [113] have shown that these are good compromises between resolution and measuring volume. The method was validated for a glass fiber content of up to 30% per weight and successfully used in [114] and [115].

Gate seal time

The gate-seal time was determined by gradually increasing the packing time and weighing the molded parts. When no significant increase in part mass was observed, the gate-seal time was defined as injection time plus current packing time.

3.3. Case Study: Mesh dependency - Material properties - Process settings

The first case study demonstrates the influence of mesh density on the solution. It provides additional information on warpage prediction in reference to the theory given in Chapter 2.3. The material properties data needed for warpage calculation is provided and its influence on the result is shown and discussed. Furthermore, the impact of packing pressure on warpage is highlighted.

As for all case studies presented in this thesis, a mesh convergence study was performed for this part to ensure valid results. The main conclusions derived from this study apply to all of the investigated parts. Therefore, the mesh convergence study is covered in detail only for this part . The aim of the mesh convergence study is to investigate the influence of the mesh density on the solution accuracy of the filling, packing, and warp analyses. This procedure is necessary to determine the optimal mesh density for a high solution accuracy while maintaining an acceptable degree of computational effort. The study was performed using Moldflow Insight release 2012. It was found that Moldflow has a very low mesh dependency and provides reliable results even on coarse meshes and in case of poor mesh quality. This is a major advantage of the finite element method, which Moldflow uses for all analysis steps. The FEM approach does not enforce the governing laws for each element. Instead, the method seeks to find a solution which satisfies the imposed differential equations in an average sense by considering the whole computational domain[80]. Therefore, inaccuracies due to a few elements of low quality hardly affect the global solution. This is not the case for finite volume method based codes, such as Moldex 3D [116] or Sigmasoft [117]. These codes require high quality meshes and a single poor element may cause divergence of the solution.

As pointed out in Section 2.3, the commonly used viscous-elastic model represents a severe simplification of the real material behavior. The solidified material is treated by the warp solver as elastic solid assuming constant mechanical properties, independent of temperature. These mechanical properties are the Young's modulus and the Poissons ratio in 1st and 2nd principal direction, the shear modulus and the transversely isotropic coefficient of linear thermal expansion in 1st and 2nd principal direction (see equation 2.30). These properties directly affect the predicted thermal in-mold stress, and, therefore, shrinkage and warpage. Hence, the influence of these properties on warpage was also investigated, and the results are presented in this section. To show the impact of pressure induced stresses on warpage, the packing pressure was also varied.

A final simulation using an optimal mesh, modified material properties, and process settings derived from the experiment was performed. Virtual short-shots were compared to real short-shots and the predicted part shape was compared to 3D scan data of the real molded part.

The investigated part was molded in a 4-cavity mold with two hot runner drops feeding a cold runner for two cavities. It was molded from DuPont Delrin 127UV, a POM grade with UV stabilization and improved impact toughness. Each cavity was gated by two submarine gates. Fig.3.1 shows two different views of the part with overall dimensions of about $72 \times 61 \times 26\,\mathrm{mm}^3$. The part has sections with thin walls in the order of 2 mm in proximity to the gate as well as very thick walls (up to 8 mm) at the two arms.

(a) View of the cavity side of the part showing its overall dimensions in mm.

(b) View of the core side of the part.
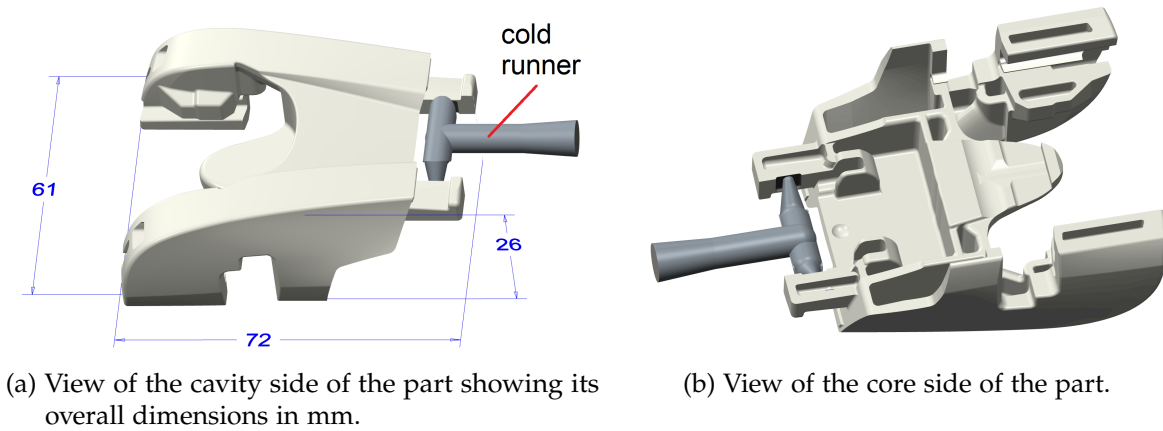
Figure 3.1.: CAD model of the investigated part including parts of the cold runner system.

3.3.1. Numerical model

The accurate prediction of warpage is the primary goal of this study. Due to the high computational cost of a full 3D simulation, one can choose to simulate the whole 4-cavity mold with very low detail or just one cavity with high detail. The main advantage of simulating the whole mold is the potentially good prediction of the temperature distribution throughout the mold. Considering warpage, an accurate prediction of the cavity wall temperature is absolutely sufficient. Therefore, the numerical model comprises just one of the 4 cavities and the surrounding cooling channels. The numerical model is depicted in Fig. 3.2.
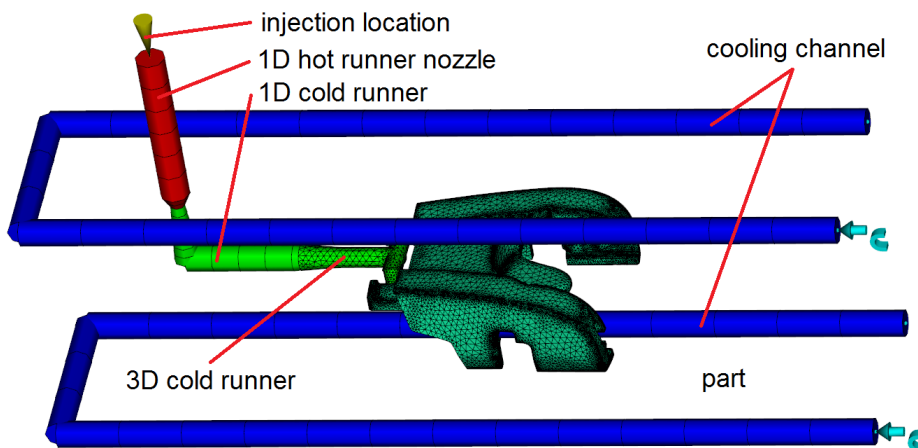
Figure 3.2.: Numerical model of the investigated part featuring one cavity, cold runner, and cooling channels.

28

The volume of the part, including the tunnel gates, is meshed with a 3D tetrahedral mesh to capture 3D flow and shear heating effects. The other part of the cold runner and the hot runner nozzle are meshed using beam elements to reduce the computational cost. The volume around part and cooling channels is filled with a tetrahedral mesh to obtain the temperature distribution in the vicinity of the cavity (not shown in Fig. 3.2).

3.3.2. Material data

According to the experimental molding trials, the simulations were performed using material data for DuPont Delrin 127UV. A full description of the material data and the model parameters used for this study is given in A.1. Due to the issues involved in modeling viscoelastic materials (as pointed out in Section 2.3) the simpler viscous-elastic model was used throughout this thesis. Therefore, the Cross-WLF model was used to model viscosity and the 2-domain Tait model served as the equation of state (see Section 2.1.4 for details about the models) in all cases.

3.3.3. Process settings and boundary conditions

Process settings and boundary conditions were set in accordance with the experimental molding trials, although some assumptions must be made since only one cavity of the 4 cavity mold is actually modeled.

A packing pressure of 120 MPa (at the tip of the screw) was defined for the molding trials. The pressure loss through machine nozzle and hot runner (which are not part of the numerical model) was estimated to be 50%.

In contrast to the experiment, the volume flow rate of the melt is just 25% for the numerical model. It is therefore more convenient to define a relative ram speed profile for the filling control in the simulation model. This definition is independent of the actual molding machine (screw diameter and stroke) and the number of modeled cavities (volume to be filled). The equivalent relative ram speed profile used for the simulation with a target injection time of 7.1 s is depicted in Fig. 3.3.

The cooling circuits of each mold half were connected with two separate temperature control units. Inlet and outlet temperatures of the coolant were measured by PT100 temperature sensors. The volume flow rate of each circuit was measured by a magnetic-inductive flow meter.

The process settings and boundary conditions used for the simulation are summarized in Table 3.1.
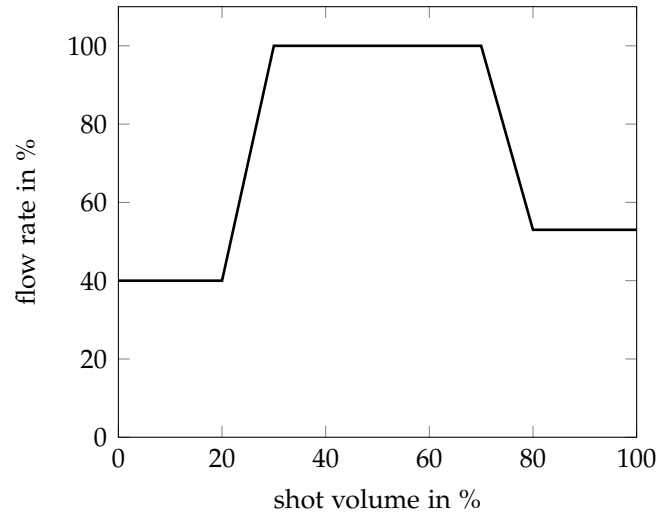
Figure 3.3.: Relative ram speed profile associated with an injection time of 7.1 s.

Cooling analysis	
Melt temperature	215°C
Injection + packing + cooling time	92.1 s
Mold-open time	19 s
Coolant	Water
Coolant temperature cavity side	57°C
Coolant volume flow rate cavity side	2.6 l/min
Coolant temperature core side	52.5°C
Coolant volume flow rate core side	4.4 l/min
Fill + pack analysis	
Injection time	7.1 s
Velocity/pressure switch-over	at 99.9% of the volume filled
Packing pressure	60 MPa
Packing time	45 s

Table 3.1.: Applied process settings and boundary conditions.

3.3.4. Solver settings

The analysis sequence used was: Cool (FEM) + Fill + Pack + Warp. In this section the selected settings for each analysis step are briefly described. Most of the settings presented here worked well and were used for all case studies.

Cool (FEM)

The uncoupled approach of the cooling analysis was used. Pure heat conduction in cavity and mold is assumed, as described in Section 2.2.2 . A steady-state cyclic transient temperature distribution in mold and part is obtained by this analysis step. All solver parameters were left to default except the number of part heat flux time steps, which was set to 30. The cavity wall temperature obtained for these time steps is passed to the next analysis step as a boundary condition.

Fill + Pack

The full Navier-Stokes equations, including compressibility and inertia, were solved on the 3D mesh. Only gravity was neglected. All default solver parameters were retained.

Warpage

Moldflow features a warp solver for small and large deflections, whereas the large deflection solver is capable of handling geometric nonlinearities such as buckling. Normally, the small deflection solver should provide reasonable results. However, for the highest accuracy, and for parts which may show unstable behavior with large deformations, the large deflection solver must be used. [118]

Furthermore, it is possible to upgrade the first order elements (4 nodes) used by the flow solver to second order elements (10 nodes) for improved accuracy. When using only first order elements, the stiffness of the part will be over predicted due to the shear locking problem [80], especially in thin walled regions. High aspect ratios of the elements may further worsen the accuracy of the warpage prediction, but are unavoidable in areas with thin walls to keep the element count acceptable. [118]

If all of the elements are upgraded to second order, the computational effort for solving the equilibrium equations vastly increases. For this reason, Moldflow has the option "mesh aggregation". When this feature is activated, first order elements in thin walled regions are collected and replaced by fewer second order elements,

while elements in heavy walled sections of the part remain untouched. This feature provides a good balance between accuracy and computational effort. [119]

In the following case studies with compact chunky parts, the difference between the small deflection solver using linear elements and the large deflection solver with quadratic elements was less then 15% of the total deflection magnitude. For parts which may show buckling behavior, this is not true.

All of the results given in this thesis were obtained with the large deflection solver at default settings and with the option of automatic upgrade to second order elements. With these settings, the best warpage predictions were obtained in all cases, although at a significantly higher computational cost.

3.3.5. Mesh

The model was finally meshed based on the findings obtained by a mesh convergence study which is summarized in what follows.

Mesh convergence study

Using Moldflow, the governing equations presented in Chapter 2 were solved on 1D beam and 3D tetrahedral (volume) elements. The meshing or spatial discretization of the different domains (part, runner, mold, ...) plays a critical role in the solution process and the accuracy of the results. Therefore, three meshes with different densities were generated to investigate the mesh dependency of the solution. The cooling system of the mold was not considered for this mesh convergence study.

Coarse mesh with poor element quality

The first mesh is rather coarse and generated without manual attempts to improve element quality. Only the Moldflow Mesh repair wizard was used to check for severe issues like inverted elements and correct them. Hence, meshing was completed after a few minutes.

The recommended value of at least 6 element layers across the part thickness was applied. Fig. 3.4a shows the resulting mesh comprising 156503 tetrahedral and 12 beam elements. Fig. 3.4b shows the element distribution inside the part, with the satisfying number of 6 elements across the thickness. The small fillets and the other fine details of the model call for elements of high aspect ratio. While the recommended

threshold of aspect ratio for 3D elements is 100, the actual mesh has a max. aspect ratio of more than 900.

Table 3.2 provides a summary of 3D mesh details and the actual element quality of the coarse mesh.

(a) Coarse mesh comprising about 156500 tetra-hedral elements.

(b) Sectional view of the mesh at the symmetry plane showing the layered element structure.
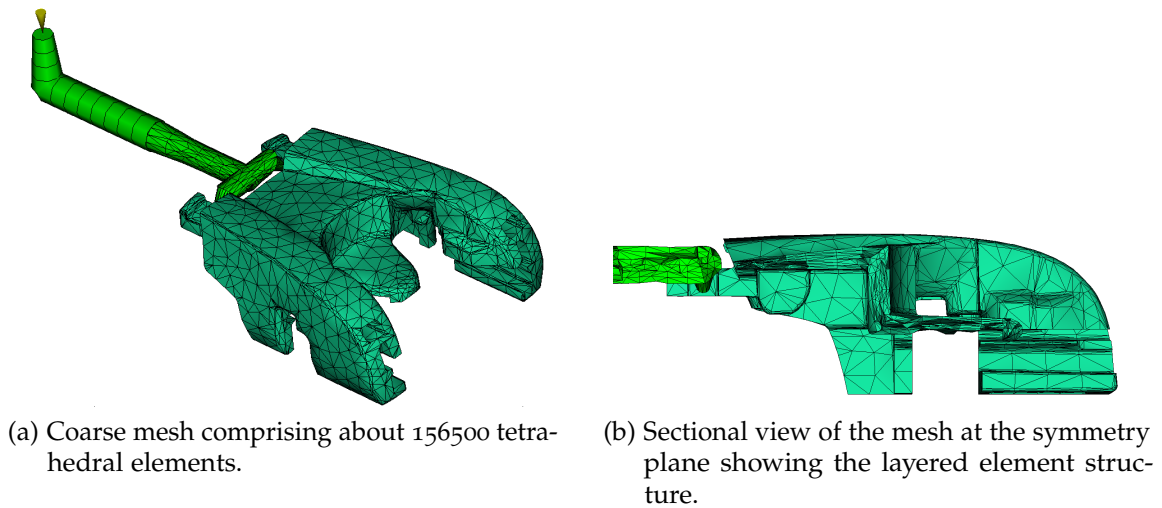
Figure 3.4.: Coarse mesh with poor element quality.

Element count	156491
Nodes	27722
Minimum number of elements through thickness	6
Bias	no
max. aspect ratio	910.7
average aspect ratio	7.09
min. aspect ratio	1.08
max. dihedral angle	179.1

Table 3.2.: Mesh properties and diagnostics of the coarse mesh.

Medium mesh with optimal element quality

To improve the aspect ratio of the elements, the second mesh was generated with a smaller edge length and in two steps. First, a surface mesh was generated and checked for issues. The aspect ratio of the triangles was then improved by means of manual mesh manipulation, such as merging nodes, or swapping edges. When a sufficient mesh quality was obtained, the next step was to generate the 3D mesh. Following this procedure, the element quality of the 3D mesh is usually much better.

The default value 6 was kept for the recommended number of elements through the thickness. The resulting mesh has 293438 tetrahedral elements and is show in Fig. 3.5a. All quality prerequisites are satisfied.
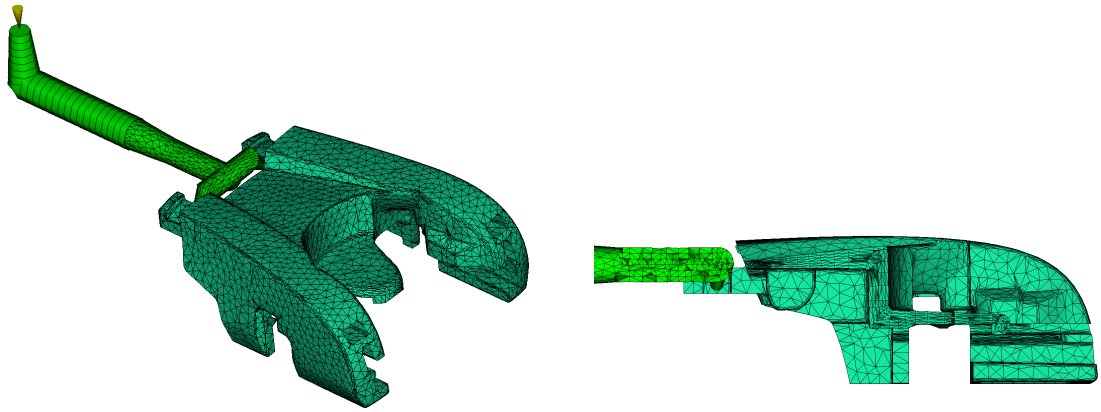
(a) Medium mesh comprising approximately 293000 elements.

(b) Cut through the mesh showing six element layers across the part thickness.

Figure 3.5.: Medium mesh with optimal element quality.

Table 3.3 provides a summary of 3D mesh details and the actual element quality of the medium mesh.

Element count	293438
Nodes	52368
Minimum number of elements through thickness	6
Bias	no
max. aspect ratio	68.3
average aspect ratio	5.36
min. aspect ratio	1.06
max. dihedral angle	176.7

Table 3.3.: Mesh properties and diagnostics of the medium mesh.

Fine mesh with optimal element quality

The fine mesh was generated in the same manner as shown in Section 3.3.5. To further improve the aspect ratio as well as the resolution of the mesh, the global edge length was once again reduced, and the number of elements through thickness was increased to 10. The fine mesh is shown in Fig. 3.6a while Fig. 3.6b reveals the element distribution through the part thickness.

(a) Fine mesh comprising about 1450000 elements.

(b) Cut through the mesh revealing 10 element layers across the part thickness.
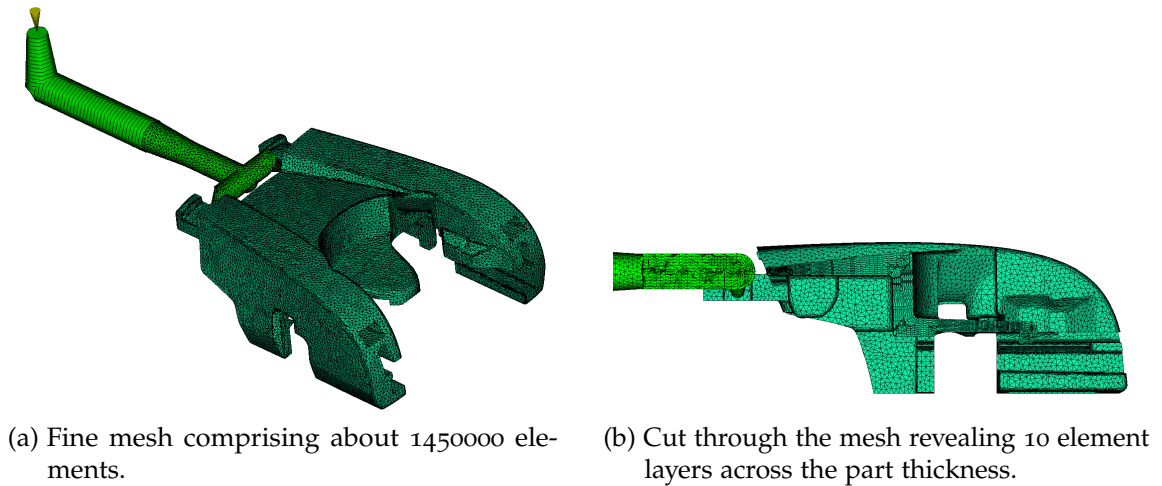
Figure 3.6.: Medium mesh with optimal element quality.

Table 3.4 provides a summary of 3D mesh details and the actual element quality of the fine mesh.

Element count	1449698
Nodes	253555
Minimum number of elements through thickness	10
Bias	no
max. aspect ratio	57.4
average aspect ratio	4.51
min. aspect ratio	1.05
max. dihedral angle	176.1

Table 3.4.: Mesh properties and diagnostics of the fine mesh.

Results of the mesh convergence study

The solution converged on both the coarse and poor quality mesh without any issues. This is a major advantage of the finite element method. From all the results obtained with the different meshes, four critical ones are compared and presented in this section. These are:

- The filling pattern: It is valuable to predict the location and properties of weld lines (see Chapter 7), for the detection of air traps as well as racetracking and hesitation effects [71].

- Pressure traces at two different locations of the cavity: An accurate prediction of the pressure history is essential for a good prediction of pressure induced stresses.
- The volumetric shrinkage averaged over the local wall thickness: Shows the variation of volumetric shrinkage over the whole part and therefore the potential for the occurrence of warpage, sinkmarks and voids.
- The total deflection magnitude (the superposition of shrinkage and warpage): Is the most critical result because it reveals the final dimensions of the molded part at room temperature. The deformed part shape can be used to determine whether or not the required size tolerances have been achieved. This result is the basis for modifications to the part geometry to compensate for warpage before the mold is actually built.

Filling pattern

Fig. 3.7 and 3.8 show the predicted flow front for the three meshes at certain time steps. The result obtained with the coarse mesh is somewhat asymmetrical, which is probably a consequence of the very poor mesh quality. The shape of the flow front is almost identical with all three meshes, although it gets smoother with increasing mesh density. Despite this, there is hardly any improvement from the medium to the fine mesh.

(a) Coarse mesh   (b) Medium mesh   (c) Fine mesh
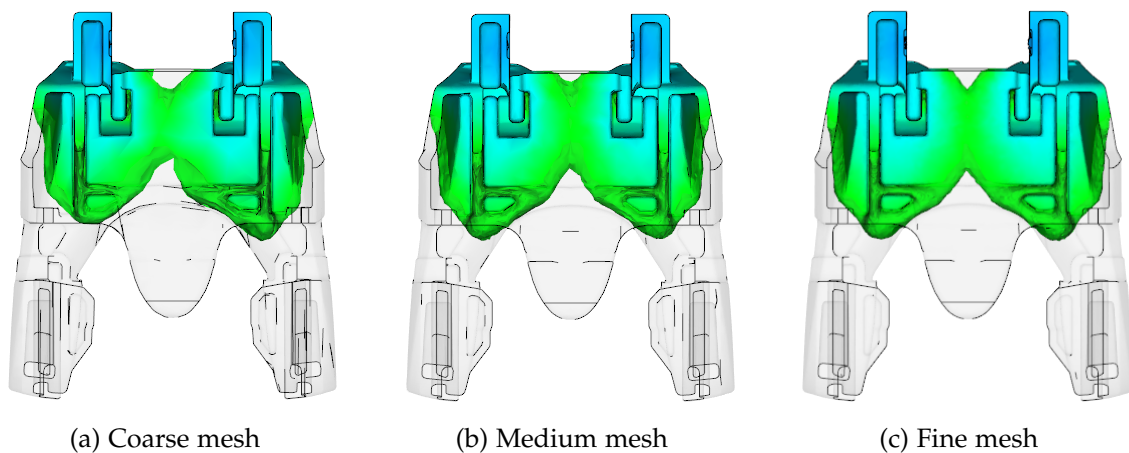
Figure 3.7.: Predicted flow front at 2.5 s.

(a) Coarse mesh   (b) Medium mesh   (c) Fine mesh
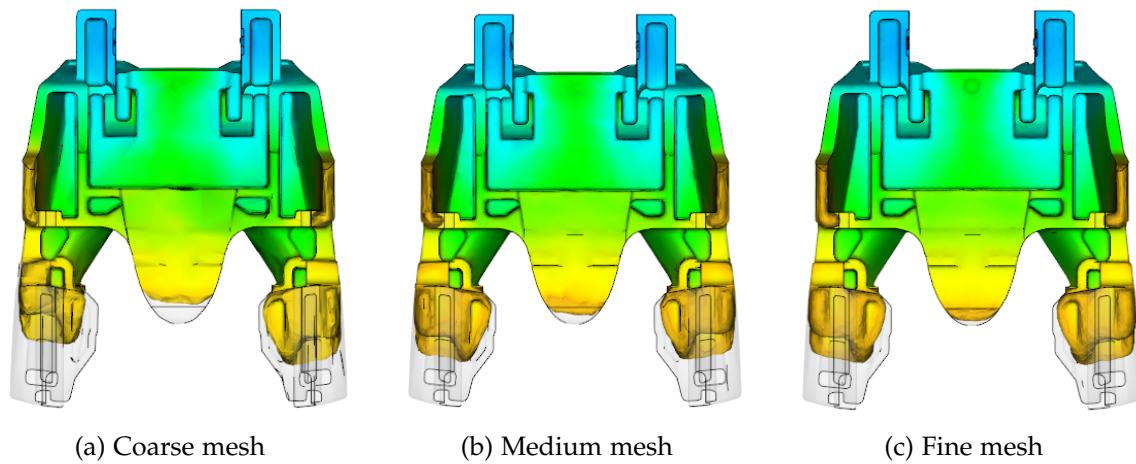
Figure 3.8.: Predicted flow front at 4.5 s.

Pressure history in the cavity

Fig. 3.10 shows the predicted pressure history on the three meshes at the locations shown in Fig. 3.9. Remember, the same process settings were applied in all three cases. The predicted rise in pressure during the filling phase and the peak pressure in the early packing phase is almost identical with the three meshes. Hence, the influence of the mesh density on the predicted pressure drop is very low. When the material cools down in the later packing phase, deviations between the three solutions arise.
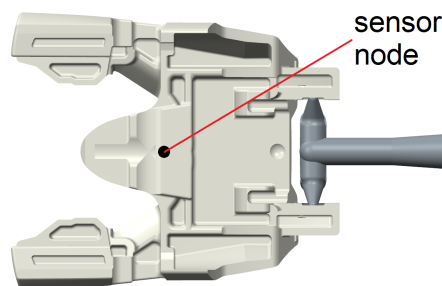
Figure 3.9.: Location of the pressure evaluation.

Volumetric shrinkage

Fig. 3.11 shows the volumetric shrinkage averaged over the local wall thickness. With increasing mesh density, the variation of volumetric shrinkage becomes larger. Regions with high wall thickness and therefore high shrinkage are clearly visible

(a) Pressure history in the filling stage.

(b) Pressure history in the packing stage.
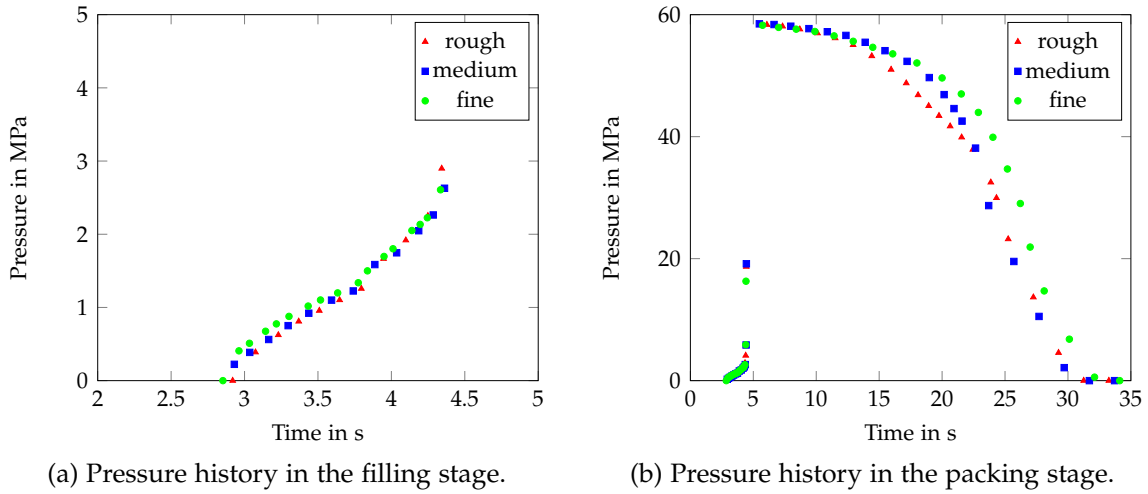
Figure 3.10.: Predicted cavity pressure history for the three meshes.

on the fine mesh. On the coarse mesh with the large distance between its nodes, the solution looks blurred. Large areas of high volumetric shrinkage in the order of 10% are visible at the thick walled regions of the part. The fine mesh, on the other hand, clearly shows the real spots of very high shrinkage with maximum values of approximately 16%. These are the spots where sink marks and/or voids can be expected.

(a) Coarse mesh

(b) Medium mesh

(c) Fine mesh
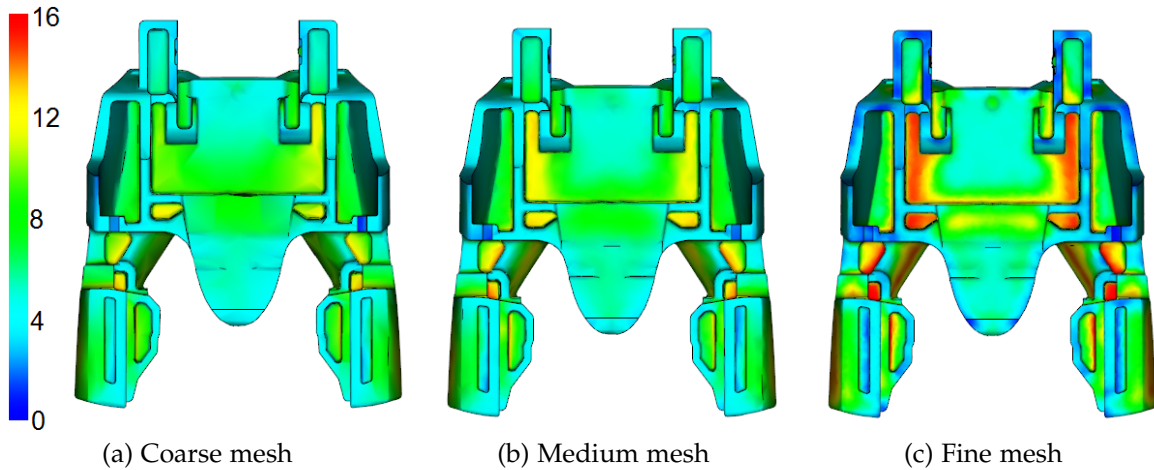
Figure 3.11.: Volumetric shrinkage averaged over the local wall thickness in %.

Warpage

At ejection, the cold runner is separated from the part and therefore has no influence on part warpage. Therefore, the cold runner is not considered for the warpage calculation.

Fig. 3.12 shows the total displacement magnitude predicted with the three meshes. The deformation mode is essentially the same for all three meshes. The deflection magnitude is almost identical on the coarse and the medium mesh. Only the prediction obtained with the fine mesh shows a larger deflection. Both the coarse and medium mesh have at least 6 element layers across the wall thickness, while the fine mesh has at least 10. A finer discretization of the local wall thickness has a much larger influence on the warpage result than a finer discretization in in-plane direction.

(a) Coarse mesh   (b) Medium mesh   (c) Fine mesh
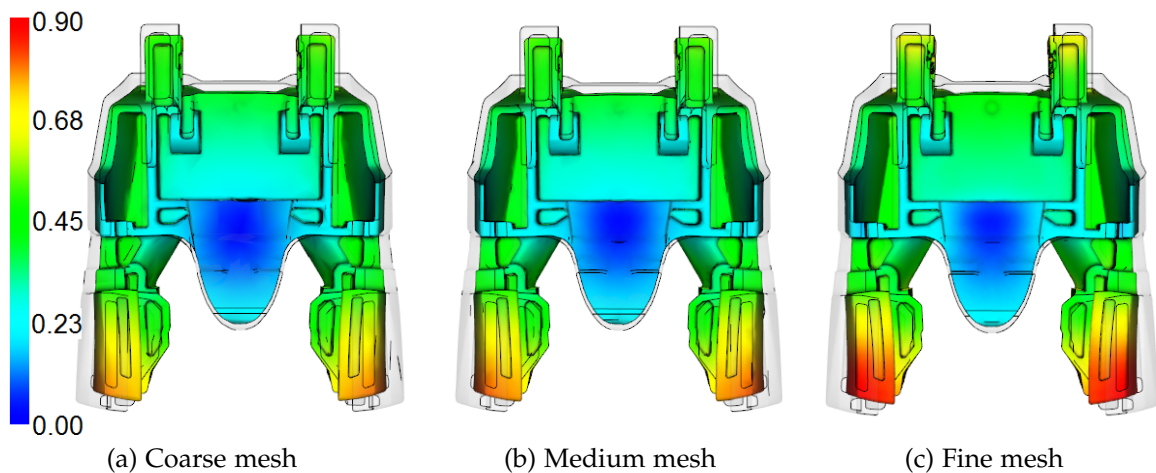
Figure 3.12.: Total displacement magnitude in mm. The deformation is shown exaggerated by a factor of 5.

Concluding remarks on the mesh convergence study

The mesh convergence study has shown that the solution converges even on very coarse meshes with very bad element quality. The quality of the results is noteworthy, yet not severely affected by the bad mesh. Only an asymmetry of the filling pattern was observed in this study. The limited resolution of the coarse mesh leads to blurred distribution fields, such as volumetric shrinkage in regions with complex geometric features. Therefore, the prediction of sink marks or voids is affected. Regarding the warpage result, the element count across the wall thickness has much more impact

than the node distance in in-plane direction. Hence, for the prediction of the filling pattern and the required filling pressure, a rough mesh (although of the proper quality) can be used. When shrinkage and warpage is the primary target of the simulation, the proper discretization of the wall thickness is required. To prevent excessively high aspect ratios, this also demands a reasonably fine discretization in in-plane direction. All parts considered in this thesis were meshed with at least 10 elements across the wall thickness, and up to 12 elements when a fiber reinforced material was used. Good to very good results were obtained with these settings at acceptable computational cost.

Final mesh for prediction vs. measurement

Based on the conclusions of Section 3.3.5, the model was finally meshed as shown in Fig. 3.2. The mesh properties are summarized in Table 3.5. All subsequent results were obtained with this mesh.

	part	cold runner 3D	mold
Element count	1082021	41762	796756
Nodes	201653	8124	154320
Elements across wall thickness	10	10	6
max. aspect ratio	96.74	44.25	600.28
average aspect ratio	3.76	4.51	5.92
min. aspect ratio	1.05	1.09	1.05
max. dihedral angle	177.6	175.2	179.6

Table 3.5.: Mesh properties and diagnostics of the final model.

3.3.6. Results: Prediction vs Experiment

In this section, two simulation results are compared to the experiment. These are the filling pattern, which is collated with experimental short shots, and the final part shape predicted by the warp solver, which is compared to a 3D scan of a molded part.

Filling pattern

Fig. 3.13 shows the comparison of experimental and simulated short shots. The part has rather thin walls in the gate area and thick walls at both arms. In this region, the flow pattern is predominantly 3D. Due to the full 3D simulation, the actual shape of

the flow front is predicted very well. In contrast to the simulated result, the actual molded parts show very large sink marks. These are a result of the excessively high shrinkage the polymer undergoes during cooling if packing is omitted. The simulated result, on the other hand, represents a snapshot of the in-rushing polymer melt at a specific point in time. Shrinkage is therefore not visible, and thus, only the predicted flow front should be compared.

Warpage

The main target of this thesis is the accurate prediction of warpage. Possible sources of error emerge from the simplified modeling approach presented in Chapter 2, the quality of the available material data, and the applied boundary conditions. For this reason, numerical experiments were performed to determine the major influencing factors on the accuracy of the predicted shrinkage and warpage. The viscous-elastic model considers pressure induced and thermal initial stresses in order to predict the final shape of the demolded, cold part (see equation (2.30)).

Pressure induced stress
The calculation of the pressure induced stresses strongly depends on the pvT relationship of the material and the applied packing pressure (profile). If the simulation tool is used for its intended purpose, namely, to make predictions before experimental data is available, process settings such as the packing pressure must be estimated. The idea of the first experiment is therefore to quantify the sensitivity of the predicted warpage on the (possibly poorly estimated) packing pressure. Fig. 3.14 shows the predicted deflection magnitude in case of ideal cooling (constant cavity wall temperature) and for various packing pressures.

Excursion: Interpretation of the deflection magnitude results
This result shows the spacial deflection magnitude of the final part surface (demolded and cooled to room temperature) to the cavity surface. Hence, the predicted shape is actually a superposition of shrinkage (a change in size) and warpage (a change in shape). The amount of shrinkage normally varies all over the part, and it is therefore not possible to accurately isolate and visualize only warpage. The largest deflection is found at the tip of both arms and increases with decreasing packing pressure. At this point, the predicted deflection varies between approx. 0.65 mm at the highest and 0.95 mm at the lowest packing pressure. Increased packing pressure naturally causes a global decrease of shrinkage and, consequently, less deflection. Therefore, a smaller deflection magnitude does not generally imply lower warpage. Section 5.2 takes a closer look at this topic.

(a) Fill time: 5.1 s

(b) Fill time: 5.5 s

(c) Fill time: 6.5 s
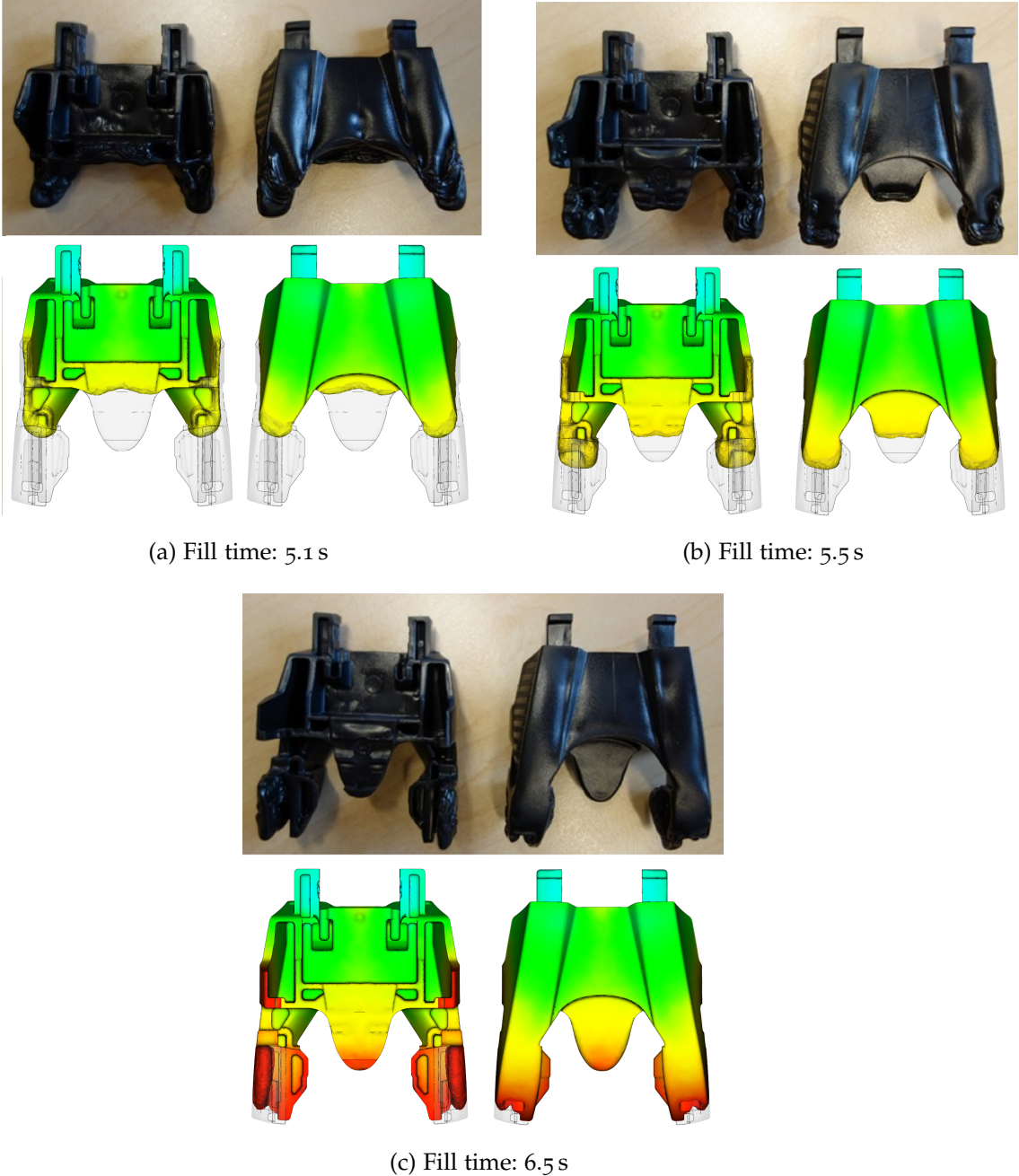
Figure 3.13.: Predicted melt front at different time steps in comparison to experimental short shots.

(a) Packing pressure: 30 MPa

(b) Packing pressure: 60 MPa

(c) Packing pressure: 90 MPa

(d) Packing pressure: 120 MPa
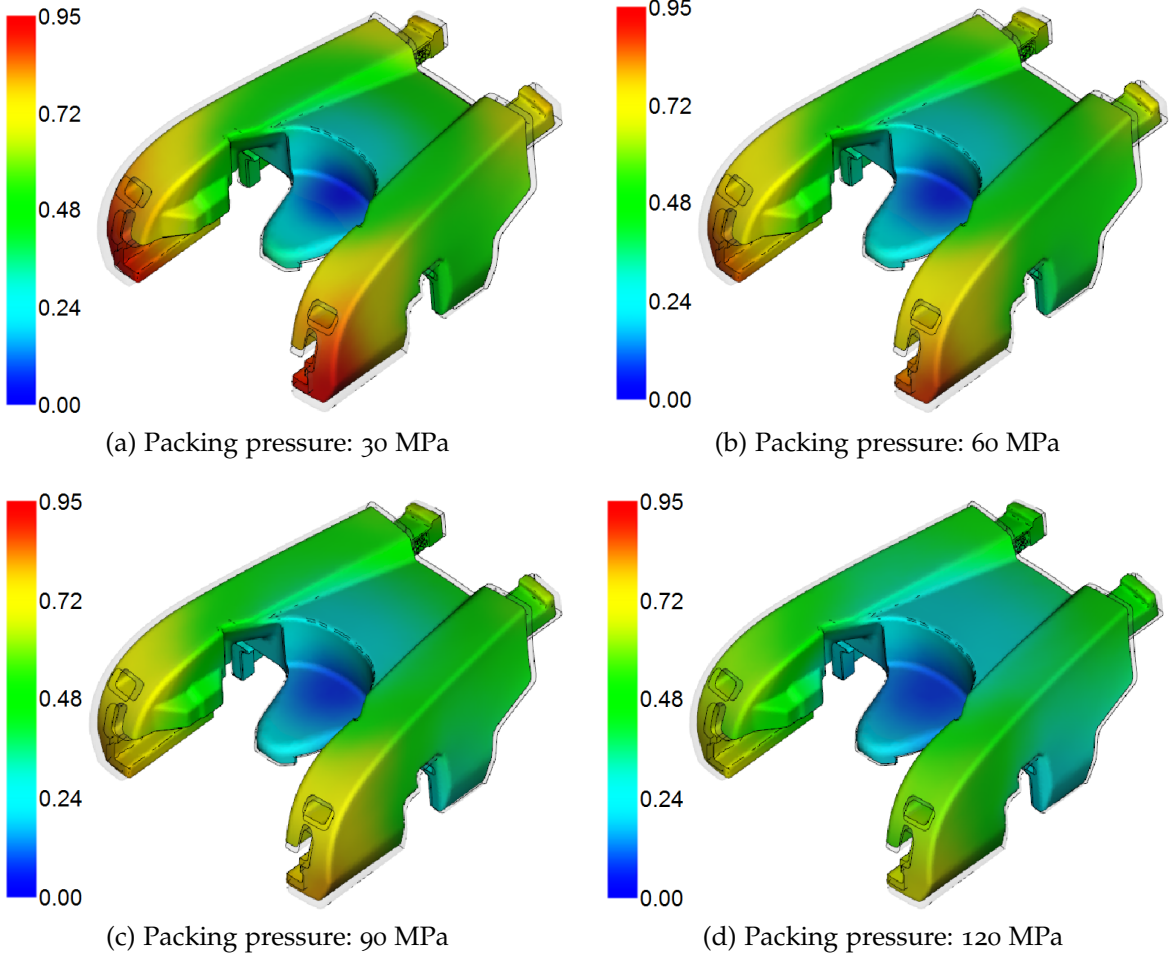
Figure 3.14.: Deflection magnitude for an ideally cooled mold (T_w = const.) and different packing pressures in mm. The deformed shape is shown exaggerated by a factor of 2.

Considering the very broad range of packing pressures applied, the impact on the warpage result is rather small.Hence, the lack of experimental pressure data and the reasonable estimation of the packing pressure implies only a small error. Therefore, the initial and reasonable assumption of 60 MPa packing pressure (see Table 3.1) was retained for the following investigations.

Excursion: Limitations of the pvT model
The meaning and importance of the pvT material data to shrinkage and warpage predictions should be also emphasized at this point: the calculation of the pressure induced stress component is based on the pvT-state of the material during the packing and cooling stages. Therefore, the shrinkage and warpage results are strongly affected by the quality of the used pvT data. In Section 2.1.4 it was mentioned that crystallization causes a significant drop in the specific volume. This behavior is accurately described by the 2-domain Tait equation (2.10). Therefore, the effect of crystallization on shrinkage is actually considered. However, the model only describes the materials pvT relationship for a specific cooling rate, at which the measurement was performed[2]. For measurements of the pvT properties, the cooling rate is typically in the order of -0.33 K/s. On the contrary, the local cooling rate observed in the actual case varies between -29 K/s and -0.65 K/s. It is very high at the surface of a thin-walled section during the early packing stage, and much lower in the core of the thickest section at the end of the cooling stage. The pvT relationships of polymers (especially of semi-crystalline grades) severely change at high cooling rates. The kinetics of crystallization, and therefore the local material density, are affected. Material which experiences higher cooling rates may have a lower degree of crystallinity and consequently undergo less shrinkage than predicted. This type of differential shrinkage is not considered by the proposed modeling approach and a source of error originates from this simplification. However, in the present case warpage of the molding originates from the thick and stiff sections of the part. The low cooling rates in those areas lead to a high degree of crystallinity. Consequently, neglecting the dependency of the pvT relationship on the cooling rate is certainly a better approximation in the case of compact parts with thick walls.

Thermal initial stress
The thermal initial stress calculation mainly depends on the predicted temperature distribution in the solidified, still constrained part, and the mechanical material properties data. As already pointed out, the warpage solver applies pressure induced and thermal initial stress obtained from the filling, packing, and cooling stages to the demolded (unconstrained) part. Elastic material behavior is assumed to calculate the equilibrium state. The mechanical properties of the dry polymer (or composite)

---

[2]The pvT properties of the POM grade used in this specific case were provided by the manufacturer (see A.1). A specific cooling rate is not mentioned. This leads to the assumption that the provided pvT data represents equilibrium states and may not properly reflect the material behavior in areas with very high cooling rates.

at room temperature are used for this analysis step. This viscous-elastic modeling approach is another severe simplification of the true material behavior. Therefore, the sensitivity of the warpage result on the mechanical material properties was also investigated. Several simulations of the same case, but with varying mechanical material properties, were performed. The study showed that the warpage result is distinctly affected by the transversely isotropic coefficient of linear thermal expansion α_1 and α_2[3]. Considering equation (2.30), this material constant is used to calculate the thermal initial stress from the temperature difference between the solidified polymer in the mold and the ambient conditions.

Fig. 3.15 shows the warpage results for different values of α. A 30% increase of α leads to a 32% increase of warpage, while a 4 times increase of the packing pressure merely causes a 22% reduction of warpage. Thus, the importance of this material parameter for accurate warpage predictions is evident.

The idea behind changing a material constant is the following: As the pvT relationship depends on the actual morphology development of the cooling polymer, the same is certainly true for α. It may be adjusted to "fit" the simulation model to experimental data obtained with a prototype mold, and further, to achieve accurate predictions for the design of the production mold.

Fig. 3.16a shows a 3D comparison of the CAD geometry and the digitized geometry of a molded part. The color indicates the local deviation of the molded (test) part from the CAD (reference) part in mm. In the green areas, the molded part is within a tolerance of ± 0.1 mm. A much higher deviation of up to 0.6 mm is found at both arms. The comparison of actual (reference) and predicted (test) part shapes, is shown in Fig. 3.16b. Exact prediction of the molded part shape would result in a uniform green color throughout the part. Hence, the prediction is not perfect with deviations of up to 0.2 mm to the molded part. The actual part geometry and the selected gate location cause poor packing of the thick-walled sections. This situation introduces another source of error, which is discussed and highlighted in Chapter 5. However, considering the complexity of the part, the accuracy of the warpage prediction is very good.

3.4. Case Study: Prediction of the pressure history

The main focus of this case study is the prediction of the pressure history in the cavity during the packing stage. The part investigated in this study is depicted in Fig. 3.17. Its overall dimensions are approximately $68 \times 68 \times 80$ mm^3, and most of the

---

[3]The material used in this study is unfilled and therefore demonstrates isotropic material behavior, meaning $\alpha_1 = \alpha_1$.

(a) $\alpha = 135 \cdot 10^{-6} \ K^{-1}$ (from Moldflow's material data base)

(b) $\alpha = 155 \cdot 10^{-6} \ K^{-1}$

(c) $\alpha = 165 \cdot 10^{-6} \ K^{-1}$

(d) $\alpha = 175 \cdot 10^{-6} \ K^{-1}$
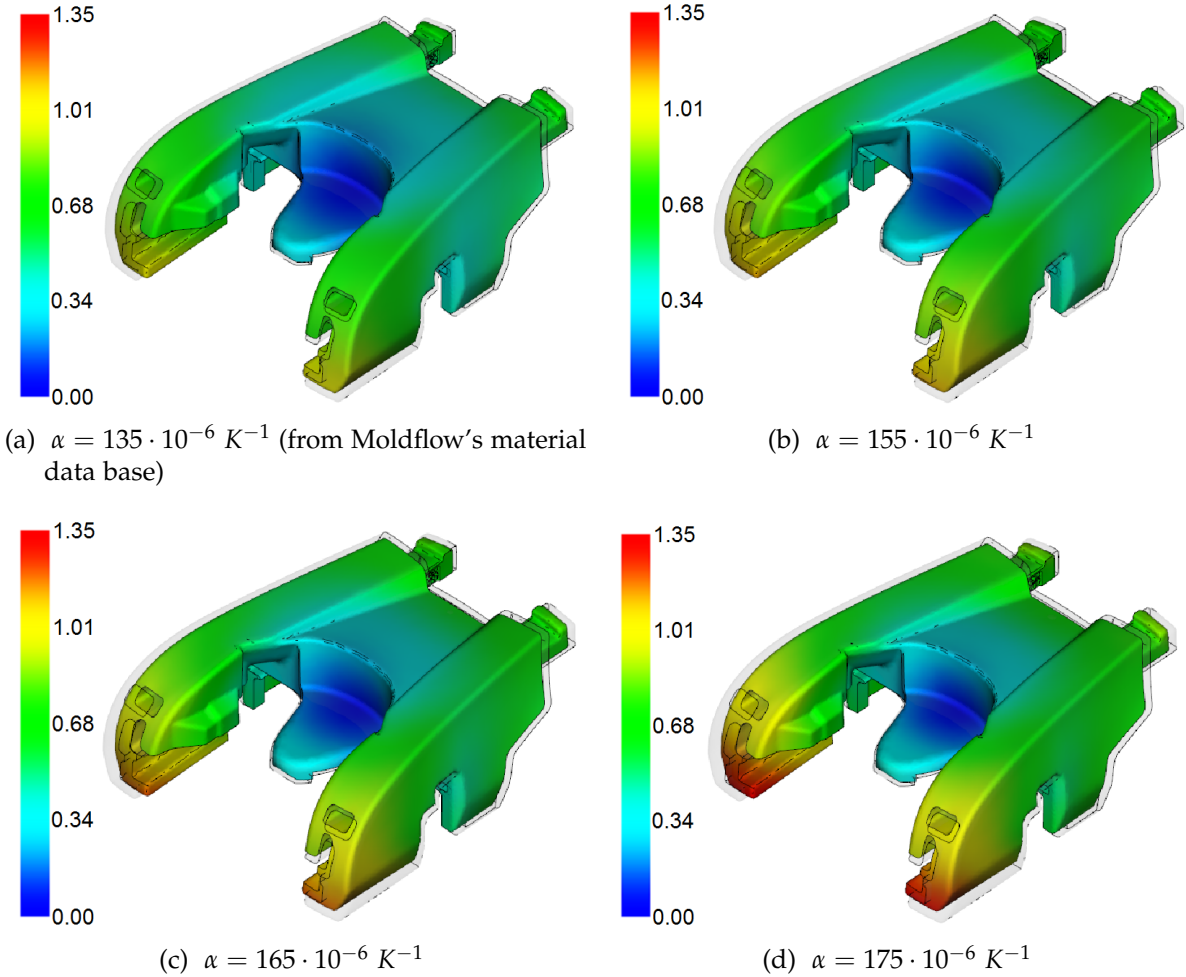
Figure 3.15.: Deflection magnitude in mm for a holding pressure of 60 MPa and various α while considering the cooling system. The deformed shape is shown exagerated by a factor of 2.

(a) 3D Comparison: Molded and measured part (test) vs CAD part (reference).

(b) 3D Comparison: Molded and measured part (reference) vs virtual part (test) calculated with $\alpha = 165$.
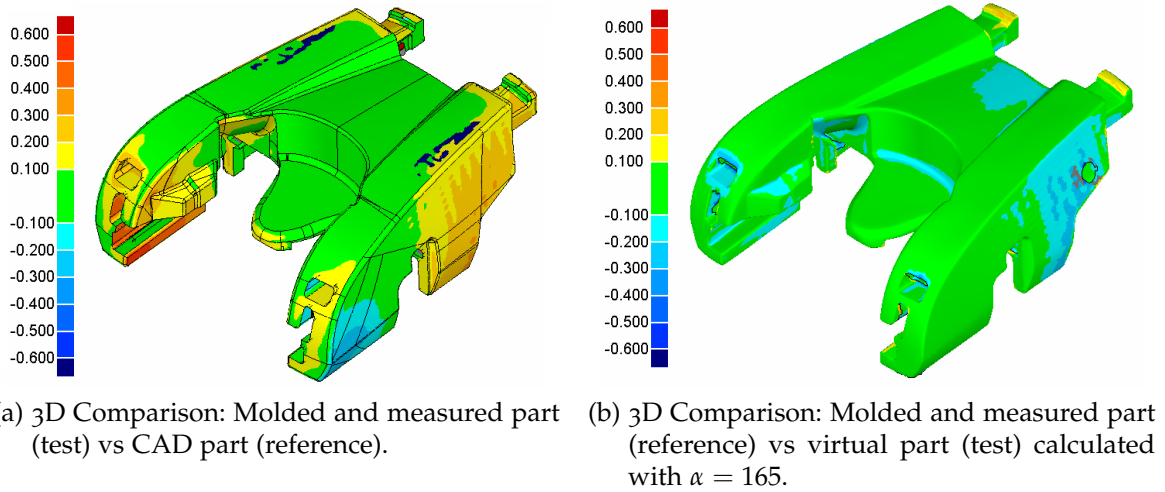
Figure 3.16.: Verification of the warpage result.

walls have a thickness of around 6 mm. It was molded in a one-cavity "bridge mold" - a mold built to bridge the gap between the prototyping and testing of the part and the series production in a larger two cavity mold. The mold was equipped with two pressure sensors: one close to the direct cold runner gate, and one at the opposite end of the cavity. The locations of the pressure sensors are shown in Fig. 3.17.

Molding trials using DuPont Delrin 127UV (POM) and UBE Nylon 1015gc9 (PA6 GF45) were performed in order to investigate the prediction accuracy of the simulation on a really chunky part.
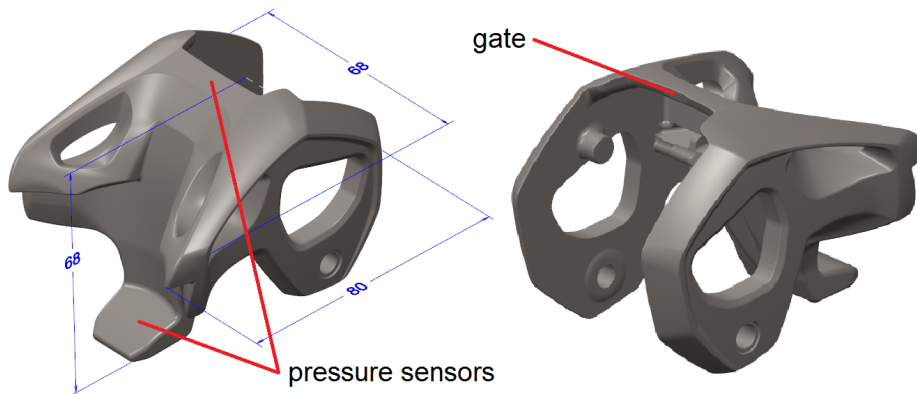
Figure 3.17.: Two views of the chunky plastic part with thick walls of up to 6 mm.

47

3.4.1. Numerical model

The numerical model showing part, runner, and cooling channels is depicted in Fig. 3.18. Due to the plain mold design, the whole runner and cooling system is modeled and no further simplification is required.
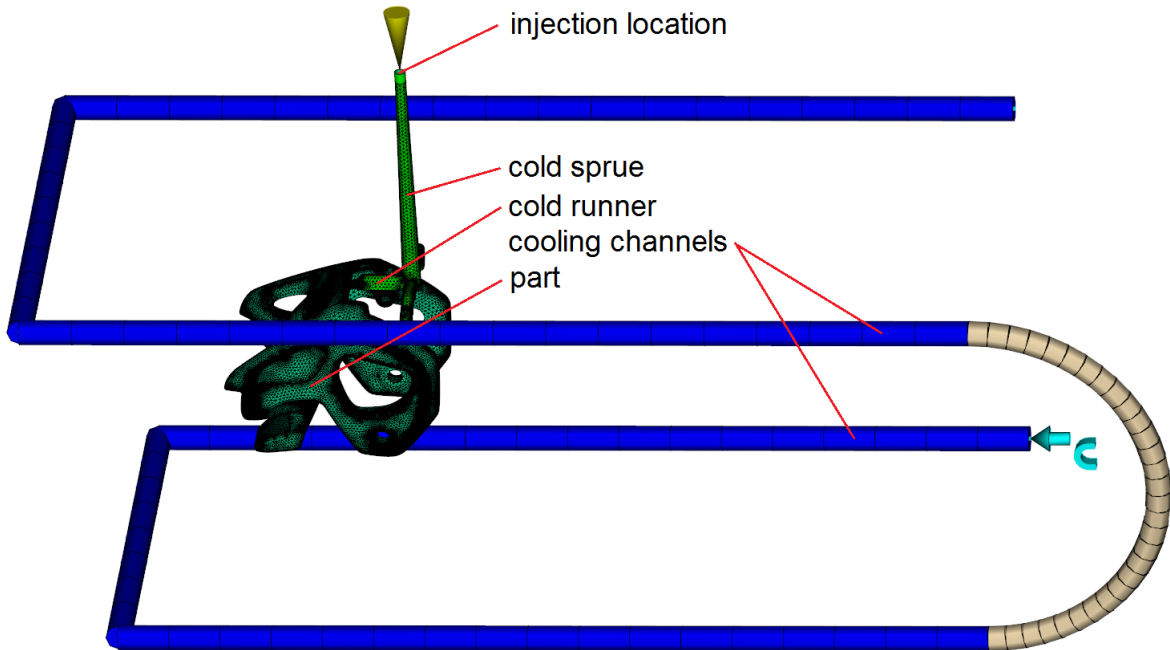
Figure 3.18.: Numerical model of the investigated part featuring cavity, cold runner, and cooling channels.

The chunky geometry of the part calls for a full 3D analysis. Shear heating effects in the runner system may have an impact on gate seal time and pressure decay in the cavity. Therefore, the runner is also represented by a volume mesh. The cooling lines are very far off the cavity walls and are therefore modeled with beam elements. A Cool (FEM) analysis was performed in advance of the fill and pack analysis which requires a volume mesh of the mold (not shown in Fig. 3.18).

3.4.2. Material data

Like the experimental molding trials, the simulations were performed using material data for DuPont Delrin 127UV (A.1) and UBE Nylon 1015gc9 (A.5). UBE Nylon was selected since all of the Material properties were measured by the Moldflow Plastics Labs. The material data has a gold quality indicator for all analysis steps. This was considered to be a sound basis for the validation of the numerical model.

3.4.3. Process settings and boundary conditions

Most of the process settings and boundary conditions were set in accordance with the experimental molding trials. The applied packing pressure was adjusted to account for the pressure loss in the nozzle and to match the measured peak cavity pressure.

An injection velocity profile was used for the molding trials. For the simulation, the experimentally determined injection time was applied, instead of defining a ram speed profile. In this case, a constant volume flow rate is applied. Therefore, the pressure profiles during the filling stage are affected. They are, however, of little interest to this study. In none of the case studies performed by the author did the injection velocity profile have a significant effect on warpage. Therefore, this simplification is justified.

Again, the inlet and outlet temperatures of the coolant were measured by PT100 temperature sensors. The volume flow rate of each circuit was measured by a magnetic-inductive flow meter. The experimentally determined values for temperature and volume flow were used for the simulation.

The process settings and boundary conditions used for the simulations are summarized in Table 3.6.

	Delrin 127UV	UBE Nylon 1015gc9
Cooling analysis		
Melt temperature	208°C	291°C
Injection + packing + cooling time	68.7 s	69 s
Mold-open time	13.3 s	12.6 s
Coolant	Water	Water
Coolant temperature	80°C	80°C
Coolant volume flow rate	6.6 l/min	6.6 l/min
Fill + pack analysis		
Injection time	3.7 s	1.4 s
Velocity/pressure switch-over	at 98% of the volume filled	
Packing pressure	75 MPa	53 MPa
Packing time	40 s	30 s

Table 3.6.: Applied process settings and boundary conditions for Delrin 127UV and UBE Nylon 1015gc9.

3.4.4. Solver settings

The analysis sequence used was: Cool (FEM) + Fill + Pack + Warp. All of the solver settings presented in Section 3.3.4 were used for this study.

3.4.5. Mesh

The part as well as the cold runner are represented by a volume mesh. Based on the conclusions of Section 3.3.5, the model was meshed with 12 elements across the wall thickness. The meshed model is shown in Fig. 3.19. The mesh properties are summarized in Table 3.7.

(a) Surface mesh of part and cold runner.

(b) Cut through the part mesh showing the layered element structure.
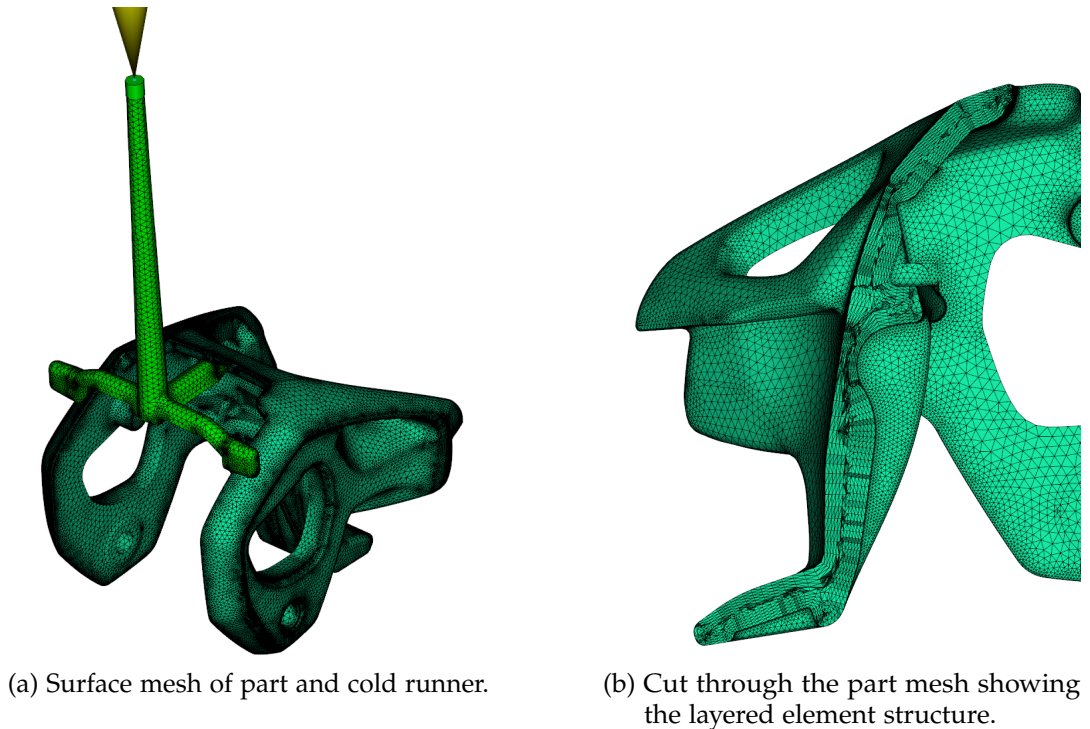
Figure 3.19.: Meshed model without mold mesh.

3.4.6. Results: Prediction vs Experiment

During the molding trials, short shots were made to validate the quality of the predicted filling pattern. Moreover, the cavity pressure was measured at two different locations, and the measurements were compared to the predicted cavity pressure. Finally, the molded parts were scanned to obtain a 3D representation of the actual part geometry. A 3D comparison with the predicted part shape was performed to investigate the quality of the warpage results on a part with very thick walls.

	part	cold runner 3D	mold
Element count	2295493	165971	1503818
Nodes	413408	29895	292935
Elements across wall thickness	12	12	6
max. aspect ratio	42.1	29.69	84.7
average aspect ratio	3.66	3.76	1.96
min. aspect ratio	1.03	1.05	1.00
max. dihedral angle	174	173	178.7

Table 3.7.: Mesh properties and diagnostics.

Filling pattern

Fig. 3.20 shows the experimental short shots obtained using Delrin 127UV compared to the predicted flow front shape. Despite the very chunky geometry of the part, very good agreement with the experimental short shot was achieved.

Pressure history

An accurate prediction of the pressure history in the cavity is the basis of pressure induced stress- and, therefore, warpage predictions. When the viscous-elastic model is used, it is important to predict the melt pressure at the time of solidification. Stress relaxation effects in the solid are not considered by this model, which means that accurate pressure prediction in the solid is not mandatory.

Fig. 3.21 shows the measured and the predicted pressure history for the two materials. The quality of the pressure predictions very much depend on the pvT and the thermal material properties. The provided pvT data of Delrin 127UV is based on calculations and not on measurements (see A.1 for more information), while the pvT data of UBE Nylon 1015gc9 was measured by the Moldflow plastics labs. Moreover, the heat capacity and thermal conductivity are assumed to be constant over temperature for the POM grade, while they were measured as a function of temperature for the PA6 GF45 grade. Despite this fact, the pressure predictions of the POM grade are in excellent agreement with the measurement, while the pressure history predicted for the PA6 GF45 grade shows a significantly steeper pressure decay in the packing stage.

51

(a)

(b)
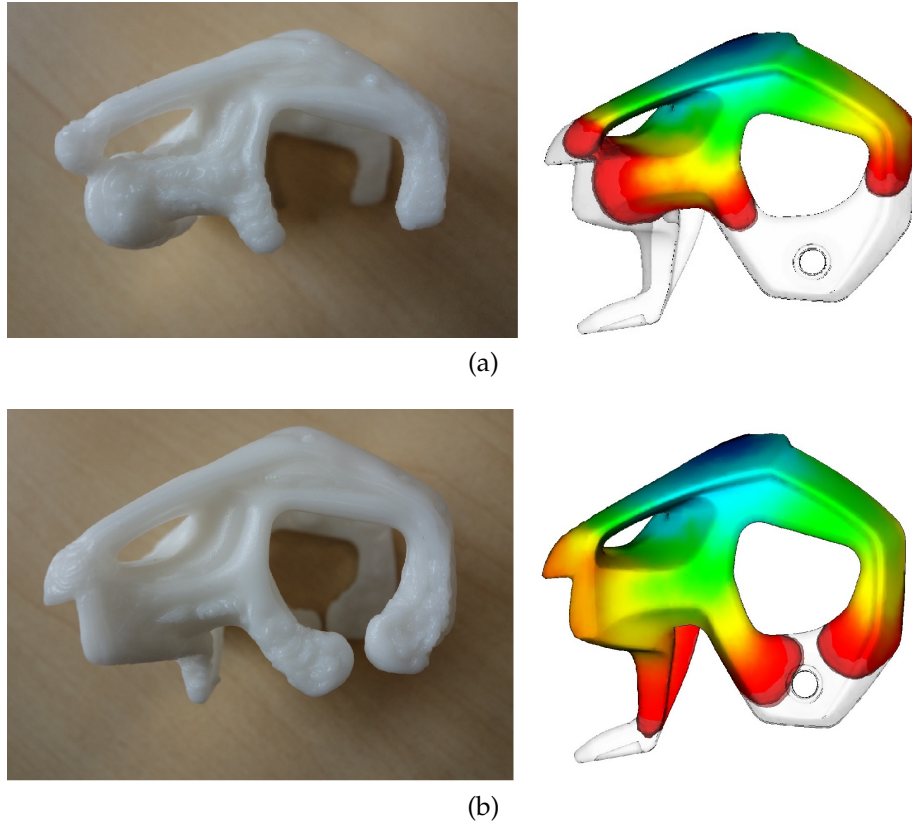
Figure 3.20.: Predicted melt front in comparison to experimental short shots of the part using Delrin 127UV.

(a) UBE Nylon 1015gc9

(b) Delrin 127UV
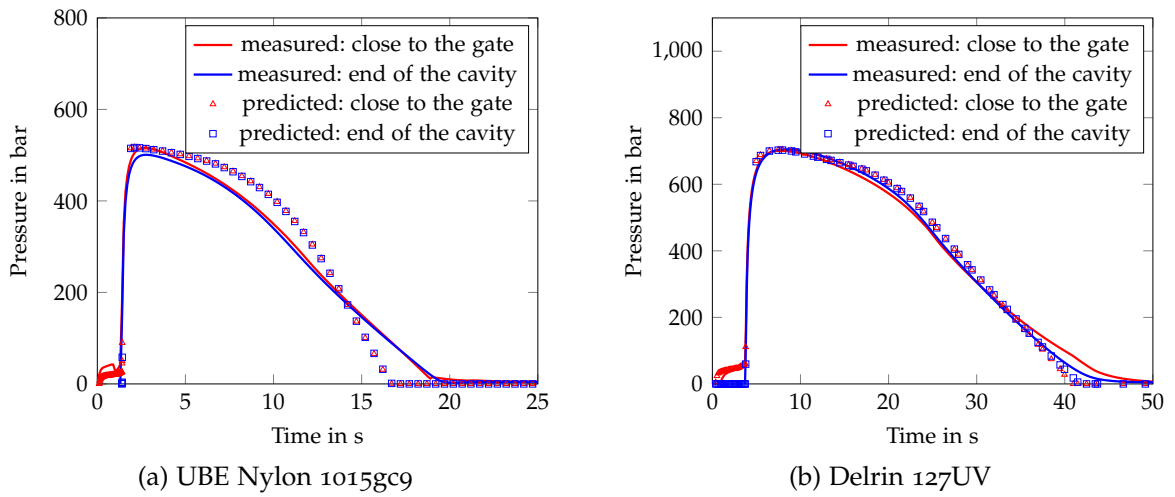
Figure 3.21.: Measured and predicted cavity pressure for two different materials.

Possible sources of error

The methods used to determine the pvT properties do not usually reflect all the conditions present in the injection molding process. The fiber orientation state, which is highly dependent on geometry and velocity field, may lead to some anisotropy of the pvT relationship, which is neither considered in the measurement, nor in the simulation. A decent overview of different ways to determine the pvT relationship of polymers can be found in [33].

A rigid mold is commonly assumed. This is generally not true, but is, nonetheless, a reasonable approximation when the mold is properly designed. For instance, mold plates which are not sufficiently supported may bend under the cavity pressure and cause a slower pressure decay in the cavity, due to the additional pressure introduced by the elastic rebound force of the mold. Among others, this effect was investigated by Leo & Cuvelliez [120]. Another issue is the introduction of the transition temperature necessary for the viscous-elastic model. As already mentioned, this temperature is not a fundamental physical property of the material. Material properties change continuously over temperature. The state in which the material can actually be treated as solid depends on many factors, including pressure, stress state, cooling rate, and the thermo-mechanical history of the polymer. Therefore, if a transition temperature is used to overcome these hurdles, one must bear in mind that this temperature would vary locally. Due to the complexity of the stated influences on T_t, it is assumed to be constant in the whole domain. Hence, the seal time of the gate strongly depends on the selection of T_t, and therefore, the predicted pressure history in the cavity is severely affected.

Warpage

The thick walls of the part call for an even thicker runner as well as a gate with a sufficient diameter to enable proper packing, otherwise, the gate freezes off very quickly and very high volumetric shrinkage occurs in the thick walled regions. This may cause either sink marks on the surface or voids inside the part. It was found and successfully demonstrated in Chapter 5 that, in those cases, warpage predictions are not reliable and may severely deviate from the true part deflection.

Fig. 3.22 shows an isosurface of a constant temperature of 144°C after 28 s. This temperature is the defined transition temperature of the POM grade. Hence, the volume enclosed in this surface represents the melt volume. The gate is already frozen and no additional material can enter the cavity to compensate for shrinkage and thus reduce warpage. The frozen volume is just below 50% at this instant. In this case, one should not expect quantitatively good warpage results.
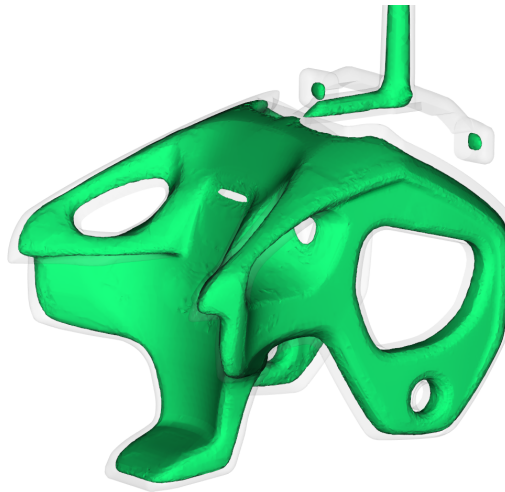
Figure 3.22.: Isosurface of transition temperature for POM after 28 s. The included volume is the melt volume.

The predicted deflection magnitude depicted in Fig. 3.23 reveals that the arms turn inside by approximately 1.4 mm at their tips. Again this value represents the shrinkage and warpage.
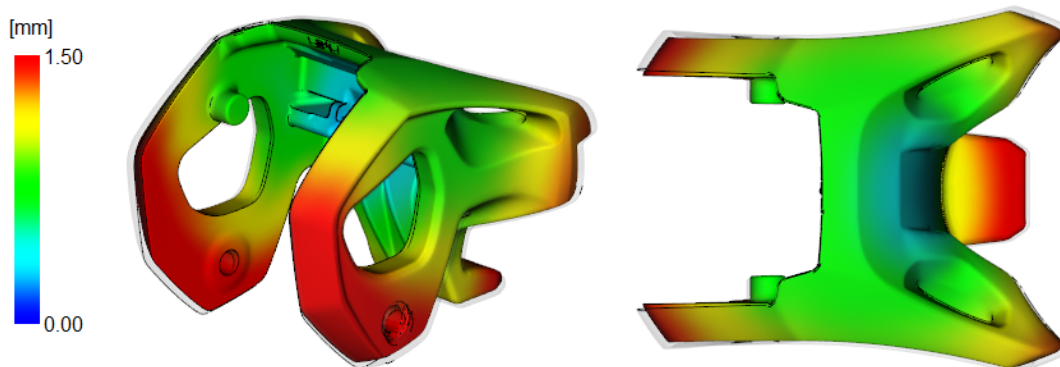
Figure 3.23.: Predicted deflection magnitude for POM in mm.

As the 3D comparison in Fig. 3.24a shows, the prediction is not that bad in the case of POM. Here, the warpage is underpredicted by about 25%, which is still a very good result considering the complexity of the situation. In the case of PA6 GF45, the warpage prediction is even better (Fig. 3.24b). The deformation mode is captured very well, although shrinkage is not predicted as well, with deviations in the order of 0.2 mm all over the body. The warpage of fiber reinforced moldings is generally less sensitive to poor packing efficiency and varying process conditions. A noticeable exception is the case presented in Section 5.1.

(a) Comparison of molded and scanned POM part (reference) and the predicted part shape (test).

(b) Comparison of molded and scanned PA6 GF45 part (reference) and the predicted part shape (test).
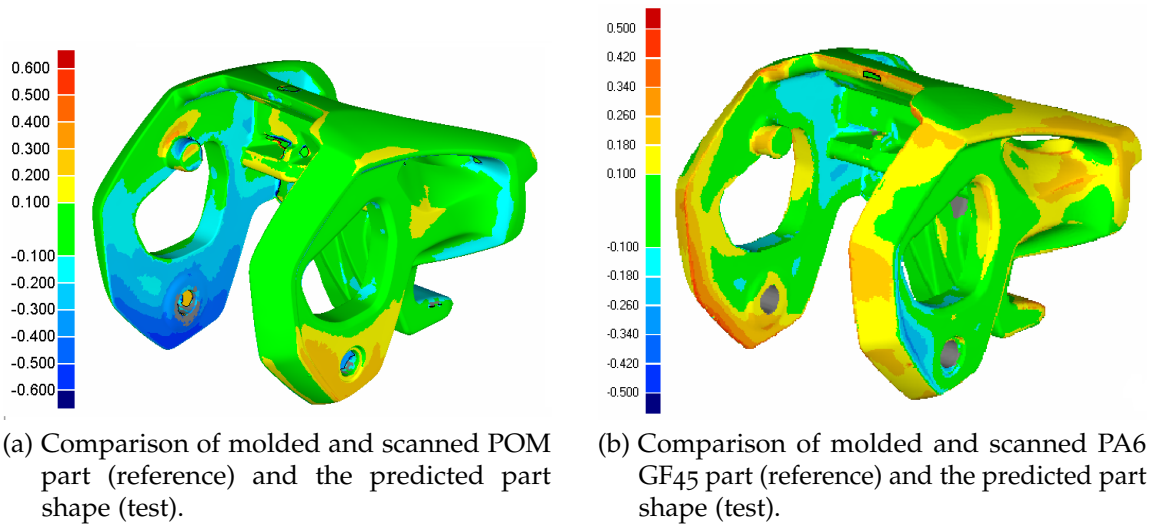
Figure 3.24.: Comparison of actual and predicted warpage for two different polymer grades.

3.5. Case study: Warpage of a ribbed plate

The main dimensions of the part investigated in this case study are approximately $196 \times 60 \times 18 \text{ mm}^3$, and the wall thickness ranges from 0.5 to 6 mm (Fig. 3.25). The part was molded from DuPont Zytel73G45 (PA6 GF45) in a four-cavity mold. Each cavity was directly gated via a hot runner nozzle. The part features a T-slot on the bottom side and is intended to slide onto a stamped sheet metal part. Severe warpage of the moldings, in conjunction with its high stiffness, significantly aggravated assembling of the parts. The main target of this case study was therefore to find out if the accurate warpage prediction of such a complex part is feasible. This is a major requirement to predict and compensate for warpage before the mold is actually built.
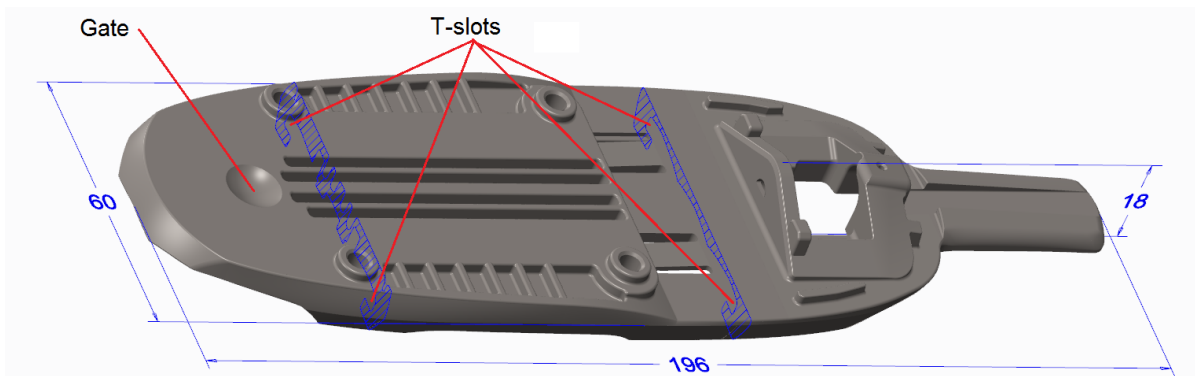
Figure 3.25.: CAD model of the investigated part.

55

3.5.1. Numerical model

The simulation of the whole four-cavity mold comes at a very high computational cost. Therefore, only one cavity, including the adjacent cooling lines and the hot runner nozzle, was modeled. Warpage is affected by the mold temperature distribution around the cavity. Modeling the polymer domains and all adjacent cooling lines is sufficient. The numerical model showing part, hot runner, and cooling channels is depicted in Fig. 3.26.
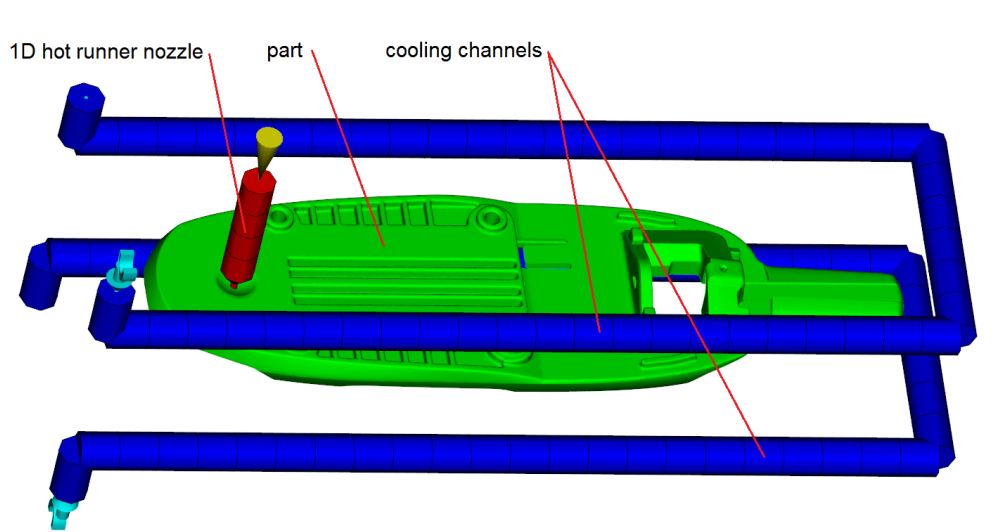
Figure 3.26.: Numerical model of the investigated part featuring cavity, hot runner nozzle, and adjacent cooling channels.

3.5.2. Material data

DuPont Zytel 73G45 a PA6 grade with a short glass fiber content of 45% by weight was used in the production of this part. The simulations were performed using the relevant material data from Moldflow's material database (A.3). It only has a silver material quality indicator for the filling and packing analysis, and bronze for the warpage analysis. This study therefore reflects what will be the normal case in practice when accurate data is not available for the specific material grade.

3.5.3. Process settings and boundary conditions

The process settings and boundary conditions used for the simulation were derived from the settings used in production. Since only one cavity was modeled, some

modifications were required. Due to its negligible impact on warpage, a target injection time was used instead of the ram speed profile used in production. In production, a packing pressure of 100 MPa was defined (at the tip of the screw). The model only contains a simplified hot runner nozzle, and neither hot runner manifold nor machine nozzle. Therefore, a pressure loss of 40% was estimated and a packing pressure of 60 MPa was used for the simulation. Alternatively, one may consider calculating the pressure drop with a model of the whole runner system. In this case, the geometry of the hot runner manifold was not known. The coolant volume flow rate as well as the inlet temperature were set according to the measurements.

The process settings and boundary conditions used for the simulation are summarized in Table 3.8.

Cooling analysis	
Melt temperature	285°C
Injection + packing + cooling time	41.5 s
Mold-open time	18.5 s
Coolant	Water
Coolant temperature	70°C
Coolant volume flow rate	5.5 l/min
Fill + pack analysis	
Injection time	1.5 s
Velocity/pressure switch-over	at 99.9% of the volume filled
Packing pressure	60 MPa
Packing time	17 s

Table 3.8.: Applied process settings and boundary conditions.

3.5.4. Solver settings

The analysis sequence used for the final simulation was: Cool (FEM) + Fill + Pack + Warp. Again, all the solver settings presented in Section 3.3.4 were used for the simulations. Additionally, a fiber model was used to predict the fiber orientation distribution and the material properties of the composite necessary for warpage calculation. The Folgar Tucker model as well as the RSC model were tested. In both cases, the default solver settings were used.

3.5.5. Mesh

Fig. 3.27a shows the meshed part with the simplified hot runner drop (red elements) and Fig. 3.27b shows a cut through the mesh. The part was meshed with approximately 3.9×10^6 tetrahedral elements, with at least 10 element layers across the part thickness. The Cool (FEM) approach requires a volume mesh representation of the mold volume which is not shown in Fig. 3.27.

(a) Partmesh with approximately 3.9 million elements and simplified hot runner drop.

(b) Cut trough the mesh showing at least 10 elment layer across the wall thickness.
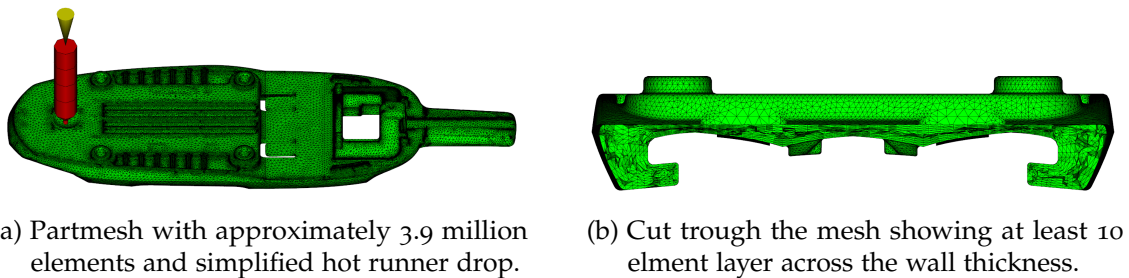
Figure 3.27.: Meshed model comprising part, simplified hot runner nozzle, and cooling lines.

	part	mold
Element count	3975925	2071028
Nodes	708557	392556
Elements across wall thickness	10	6
max. aspect ratio	99.94	337.04
average aspect ratio	4.63	5.57
min. aspect ratio	1.03	1.03
max. dihedral angle	177.9	178.4

Table 3.9.: Mesh properties and diagnostics.

3.5.6. Results: Prediction vs Experiment

Filling pattern

In production, the four cavities did not fill equally, and therefore, the whole shot is depicted in Fig. 3.28. In contrast to the other cases, the prediction of the flow front is not as accurate. In comparison to the simulation result, the melt front is always ahead in the thick sections of the cavity. This can be seen in Fig. 3.28c where the flow front of the short shot on the right is in good agreement with the simulation result, while the two thin walled flaps are already completely filled in the simulation, and only partly filled in experiment. The higher discrepancy in this case is not caused by

(a)

(b)

not filled

completely
filled

(c)
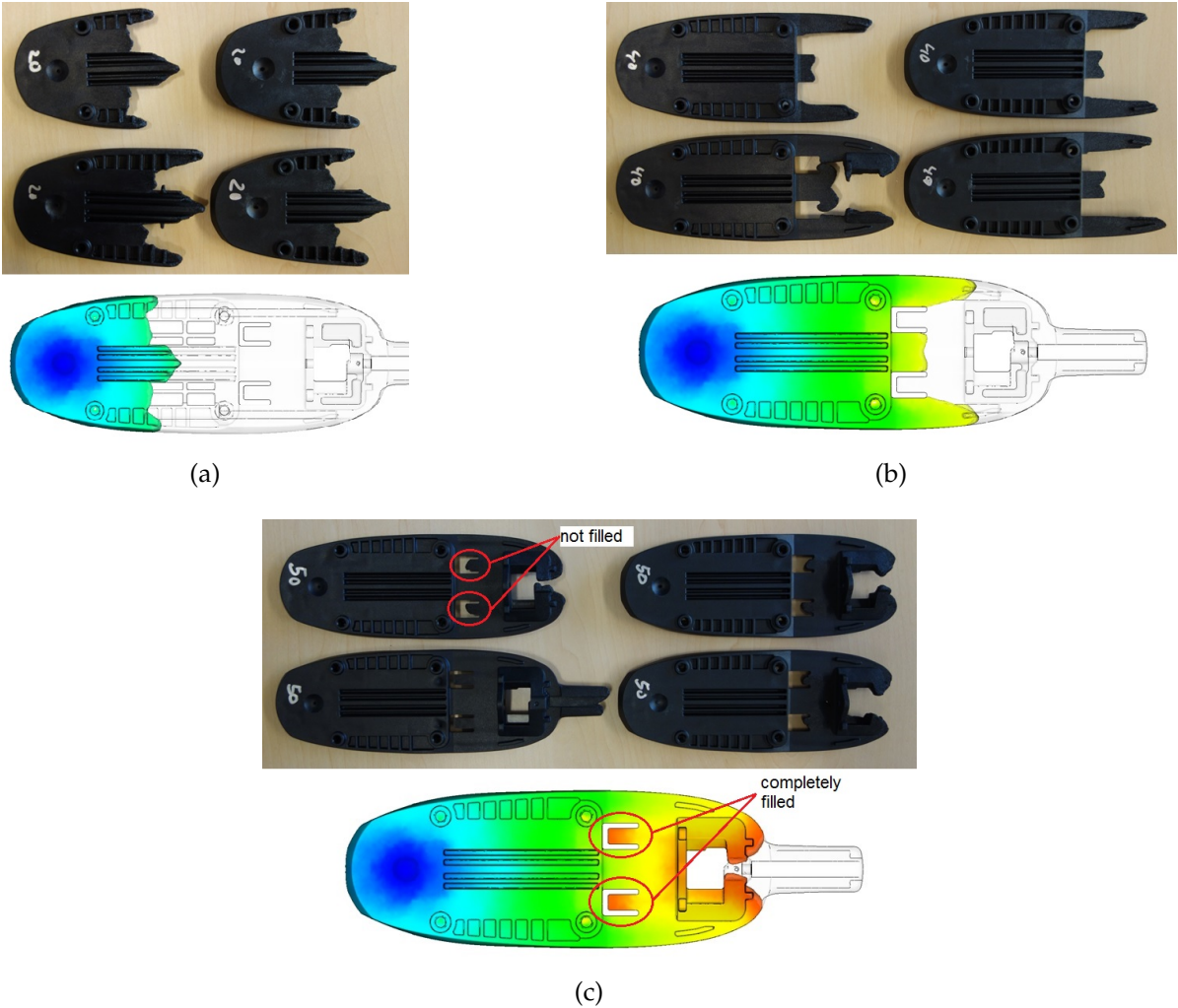
Figure 3.28.: Predicted melt front in comparison to experimental short shots of the ribbed plate. The part was molded from PA6 GF45.

poor material data or discretization. It is probably caused by the different rheological behavior of fiber filled polymer melts. The rheological properties of a fiber reinforced material are measured in exactly the same way as unfilled materials. Hence, the same models are used (in this case the Cross-WLF model) for the simulation. This is a major simplification since the viscosity is not only dependent on temperature, shear rate and pressure, but also on the fiber orientation state. The fiber orientation depends on the velocity field, which is affected by the viscosity. Hence, a coupled simulation of flow and fiber orientation based on a constitutive equation for the suspension of rigid particles in a generalized newtonian fluid would be required to capture this effect. Considering this effect would dramatically increase the computational effort, and is therefore usually neglected.

Tucker [121] discussed the importance of coupling in the field of injection molding with a focus on the resulting fiber orientation. He stated that the effect is negligible in shear-dominated flows, as is the case in small gaps. For complex situations, as in 3D flow regimes, this may not be true anymore.

Fig. 3.29 shows a direct comparison of two short shots of another part. They were produced under the same processing conditions but with different materials. The upper part was molded using a short glass fiber reinforced PA6 with a fiber content of 45% per weight, while the lower part was molded with unreinforced PA6. The simulated flow front is identical for both material grades since the effect of fiber orientation on viscosity was neglected. While the flow front was predicted extremely well for the unfilled material, the result of the fiber filled material showed similar deviations as those observed in Fig. 3.28.

Figure 3.29.: Comparison of short shots made with PA6 GF45 (upper part) and unfilled PA6 (lower part). The simulated flow front was obtained using PA6 GF45.

Warpage

Warpage of parts molded with fiber filled polymers is dominated by orientation effects. Fibers prevent the unrestricted shrinkage of the polymer matrix. Shrinkage parallel to the oriented fibers is therefore lower than in the perpendicular direction. Using the thermo-elastic model, this effect is captured by the coefficient of linear thermal expansion, which is now a function of the fiber orientation state and must be calculated by a micro-mechanics model, as indicated in Section 2.3. This calculation is based on the parallel and transverse α values of a unit cell with perfect alignment of the fibers. These values are part of the required material data and vary significantly depending on the source. Thus, the quality of the warpage prediction heavily depends on the accuracy of the fiber model, the micro-mechanics model, and the mechanical material properties data. Viscoelastic effects like stress relaxation in the constrained state during the packing and cooling stages are of little importance. The influence of the cooling time on warpage is therefore very low.

Fig. 3.30 shows the predicted deflection magnitude, assuming perfect cooling, the actual processing conditions according to the experiments, and the default fiber model (F-T model). It shows a significant level of warpage. The part bends toward the fixed side of the mold with a maximum deflection of 1.26 mm.
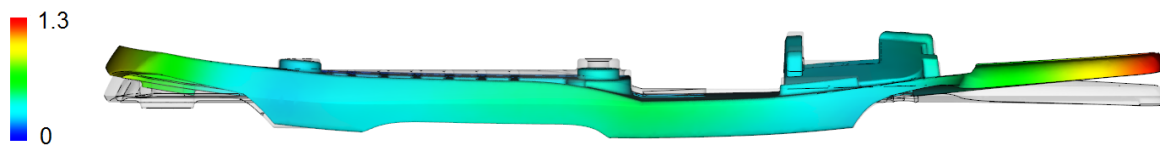
Figure 3.30.: Predicted warpage magnitude in mm of the plate by assuming perfect cooling. The z-component of the deflection is shown exaggerated by a factor of 5.

In the case of ribbed plates, the ribs and therefore the larger part of the plastic volume is in touch with the moving mold half. Hence, more of the heat introduced by the hot polymer melt is conducted away in the moving mold half, which leads to a higher cavity surface temperature. Fig. 3.31 shows the predicted cavity wall temperature at the time of ejection. The cooling system of the mold is not optimal, and therefore, the temperature varies from 72°C to 91°C. The moving mold half is somewhat hotter than the fixed half, although it must be noted that the heat introduced by the hot runner nozzle was neglected in this case. The temperature difference causes an unbalanced thermal stress profile across the wall thickness, and the plate will tend to bend towards the hotter side of the mold. Considering the mold cooling conditions does lead to lower warpage in this case.

The RSC fiber model, on the other hand, predicts a lower degree of orientation, and consequently, a higher amount of warpage. Fig. 3.32 shows the predicted warpage
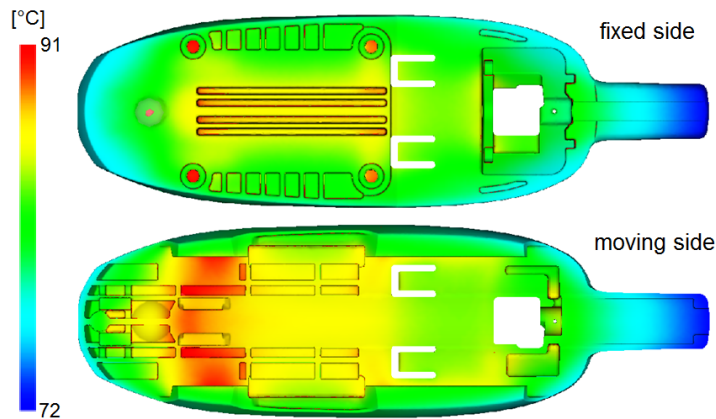
Figure 3.31.: Predicted temperature of the cavity wall at ejection. The temperature distribution of the fixed mold half is shown on the top, the moving mold half below.

when considering the cooling system of the mold, the better RSC fiber model, and α values from a different source [4]
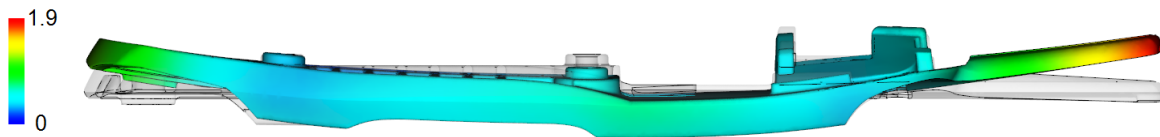
Figure 3.32.: Predicted deflection magnitude of the plate in mm. The cooling system of the mold was considered and the RSC fiber model used.

The maximum deflection of the part has increased by approximately 47%. Fig. 3.33 shows a 3D comparison of the molded and scanned part (reference) and the predicted part shape given in Fig. 3.32. Again, excellent agreement of prediction and measurement was achieved. While the warpage is captured almost perfectly, the predicted shrinkage is too high, so that deviations of 0.35 mm were found at the ends of the plate. Modeling the heat input of the hot runner would most likely further improve the accuracy of the warpage prediction. One approach to modeling the heat flux from the hot runner nozzle into the mold is given in Section 3.6.1.

---

[4]The original values provided by the Moldflow material database were replaced by those found in the Campus material database (http://www.campusplastics.com/) for the same polymer grade. Warpage predictions performed with $\alpha_1 = 16 \times 10^{-6}$ 1/K and $\alpha_2 = 100 \times 10^{-6}$ 1/K were always in better agreement with the experiment.
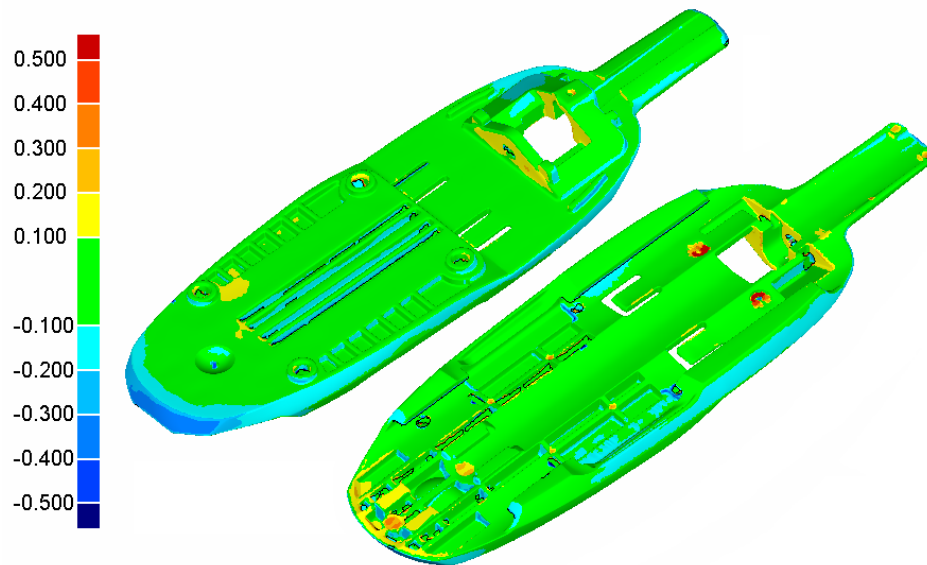
Figure 3.33.: 3D comparison between modeled part (reference) and predicted part shape (test). Deviations are given in mm.

3.6. Case study: Warpage caused by mold design

The part investigated in this section was molded from DuPont Zytel73G45 (PA6 GF45) in a four-cavity mold and has both thin and very thick walls. Fig. 3.34 shows the CAD model of the part. Parts with a similar shape have been made in the past, without significant warpage problems. For this part, however, the gate was moved from the cavity side of the part to the core side, where a hot runner nozzle was placed. The reason for this decision was an aesthetic requirement. Finally, an incident of unexpected warpage occurred, which was obviously caused by the additional heat flux from the hot runner nozzle as well as the poor cooling design of the mold.

3.6.1. Numerical model

To investigate what actually happens in the mold, simulations, with two different models were performed. The first model represents a standard simulation, considering the cooling system of the mold and the actual processing parameters used in the experiment. As is common practice, the hot runner nozzle was simply modeled using beam elements (1D calculation). In the following section, this model is therefore referred to as a "simplified model".

The second model features a detailed 3D representation of the hot runner nozzle in order to accurately capture the additional heat flux and the resulting temperature
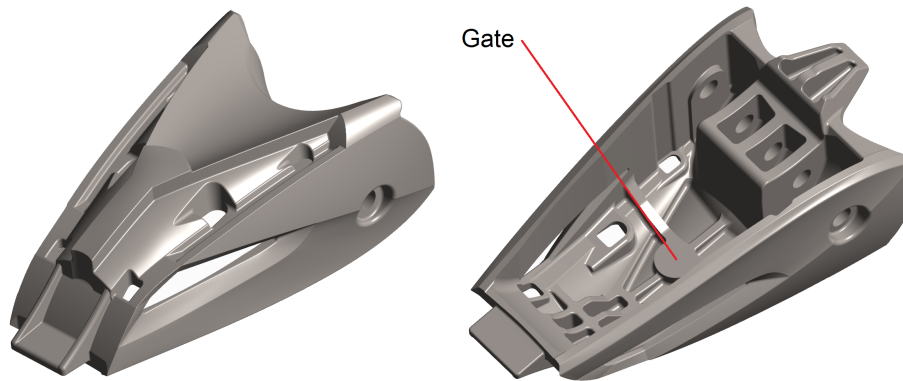
Figure 3.34.: Two views of the investigated part with thin and thick walls. The part is directly gated with a hot runner nozzle on the inside.

distribution in the core side of the mold. This model is called the "detailed model".

Simplified model

While the actual mold features four cavities, the simulation model comprises only one, including adjacent cooling channels and the simplified hot runner nozzle. This was done for the same reasons as stated earlier (see Section 3.3.1). Fig. 3.35 shows the simplified model with the cooling system comprising two different circuits and the hot runner nozzle. The core side cooling channel closer to the cavity (depicted in blue) was fed with cold water to reduce the core temperature.

Detailed model

The detailed model is depicted in Fig. 3.36 and shows the same cooling system and part mesh, although a detailed model of the hot runner nozzle and two mold inserts were added. A cross section of the mesh is shown in Fig.3.37. The mesh of the air gap is hidden, and the heating cord, which is normally wrapped in a helix around the body of the nozzle, was replaced by a simple tube-shaped heater. As in the simplified cases, a decoupled transient thermal analysis was performed to reduce the computational effort.

Hot runner systems are usually insulated from the mold by air gaps. The hot runner components only touch the mold plates on several spots in order to minimize heat transfer to the cooler mold components. For warpage predictions, it is not necessary to model the whole hot runner system. Of primary interest is how the heat flux from the nozzle affects the temperature distribution close to the cavity. The nozzle
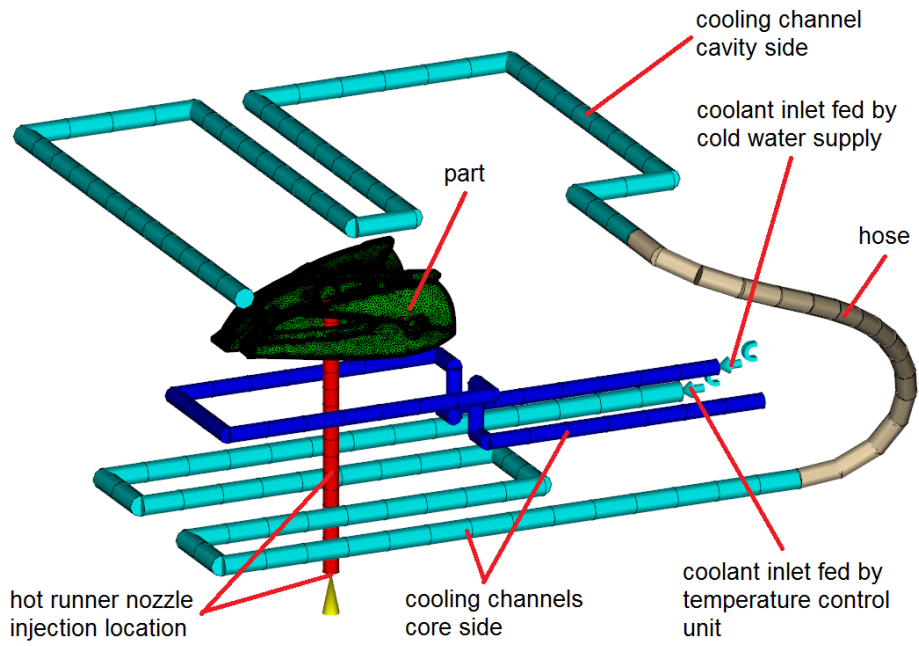
Figure 3.35.: Case setup of the simplified model. The hot runner nozzle was modeled with beam elements.
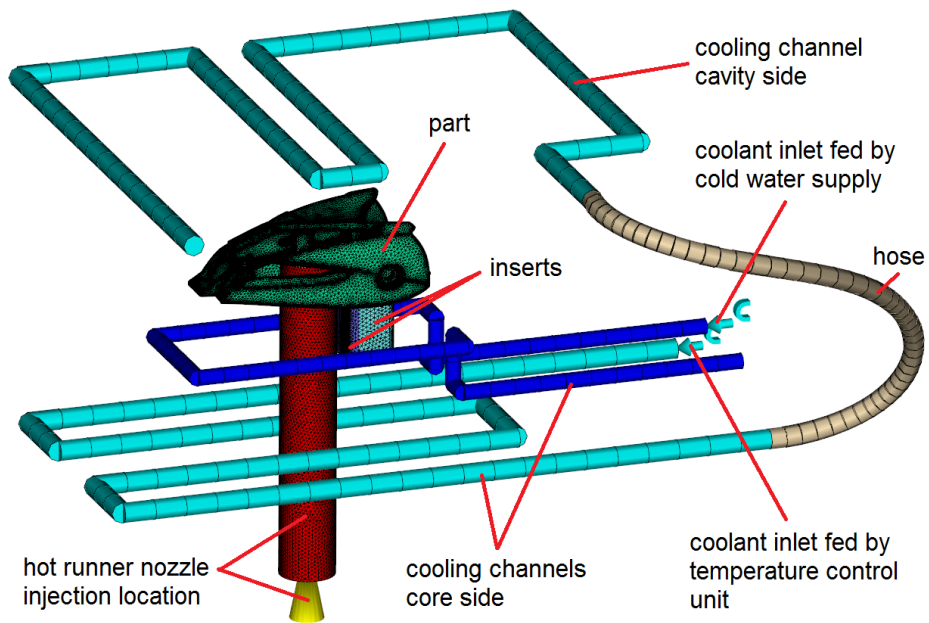
Figure 3.36.: Case setup of the detailed model. Hot runner modeled in 3D. True Geometry and heat input of the hot runner considered.
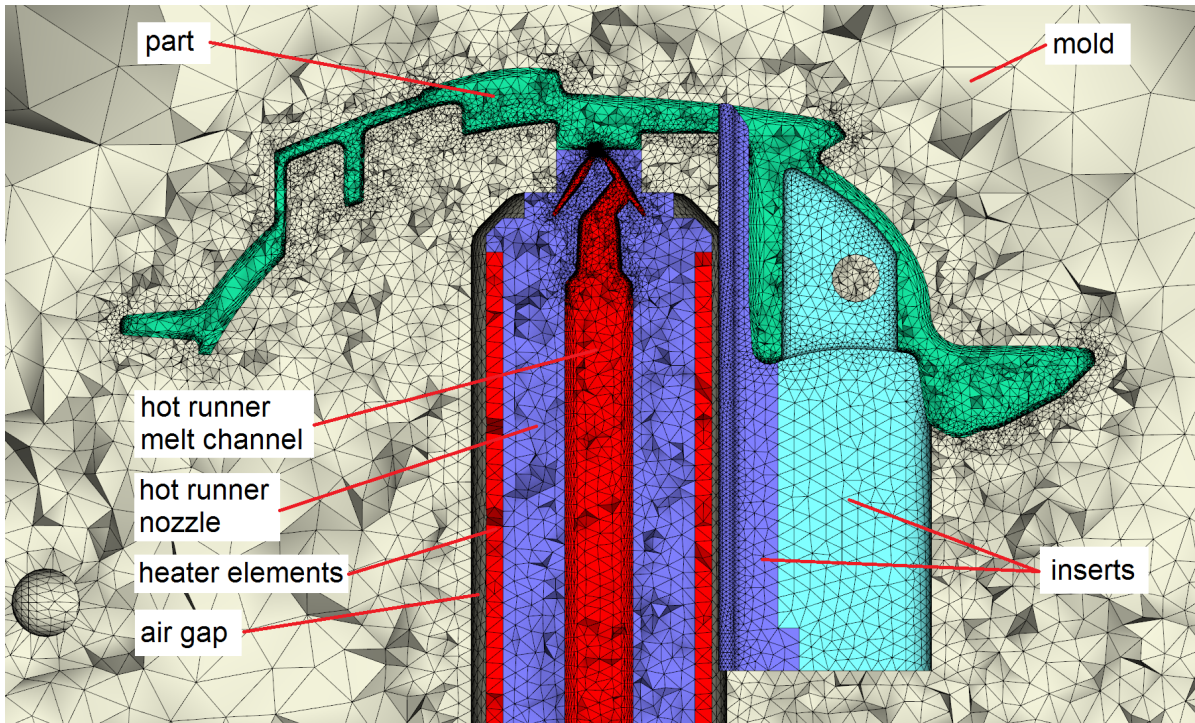
Figure 3.37.: Cut through the meshed model.

is insulated by an air gap over the whole length. It usually only touches the mold insert at its very tip, in order to seal the cavity and prevent a backflow of the polymer into the air gap. So, there is a heat transfer into the mold caused by pure conduction through the tip into the mold, but there is also a heat flux due to conduction and radiation across the air gap. Moreover, there could be heat transfer in the gap caused by natural convection. However, as will be shown later, the dimensions of hot runner nozzels and air gaps are usually small enough to prevent natural convection. In contrast to general CFD solvers, commercial injection molding simulation software is not designed to solve radiation or natural convection problems. Hence, the heat transfer through the air gap must be approximated in some way to address the presence of the hot runner nozzle. The following analysis presents one way of doing so.

First of all, calculating the Rayleigh number shows whether natural convection or pure conduction must be considered. When

$$Ra_s = Gr_s Pr < 10^3 \qquad (3.1)$$

where Gr_s is the Grashof number calculated using the length scale s and Pr is the Prandtl number, no natural convection occurs. For annular gaps, s is given by

$$s = \sqrt{r_o r_i} \ln \frac{r_o}{r_i} \qquad (3.2)$$

66

with the inner radius r_i and the outer radius r_o. The Grashof number is given by

$$Gr_s = \frac{gs^3}{\nu^2}\beta\Delta T \tag{3.3}$$

where g is the gravitational constant, ν is the kinematic viscosity of the air, β is the coefficient of thermal expansion and ΔT is the temperature difference between hot runner nozzle and mold wall. For air, β may be calculated by $\beta = 1/T_\infty$ with T_∞ as the temperature outside the boundary layer. For pure conduction, the heat flux through the air gap is calculated by

$$Q_c = \frac{\lambda 2\pi l}{ln\,(r_o/r_i)}(\Delta T) \tag{3.4}$$

where λ is the thermal conductivity of the air and l is the length of the hot runner nozzle.

The second contributor to the total heat flux across the air gap is the radiative heat flux, which is given by

$$Q_{12} = C_{12}A_1\left(T_1^4 - T_2^4\right) \tag{3.5}$$

where A_1 is the surface area of the cylindrical part of the hot runner nozzle, T_1 its temperature, T_2 the temperature of the surrounding mold wall, and C_{12} is the view factor. For coaxial cylindrical surfaces, C_{12} is calculated by

$$C_{12} = \frac{\sigma}{\frac{1}{\epsilon_1} + \frac{A_1}{A_2}\left(\frac{1}{\epsilon_2} - 1\right)} \tag{3.6}$$

with σ being the Stefan-Boltzmann constant, ϵ_1 & ϵ_2 being the emissivities of nozzle and mold wall, respectively, and finally, A_1 & A_2 the surface areas of nozzle and mold wall. The emissivities strongly depend on the materials used and the condition of the surfaces, and may be somewhere between 0.2 and 0.9 for typical materials and surface finishes. These values as well as the temperature of the mold wall must be estimated in order to perform the heat flux calculation. Since the temperature of the hot runner nozzle is measured and controlled, it can be assumed to be constant. The predicted heat flux may then be directly applied to the mold wall. When a detailed 3D representation of the nozzle is preferred, as in this study, it is possible to calculate equivalent thermal properties and model the air as a solid body. The thermal conductivity λ of this fictive body and the heat transfer coefficient (HTC) at its interfaces to nozzle and mold wall must be selected to achieve the calculated heat flux. A convenient value is chosen for one parameter and the other is calculated. In this study λ was chosen to be $0.1\,\mathrm{W/m\,K}$ and the HTC was calculated by

$$HTC = \frac{(Q_c + Q_{12})\lambda 2(r_o + r_i)}{r_i\left(2\lambda(T_1 - T_2) - 2r_o(Q_c + Q_{12})\ln\frac{r_o}{r_i}\right)} \tag{3.7}$$

giving a reasonable value in the order of $300\,\mathrm{W/m^2K}$. Lower values of λ led to convergence issues and should be avoided.

3.6.2. Material data

DuPont Zytel 73G45 a PA6 grade with a short glass fiber content of 45% by weight was used in production. The simulations were performed using the relevant material data from Moldflow's material database (A.3). The values for the coefficient of thermal expansion were modified, as described in Section 3.5.6.

3.6.3. Process settings and boundary conditions

A relative ram speed profile with a target injection time was defined in order to model the filling stage (Fig. 3.38). The model comprises only one of the four cavities, and therefore, the packing pressure was estimated for the simulation.
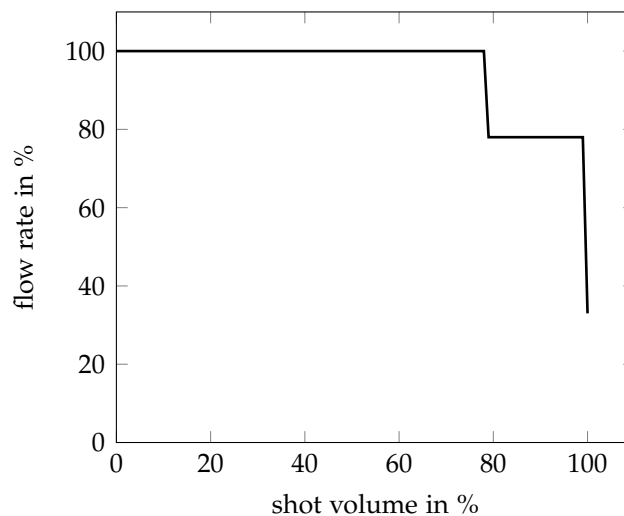
Figure 3.38.: Relative ram speed profile associated with an injection time of 2 s.

The inlet and outlet temperatures of the coolant as well as the volume flow rates were measured for both circuits. The experimentally determined values for temperature and volume flow were used for the simulation.

The process settings and boundary conditions used for the simulations with both models are summarized in Table 3.10.

Cooling analysis	
Melt temperature	285°C
Temperature of the hot runner nozzle	295°C
Injection + packing + cooling time	62 s
Mold-open time	28 s
Coolant	Water
Coolant temperature hot water	76°C
Coolant volume flow rate hot water	3.15 l/min
Coolant temperature cold water	25°C
Coolant volume flow rate cold water	5.3 l/min
Fill + pack analysis	
Injection time	2 s
Velocity/pressure switch-over	at 99.9% of the volume filled
Packing pressure	25 MPa
Packing time	25 s

Table 3.10.: Applied process settings and boundary conditions.

3.6.4. Mesh

For both models, the part was meshed with at least 12 elements across the wall thickness. The same is true for the 3D hot runner, in the case of the detailed model. Both models require a volume mesh of the mold for the transient cooling analysis. The meshed simplified model is shown in Fig. 3.35, while the mesh of the detailed model is shown in Fig. 3.36 and 3.37 respectively.

The mesh properties of the simplified model are summarized in Table 3.11 and those of the detailed model in Table 3.12[5].

	part	mold
Element count	2965673	5623538
Nodes	536652	1013354
Elements across wall thickness	12	6
max. aspect ratio	26.87	215.56
average aspect ratio	4.08	1.86
min. aspect ratio	1.04	1.01
max. dihedral angle	175.1	179.5

Table 3.11.: Mesh properties and diagnostics of the simplified model.

---

[5]The surface mesh of the detailed model was created with another software to obtain a conformal mesh between mold components. The different meshing algorithm led to a lower element count of the part mesh although the same discretization in thickness direction is maintained.

	part	hot runner 3D	mold
Element count	1845632	171261	2519420
Nodes	336410	31580	488704
Elements across wall thickness	12	12	6
max. aspect ratio	23.42	17.04	22.65
average aspect ratio	4.24	4.22	1.69
min. aspect ratio	1.02	1.04	1.00
max. dihedral angle	173.3	168.3	165.1

Table 3.12.: Mesh properties and diagnostics of the detailed model.

3.6.5. Results

Mold temperature distribution: simplified vs detailed model

Fig. 3.39 shows the temperature distribution in mold and part after 23 s, obtained with the simplified model. Although the core was cooled with a separate circuit and cold water, the temperature in the core was significantly higher than in the surrounding areas of the mold. This was caused by the large distance between the cooling lines and the cavity wall, and by the poor thermal conductivity of the mold, made from tool steel.

(a) Cut at the symmetry plane.

(b) Cut perpendicular to the symmetry plane and through the hot runner nozzle.
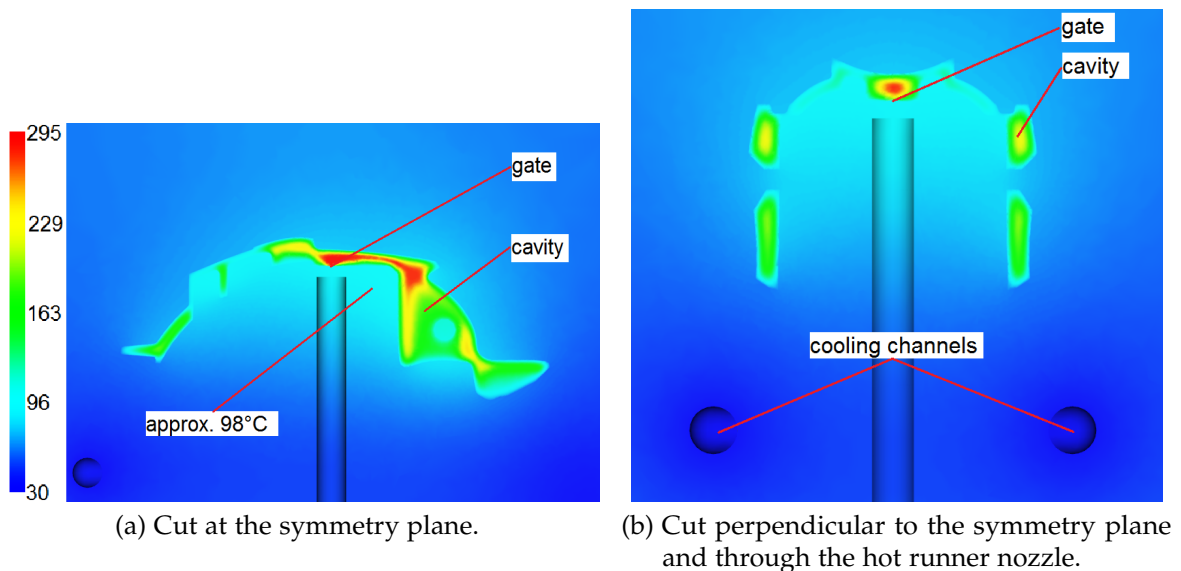
Figure 3.39.: Temperature distribution in mold and cavity obtained with the simplified model. Color coded is the temperature in °C after 23 s.

Fig. 3.40 shows the cavity surface temperature at the end of the cooling stage.

(a) Surface temperature cavity side.   (b) Surface temperature core side.
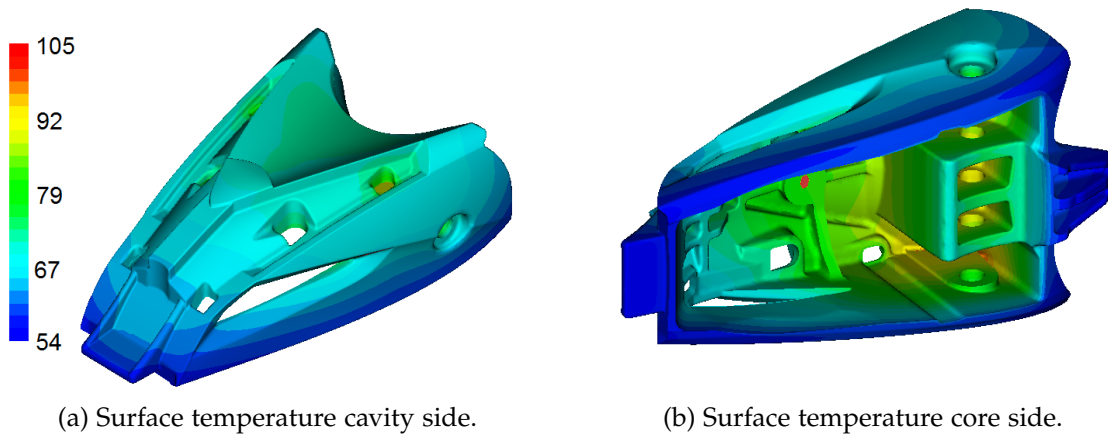
Figure 3.40.: Contours of cavity wall temperature at the end of cooling stage in °C. Obtained with the simplified model.

For this material, a target cavity wall temperature of 80°C is desired. According to the recommendations of common practice, the actual wall temperature should not deviate more than 5°C over the whole cavity surface. Otherwise, process related issues like poor surface quality or warpage may arise. In the case of complex parts, like those considered in this thesis, this limit is usually unattainable with conventional cooling methods. In the present case, the temperature deviation was much greater. Thís part, however, was made from fiber reinforced material, and the part design is quite rigid. Under such circumstances a much higher temperature deviation than 5°C is tolerable without excessive warpage. Due to the poor mold and cooling system design, the simulation with the simplified model already shows deviations of up to 50°C. Therefore, even the simplified model reveals the poor design of the cooling system. As the warpage results presented in Section 3.6.5 indicate, this would still be tolerable.

Fig. 3.41 shows the temperature distribution in mold and part obtained with the detailed model. The temperature was evaluated at the same time (after 23 s) and at the same locations as before. Due to the presence of the hot runner nozzle and its additional heat input, the predicted core temperature is much higher compared to the solution obtained with the simple model (Fig. 3.39). Moreover, it is obvious that proper cooling of the core is hardly possible due to the limited space around the nozzle.

The cavity temperature distribution at the end of the cooling stage is shown in Fig. 3.42. Much higher temperature deviations were predicted. While the wall temperature on the cavity side is hardly affected, the core side temperature was dramatically higher. The large temperature difference between inside and outside walls causes warpage of

71

(a) Cut at the symmetry plane.

(b) Cut perpendicular to the symmetry plane and through the hot runner nozzle.
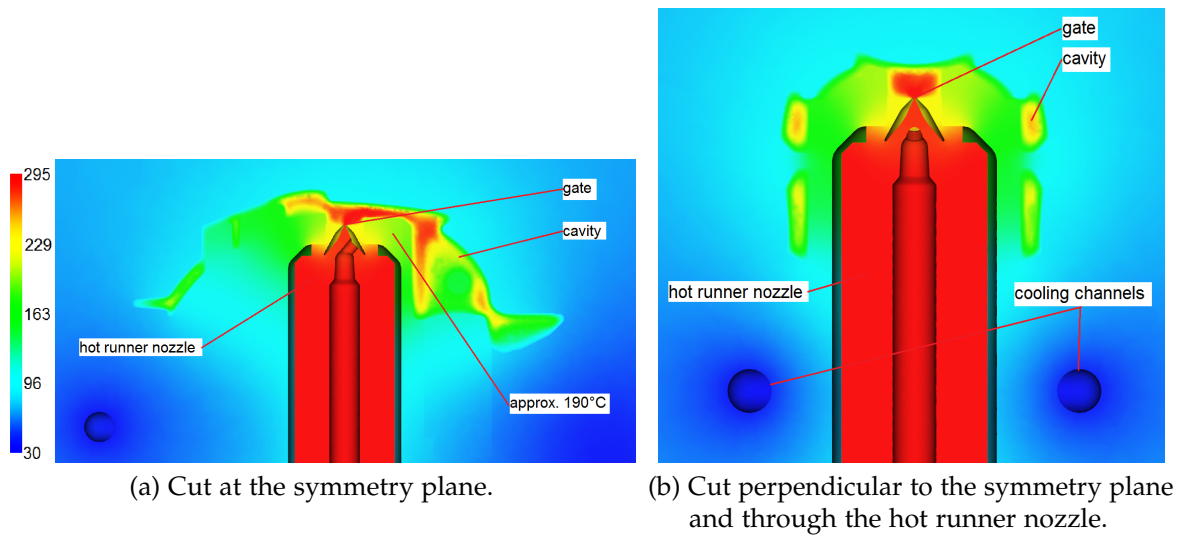
Figure 3.41.: Temperature distribution in mold and cavity obtained with the detailed model. Color coded is the temperature in °C after 23 s.

the part where its local stiffness is low.

Warpage

The rather straight side walls tend to bend towards the hotter core, which is the expected result of the warpage prediction shown in Fig. 3.43. One should bear in mind that the warpage magnitude plot shows the total deflection, including shrinkage. Due to the anisotropic shrinkage of fiber reinforced composites, it is not possible to isolate the out of plane deflection (warpage). The deflection magnitude predicted by the simple model mainly shows shrinkage in all directions and a slight warpage of the side walls in the order of 0.1 mm (Fig. 3.43a). This is much less than was observed experimentally.

Fig. 3.43b shows the predicted deflection magnitude obtained with the detailed model. The warpage of the side walls around the nozzle is much higher. This additional deflection is only caused by the high temperature difference between cavity and core side.

A 3D comparison of the predicted part shape with the actual molded and scanned part again shows extremely good correlation (Fig. 3.44b). The largest deviations to the molded part are in the order of only 0.2 mm.

Assuming an ideally cooled mold (T_w =const.), the simulation results shown in Fig. 3.45 indicate that no significant warpage occurs. Hence, the warpage related

(a) Surface temperature cavity side.

(b) Surface temperature core side.
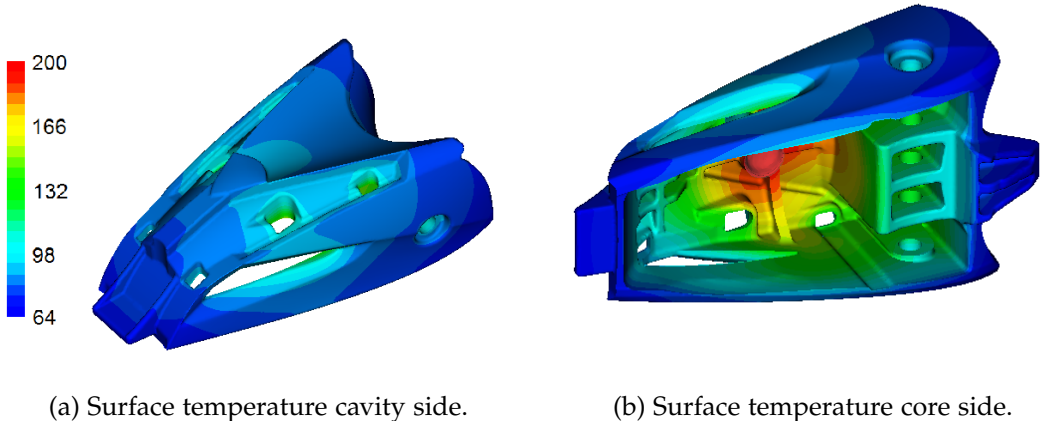
Figure 3.42.: Contours of cavity wall temperature at the end of the cooling stage in °C. Obtained with the detailed model.

(a) Simplified model
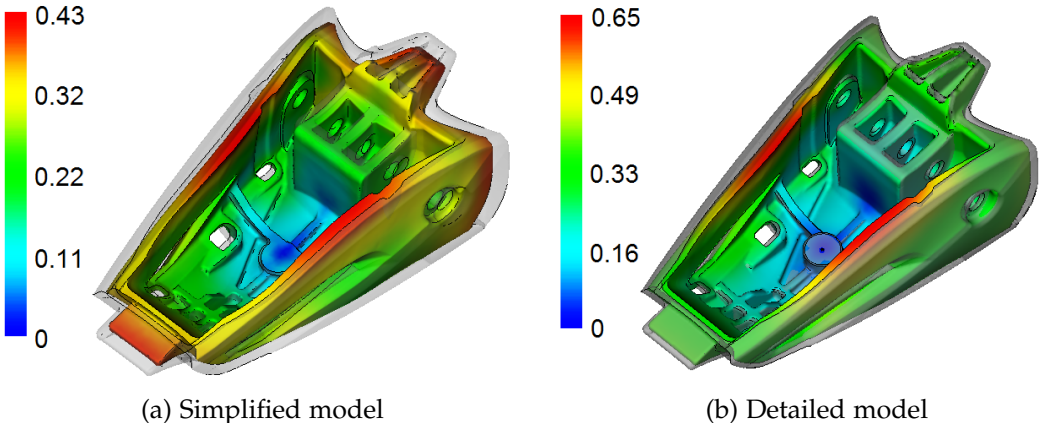
(b) Detailed model

Figure 3.43.: Predicted deflection magnitude in mm obtained with both models.

(a) 3D Comparison: Molded and measured part (reference) vs CAD part (test).

(b) 3D Comparison: Molded and measured part (reference) vs virtual part (test).
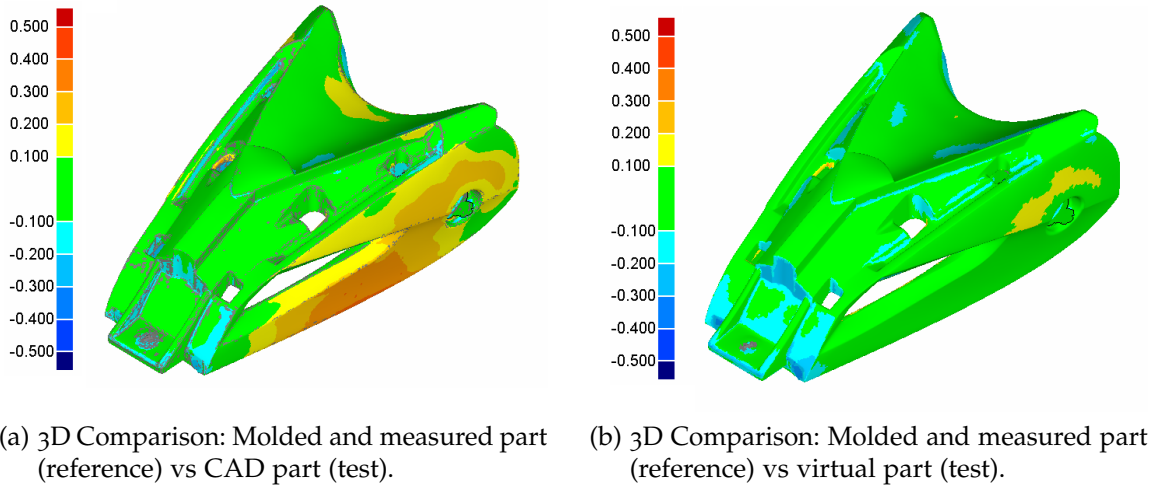
Figure 3.44.: Warpage result verification of the detailed model.

problems are essentially caused by poor mold design and could have been eliminated before actually cutting the mold. This study further shows the requirement of large temperature differences if one aims to compensate for warpage due to the orientation effects of fiber reinforced polymer grades with measures of mold cooling design. In the majority of cases (for instance the case presented in Section 3.5) the required temperature difference would be too high to do this.
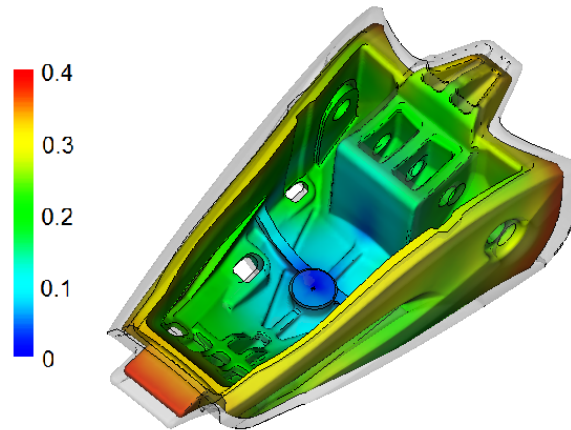
Figure 3.45.: Deflection magnitude obtained with ideal cooling condition ($T_w = $ const.)

3.7. Case study: Compensation for warpage

The last part presented in this Chapter was actually analyzed and optimized before the mold was cut. As is the case for all parts considered in this work, the part has a very complex shape with thin-walled regions as well as very thick-walled regions. Its dimensions are approximately $169 \times 72 \times 52\,\mathrm{mm}^3$, and the wall thickness is in the range of around $1\,\mathrm{mm}$ to up to $8\,\mathrm{mm}$. A bridge mold with only one cavity was planned. The part was molded from DuPont Zytel73G45 (PA6 GF45).

Preliminary calculations showed some design weaknesses and revealed a much better way of gating the part. Fig. 3.46 shows the final shape of the part, including a deformation of the plate-like section to compensate for warpage.

(a)   (b)
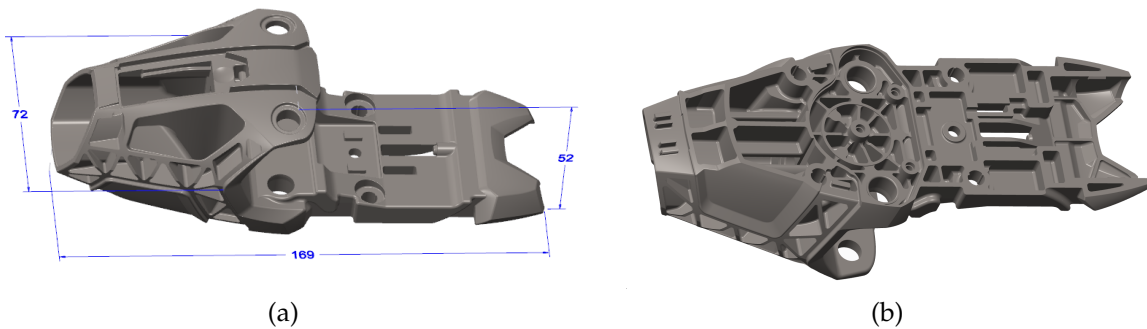
Figure 3.46.: Two views of the investigated part with the optimized geometry.

3.7.1. Numerical model

In this case, several models were required to improve part design and gate location. While only the final model is presented in detail in the subsequent sections, a brief explanation of the various models is given here.

The first model was a simple standard simulation considering only the part geometry without runner or cooling system. Due to the complexity of the part geometry, a 3D simulation was necessary. This model was used to predict the filling pattern, as well as the location and shape of weld lines with. In the case of fiber filled polymer grades, shrinkage and warpage are dominated by orientation effects. Hence, the simple model is also suitable to investigate the influence of the gate location (and therefore the fiber orientation) on warpage. However, warpage predictions obtained with this model only show if one gate location causes more or less warpage than another. The model should not be used to predict the warpage magnitude. Different gate locations were tested to investigate the position of weld lines, the packing efficiency, and the risk of warpage.

A more detailed model, featuring a simplified hot runner nozzle (similar to Fig. 3.26), and a preliminary cooling layout, was made to gain a clearer picture of the actual warpage magnitude. The part was then modified based on the findings obtained with this model. Large areas with high wall thickness were cored out and the warpage was compensated for by deforming the part in the opposite direction of the predicted out-of-plane deflection. After completion of the mold design, a final simulation with an even more detailed model was performed in order to check if further modifications to the mold design were necessary. This model was also used to validate the simulation results with the measurements, and is therefore described in detail. The model showing part, hot runner, and cooling channels is depicted in Fig. 3.47.
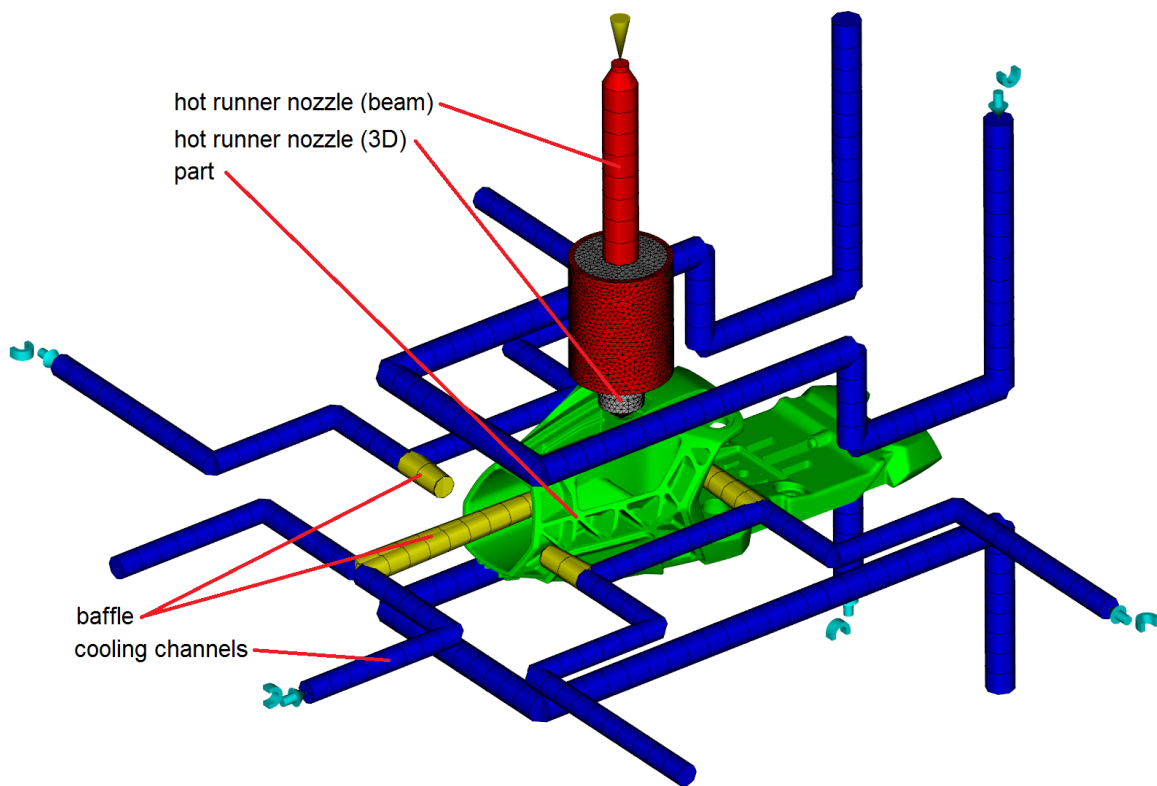
Figure 3.47.: Numerical model of the investigated part featuring cavity, detailed hot runner, and cooling channels.

3.7.2. Material data

DuPont Zytel 73G45 a PA6 grade with a short glass fiber content of 45% by weight was used in the simulation and for the first molding trials. The material data used for the simulation came from Moldflow's material database (A.3).

3.7.3. Process settings and boundary conditions

The simulations were performed before the mold was actually built. Therefore, all process settings were estimated based on experience. These settings are summarized in Table 3.13.

Cooling analysis	
Melt temperature	285°C
Injection + packing + cooling time	50 s
Mold-open time	12 s
Coolant	Water
Coolant temperature	60°C
Coolant volume flow rate	3 l/min
Fill + pack analysis	
Injection time	2 s
Velocity/pressure switch-over	at 99% of the volume filled
Packing pressure	40 MPa
Packing time	30 s

Table 3.13.: Applied process settings and boundary conditions for DuPont Zytel 73G45.

3.7.4. Solver settings

The analysis sequence used was: Cool (FEM) + Fill + Pack + Warp. All the solver settings presented in Section 3.3.4 were retained for this study.

3.7.5. Mesh

According to the findings presented earlier, all polymer domains were meshed with at least 12 element layers across the wall thickness. These are the part and the 3D hot runner. The tip of the hot runner nozzle was modeled and meshed in 3D to capture the influence of its heat input on the warpage of the part. The meshed model is shown in Fig. 3.48 and the mesh properties are summarized in Table 3.14.
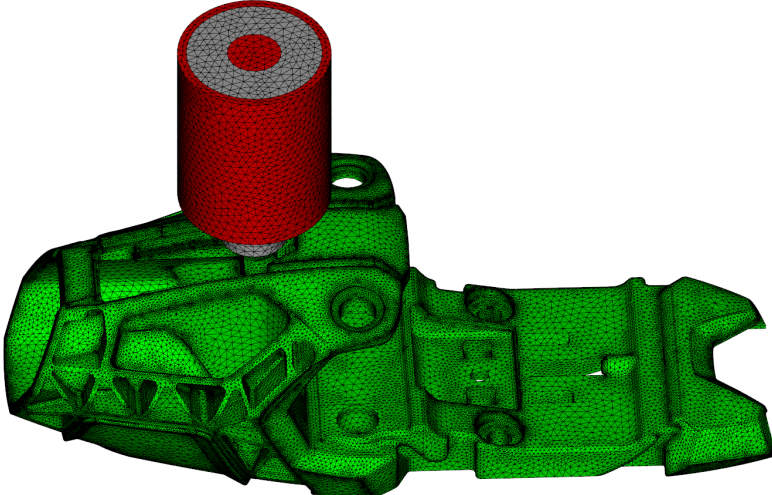
(a) Surface mesh of part and hot runner nozzle.
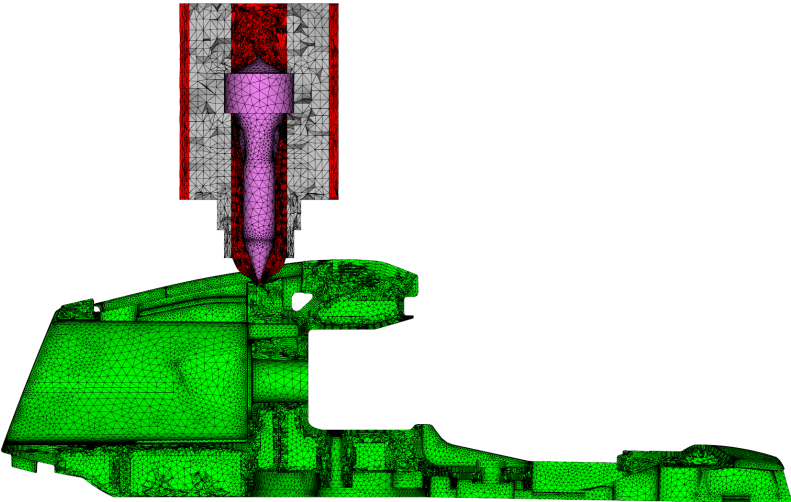
(b) Cut through the part mesh showing the layered element structure and the geometry of the hot runner nozzle.

Figure 3.48.: Mesh of the model. The mold mesh is not shown.

	part	hot runner 3D	mold
Element count	8210968	260114	4144027
Nodes	1412600	45437	794639
Elements across wall thickness	12	12	6
max. aspect ratio	103.51	87.82	357.14
average aspect ratio	5.22	6.81	2.37
min. aspect ratio	1.02	1.04	1.01
max. dihedral angle	177.4	177.2	178.9

Table 3.14.: Mesh properties and diagnostics.

3.7.6. Results

First warpage predictions with the simple model

The first version of the part was meant to be gated via a cashew gate at the right end of the part in a thin walled section. Moreover, there were also large regions with very high wall thickness. The first calculation, assuming ideal cooling and with estimated process parameters, led to the warpage prediction shown in Fig. 3.49a. The plate-like section warps upwards, which is not acceptable for this part. Moreover, the selection of the gate location turned out to be highly undesirable since proper packing of the heavy walled sections was not possible and may have led to poor strength properties of the part as well as unreliable warpage predictions.

A more suitable gate location, at the thick walled region of the part, was selected and an additional calculation was performed. Ideal cooling conditions were assumed. The predicted deflection magnitude was significantly lower, as Fig. 3.49b shows. The proper packing of the thick sections was also guaranteed (Fig. 3.49c).

Final warpage prediction with the detailed model

Based on the findings, the part design was further improved by coring out some of the thick walled areas. Moreover, the part was deformed in the opposite direction of warpage. The preceding case studies revealed that warpage is generally underpredicted by moldflow. Therefore, warpage was overcompensated for by approximately 40%. An additional simulation, considering a preliminary cooling layout, was also conducted. Due to the ribbed structure of the plate-like section, the mold temperature of the core side is likely to be higher than the cavity side, leading to thermal stresses which tend to reduce warpage. Therefore, the cooling system of the mold has to be taken into account for quantitative warpage predictions. The results indicated that the part design had been sufficiently improved, and the mold design was started.
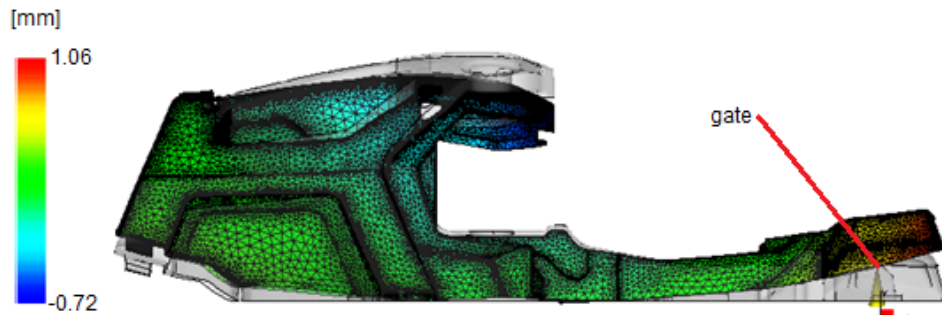
(a) Predicted deflection magnitude of the first version in mm, assuming ideal cooling.
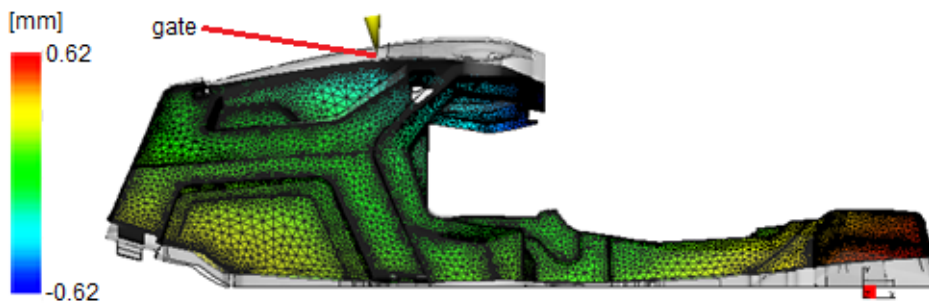
(b) Predicted deflection magnitude in mm, with a better gate location, assuming ideal cooling.
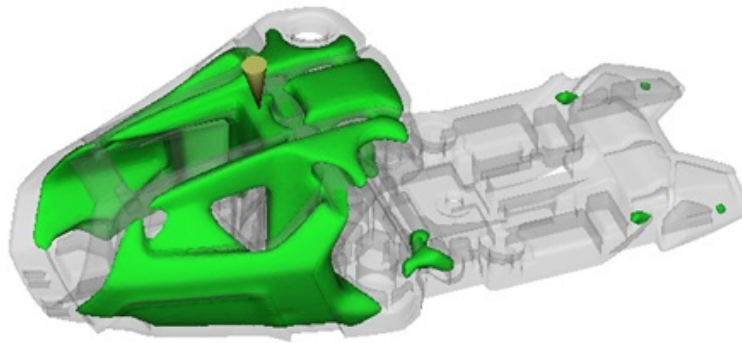
(c) Isosurface of the transition temperature after 31.5 s. It shows the region with high wall thickness. The gate was placed to properly feed this region during the packing stage.

Figure 3.49.: The preliminary simulation results were used to determine a suitable gate location and detect potential warpage.

After the completion of the hot runner and cooling layout design, a final calculation
was performed comprising the actual cooling lines as well as the hot runner nozzle.
The model is shown in Fig. 3.47 and the predicted deflection magnitude is shown in
Fig. 3.50a . According to the simulation results, the bottom of the part keeps a slight
curvature towards the core side. This was accepted since all of the earlier case studies
had shownthat warpage is usually underpredicted.
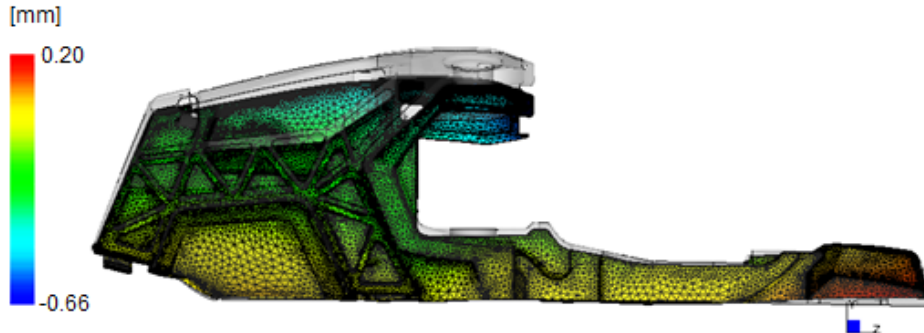
(a) Predicted deflection magnitude in mm, obtained with the final model.
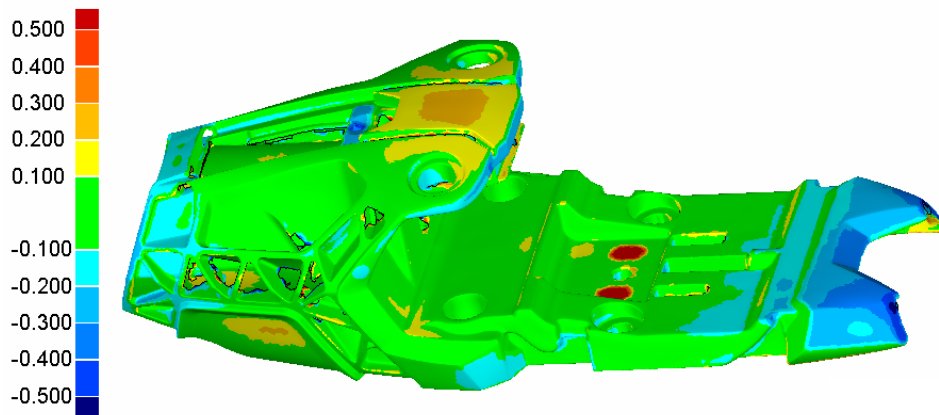
(b) 3D comparison of molded part (reference) and predicted part shape (test).
Color coded is the deviation magnitude in mm.

Figure 3.50.: Warpage prediction obtained with the final, detailed model, based on estimated process
and boundary conditions, compared to a molded part.

Fig. 3.50b shows the 3D comparison of the actually molded and scanned part (ref-
erence) and the predicted part shape obtained with the latest model, as well as the
estimated process parameters. The molded parts had a nearly perfectly flat bottom
face, which means that the true warpage is somewhat larger than predicted. As
already mentioned, this behavior was expected. The deviations are below 0.2 mm in
most areas of the part. The highest deviation is in the order of 0.4 mm and found at
the end of the plate-like section. Despite the complexity of the part and the estimated
process settings, very good accordance was achieved.

81

3.8. Concluding remarks

All of the case studies presented in this chapter consider parts which do not have the classic thin-shell structure of common plastic parts. They all have a complex geometry with thin and very thick walls, which causes a 3D flow regime in most regions of the cavity. Hence, common simplifications, such as the Hele-Shaw flow approximation, cannot be used in these cases. Although much research work was conducted on simple parts, such as rectangular flat plates or center-gated disks, and, to a lesser extent, on more complex, yet still class thin-shell plastic parts, such as housings and boxes, hardly any studies demonstrate the applicability to really complex parts. The investigations performed in this work showed that quantitative warpage prediction is possible even for such complex and chunky parts as those described here. This chapter highlights the great potential of injection molding simulation software, as well as its proper application to chunky parts.

However, good accordance of the predicted and measured warpage was not achieved in all cases. Chapters 5 and 6 deal with parts for which the simulation failed to predict the observed warpage with reasonable accuracy. So far, it is possible to conclude that reliable warpage predictions are possible even for complex parts as long as the following prerequisites are met:

- The part is gated in the region with the highest wall thickness.
- Gate and runner are properly sized to ensure low volumetric shrinkage throughout the part.
- If warpage of a fiber reinforced part is predicted, the warpage occurs in a thin walled region of the part.
- A cooling analysis is performed to consider the temperature effect on warpage.
- The quality of the available material properties was verified by true test cases.

Reliable warpage prediction is the basis for the compensation for warpage before the mold is built. With this approach, costly and time consuming reworking of the mold could be minimized or even avoided completely. The advantages brought about by reliable warpage prediction are thus:

- shorter time to market due to less reworking of the mold
- lower cost of the mold
- more freedom in mold design (for instance at the cooling layout) because of the strongly reduced probability of major reworking requests.

4. The elastic mold deformation during the filling and packing stages[1]

The case study presented in this chapter deals with one effect caused by a mold with poor stiffness. Injection molding simulation tools normally suppose a rigid mold. If the injection mold is properly designed, this assumption is absolutely feasible. However, in practice, mold design is quite often based on empirical knowledge. In this case, the mold designer does usually not posses the ability and/or the tools to predict the acting forces and the deformation of the mold. This can be a severe issue if the mold design is for a plastic part of a completely different shape. This case study was set apart from Chapter 3 since it essentially shows a consequence of poor mold design. Considering the elasticity of the mold in simulation is, on the one hand, hardly feasible, and, on the other hand, not necessary if the mold is designed well. A noteworthy exception is, for instance, the deformation of a slender core.

The present study shows a long and mostly thin-walled ribbed plate where the predicted filling pattern did not match the experimental short shots. A number of simulations were performed to investigate the influence of mesh, material data, process settings, and mold temperature on the filling pattern. It was found that the predicted filling pattern is hardly affected by those influencing factors. The simulations did not provide an explanation for the high deviation between experiment and prediction.

A simplified structural finite element analysis of the moving mold half, under filling and packing pressure, revealed the low stiffness of the mold. Adding additional supporting pillars under the moving mold plate significantly improved the stiffness, and led to a significantly different filling pattern. The short shots produced with the stiffer mold were finally in good agreement with the prediction.

As previously mentioned, the mold is assumed to be rigid for the simulation of the injection molding process. Therefore, the cavity pressure does not affect the shape or dimensions of the cavity. High cavity pressure in conjunction with a poorly designed mold, on the other hand, can lead to considerable deformation of the mold components.

---

[1]Parts of this chapter were published in Smart Science under the title "The Elastic Mold Deformation During the Filling and Packing Stage of the Injection Molding Process" [125]

Leo & Cuvelliez [120] found that the elasticity of the mold has a great influence on the pressure history in the cavity. For accurate pressure predictions in the cavity, the elasticity of the mold may not be negligible. A reasonable agreement with pressure measurements was achieved by means of simulations considering the compliance of the mold plates. They further concluded that the elasticity of the mold also affects shrinkage, residual stresses, warpage and the final dimensions of the part. Investigations performed by Pantani *et al.* [122] led to similar conclusions. They investigated the influence of the thermal boundary conditions on the pressure history in the cavity by means of simulation and measurements. They concluded that the thermal boundary conditions have only a minor effect. In contrast, the false assumption of a rigid mold can lead to wrong pressure results, while even a simple modeling approach to consider mold elasticity is able to dramatically improve pressure predictions in the cavity. Attempts to consider the elasticity of the mold were made, for instance, by Giacomin *et al.* [123]. They derived an analytical solution to model the deformation of a slender core and to predict the pressure development in the gap between core and cavity. A more general approach was proposed by Bakharev *et al.* [124]. They developed a method to couple the plastic flow and the deformation of an elastic core in injection molding simulations. The approach is two-way coupled, which means a core deflection will change the local wall thickness of the molding, and hence, pressure distribution and history, as well as the final part dimensions.

This case study shows that the elasticity of the mold can also severely affect the filling pattern. If the melt pressure causes an elastic deformation of the mold, the local wall thickness also changes. Hence, the actual flow resistance and, consequently, the filling pattern changes.

4.1. Problem description

Fig. 4.1a shows two views of the part considered in this study. Its overall dimensions are approximately $554 \times 60 \times 16 \, \mathrm{mm}^3$, and it has a wall thickness ranging from 1 to 4 mm. The ribs on the bottom side have a thickness of about 1.5 mm. The part was molded from DuPont Zytel 73G45 (PA6 GF45) in a two-cavity mold. The mold has two hot runner drops, which feed a cold runner with two submarine gates, as shown in Fig. 4.1b. The first molding trials revealed an unbalanced filling pattern. As Fig. 4.1c shows, the right hand side of the short shot was already filled, while around 40 mm were missing on the left hand side. Moreover, a distinct tendency to flash was observed on the right side of the plate. A numerical simulation of the plate was performed in order to determine the location of flow leaders so as to obtain a more balanced mold filling.
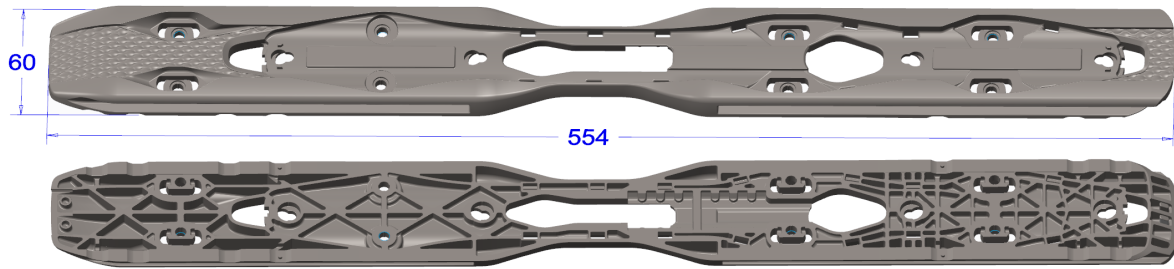
(a) CAD model of the ribbed plate with its overall dimensions.
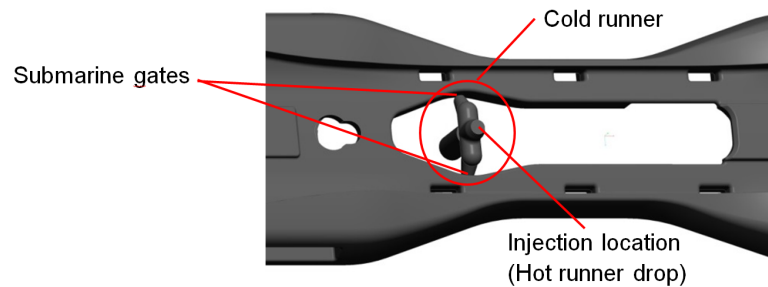
(b) Close-up of cold runner and tunnel gates at the center of the part. [125]
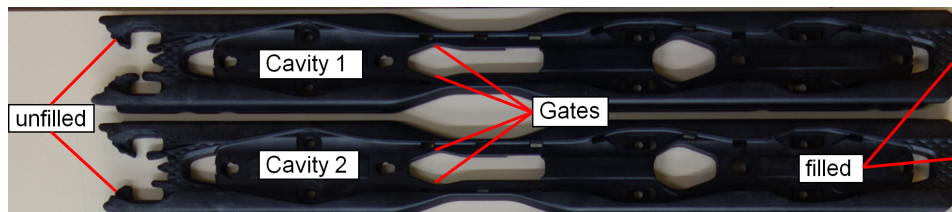
(c) Experimental short shots produced with PA6 GF45: Right hand side completely filled with burrs along the parting line. Left side: still unfilled. [125]

Figure 4.1.: CAD model and short shots of the part investigated in this case study.

It was found that the predicted filling pattern was actually quite different from the experimental short shots. Fig. 4.2 shows the predicted filling pattern obtained with the model described in the next sections. The geometry of the cavity and the simulation model was indeed the same. The short shot was taken at the p/v switch over and compared to the predicted flow front after 1.65 s. This extraordinarily high deviation between simulation and experiment precipitated the thorough case study presented in this chapter.
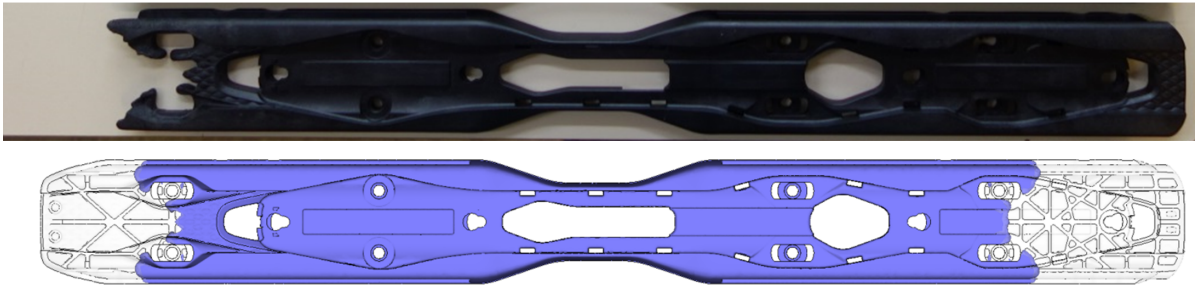
Figure 4.2.: Comparison of the experimental short shot (top) and the prediction (bottom). [125]

4.2. Injection molding Simulation

4.2.1. Numerical model

Fig. 4.3 shows the numerical model of the ribbed plate, including cold runner and cooling channels. For the reasons pointed out earlier (see Section 3), only one of the two cavities was modeled. As is common practice, the mold was assumed to be rigid. This model was used to investigate the influence of mold temperature, mesh, as well as solver- and process settings on the filling pattern.
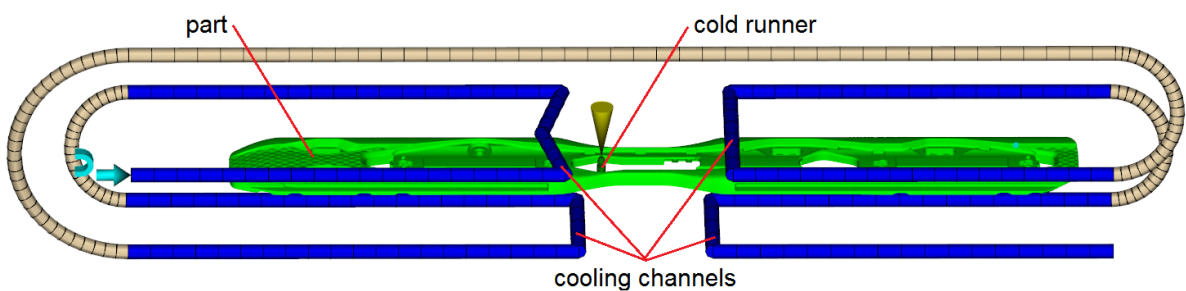
Figure 4.3.: Numerical model of the investigated part featuring cold runner and cooling channels.

4.2.2. Material data

The material used in the molding trials was DuPont Zytel 73G45 a PA6 grade with 45% short glass fiber reinforcement by weight. The material properties for the simulations were taken from Moldflow's material database and are summarized in A.3. As in all studies presented in this thesis, the rheological behavior of the material was modeled using the Cross-WLF equation, and the pvT relationship was expressed by the 2-domain Tait equation.

4.2.3. Process settings and boundary conditions

The preceding studies have shown that using an injection velocity profile has no significant influence on the filling pattern in the case of chunky parts. A simulation assuming a constant volume flow rate with a total injection time according to the experiment is therefore a sufficiently good approximation. Considering a short injection time and thick walls, the frozen layer will be very thin when the v/p switchover is reached. The local flow resistance is therefore hardly affected by the blocking effect of the thin frozen layer.

In this case, however, the flow length was high and some of the walls were rather thin. Therefore, the experimental injection velocity profile was modeled correctly to simulate mold filling with minimal error. A relative ram speed profile with a target injection time of 2 s was used (FIG.4.4). The pressure loss in the machine nozzle and the hot runner system was estimated to be 40%. A packing pressure of 50 MPa was applied at the cold runner. Both the coolant volume flow rate and the temperature were set in accordance with the measurements obtained during molding trials.
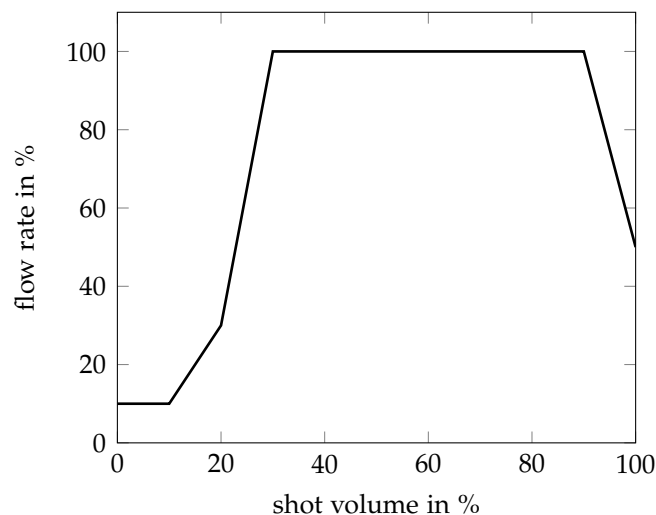
Figure 4.4.: Relative ram speed profile associated with a target injection time of 2 s.

The process settings and boundary conditions used for the simulation are summarized in Table 4.1.

4.2.4. Mesh

In this case, the simulation result of prime interest was the filling pattern. The complexity of the part geometry does not allow the Hele-Shaw approximation to

4. The elastic mold deformation during the filling and packing stages

Cooling analysis	
Melt temperature	295°C
Injection + packing + cooling time	45 s
Mold-open time	13 s
Coolant	Water
Coolant temperature	68°C
Coolant volume flow rate	4.4 l/min
Fill + pack analysis	
Injection time	2 s
Velocity/pressure switch-over	at 95% of the volume filled
Packing pressure	50 MPa
Packing time	10 s

Table 4.1.: Applied process settings and boundary conditions.

be used. Therefore, a 3D simulation was performed. The level of detail of the part requires a fine discretization of the surface, which causes a high element count. To maintain an acceptable computational effort, the number of element layers across the wall thickness was limited to 6. The mesh properties and diagnostics are summarized in Table 4.2.

	part	cold runner 3D	mold
Element count	5307188	20249	3827572
Nodes	973046	4143	741699
Elements across wall thickness	6	6	6
max. aspect ratio	99.08	57.33	433.60
average aspect ratio	3.95	4.77	6.17
min. aspect ratio	1.03	1.10	1.02
max. dihedral angle	178.7	176.2	179.6

Table 4.2.: Mesh properties and diagnostics.

A second mesh with 12 element layers across the wall thickness was generated to check the influence of the mesh density on the solution. The finer mesh comprised approximately 18×10^6 tetrahedral elements. Due to the very high computational cost, this mesh was only used for a fill analysis with a constant cavity wall temperature.

4.2.5. Analysis and solver settings

Several different settings were used in this case, and their influence on the filling pattern was investigated:

1. The first, and usually sufficiently accurate, approach to predicting the filling pattern is to assume a constant cavity wall temperature. In this case, no cooling channels were required, and consequently no mold mesh. The same solver settings were used as described in Section 3.3.4. Only a fill analysis assuming a cavity wall temperature of 80°C was performed.

2. The second simulation also included the mold cooling system in order to consider the local cavity wall temperature in the fill analysis.

3. The third simulation aimed to check if the problem was caused by numerical errors. A fill analysis (no cooling considered) with a finer discretization in space and time was performed. The fine mesh (with 18×10^6 elements) was used in conjunction with more stringent solver settings to enforce smaller time steps. The convergence tolerance factor was reduced from the default value of 1 to 0.1. Moreover, the parameter "maximum % volume to be filled per time step" was reduced from 4 to 1%. With these settings, the time to solution for the filling simulation increased by 900%.

4. The last analysis also considered poor venting conditions in the mold, although no burn marks were observed on the molded parts. The mold has continuous vents with a gap of 0.02 mm on either side of the cavity. For the simulation, vents with a gap of 0.01 mm were defined on the left hand side of the cavity to model the blockage of the small gaps caused by deposits. On the right hand side of the cavity, the thickness of the vents was set to 0.15 mm to model the widening of the parting line due to the deformation of the mold. In this case, the air in the cavity was able to easily escape on the right side, but caused a counter pressure to the melt front on the left side.

4.3. Results of the injection molding simulations

As shown in Fig. 4.2, a standard fill analysis (simulation 1) did not produce results which matched the experiments. Therefore, different simulations were performed to check their influence on the solution accuracy of the flow front prediction. Fig. 4.5 shows the results obtained with simulations 1-4. In all cases, a time step was chosen where the left flow front was in approximately the same position.

4.3.1. Influence of the thermal boundary conditions on the filling pattern

Fig. 4.6 shows the predicted cavity wall temperature at the beginning of the molding cycle. This result was obtained with simulation 2. The temperature level is generally
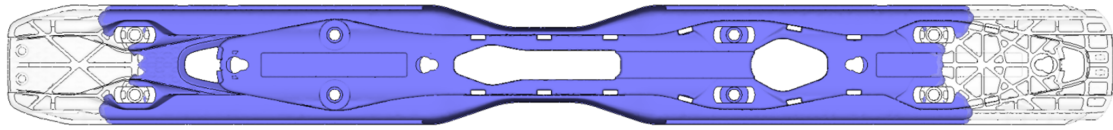
(a) Simulation 1: Melt front at 75% of the cavity volume filled. Assuming a constant cavity wall temperature.
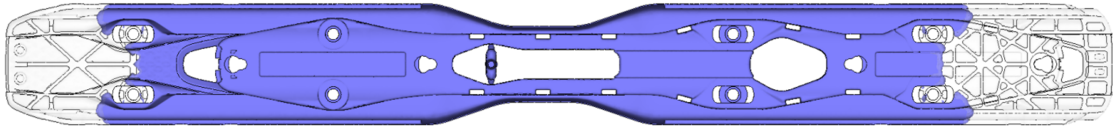
(b) Simulation 2: Melt front at 74.5% of the cavity volume filled. Considering a transient temperature distribution of the cavity walls.
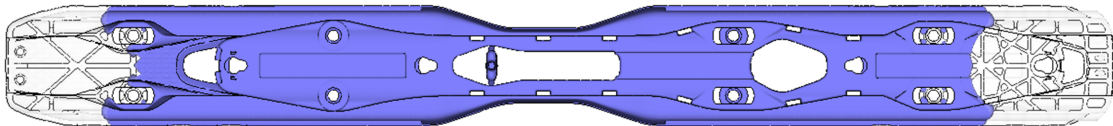
(c) Simulation 3: Melt front at 76.5% of the cavity volume filled. Solution obtained with a finer mesh.
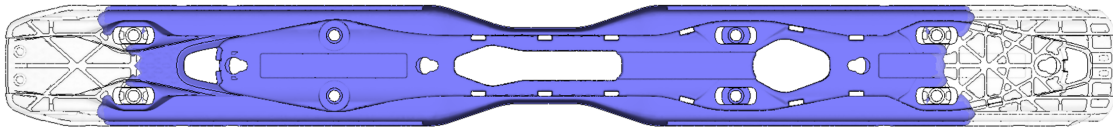
(d) Simulation 4: Melt front advancement in the case of poor venting on the left side of the cavity. 74% of the cavity volume filled.

Figure 4.5.: The predicted flow front obtained with simulations 1-4.[125]

higher on the core side of the cavity. The high number of ribs on the right side of the part caused a large hot spot with a temperature of up to 102°C. The transient cavity wall temperature distribution was, in this case, used as boundary condition during the fill analysis. As Fig.4.5b shows, the influence of the cavity wall temperature on the filling pattern is not significant. The positions of the two flow fronts are barely different.

4.3.2. Influence of the mesh density on the filling pattern

The results obtained with simulation 3 shows that a finer discretization in space and time actually has a greater effect on the solution than the thermal boundary conditions at the cavity walls. The flow front on the right side has moved somewhat
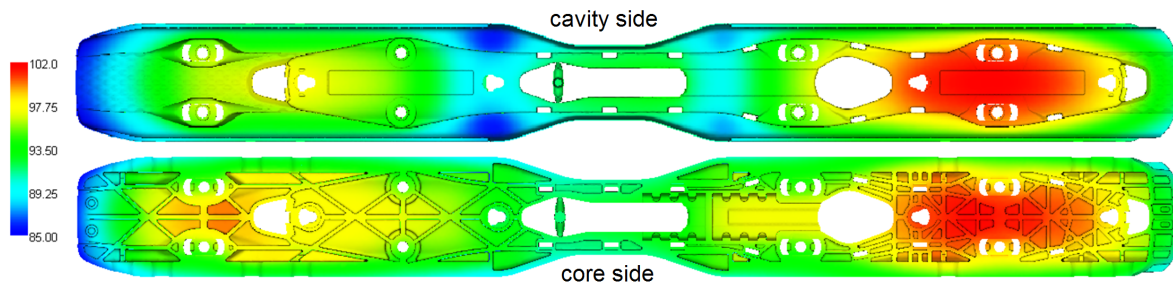
Figure 4.6.: Temperature distribution of the cavity walls at the beginning of the molding cycle. Color coded is the temperature in °C. [125]

farther. Compared to the experimental short shot presented in Fig. 4.2, the solution is still way off the experiment.

4.3.3. Influence of the venting conditions on the filling pattern

Fig. 4.5d shows the mold filling result obtained with simulation 4, considering the poor venting of the cavity. Even in this case, the predicted filling pattern hardly changes. The restricted venting conditions on the left side of the cavity cause a pressure rise of the trapped air to 0.5 MPa. Compared to the injection pressure of up to 35 MPa at the cold runner sprue, this effect is again negligible.

4.4. Influence of the mold elasticity on the filling pattern

The experimental and simulated results indicated that the elastic deformation of the mold under melt pressure may have caused the poor accordance of the predicted filling pattern.

Modeling the interaction between mold deformation and melt pressure requires a strong coupling between flow and structural analysis, as proposed by Bakharev *et al.* [124]. This method has several limitations. It is not possible to model interactions, such as contacts between elastic bodies. This would, on the one hand, enable the accurate prediction of the stiffness of the assembly, but, on the other hand, make the structural analysis nonlinear and very time consuming. Modeling the whole assembly of the moving mold half as one single block is feasible, but would dramatically overpredict the stiffness of the mold. Therefore, a severely simplified, decoupled modeling approach was proposed to approximately calculate the mold deflection.
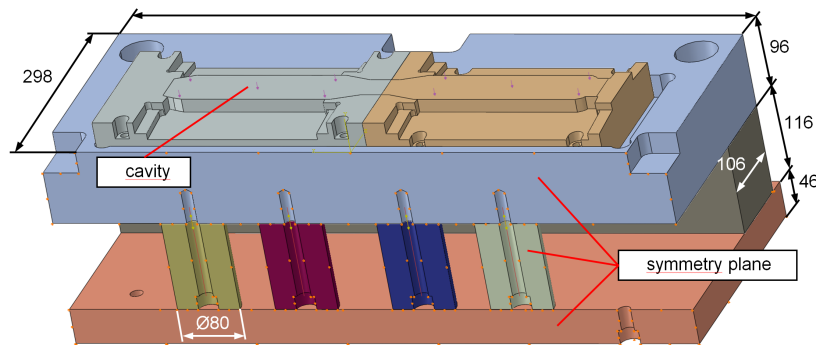
Figure 4.7.: CAD model of the simplified moving mold half. All dimensions are given in mm.[125]

4.4.1. Modeling the elasticity of the mold

The commercial high-end FEM software ABAQUS from Dassault Systèmes was used to calculate the elastic deformation of the moving mold half. An approximated analytical pressure distribution based on a Moldflow fill and pack analysis was applied as load.

All of the features of the mold parts that do not significantly contribute to the stiffness of the mold (fillets, chamfers, small holes, etc.) were neglected in order to minimize the meshing effort and computational cost. Additionally, the complex shape of the core side cavity was substituted with a plane surface of approximately the same projected area. Due to the symmetry of the mold, only one half of the moving side was modeled. Fig. 4.7 shows the CAD model of the simplified, moving mold half, including its overall dimensions.

The core side of each cavity consists of two mold inserts and four slides. Due to the complexity and nonlinearity of the interaction between clamp force, pressure force, and the inherent contact forces between all the mold components, only a simplified model was used to investigate the deformation of the moving mold half. In reality, even the clamp force of the injection molding machine could cause the elastic deformation of the mold. However, the aim of this analysis was to determine whether or not the mold plates undergo a significant deformation during the molding process. Hence, only the core side inserts, mold plate, spacer blocks and supporting pillars were considered. A hard contact was defined between the mold components. All screws were modeled as beams. Only the melt pressure force and the pretension of the screws were taken into account.

4. The elastic mold deformation during the filling and packing stages

Material

All the mold components shown in Fig. 4.7 were made of different grades of tool steel. Plastic deformation of any component of the mold was not taken into account. Thus, a simple linear elastic material model with the elastic properties:
Young's Modulus E = 200 GPa
Poisson's Ratio ν = 0.3
was used.

Boundary conditions

A symmetry boundary condition was defined at the symmetry plane of the mold. The machine plate was assumed to be rigid. For this reason, the nodes on the base face of the clamping plate were fixed in the normal direction. Only one node of the base face was fixed in tangential direction in order to remove the last degree of freedom.

Loads

The deformation of the mold is, of course, time dependent. In this case, only two load states were considered:

- First state: The cavity is almost filled. The pressure distribution was approximated from the Moldflow fill analysis with $p(x) = 35e^{-5\cdot10^{-5}x^2}$. Fig. 4.8a shows the simulated pressure distribution in the cavity at the end of the filling stage and the approximated analytical pressure distribution used for the FEM-analysis.
- Second state: Peak cavity pressure during packing phase. The Moldflow packing analysis shows an almost constant peak pressure in the whole cavity for a short moment (Fig. 4.8b). So, in the second load step a constant pressure of 50 MPa was applied to consider this highest load case.

Mesh

Due to the quick and effortless meshing, a second order tetrahedral mesh was generated for all 3D parts of the mold. The total number of elements was 468804 and the number of nodes was 691911.

4. The elastic mold deformation during the filling and packing stages
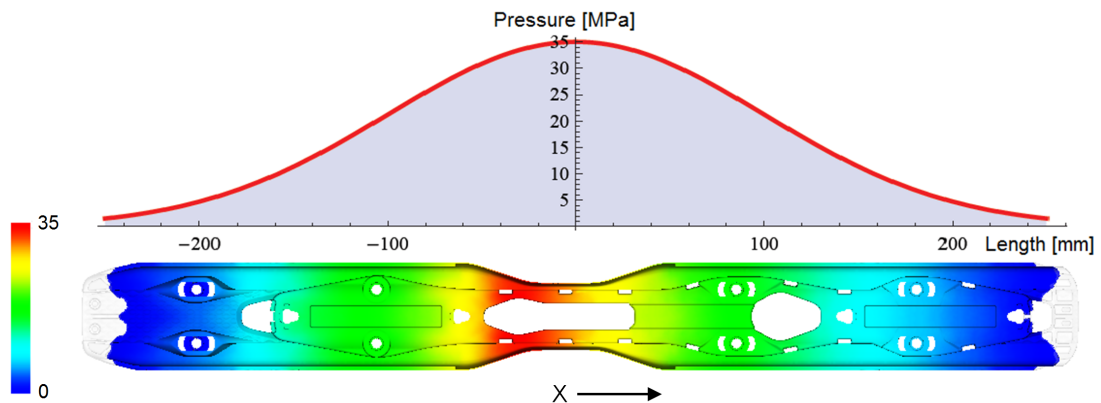
(a) Predicted pressure distribution at the end of the filling stage in MPa and the analytical approximation.
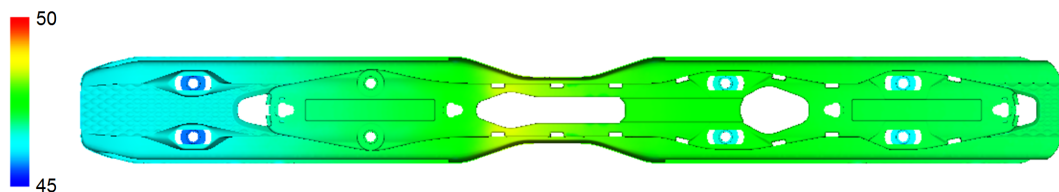
(b) Predicted peak pressure during packing stage in MPa.

Figure 4.8.: Cavity pressure distribution used for the structural simulation.[125]

Solver settings

A static analysis neglecting the nonlinear effects of large displacements with automatic load incrementation was performed for three load steps:

- pretension of the screws (This load step is defined for stability purposes only and is not further mentioned in the discussion of the results)
- melt pressure load in the filling stage
- melt pressure load in the packing stage

All other solver settings were left to default.

4.4.2. Results of the structural FEM analysis

Fig. 4.9a shows the displacement magnitude for the first load state, representing the mold deformation at the end of the filling stage. In the middle of the cavity, near the injection location, the mold deflection is about 0.05 mm. Although the cavity is not yet filled completely and the pressure at the both ends of the cavity is close to zero, the displacement at both ends is still in the order of 0.025 mm.

The second load state is shown in Fig. 4.9b. There is a quite large deflection of the whole mold plate with a maximum value of 0.15 mm at the right hand side of the cavity. The supporting pillars are too weak and the unsupported part of the mold plate is too large. Recalling the comparison of the experimental and predicted filling patterns (Fig. 4.2), the quicker filling of the right cavity half may have been caused by the large deflection of the mold. The calculated mold deflection also provided an explanation for the burrs, which were observed on the right hand side of the moldings.
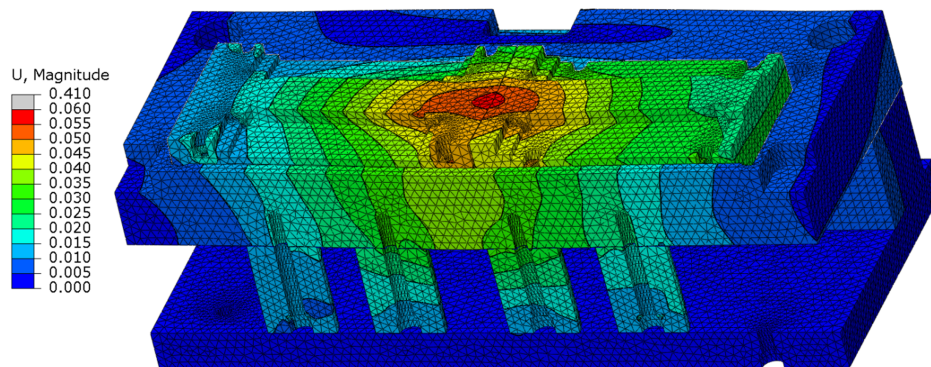
(a) Displacement magnitude at the end of the filling stage in mm.
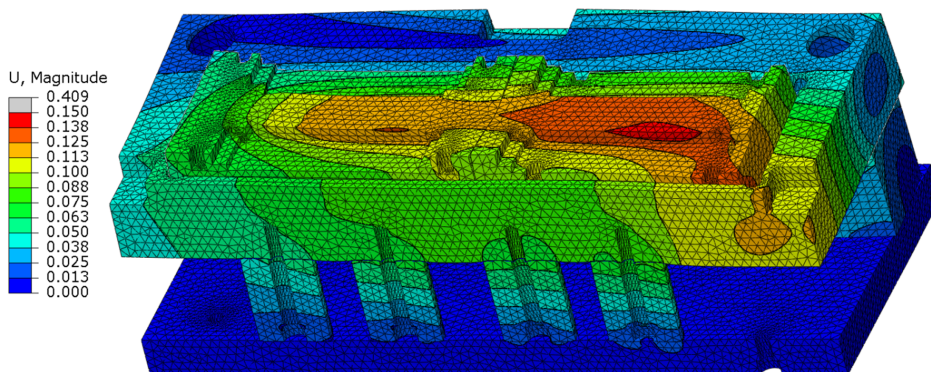
(b) Displacement magnitude at peak pressure during packing stage in mm.

Figure 4.9.: Predicted mold deflection under the melt pressure load. [125]

4.4.3. Results of the structural FEM analysis with a stiffened mold

Additional supporting pillars were placed below the far ends of the cavity in order to improve the stiffness of the mold. Again, a structural finite element analysis was performed to calculate the mold deformation. The same boundary conditions and loads as defined in Sections 4.4.1 and 4.4.1 were applied to the FEM model. Fig.

4.10a shows the displacement plot of the moving mold half at the first load step, representing the filling stage. While the deformation hardly changes at the center of the cavity, a huge improvement was observed at the far ends of the cavity. The second load step representing the packing stage is shown in Fig. 4.10b. Obviously, the additional supporting pillars cause a significant reduction of the plate deflection at the far ends of the cavity. The maximum displacement was reduced by approximately 50%. However, in the center of the cavity, the mold assembly is still too weak and further improvements would be advisable.
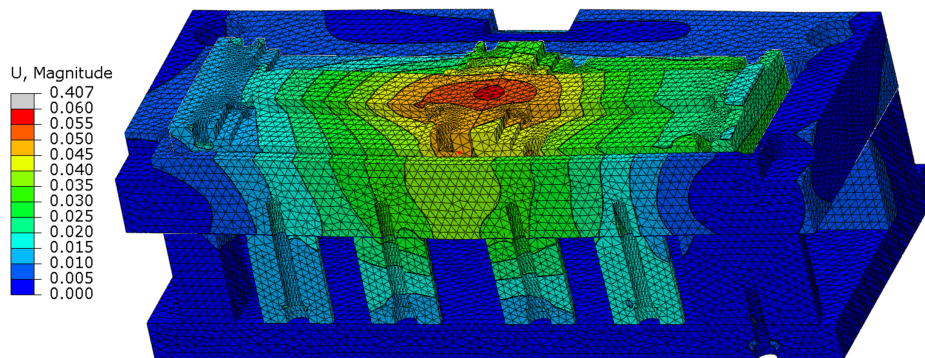
(a) Nodal displacement magnitude at the end of the filling stage with improved mold stiffness in mm.
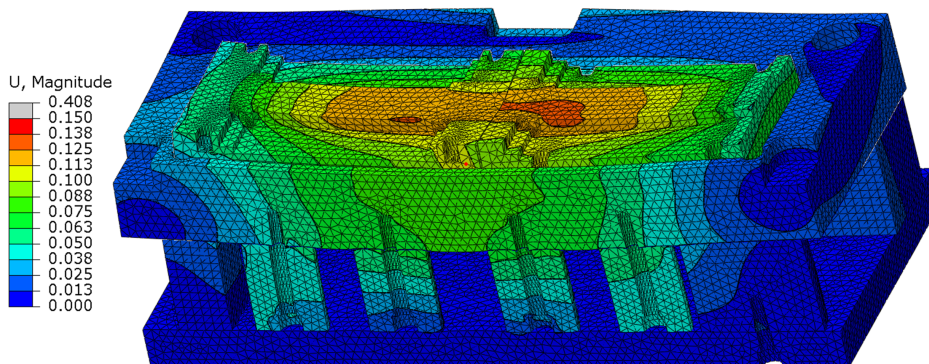
(b) Nodal displacement magnitude at peak pressure during the packing stage with improved mold stiffness in mm.

Figure 4.10.: Predicted mold deflection under the melt pressure load with additional supporting pillars.[125]

4.5. Experimental results with a stiffened mold

After the mold was modified with the additional supporting pillars, new experimental short shots were produced. Fig. 4.11 shows the comparison between four different short shots obtained with both the old and the new mold designs to visualize the advancement of the melt front. In both cases, the parts of cavity one and two are shown. It should be noted that no other modifications of the mold were made, neither to the cavity geometry nor to the runner system. The material grade, molding machine and process settings used for the experiments were identical in both cases. The filling pattern was much more balanced with the stiffer mold and the flashing problem on the right side of the plate was resolved.

(a) Short shots obtained with the original mold design.

(b) Short shots obtained with the modified, stiffer mold design.

Figure 4.11.: Comparison of short shots made before and after stiffening of the mold. [125]

4.6. Experiment vs simulation: stiffened mold

The predicted filling pattern is now in fairly good accordance with the experimental short shots obtained with the stiffer mold (Fig. 4.12a and 4.12b). The right half of the cavity is still filling somewhat quicker. This could be explained by the sum of all the influencing factors mentioned. Despite this, the simulation results and the experiment are now in good quantitative agreement.
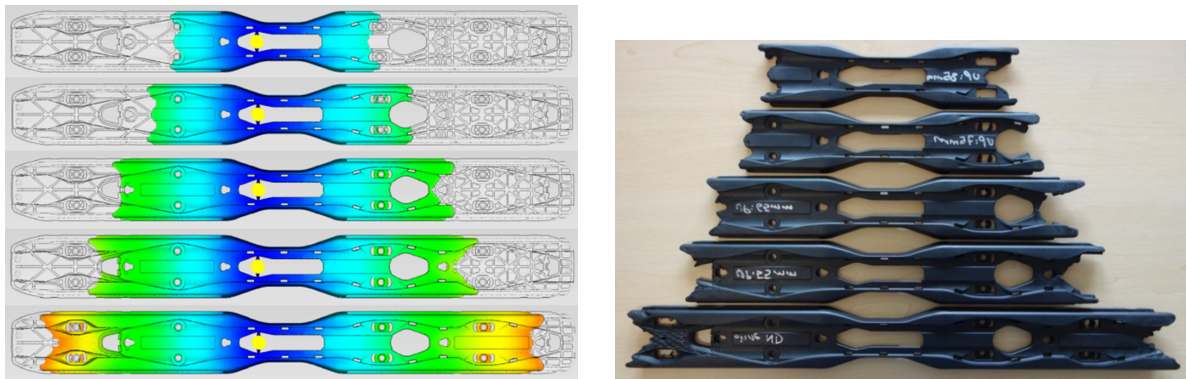
(a) Predicted filling pattern assuming a rigid mold. (b) Experimental short shots obtained with the stiffer mold design.

Figure 4.12.: Comparison of the predicted flow front and the experimental short shots produced with the stiffer mold.[125]

4.7. Concluding remarks

This case study demonstrated that the assumptions of a rigid mold and a constant and uniform cavity wall temperature are basically suitable for the simulation of the filling stage. Thermal boundary conditions, process settings, and even venting conditions have little effect on the predicted filling pattern as long as the appropriate settings are defined.

However, it also revealed that improper mold design may lead to poor accordance between simulation and experiment. The elastic deformation of the mold does not only affect the pressure history and the final dimensions of the part. A significant change of the filling pattern could also occur in cases where long, flat and thin-walled parts are considered. Hence, the prediction of issues which are related to mold filling (for instance, the position of air traps or weld lines) is affected and may lead to false conclusions. Compact and chunky parts, on the other hand, require less injection pressure, have a smaller projected area, and fit into a more compact and therefore inherently stiffer mold base. Hence, the assumption of a rigid mold is generally more suitable for this class of plastic parts. A simple structural FEM analysis is sufficient to detect an unacceptably large deformation of the mold.

5. Voids and their impact on warpage predictions

The case studies presented in Chapter 3 showed that accurate warpage predictions are indeed possible, even on such complex and chunky parts. In one case study, however, the simulation failed to predict the warped shape even qualitatively. This issue indicated that there are influencing factors that are not taken into account by the proposed modeling approach. A thorough investigation was performed in order to figure out the cause of the warpage as well as why it was not predicted by the simulation model. Several experiments led to the assumption that the poor warpage results were caused by a weakness of the fiber models or the presence of voids in the molded parts. Voids are not predicted, and therefore not considered by the simulation model. The fiber models used were indeed extensively tested and validated by different authors. Nonetheless, this does not apply to chunky parts where a 3D flow regime exists in most regions. The ability to accurately predict the fiber orientation in such a geometry has not yet been shown. Additional molding trials, including modifications of the cold runner, were performed. Measurements by means of computed tomography (μCT) were also performed on molded parts. This was done in order to quantify the void volume in the moldings and to gain experimental fiber orientation tensor data. It was found that the amount of warpage correlates with the void volume in the thick sections of the part. This case study is covered in detail in the following section. Furthermore, the experimental fiber data was used to validate the simulated fiber orientation. The results are presented in Chapter 6.

Further research work was conducted based on these findings. A simple U-shaped test part was designed to gain further insight into the impact of voids on warpage predictions. The U-shaped part has thick walls in the corner where voids form. The parts were produced in an instrumented mold featuring several temperature and two pressure sensors. Moreover, the mold was equipped with conformal cooling channels. The measurements were used to calibrate the numerical model by adjusting the process settings and boundary conditions. Molding trials and simulations were performed by using three different materials and a number of different process settings. Good accordance between the predicted and measured warpage was achieved with POM when the void volume was low. Moldings with a high void volume also

showed a substantially higher amount of warpage not predicted by the model. In the case of PA6+GF, it was found that the presence of voids hardly affects the amount of warpage. Warpage and shrinkage predictions were only sensitive to the fiber models used. The whole case study is presented in detail in Section 5.2.

5.1. Case study: Warpage of a complex, chunky part[1]

A lot of research has been conducted in the field of injection molding simulation. Most of the work has focused on parts with simple geometry such as flat plates, center gated disks, and classic thin-shell parts. 3D effects in flow and fiber orientation, as well as part defects such as voids, are negligible in thin walled products. This is not necessarily true for chunky parts like the one presented here.

5.1.1. Problem description

Fig. 5.1 shows the investigated part with the cold runner. Its dimensions are approximately $95 \times 60 \times 54\,\text{mm}^3$ and it was molded from EMS Grilon BGZ-35 FC a PA6 grade with a short glass fiber content of 35 % by weight. The wall thickness varies in the range of 1.5 - 12 mm. It was molded in a two cavity hot runner mold with a short cold runner between the drop and the cashew gate.
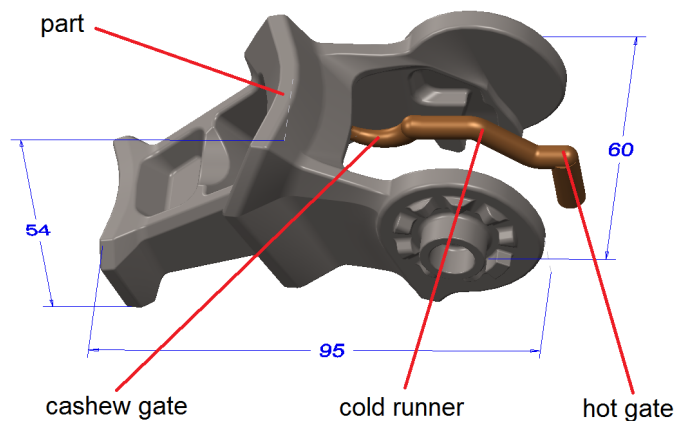
Figure 5.1.: Geometry of the investigated part made of PA6 GF35, including cold runner with cashew gate. [126]

---

[1]Parts of this section were published in International Polymer Processing under the title "Measurement and Numerical Simulation of Void and Warpage in Glass Fiber Reinforced Molded Chunky Parts" [126]

Fig. 5.2 shows a comparison between the nominal (CAD) geometry of the part, drawn in red and the molded and measured part, drawn in black, at the sectional planes indicated. The two arms turned inside by up to 2 mm. The dimensions of the molded part were out of the prescribed tolerances.
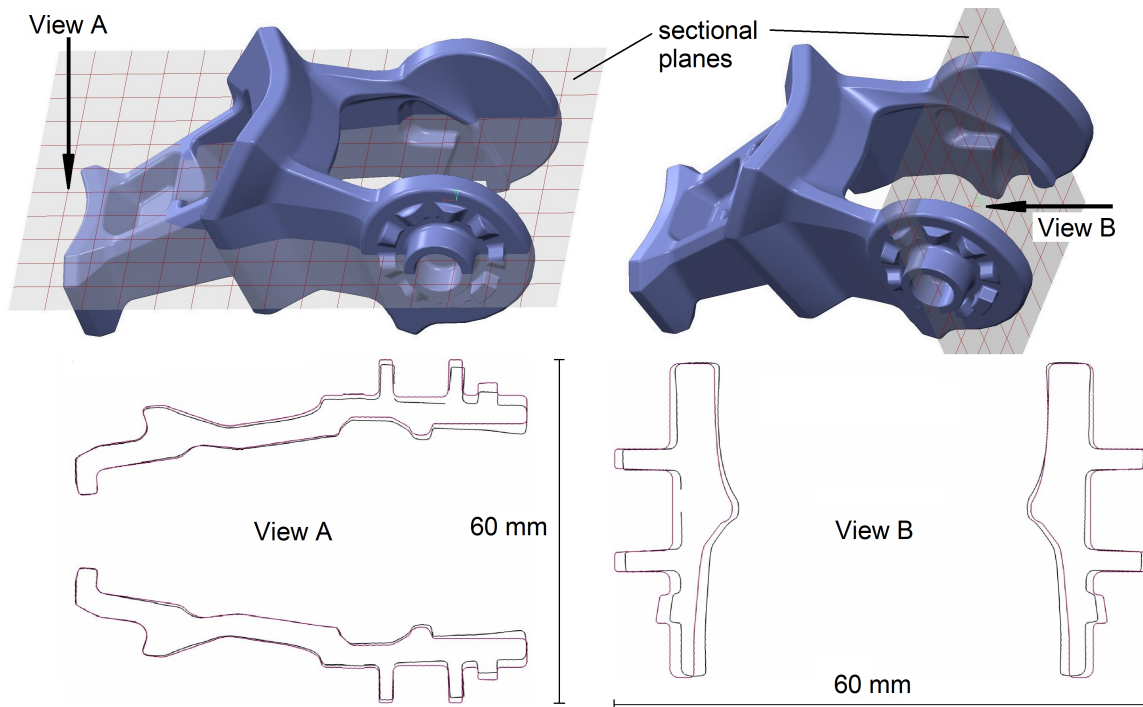
Figure 5.2.: Comparison of nominal geometry (red) and measured part geometry (black) at two different sectional planes. [126]

Several molding trials and a numerical analysis of the molding process were performed. The warpage of the molded parts was strongly dependent on the pressure history during the packing stage. On the one hand, this is not unusual, and, in fact, commonly observed when unfilled materials with high shrinkage are processed. On the other hand, this was the only case investigated by the author where this behavior was observed in a part molded from a short glass fiber reinforced polymer grade (with a significantly high fiber content). In all other cases presented in this thesis (as well as many others not published), warpage was essentially dominated by orientation effects, and the packing pressure profile had little effect on warpage. This seemed to be a characteristic of the chunky parts considered in this thesis.

In contrast to these findings, Leo [127] states that the packing profile and efficiency (pressure and time) normally has a significant effect on warpage and is thus the most effective way to reduce warpage. The argument is the following: The presence of oriented fibers causes anisotropic shrinkage. While the polymer matrix would normally shrink uniformly in all spacial directions,in this case, it is constrained by

the fibers. When the fibers are highly oriented in one direction, as is the case in the shear layers close to the mold walls, shrinkage of the matrix is restricted parallel to the fibers, and hardly hindered in the perpendicular direction. Hence, the difference between the shrinkage in parallel and perpendicular direction to the oriented fibers (the anisotropy) is high. Higher packing pressure and longer packing time causes a lower volumetric shrinkage of the polymer matrix. Lower volumetric shrinkage also means less impact of the fiber constraints, less anisotropy, and finally, less warpage of the part. [127]

At the first glance, this would be a convenient explanation for the pressure dependency in this case. What makes the present case so special is the following fact: The simulation model does not show any warpage although the effect of anisotropic shrinkage is actually considered. As in all other cases, one would expect at least a qualitative estimation of the deformation mode. The main goal of this case study was to find the reason for the poor warpage prediction results, and, as a consequence, to highlight the influence of material defects on the warpage prediction accuracy.

5.1.2. Experiments

Initial Case

The mold was equipped with two 8 mm heat pipes in the core side insert, which were used to locally cool the mold insert between the two arms of the part. These heat pipes were connected to a separate cooling circuit, so the water temperature was set independently from the mold circuit. The process parameters initially used are shown in Table 5.1 and the injection profile is shown in Fig. 5.3.

Melt temperature	293°C
Injection time	1.1 s
Packing pressure	30 MPa
Packing time	20 s
Cooling time	30 s
Cycle time	65.4 s
Temperature of the cooling water	80°C

Table 5.1.: Process settings initially used. [126]

Variants

In order to investigate the influence of the process parameters on part warpage, several experiments were performed.
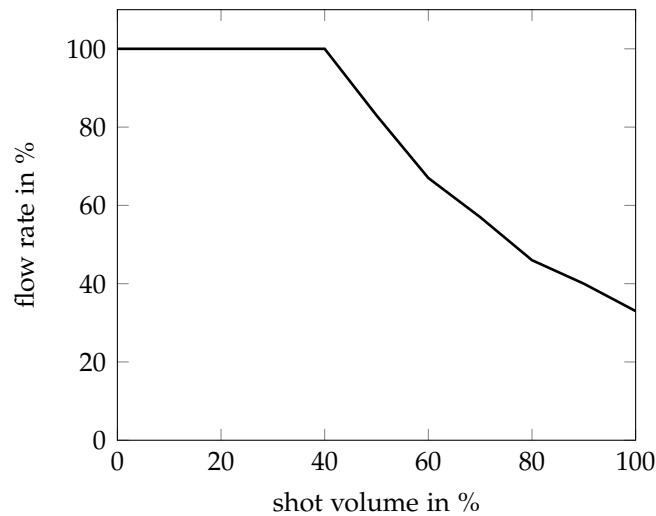
Figure 5.3.: Initial injection profile used for the molding experiments associated with an injection time of 1.1 s. [126]

Mold temperature: Different temperatures of mold and heat pipes in the core side insert were tested. Little influence on warpage was observed. It is therefore not reasonable to discuss the different molding experiments with varying temperatures in detail. However, it must be noted that compensating for warpage with the temperature settings of the coolant was not possible. The melt temperature varied between 280 and 300°C. Its impact on warpage was also negligible.

Injection profile: The numerical simulation revealed very high shear rates in the gate area, due to the small gate diameter and the short injection time. The calculated values exceeded the limits recommended by the manufacturer (6×10^4 s^{-1}) by a factor of 4. Hence, material damage such as excessive fiber breakage may occur. This would result in the reduced anisotropy of the mechanical properties of the material, which are not captured by the numerical simulation. The injection profile was adapted to obtain a more uniform melt front velocity, while the injection time was increased to about 4 s to reduce the high shear rates (Fig. 5.4).

Packing pressure profile: To reduce the void volume in the moldings, the pressure profile was changed from a constant value of 30 MPa to a ramp from 22.3 MPa at the p/v switch-over up to 81 MPa after 6 s. The pressure was then held for another 14 seconds. The sealing point was determined by following the procedure described in Section 3.2. In all cases, the gate was sealed within the packing time. Pressure profile and melt temperature were chosen to obtain the highest possible packing pressure without flashing.

Runner and Gate diameter: In addition to the new process settings, runner and gate diameter were increased in order to prolong the gate seal time. The gate diameter
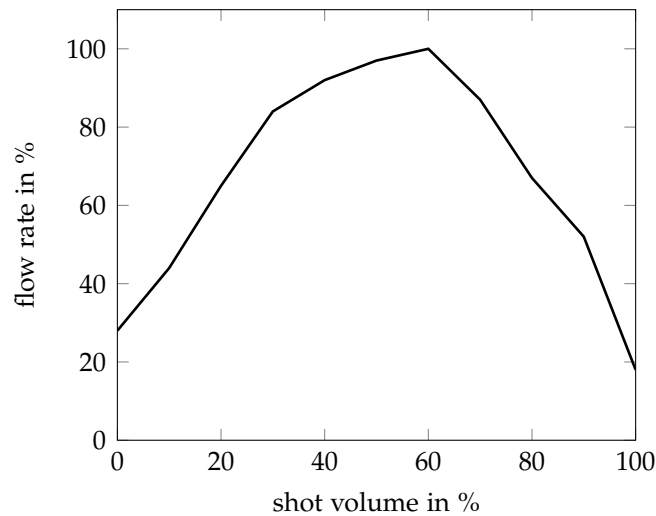
Figure 5.4.: New injection profile associated with an injection time of 3.9 s.[126]

was changed from 1.2 mm to 1.8 mm and the diameter of the cold runner from 5 mm to 7 mm. The aim of these changes was to achieve a reduction of volumetric shrinkage and void volume in the molding.

5.1.3. Numerical model

The numerical model comprised one cavity, the cold runner, the hot runner nozzle, and the cooling channels adjacent to the cavity. All polymer domains were represented by a volume mesh. A detailed model of the hot runner nozzle was used to consider the heat flux from the nozzle into the mold (see 3.6.1 for details). Cooling channels were modeled using beam elements. The heat transfer in the heat pipe is governed by the continuous evaporation of a fluid on the hot side of the pipe, and its condensation on the cold side. Modeling this complex process within the context of injection molding simulation is not feasible. A major simplification was therefore needed to consider the heat pipes in the mold cooling analysis. One characteristic of a heat pipe is the very small temperature gradient along the pipe [128]. In the present case, one end of the heat pipe is connected to a separate cooling channel. The turbulent flow around the pipe ensures a very good heat transfer. This implies a very small temperature difference between pipe surface and coolant. One simplified modeling approach is therefore to assume a constant temperature of the heat pipe which is somewhat higher than the coolant temperature. Additionally, an HTC value was defined at the interface of heat pipe and mold insert, in order to address the imperfect contact. This approach was used in the present study.

hot runner nozzle
cooling channels
cold runner
part
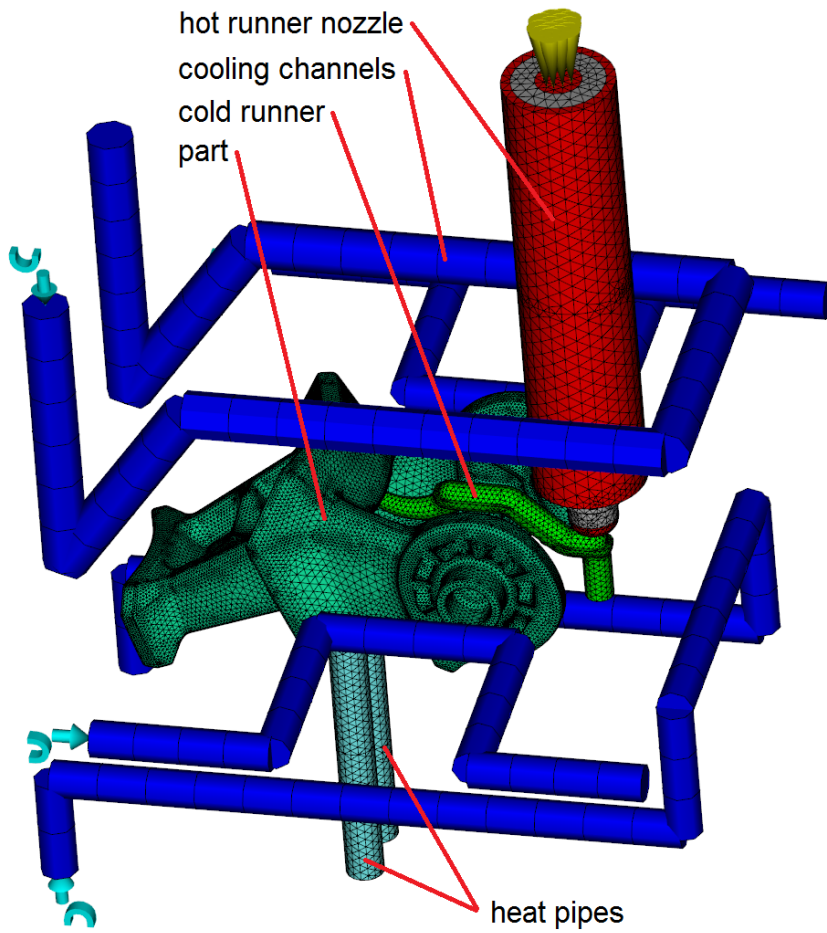
heat pipes

Figure 5.5.: Numerical model of the investigated part featuring one cavity, cold runner, hot runner nozzle, heat pipes and cooling channels.

Material data

Material data for EMS Grilon BG-35 was used for the numerical part of this study. It was taken from the Moldflow material database and is also given in A.4. The material data has a gold quality indicator for all analysis steps.

Process settings and boundary conditions

The initial filling simulation was carried out with a melt temperature of 293°C, and a target injection time of 1.1 s. The injection flow rate for the simulation was defined as analogous to the molding machine settings used for the experiments (see Section 5.1.2). The mold was not equipped with pressure transducers. Therefore, the packing pressure applied to the melt inlet boundary at the hot runner drop was estimated based on the hydraulic pressure defined at the molding machine. Hence, the packing pressure for the simulation was set to 20 MPa for the initial case. However, several simulations with different values for the packing pressure made little impact on the predicted part deflection.

Cooling analysis	
Melt temperature	295°C
Injection + packing + cooling time	51.5 s
Mold-open time	13.9 s
Coolant	Water
Coolant temperature cavity side	80°C
Coolant volume flow rate cavity side	3 l/min
Fill + pack analysis	
Injection time	1.1 s
Velocity/pressure switch-over	at 99% of the volume filled
Packing pressure	20 MPa
Packing time	20 s

Table 5.2.: Applied process settings and boundary conditions. [126]

Solver settings

The analysis sequence used was: Cool (FEM) + Fill + Pack + Warp. A number of simulations with different solver settings were performed. As it turned out, their influence on warpage was always negligible. Therefore, all the solver settings presented in Section 3.3.4 were retained for the initial simulation. The fiber orientation was predicted by the reduced strain closure model (RSC-model) with orthotropic 3

closure approximation. A thorough investigation into the quality of the predicted fiber orientation is covered in Chapter 6.

Computational Mesh

Fig. 5.6a shows parts of the meshed model with the larger runner and gate. All mold inserts and side cores were meshed separately, while a conformal mesh was maintained on all contact faces. In this way, it is possible to model imperfect contact between all mold components, which affects the heat flux across the interfaces, and consequently, the temperature distribution in the mold. Meshing several mold components implies a tremendous amount of modeling effort. This was essentially done to simulate the mold temperature distribution and its impact on warpage as well as possible. Fig. 5.6b shows a cut through the mesh of part and cold runner. The polymer domains (part, cold runner, hot runner) were meshed with at least 12 element layers across the wall thickness. Mesh properties and element metrics for this case are summarized in Table 5.3. The meshed model with the initial, smaller gate and runner diameter basically has the same mesh properties. It is therefore not presented in detail.

(a) Surface mesh of part, cold runner, hot runner nozzle and mold components of the moving mold half.

(b) Cut through the 3D part mesh at the symmetry plane showing at least 12 element layers across the wall thickness.
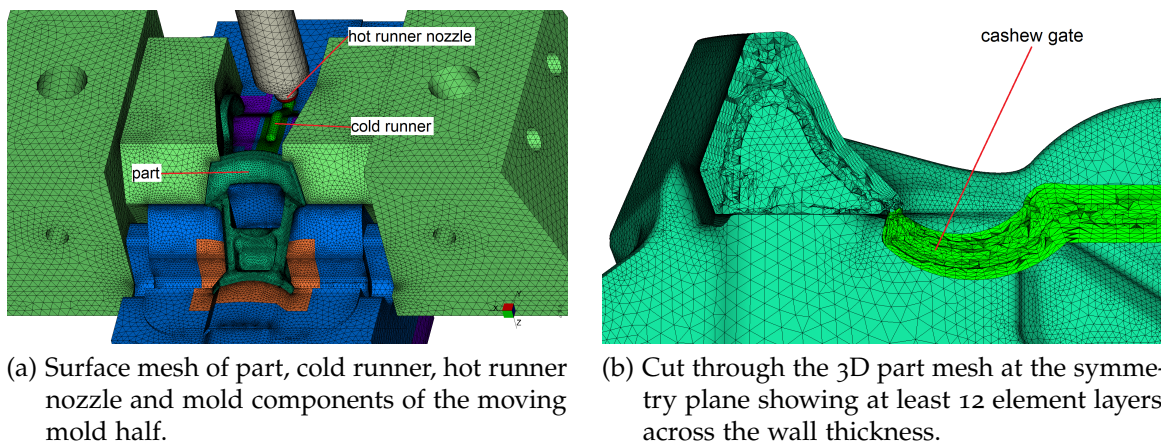
Figure 5.6.: Meshed model of the moving mold half. [126]

	part	cold runner 3D	hot runner	mold
Element count	1436217	56296	166193	2977040
Nodes	253600	10095	29163	585752
Elements across wall thickness	12	12	12	6
max. aspect ratio	28.02	24.46	54.01	67.5
average aspect ratio	4.06	3.76	5.70	1.66
min. aspect ratio	1.03	1.09	1.08	1.00
max. dihedral angle	173.4	172.9	175.6	176

Table 5.3.: Mesh properties and diagnostics.

5.1.4. Results and discussion

Experimental Results

To summarize the findings of the various experiments, four different cases were defined[2] and the results presented:

- **Case A:** Initial geometry and process conditions
- **Case B:** Initial geometry with modified injection velocity profile (Fig. 5.4)
- **Case C:** Initial geometry with modified injection velocity and packing pressure profile
- **Case D:** Larger runner and gate diameter with modified injection velocity and packing profile

The three dimensions, L1-L3 shown in Fig. 5.7, were measured on the molded parts in order to quantify the impact the actions undertaken had on warpage. Table 5.4 shows the nominal and measured values for each of the four cases, with the delta values in brackets. All values were averaged over at least 10 shots and both cavities.
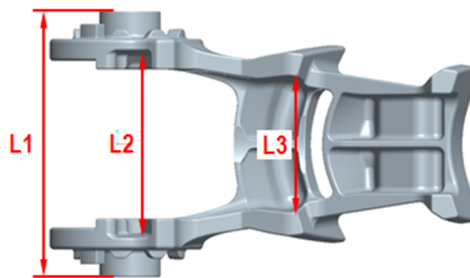
Figure 5.7.: Dimensions used for the evaluation of the part warpage. [126]

---

[2]see Section 5.1.2 for details

	Nominal Dimension	Case A	Case B	Case C	Case D
L1 [mm]	60	58.71 (-1.29)	58.92 (-1.08)	59.54 (-0.46)	59.7 (-0.3)
L2 [mm]	42.2	40.54 (-1.66)	40.80 (-1.4)	41.29 (-0.91)	41.27 (-0.93)
L3 [mm]	30.74	29.85 (-0.89)	29.85 (-0.89)	30.14 (-0.6)	30.15 (-0.59)

Table 5.4.: Measured dimensions for Cases A-D. [126]

The very high shear rates observed with the initial process conditions may have caused excessive fiber breakage. With the modified injection profile and the extended injection time used in Case B, the shear rates were within recommended limits. This measure led to little improvement on warpage. The new packing pressure profile used in Case C, on the other hand, caused a major decrease in the warpage of the part. Increasing the gate and runner diameter in conjunction with the new process settings led to a further, but less pronounced reduction (Case D). The molding trials showed that warpage is primarily affected by the packing pressure and efficiency, respectively.

μCT Results

The molded parts were scanned by means of μCT to characterize defects. The CT images are grey scale images, wherein each shade of grey represents a specific density of the scanned object. Bright areas correspond to a material of high density, such as glass or the polymer matrix, while dark areas correspond to a substance with low density, such as gas. Areas with very high volumetric shrinkage either show few large voids, or many small, highly dispersed voids. The latter is referred to as a "porous zone" within this thesis. Voids are visible as black spots in the thick sections of the part. Fig. 5.8 shows μCT slices of parts from the initial Case A and the final Case D. The location and orientation of the slices are depicted on the left side. The μCT images show the regions with the largest voids or porous zones. The improved packing efficiency obtained in Case D led to a major reduction of the void volume and the size of the porous zones. Compared to Case A, the large voids can be seen to have vanished completely.

The pore volume and porosity of Cases A, C and D are summarized in Table 5.5. It should be noted that the accuracy of the calculation of the pore volume is limited by the voxel edge length of the μCT data. While the part molded with the initial settings from Case A has rather large voids, the parts from Cases C and D have a fine distribution of very small voids with a size in the same order of magnitude as the voxel size. Hence, there is a visible difference in porosity between Case C and Case D, although the calculation of the pore volume results in the same value.
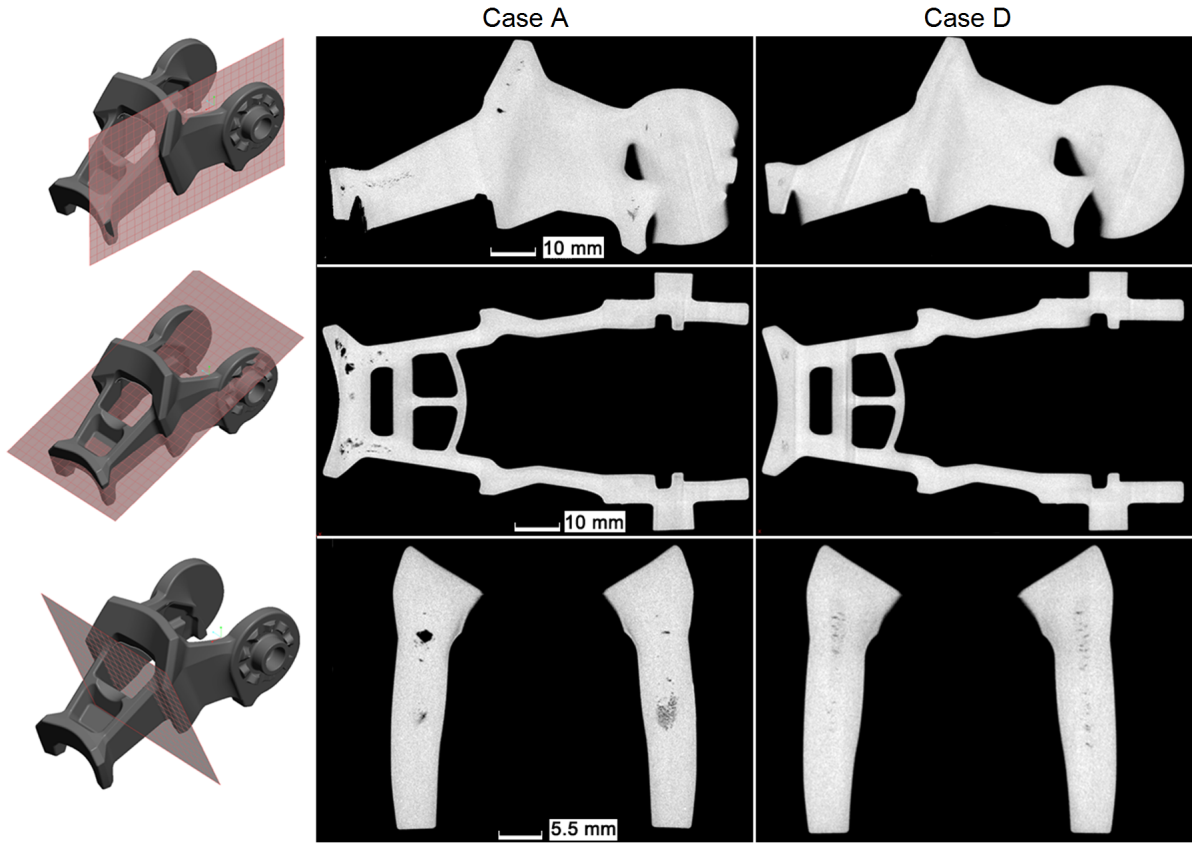
Figure 5.8.: Comparison of voids at three different sectional planes for a part from Case A (center) and Case D (right).[126]

		Case A	Case C	Case D
Pore volume	[mm^3]	97.3	35.9	35.9
Total volume	[mm^3]	32932.2	32932.2	32932.2
Porosity	[%]	0.3	0.11	0.11

Table 5.5.: Calculated porosity based on the μCT measurements. [126]

Simulation Results

Fig. 5.9 shows the predicted deflection magnitude for the initial case, exaggerated by a factor of 5. Qualitatively, the result shows shrinkage in all directions, but no distinct warpage of the part. Several variants of the numerical model presented were tested to investigate the influence of thermal boundary conditions, processing conditions, mesh, material data, fiber orientation model, and solver settings on the predicted part shape. It was found that the warpage prediction is only sensitive to the cooling conditions in the mold. The warpage result of Case A was almost identical to that of Case D.
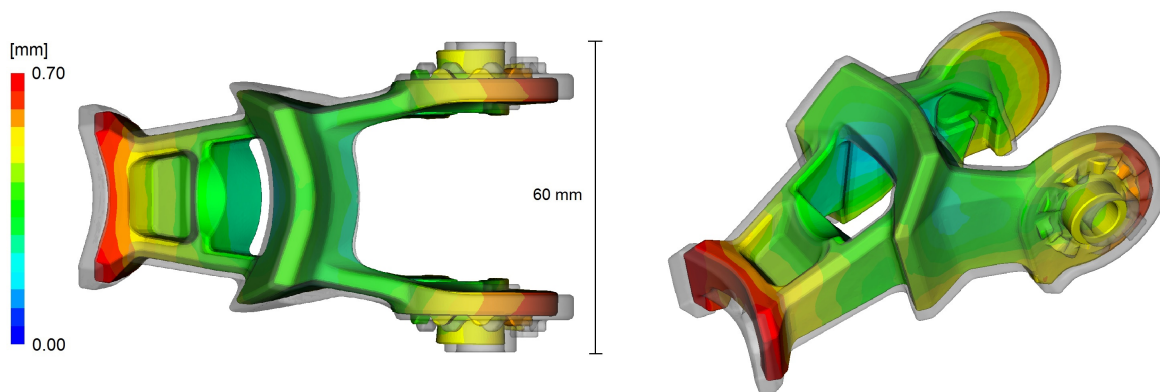
Figure 5.9.: Predicted deflection magnitude in mm for Case A. The plot shows the deformed part exaggerated by factor 5, overlayed with the undeformed part shape (transparent).[126]

Fig. 5.10 shows the 3D comparison of measured and predicted geometry for Cases A and D. The deviation magnitude of the simulation part to the molded and measured part is color coded. The color bars have a different scaling for better visibility. In both cases, however, the deviation in the green areas is less than 0.1 mm. In Case A, a maximum deviation of more than 1.7 mm was found at the very tip of both arms. Hence, the simulation result does not show the large warpage observed in the experiment. In Case D, the maximum deviation is about 0.5 mm, and once again found at the tip of both arms. In most areas of the part, the deviation is below 0.1 mm. Shrinkage was predicted very well, but the warpage of the two arms was not predicted. See Table 5.4 and Fig. 5.7 to get an idea of the actual part dimensions.

In the numerical model, part warpage is not sensitive to processing conditions or the chosen fiber model. Hence, varying the packing pressure profile only affects volumetric shrinkage, but hardly has any effect on the predicted shape. This is in clear contrast to the experimental results, where a major dependence of the part warpage on the packing pressure history was determined. The variation of

(a) Case A   (b) Case D
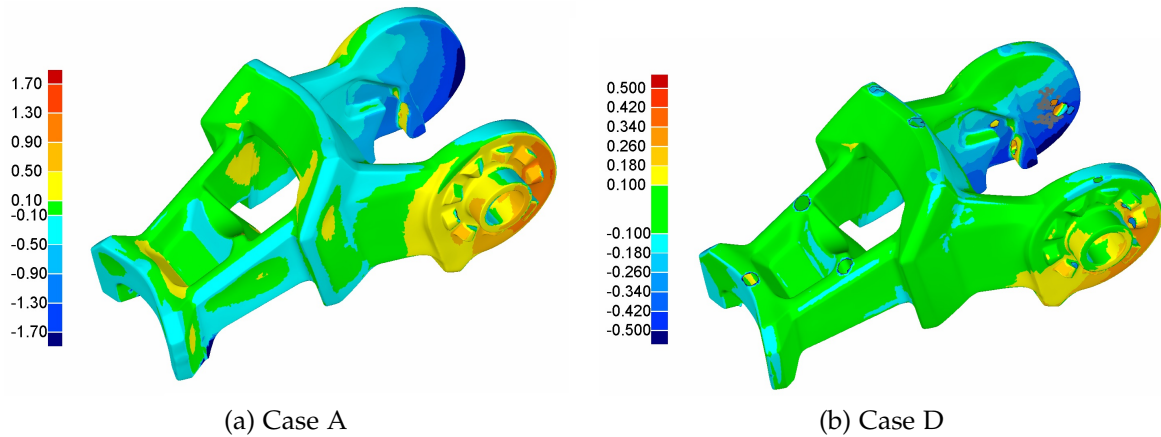
Figure 5.10.: 3D comparison of molded part and predicted part geometry. The deviation values are given in mm. [126]

temperature settings for the different cooling circuits had only a minor effect on the experimentally observed warpage.

Additional experiments and simulations were carried out using UBE Nylon 1015gc9 a PA6 GF 45 grade with material properties measured in the Moldflow Plastic Labs (see A.5 for details). The results were similar to those obtained with the original material: Excessive warpage of the molded parts and almost no warpage in the simulation.

Prediction of porous zones

It is assumed that voids may only appear when the melt freezes without pressure and when the frozen layer is stiff enough to keep its shape. In this case, neither the compressibility of the melt nor the flexibility of the already frozen part surface allows for the compensation of the "missing" material in the core of the part, due to volumetric shrinkage. If the frozen layer is not stiff enough, the shrinking material in the core of the part will cause sink marks on the part's surface. The longer a sufficient cavity pressure is maintained, the more material will freeze without the formation of porosity or voids. Therefore, the influence of the process settings on the pressure history in the cavity was investigated with the simulation model. The predicted pressure curves for Cases A, C and D are shown in Fig. 5.11a. Fig. 5.11b shows the location of the pressure sensor node. The changes made in Case B had only little influence on warpage, and are therefore not included in the following considerations.

Although the gate seal time is hardly affected, the higher packing pressure applied in Case C causes a higher pressure level and a prolonged time span of non-zero pressure.

112

(a) Predicted cavity pressure history for Cases A, C and D in MPa.

(b) Location of the sensor node.
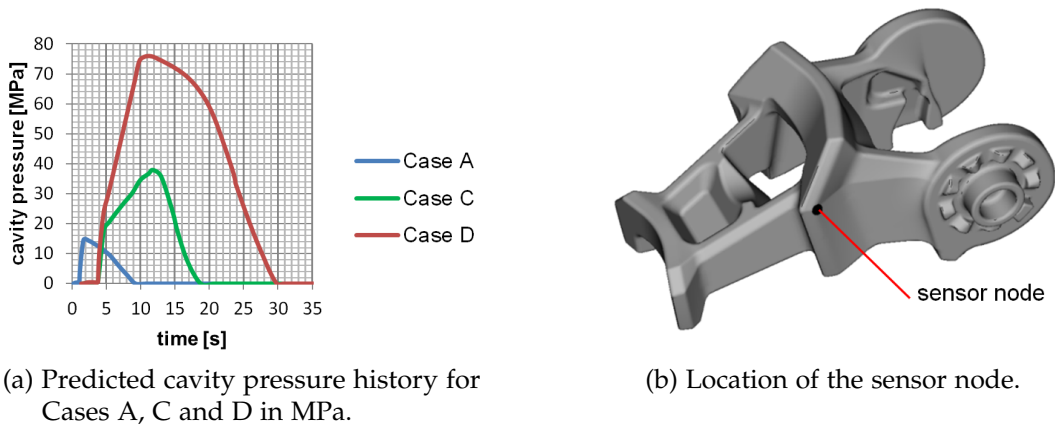
Figure 5.11.: Predicted pressure history at the specified location. [126]

Due to the larger runner and gate diameter in Case D, the gate seal time was extended and the pressure drop of the cold runner reduced. Therefore, the pressure level and duration were further increased. Fig. 5.12 shows the melt volume for the three cases at the time step when the cavity pressure had just dropped to ambient pressure. This is the volume where the formation of voids or porous zones can occur. However, with this plot, it is not possible to conclude that voids will actually appear.

(a) Case A: 42 % of the volume frozen.

(b) Case C: 70.63 % of the volume frozen.

(c) Case D: 87.77 % of the volume frozen.
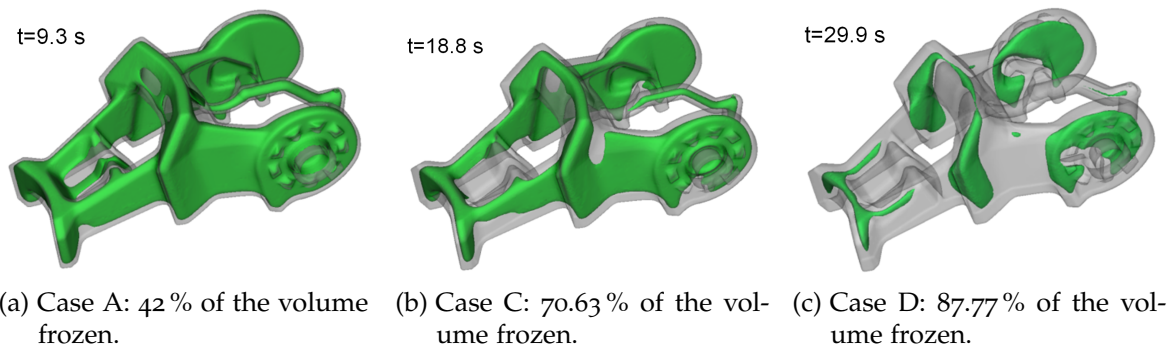
Figure 5.12.: Melt volume at the moment when the cavity pressure has just dropped to ambient pressure. [126]

Thus, a further assumption can be made: The material is not able to resist more volumetric shrinkage than a critical value without forming defects. Fig. 5.13 shows an isosurface of 11 % volumetric shrinkage for the same three cases. Of course, a higher packing pressure and the longer duration of the cavity pressure also cause lower volumetric shrinkage. All the voids and porous zones found in the molded parts lie within the volume described by the isosurface shown in Fig. 5.13. However, the value of 11 % is arbitrarily defined and not completely physically meaningful. Fig.

113

5.14 shows 3D renderings of the semitransparent specimen with pores obtained from the μCT measurements.The pores were color coded according to their volume. The resolution applied could lead to the aggregation of many nested small pores into one bigger pore. Especially for Cases C and D, where more nested pores were found, the color coding shows large volumetric pores. Fig. 5.14 can be used for the comparison of prediction and reality in terms of the location of pores. A quantitative comparison of void volumes is given in Table 5.5.

(a) Case A   (b) Case C   (c) Case D
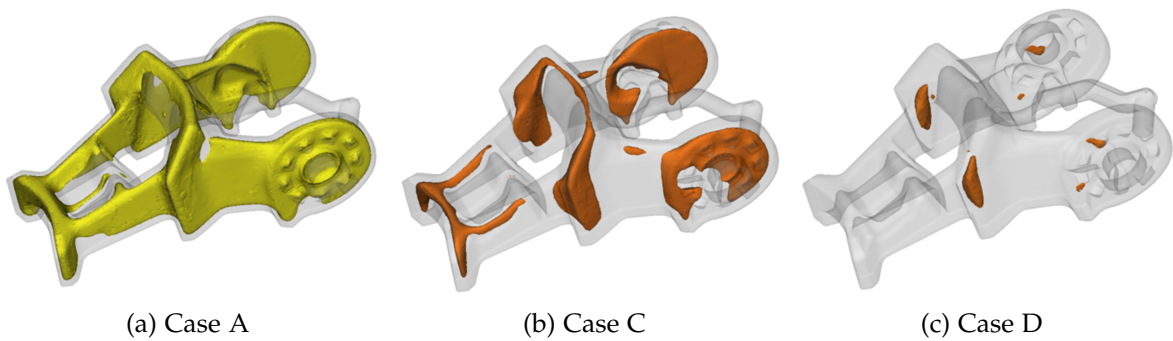
Figure 5.13.: Isosurface of 11 % volumetric shrinkage. [126]
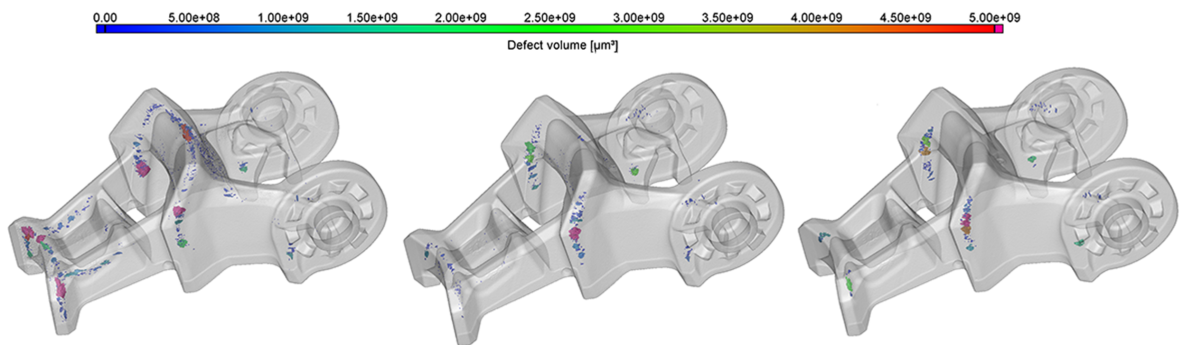
Figure 5.14.: 3D renderings of semitransparent specimens with pores. The volume is color coded. (a) Case A. (b) Case C. (c) Case D. [126]

While the predicted volumes shown in Fig. 5.13 are too large in Cases A and C, Case D presents an excellent match of predicted and measured porous zones. Due to the complex physics involved in the formation of both voids and porous zones, including phase change, crystallization, material damage, and fiber orientation, a more accurate prediction does not yet seem feasible. The very simple approach presented here does not require any additional modeling effort, and yields at least a qualitative estimation of the locations where voids may form.

Discussion

As supposed from the experimental findings, there is a correlation between void volume and warpage of the molded parts. A great reduction in warpage was achieved by introducing a new injection and packing profile. From the results shown in Fig. 5.14, it is clear that a significant reduction in void volume was also attained. The change in part warpage between Cases C and D is rather small, as is the reduction in void volume.

Considering the experiments, it is assumed that the formation of voids or porous zones must have a major impact on the warpage results obtained experimentally. Since voids are not predicted or considered by the numerical simulation, the local stiffness of the simulated part is not modeled correctly. Depending on where the voids appear, even a symmetrical distribution of the residual stresses across the wall thickness may cause a bending moment that is not captured by the numerical simulation. Due to the present mold and part design, it is not possible to eliminate all voids.

There are several other limitations in the numerical model, which could contribute to the deviations in the warpage predictions. The most critical of these are ranked as follows:

1. **Orientation effects:** Molecular orientation as well as fiber orientation affect the local stiffness properties of the molding, and therefore influence the final shape of the product. Due to the high relaxation rates and the relatively low cooling rates in the thick walls of the part, it can be assumed that the effect of molecular orientation on the stiffness and shrinkage properties of the material is negligible compared to the dominating effect of fiber orientation. Simulations with different fiber models and model constants did not improve the warpage prediction. A comparison of measured and predicted fiber orientations is presented and discussed in Chapter 6. The limited accuracy of the predicted fiber orientation in the thick walls is certainly a potential source of error. However, several other case studies also featured chunky parts with thick walls, and the prediction of warpage succeeded with reasonable precision.

2. **Crystallization and the pvT relationship:** Crystallization is a highly complex process, which is dependent on several factors, such as the thermo-mechanical history experienced by the material during processing. It affects the solidification and shrinkage of the material, and therefore, also the quality of the warpage prediction. Modeling crystallization is still an ongoing and challenging field of research. In the case of semi-crystalline resins, the pvT relationship given by the 2-domain Tait equation lacks precision. The pvT measurements cannot reflect the locally varying thermo-mechanical conditions experienced by the polymer in the cavity of the injection mold. Investigations into the influence of pvT properties

115

on warpage prediction have been carried out by, for instance, [129]. [104] and [130] examined the effect of the transition temperature on the warpage results. In all these studies, however, the pvT data used only affected the magnitude of the predicted warpage, not the deformation mode. In the present case, the simulation does not even predict the deformation mode correctly (Fig. 5.8), despite the fact that 2 different materials with reliable material data were used. From the experiments, it is known that the warpage of the actual part is only marginally affected by variations in mold- and melt temperature (cooling rates) and injection speed (shear rate). Hence, it seems unlikely that crystallization and its influence on the pvT relationship is the dominant cause of the large deviation between the measured and predicted warpage.

3. **Viscoelasticity:** Moldflow uses a thermoelastic model to predict the warpage of the part. Stress relaxation in the solid state is therefore not modeled. This should only be a minor drawback since stress relaxation would probably lead to a reduction in warpage, and therefore make little difference in the present case.

4. **Elasticity of the Mold:** Under pressure, the mold will undergo a certain amount of deformation not included in the numerical model. The elastic rebound forces of the mold will then cause a somewhat different pressure history in the cavity than predicted by the simulation [74, 120]. Consequently, the higher the pressure in the cavity, the greater the error in the numerical model. In the present case, however, the highest packing pressure yielded the best correlation between measured and predicted warpage. Thus, the effect of mold deformation seems unimportant in this case. More on the topic of the elasticity of the mold can be found in Chapter 4.

5.1.5. Concluding remarks

In the present case study, the warpage of a compact and chunky injection molded part has been investigated. The part was molded from a PA6 grade with a glass fiber content of 35 % by weight and showed distinct warpage. Several experiments were carried out in order to investigate the sensitivity of warpage on the process parameters. It was found that packing pressure is the dominant variable. With a modified injection velocity profile, higher packing pressure, and larger runner and gate diameter, the warpage of the molded parts was reduced by up to 77 %. A numerical injection molding simulation using Autodesk Moldflow Insight failed to predict even the deformation mode correctly. In contrast to the experimental findings, the numerical model is not sensitive to varying process conditions. μCT scans of the molded parts were performed and revealed voids and porous zones in the thick walled areas of the part. From experiments on the molding machine and μCT measurements of the molded parts, it is evident that a reduction of the void

volume due to modified process settings also causes a reduction in part warpage. With decreasing void volume, the measured dimensions of the molded parts converged towards the nominal dimensions. Commercial injection molding simulation software is not capable of predicting the formation of voids or of considering their influence on the local stiffness of the part. Hence, it can be concluded that the formation of voids may lead to part warpage which cannot be captured by commercial injection molding software. In this case, numerical warpage predictions are not reliable. A simple way of identifying zones where voids may form has been indicated in this study. The results were compared to the void volume data obtained with µCT measurements and showed very good agreement.

5.2. Case study: A simple test geometry[3]

5.2.1. Introduction

The case study presented in this section is based on the findings of the preceding case, which was outstanding in one regard. It was found that a reduction in the void volume in the heavy walled sections of the part correlated with a reduction in the amount of warpage. A special packing profile was used to reduce the void volume, and this led to a significantly lower warpage magnitude. The simulation model failed to predict warpage even qualitatively, nor did it reflect the impact of the new packing profile. Moreover, it was found that the fiber orientation prediction in thick walls lacks precision. Thus, two potential issues were identified which could impede the accurate warpage prediction of chunky parts.

A simple U-shaped part was specially designed in order to gain more insight into these findings. The part has thick walls in the corners where voids or porous zones may form, and where a 3D flow pattern challenges the capabilities of the fiber models. Put another way, the part has all of the geometric properties that were assumed to cause unreliable warpage results.

This study aimed to investigate the influence of voids on the warpage of a part with simple geometry, under repeatable conditions. For this reason, the mold was equipped with pressure and temperature sensors. The measurements provided experimental results for the validation of the numerical model. Molding trials and simulations were performed using POM and PA6 +GF. The numerical model features a full 3D representation of all mold components, including the conformal cooling system, to

---

[3]Parts of this section were published in International Polymer Processing under the title "Experimental and Numerical Investigation of Shrinkage and Warpage of a U-Shaped Injection Molded Part" [132]

consider all influencing factors that the state-of-the-art injection molding simulation software, Autodesk Moldflow Insight, is currently able to capture [131].

This case study contains a thorough experimental and numerical investigation, as well as decent measurements to support the validity of the simulation model.

5.2.2. Problem description

The part investigated in this study is shown in Fig.5.15. It has a U-shape with a thin-shell structure at both arms, a thicker core connecting both arms, and massive corners. While the arms are quite stiff and will hardly warp, the corners are prone to warpage. Due to the simple shape of the part, it is fairly easy to measure te shrinkage and warpage of the molded parts with little effort. Defects such as voids or porous zones will form in the massive corners. The aim of this study was to find out whether or not these defects contribute to warpage as well as if injection molding simulation software should consider such defects in its warpage predictions. Two classes of thermoplastic materials were used for the experimental part. These were unfilled and short glass fiber reinforced, semicrystalline grades. For each grade, a number of different sets of process conditions were used in order to investigate their impact on the shrinkage and warpage of the moldings, as well as on the defects inside the moldings. Simulations using Moldflow Insight Releases 2015 and 2016 were performed to validate the software's ability to predict the shrinkage and warpage of parts with large variations in wall thickness.
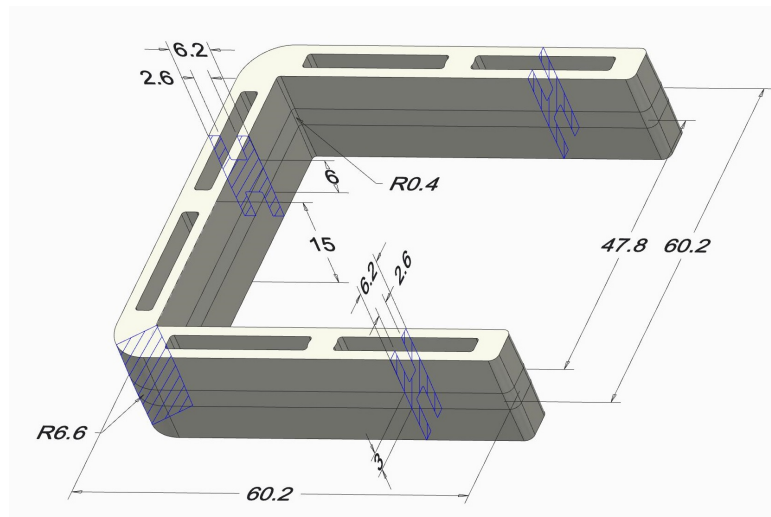
Figure 5.15.: Geometry and dimensions of the investigated part. [132]

5.2.3. Experiments

Mold design

The parts were molded in a two-cavity mold, in which each cavity is gated differently. One cavity has a direct gate into the thick core at the bottom of the U-shape, with a diameter of 4 mm, while the other is gated at the two arms by submarine gates with a diameter of 2.5 mm (Fig. 5.16). The cold runner is fed by a single hot runner nozzle in the center of the mold. A well known contributor to Corner warpage is non-uniform cooling. A much higher specific heat flux is needed on the inner side of the corner to achieve a uniform cooling rate throughout the corner. To minimize the effect of non-uniform cooling on the warpage of the part, the mold was equipped with a conformal cooling system, as shown in Fig. 5.16. All mold components were made from tool steel (1.2083), and inserts of Moldmax HH[4] were placed in the inside of the corners to improve cooling in these areas. The mold inserts were placed on thermal insulation boards and did not directly touch the mold plates.
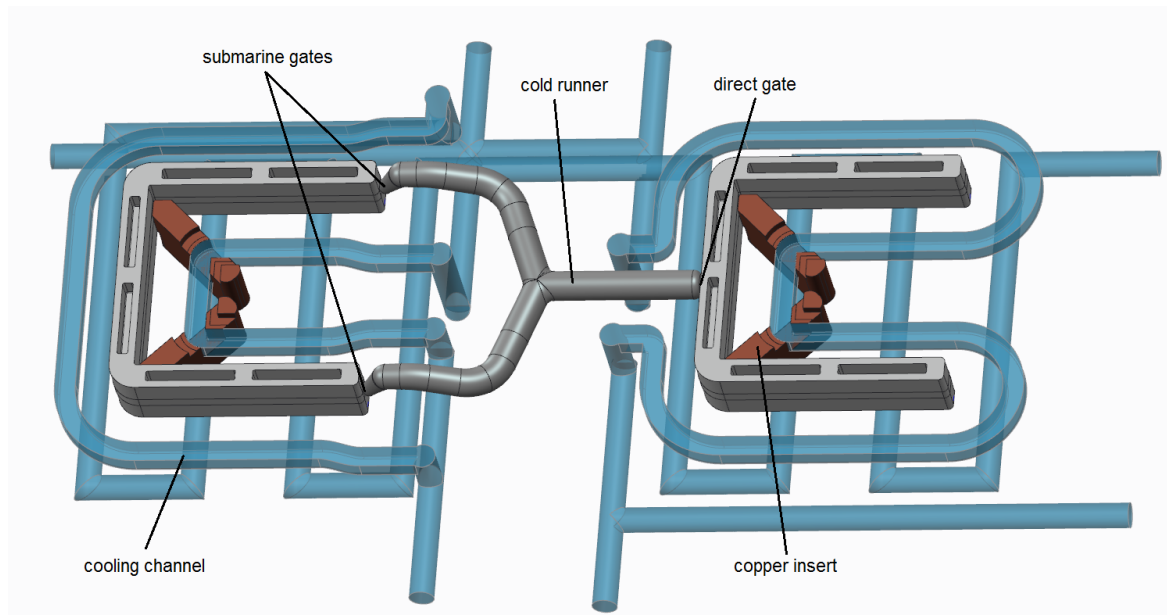
Figure 5.16.: Mold layout showing cold runner, copper inserts, and cooling channel of the moving mold half. The cooling layout in the fixed mold half is identical. [132]

---

[4]Moldmaxx HH is a CuBe2 alloy made by Materion Brush Performance Alloys

Measurements

The mold was equipped with 10 type k thermocouples, with a diameter of 1.5 mm, and two cavity pressure sensors, with a diameter of 2.5 mm. The thermocouples are located around the cavities, as shown in Fig. 5.17. They are embedded in the mold insert and placed just 3 mm below the parting plane (TC1 - TC8) and the cavity (TC9 - TC10). The pressure sensors were placed in the same position in both cavities, although this position is close to the direct gate and far from the submarine gate (Fig. 5.17). The measured linear shrinkage and warpage values were averaged over 10
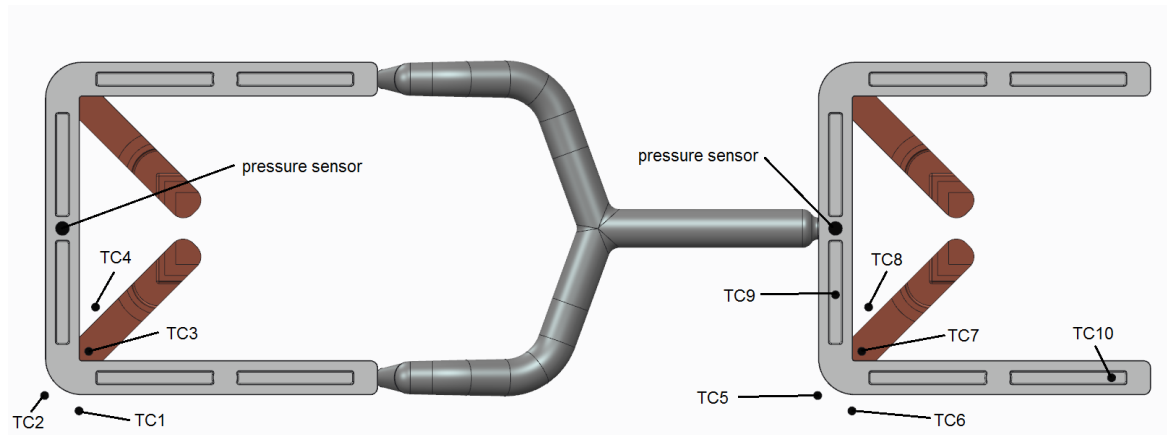
Figure 5.17.: Temperature profiles are measured by ten thermocouples placed nearby the cavities and embedded in the mold insert. Each cavity is equipped with a Kistler cavity pressure sensor. [132]

shots, and determined as follows (Fig. 5.18):

- Shrinkage was determined by measuring L_1 and evaluating $s = \frac{L_{1,cavity} - L_1}{L_{1,cavity}} 100$ %.
- Warpage was defined as $\Delta = L_1 - L'_1$ in mm.

The dimensions L_1 and L'_1 were measured using a digital caliper. Moreover, the averaged weight of the moldings was measured for all experiments with all material grades.

Experimental design

The following material grades were used:

- DuPont Delrin 127UV; POM
- UBE Nylon 1015gc9; PA6 GF45
- EMS Grilon XE5046SW; PA6 GF35
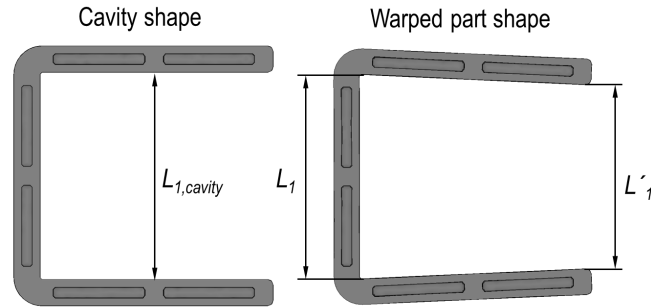
Figure 5.18.: Dimensions measured on the molded, warped parts. [132]

Different process conditions were tested with all material grades in order to investigate their influence on the warpage of the moldings and the defects inside the moldings. Based on the case studies presented in Chapter 3 (and many others not published), it is believed that melt and mold temperature only have a minor effect on warpage. Furthermore, the applicable range of mold and melt temperature is often quite limited due to limitations placed on the injection pressure, thermal degradation of the material, crystallization, and/or surface quality of the molding. Therefore, these parameters were selected from the optimal range for each material grade and kept constant for all experiments.

All experiments were performed according to the scheme given in Table 5.6.

Experiment No.	Injection time	packing pressure	packing time	cooling time
1	$t_{injection}$	low	gate-seal time	normal
2	$t_{injection}$	mid	gate-seal time	normal
3	$t_{injection}$	high	gate-seal time	normal
4	$t_{injection}$	low	$0.5\times$gate-seal time	normal
5	$t_{injection}$	mid	$0.5\times$gate-seal time	normal
6	$t_{injection}$	high	$0.5\times$gate-seal time	normal
7	$t_{injection}$	mid	gate-seal time	+ 30 s
8	$t_{injection}$	mid	$0.5\times$gate-seal time	+ 30 s
9	$0.5 \times t_{injection}$	mid	gate-seal time	normal
10	$1.5 \times t_{injection}$	mid	gate-seal time	normal

Table 5.6.: The process parameters and their settings.[132]

The actual numbers were chosen dependent on the material grade and are presented, along with the experimental results, in Section 5.2.5. When the applied packing pressure is too low, the part quality will suffer from high shrinkage, causing sink marks and poor surface quality. Very high packing pressure may lead to negative shrinkage in some areas of the cavity, and therefore cause ejection problems. Hence,

the range of packing pressure was chosen to ensure good part quality at the low pressure setting and to prevent ejection problems at the high pressure setting.

The gate-seal time was determined as described in Section 3.2. Naturally, the gate-seal time of the smaller submarine gates was about 50% shorter in all cases. When the packing time is decreased to 50%, the void volume or porous zones in the direct gated cavity are expected to become larger. Additionally, the influences of cooling time (viscoelastic effects) and injection speed (flow induced residual stress) on warpage were determined.

5.2.4. Numerical model

In the present case, warpage results considering fiber orientation obtained with Moldflow Insight 2016[5] were found to be considerably different from the results obtained with the 2015[6] release. Therefore, both versions were used, with exactly the same models and settings, and the results are compared and discussed below.

In this case, the same part was gated differently, and therefore, both cavities were modeled. Two different models, namely, a detailed model and a simple one, were used to predict the warpage of the molded parts.

- **The detailed model** contains a 3D cold runner, a 3D hot runner including all solid hot runner components, 3D cooling channels, all mold inserts, the thermocouples and the thermal insulation platens. The flow in the cooling channels was simulated by the Moldflow CFD solver using the $k - \epsilon$ turbulence model. The temperature distribution in the solid mold components is solved coupled with the polymer flow (see Section 2.2.1 for more information), providing the best thermal boundary conditions at the cavity walls. This model is used to accurately capture the effect of cooling conditions on the warpage of the moldings. This model takes a very long time to solve.
- **The simple model** just comprises the polymer domains, namely, both cavities, as well as cold and hot runner. No cooling analysis was performed and the cavity wall temperature was set to a constant and uniform value. This measure greatly reduces the computational cost and allowed the simulation of a large number of different process settings within a reasonable time frame. The temperature effect on warpage is then neglected.

---

[5]Synergy Build - 20150506.1305_C76oL87; Insight Build - 20150506.1305_C76oL80
[6]Synergy Build - 14374-768-Ins8; Insight Build - 14374-768-Ins5

Some notes on the corner effect:

Injection molded parts with corners are known to often show a decrease in the included angle in the corner [133]. This is believed to be mainly caused by two effects. The first is the temperature difference between outside and inside of the corner due to the slower heat transfer inside the corner. The second one is commonly called "spring forward" or the "corner effect" and is caused by the difference between in-plane and thickness shrinkage. It was first observed in compression molded SMC parts [134, 135]. Bakharev *et al.* [136] successfully modeled the corner effect for consideration in warpage calculations performed with mid-plane and dual domain models. They also state that no special considerations are required in the case of a true 3D warpage analysis which is used here.

Material data

The quality of the simulation results highly depends on the quality of the material data. Hence, material grades where the source of the available material data is known and reliable (gold quality indicator) were preferred.

With regard to Delrin 127UV, the material data is not entirely based on measurements (see A.1 for details). Heat capacity and thermal conductivity are assumed to be constant over temperature. This is a rough approximation for a semi-crystalline polymer. For Delrin 100, on the other hand, all material properties, including heat capacity and thermal conductivity over temperature, were measured in the Moldflow Plastics Labs (the material data is given in A.2). In several case studies performed by the author (not published), it was found that simulations using the Delrin 100 material data yielded better warpage results, but slightly worse shrinkage predictions when compared to molding trials performed with Delrin 127UV. Therefore, Delrin 100 was preferred for the numerical part of this study.

The second grade used for the experiment was EMS Grilon XE5046SW. It is a slightly modified EMS Grilon BG-35 of which material data with gold quality indicator exists (see A.4 for detailed material data).

Excellent material data with gold quality indicator was also available for the third grade used: UBE Nylon 1015gc9. All of the material properties are summarized in A.5.

Process settings and boundary conditions

All process settings were defined in accordance with the experimental molding trials. The actual numbers are given in Section 5.2.5. The applied packing pressure was adjusted to account for the pressure loss in the nozzle and to match the measured peak cavity pressure.

Fiber orientation must be defined as an inlet boundary condition at the injection location. The model, however, contains hot and cold runner. Therefore, the orientation defined at the inlet will be washed out before the melt enters the cavity. Hence, the default definition is retained.

A coolant volume flow rate of 2.2 l/min was measured and also defined as an inlet boundary condition of the cooling channels. The water temperature at the inlet boundary conditions was derived from the measured water temperatures and depends on the material processed.

Solver settings

The analysis sequence used for the detailed model was: Cool (FEM) + Fill + Pack + Warp. Whereas the transient mold temperature was calculated by the flow solver. The analysis sequence used for the simple model which neglected mold temperature effects was: Fill + Pack + Warp. All the solver settings presented in Section 3.3.4 were used for this study. Additionally, a number of simulations, using different settings for the fiber model, were performed. These settings are presented along with the associated simulation results in Section 5.2.6

Computational Mesh

Both models, detailed and simple, use the same tetrahedral mesh for the polymer domains. They were meshed with at least 12 elements over the wall thickness, leading to approximately 1.7×10^6 elements for the cavities and another 3.2×10^5 elements for hot and cold runner. The cooling channels were meshed with around 2×10^6 elements, and the mold components with about 4×10^6 elements. For the best accuracy and convergence behavior of the solution, the mesh was made conformal at all contact faces. Fig. 5.19 shows the mesh of the moving mold half and the hot runner nozzle.
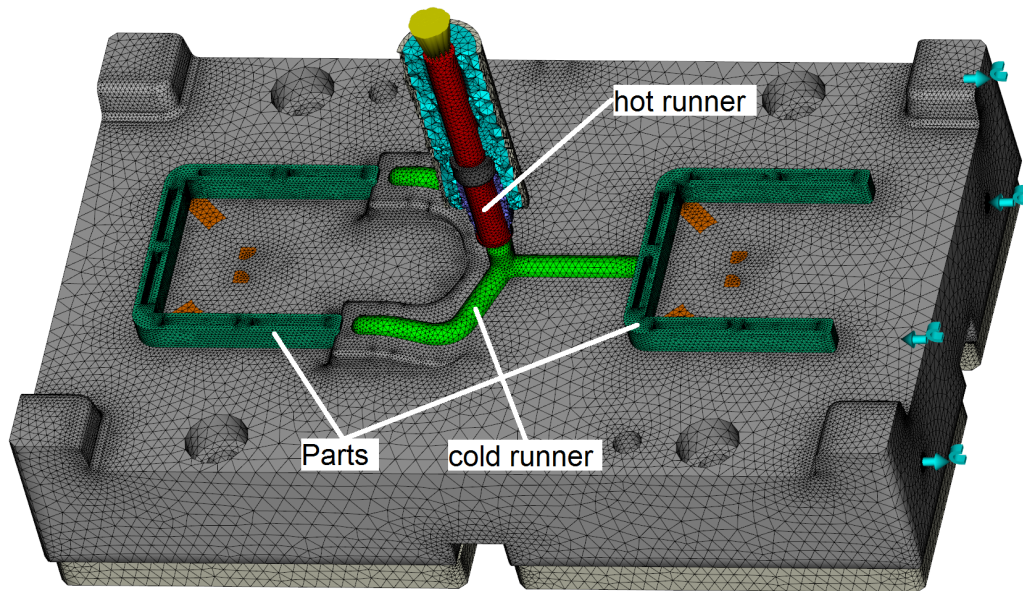
(a) Mesh of part, cold runner, hot runner nozzle, and mold components of the moving half.
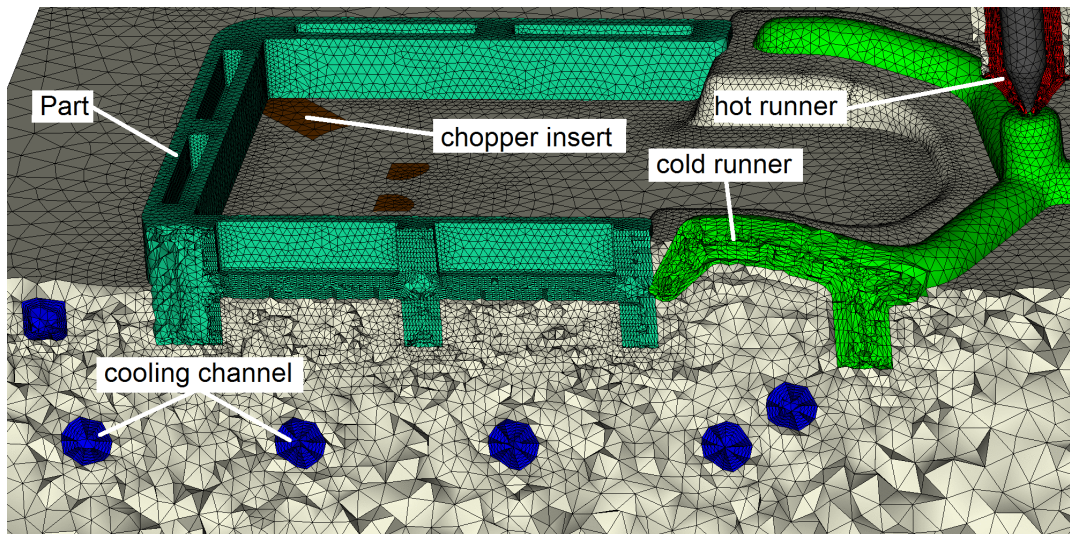
(b) Cut through the 3D mesh showing the layered element structure in the polymer domains, and the 3D cooling channel.

Figure 5.19.: Meshed numerical model of the two-cavity mold. [132]

	part	cold runner 3D	hot runner	mold
Element count	2295493	165971	1503818	4201066
Nodes	413408	29895	292935	817332
Elements across wall thickness	12	12	6	6
max. aspect ratio	42.1	29.69	84.7	103.14
average aspect ratio	3.66	3.76	1.96	1.85
min. aspect ratio	1.03	1.05	1.00	1.00
max. dihedral angle	174	173	178.7	178.4

Table 5.7.: Mesh properties and diagnostics.

5.2.5. Experimental results

The pressure drop in the nozzle and the runner system is of little importance in the present study. Instead of the hydraulic or specific packing pressure defined on the injection molding machine, the approximate maximum cavity pressure obtained by the pressure transducer is given in the following result tables. The wall thickness is greatest in the corners and the bottom of the U-part. Therefore, some molded parts were cut open at the symmetry plane to have a look on the inner defects such as voids or porous zones. This was done on the POM parts since they form visible voids and on the PA6 GF45 parts, which tend to form porous zones. With the natural opaque material used, these porous zones are visible even under the surface of the molding. While the dense fiber-matrix composite has some level of transparency (despite the semi-crystalline matrix), the porous zones appear "milky white". Pressure and temperature profiles were measured to validate the quality of the numerical model and are therefore presented in Section 5.2.6 together with the simulation results.

POM

The experiments with POM were carried out using a melt temperature of 210°C, a hot runner temperature of 200°C, and a mold temperature of around 95°C. The standard deviations of the measured dimensions L_1 and L_1' (Fig. 5.18) are less than 0.02 mm and 0.15 mm, respectively, in all cases. Therefore, the process was stable and the measurements are reliable. The results are presented in Table 5.8 where t is the time, p the pressure, s the shrinkage, Δ the warpage and m the mass. The index i stands for injection, p for packing, c for cooling, cav for cavity, dir for direct gate and sub for submarine gate. The deformed shape of the molded parts was as shown in Fig. 5.18. The main place in which warpage occurred was the corners, while the bottom of the U as well as both of its arms remained relatively straight.

126

No.	t_i [s]	p_{cav} [MPa]	t_p [s]	t_c [s]	s_{dir} [%]	s_{sub} [%]	Δ_{dir} [mm]	Δ_{sub} [mm]	m_{dir} [g]	m_{sub} [g]
1	4.92	26	45	10	2.58	2.87	0.27	2.87	15.48	15.32
2	4.92	65	45	10	2.26	2.61	0.71	2.70	15.63	15.51
3	4.92	100	45	10	1.97	2.35	0.96	2.61	15.76	15.67
4	4.92	26	22.5	32,5	2.68	2.86	2.09	2.89	15.34	15.33
5	4.92	65	22.5	32,5	2.41	2.60	2.18	2.74	15.49	15.52
6	4.92	100	22.5	32,5	2.10	2.30	2.02	2.53	15.61	15.67
7	4.92	65	45	40	2.08	2.36	0.89	2.25	15.65	15.52
8	4.92	65	22.5	62,5	2.21	2.39	1.76	2.28	15.49	15.52
9	2.3	65	45	10	2.30	2.60	0.90	2.77	15.63	15.52
10	7.4	65	45	10	2.23	2.78	0.69	2.54	15.64	15.51

Table 5.8.: Process settings and measured results: POM. [132]

When the packing pressure is applied until the gates are frozen (Experiments No. 1-3), the part with the large direct gate shows a much lower warpage (Δ_{dir}) than the tunnel gated one. Increasing the packing pressure causes an increase in warpage in the case of direct gating and a decrease in warpage in the case of submarine gating (Δ_{sub}). When the packing pressure is relieved before the direct gate is actually frozen, warpage increases dramatically (Experiments No. 4-6). Since the submarine gates seal much earlier, no significant difference in shrinkage or warpage is observed on these parts. An increase in cooling time causes a reduction in warpage of the submarine gated parts and the not fully packed direct gated parts (Experiments No. 7-8). Interestingly, the direct gated parts produced with full packing and prolonged cooling time (Experiment No. 7), show a somewhat lower shrinkage, but more warpage than their counterparts produced in Experiment No. 2. Viscoelastic stress relaxation in the constrained state during cooling time generally leads to lower shrinkage and warpage levels. In this case, however, shrinkage is reduced but warpage increased. A possible explanation is that the longer cooling time also causes a lower mold temperature. This is especially the case at the gates where additional shear heat is introduced during filling. A lower mold temperature in the gate area causes a decrease in packing efficiency, and therefore affects warpage. A lower injection velocity generally leads to a minor reduction in warpage, while warpage increases at the higher injection velocity (Experiments No. 9-10). The lowest warpage of just 0.27 mm was achieved when low packing pressure was combined with high packing efficiency, due to a large gate in the thick walled section of the part (Experiment No. 1, direct gate).

Fig. 5.20 shows some molded parts made of POM which were cut open at the bottom of the U. There are always parts from two shots shown, which are placed back to back. All of the sliced parts show voids (Fig. 5.20). Even the high packing efficiency enabled by the large direct gate does not lead to parts without defects. The parts with the direct gate show a fine void distribution in the bottom of the U, without large formations in the corner, as long as the packing pressure is applied until the gate freezes off. Moreover, the void volume seems to be unaffected by the packing pressure applied. The gain in part mass only causes a reduced shrinkage. With regard
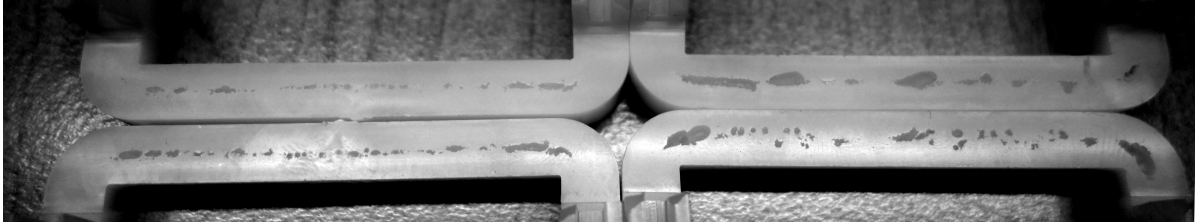
(a) Experiment No. 1: $p_{cav} = 26\,\text{MPa}$; $t_p = 45\,\text{s}$
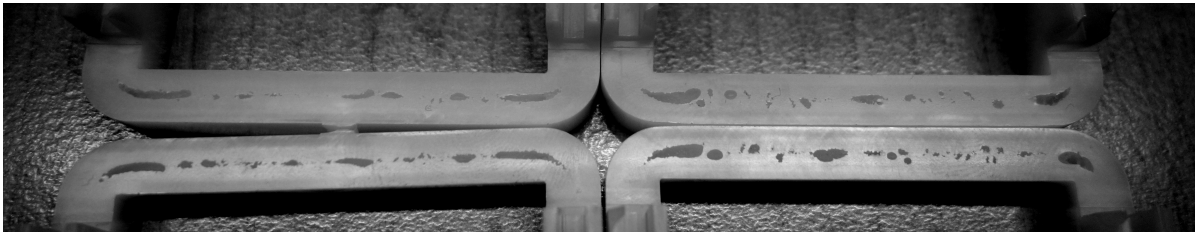
(b) Experiment No. 2: $p_{cav} = 65\,\text{MPa}$; $t_p = 45\,\text{s}$
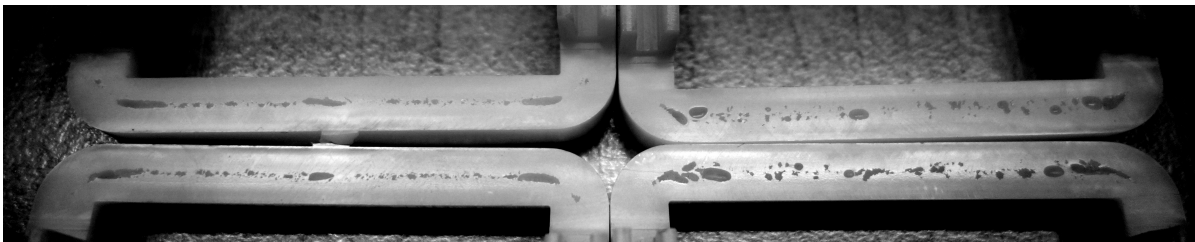
(c) Experiment No. 3: $p_{cav} = 100\,\text{MPa}$; $t_p = 45\,\text{s}$
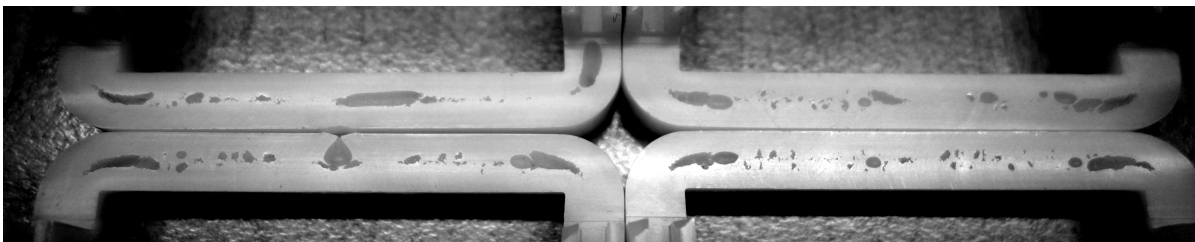
(d) Experiment No. 5: $p_{cav} = 65\,\text{MPa}$; $t_p = 22.5\,\text{s}$

Figure 5.20.: Delrin 127 UV: Two shots placed back to back and cut at the symmetry plane showing voids. Left: direct gate. Right: submarine gate. [132]

to all of the submarine gated parts, as well as the direct gated parts from Experiment No. 5, fewer, but much larger voids are visible. The voids in the submarine gated part seem to become smaller and more evenly distributed with increased packing pressure. It is also interesting to see that the voids do not form directly in the area with the largest volume, namely, the corners. Regardless of the gating, the largest voids form in the bottom of the U, and extend into the corner regions. When the packing pressure is released too early, as happened in Experiments No. 4-6, mass flows back through the gate and causes large voids in the cooled moldings along with a massive increase in warpage.

PA6 GF45

For this material, a melt temperature of 290°C, a hot runner temperature of 285°C, and a mold temperature of about 85°C were used. All process settings and results are provided in Table 5.9. The standard deviations of the measured dimensions L_1 and L_1' are less than 0.02 mm and 0.06 mm, respectively, in all cases indicating a stable process. All of the produced parts exhibited warpage in the order of 4 mm.

No.	t_i [s]	p_{cav} [MPa]	t_p [s]	t_c [s]	s_{dir}[%]	s_{sub} [%]	Δ_{dir} [mm]	Δ_{sub} [mm]	m_{dir} [g]	m_{sub} [g]
1	2.15	16.5	30	15	0.23	0.49	4.13	3.83	16.88	16.84
2	2.15	33	30	15	0.24	0.53	4.06	3.86	16.97	16.94
3	2.15	59	30	15	0.22	0.51	4.02	3.93	17.10	17.06
4	2.15	16.5	15	30	0.23	0.50	4.06	3.86	16.90	16.84
5	2.15	33	15	30	0.23	0.51	4.16	3.93	16.95	16.93
6	2.15	59	15	30	0.24	0.48	4.20	3.96	17.04	17.05
7	2.15	33	30	45	0.20	0.49	3.82	3.60	16.97	16.93
8	2.15	33	15	60	0.21	0.47	3.86	3.66	16.99	16.96
9	0.95	33	30	15	0.21	0.56	3.93	4.17	16.96	16.93
10	4.00	33	30	15	0.24	0.55	4.07	4.01	16.97	16.92

Table 5.9.: Process settings and measured results: PA6 GF45. [132]

Warpage of the direct gated parts was, in most cases, around 5% higher than that of the submarine gated parts. The only exception was the experiment with the shorter injection time (Experiment No. 9), where the direct gate produced parts with slightly lower warpage. At full packing time, warpage of the direct gated parts decreased with increased packing pressure (Experiments No. 1-3). In the case of the submarine gate, the opposite was found to be true. When the packing time was reduced (Experiments No. 4-6), warpage of the direct gated parts increased slightly. In both cases, a prolonged cooling time caused a small reduction in warpage (Experiments No. 7-8). Injection speed had only a minor influence on warpage (Experiments No. 9-10). The molding trials indicated that optimized process settings would not lead to a significant reduction in warpage. Furthermore, the improved packing efficiency of the direct gate does not lead to lower warpage levels, despite

the fact that shrinkage is around 50% lower. In this case, warpage seems to be entirely dominated by the orientation effect of the glass fibers.

Sliced parts are shown in Fig. 5.21. The "milky white" areas of the parts are porous or have larger voids. Looking at the direct gate, a porous zone of around 1.5 mm width extends from the gate at the bottom of the U to the corners of the part. In the corners, its width increases to about 2.5 mm, and it is closer to the inside wall of the corner. This is certainly caused by the lower cooling rates inside the corner (see Section 5.2.6 for temperature measurements inside and outside the corner) and the subsequent slower development of the frozen layer. The porous zone forms up where the frozen layer, growing from the outside wall of the corner, and the frozen layer of the inside wall finally meet. The porous zone seems to become denser (lower porosity) with increasing packing pressure (Experiments No. 1-3), although its size does not change. The submarine gated parts have a much larger porous zone with a width of about 4 mm and numerous nested, small voids, visible to the naked eye. This is obviously a result of the low packing efficiency caused by the smaller gate placed in the thin walled sections of the part.

PA6 GF35

A melt temperature of 280°C, a hot runner temperature of 275°C and a mold temperature of about 75°C, were used for the black PA6 GF35 grade. The process settings and results are summarized in Table 5.10. The standard deviations of the measured dimensions L_1 and L_1' were less than 0.02 mm and 0.11 mm, respectively, in all cases. Due to the black color of the material, the porous zones can't be visualized by merely cutting the moldings open. Therefore, no photographs are presented for this grade. This material behaved quite similarly to its higher filled counterpart, presented in

No.	t_i [s]	p_{cav} [MPa]	t_p [s]	t_c [s]	s_{dir} [%]	s_{sub} [%]	Δ_{dir} [mm]	Δ_{sub} [mm]	m_{dir} [g]	m_{sub} [g]
1	2.30	11	35	15	0.26	0.60	4.81	5.30	15.16	15.08
2	2.30	26	35	15	0.27	0.63	4.69	5.24	15.27	15.20
3	2.30	49	35	15	0.26	0.61	4.57	5.17	15.40	15.34
4	2.30	11	15	35	0.24	0.61	4.58	5.27	15.20	15.09
5	2.30	26	15	35	0.25	0.64	4.84	5.28	15.26	15.21
6	2.30	49	15	35	0.26	0.62	4.88	5.19	15.35	15.33
7	2.30	26	35	45	0.19	0.53	4.18	4.61	15.27	15.20
8	2.30	26	15	65	0.19	0.49	4.25	4.61	15.26	15.20
9	1.2	26	35	15	0.25	0.63	4.64	5.51	15.27	15.21
10	4.07	26	35	15	0.25	0.61	4.71	5.45	15.26	15.18

Table 5.10.: Process settings and measured results: PA6 GF35. [132]

Section 5.2.5. Warpage was generally even higher, with values in the order of 5 mm. Due to the lower fiber content, the process settings had a bit more impact on it. In contrast to PA6 GF45 (Table 5.9), the direct gated parts generally show around 10% lower warpage. Their shrinkage is also approximately 60% lower. Independent of

(a) Experiment No. 1: $p_{cav} = 16.5\,\text{MPa}$; $t_p = 30\,\text{s}$

(b) Experiment No. 2: $p_{cav} = 33\,\text{MPa}$; $t_p = 30\,\text{s}$

(c) Experiment No. 3: $p_{cav} = 59\,\text{MPa}$; $t_p = 30\,\text{s}$

(d) Experiment No. 5: $p_{cav} = 33\,\text{MPa}$; $t_p = 15\,\text{s}$
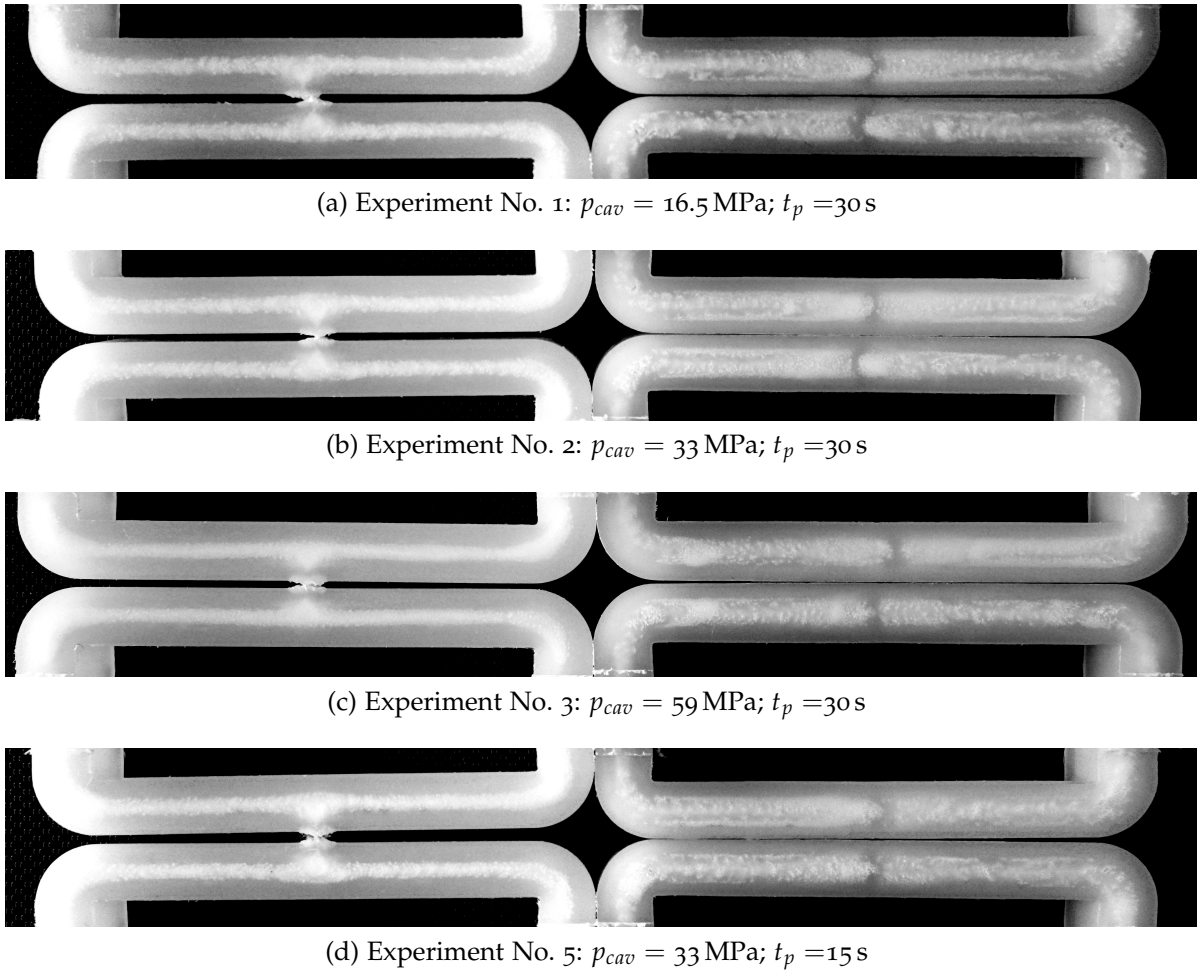
Figure 5.21.: PA6 GF45: Two shots placed back to back and cut at the symmetry plane showing porous zones and some small voids. Left: direct gate. Right: submarine gate.[132]

the gate, increasing packing pressure results in a reduction in warpage. Shortening the packing time increased warpage of the direct gated parts in Experiments No. 2 and 3 by around 5%, but had the opposite effect in Experiment No. 1. A prolonged cooling time causes a reduction in warpage of around 12%, while the location of the gate makes no difference. The lower fiber content has a less linearizing effect on the viscoelastic polymer matrix. Increasing or decreasing the injection time has little effect on the warpage of the direct gated parts, but slightly increases the amount of warpage of the submarine gated parts in both cases.

5.2.6. Simulation results and discussion

Temperature history

Fig 5.22 shows the simulated and the measured temperature history at the locations shown in Fig. 5.17 for Experiment No. 2 (see Table 5.8) when processing POM. The temperature results were obtained with the detailed model, since no cooling analysis was performed with the simple model. The predicted peak temperatures were somewhat higher at all measuring points, while significant deviations of more than 2 Kelvin were only found at the two locations underneath the cavity. Despite this, the predicted temperatures were within the measuring uncertainty of $\pm 1\,\mathrm{K}$. Improvements to the numerical model would be possible however, by altering the estimated HTC values at the contact interfaces, and modifying the thermal conductivity of the mold components within a physically meaningful range. However, to capture the effect of the transient cavity wall temperature on warpage, this accuracy is certainly sufficient.

Both the predicted and measured temperature profiles for PA6 GF35 are shown in Fig. 5.23. The predicted temperatures were in very good agreement with the measured data. A noteworthy deviation was only found at points TC6 to TC8. Generally, all the temperature predictions fit extremely well with the experimental data. However, as is shown in Section 5.2.6, the influence of the cavity wall temperature on warpage prediction is very small, and thus, there is no need to provide more temperature validation data at this point.

Pressure history

As already pointed out in Section 3.4.6, an accurate prediction of the cavity pressure history is needed to calculate the pressure-induced in-mold stress. The resulting stress distribution through the part thickness is essential for the calculation of shrinkage and warpage. Fig. 5.24 shows the predicted and measured pressure profiles of both cavities
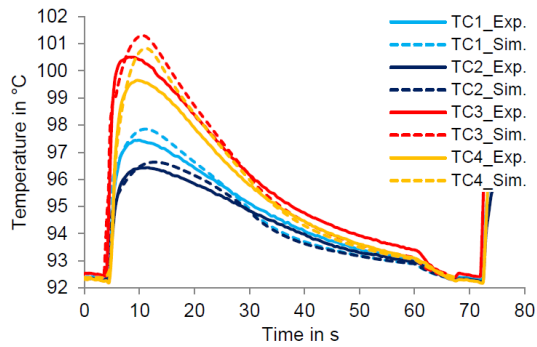
(a) Submarine gated side: Temperature inside (TC3 & TC4) and outside (TC1 & TC2) the corner.
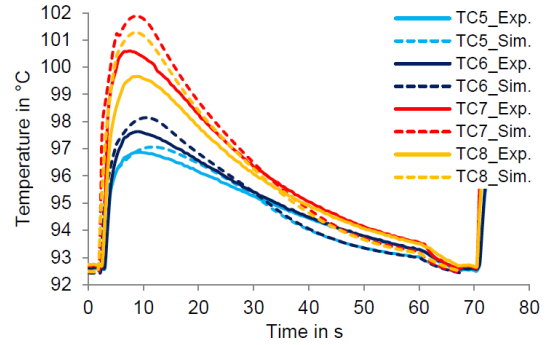
(b) Direct gated side: Temperature inside (TC7 & TC8) and outside (TC5 & TC6) the corner.
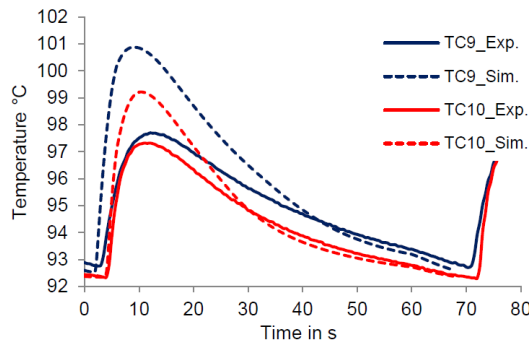
(c) Direct gated side: Temperatures underneath the cavity.

Figure 5.22.: POM: Measured and simulated temperature history for Experiment No. 2. [132]

and for three different materials for Experiment No. 2. The results were obtained with the simplified model. When using the detailed model, the gate seal is slightly delayed due to the shear heat introduced during filling. In all three cases, there is an excellent agreement between predicted and measured pressure history at the submarine gated cavity. However, the results of the direct gated cavity dramatically deviate from the measurements.

This problem is certainly the result of an ill-conceived selection of pressure sensor location by the author. During the molding trials, it was observed that the measured pressure at the direct gated cavity commonly reached ambient conditions before the gate was actually sealed. Hence, new material was still being forced into the cavity, but the pressure in the melt core could no longer reach the pressure sensor. Fig. 5.25 may help to explain and clarify this relation. It shows the roughly sketched cross section at the pressure sensor location (compare Fig. 5.17) and the conditions at two points in packing time. The left side shows the solidified material and the melt core
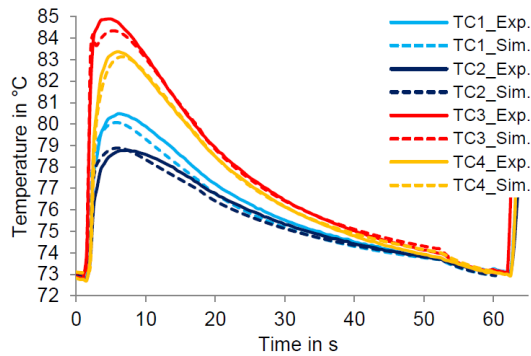
(a) Submarine gated side: temperature inside (TC3 & TC4) and outside (TC1 & TC2) the corner.
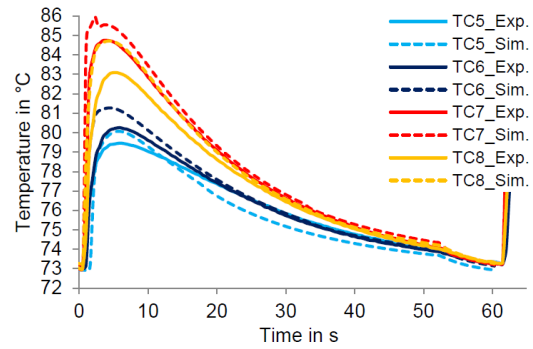
(b) Direct gated side: temperature inside (TC7 & TC8) and outside (TC5 & TC6) the corner.
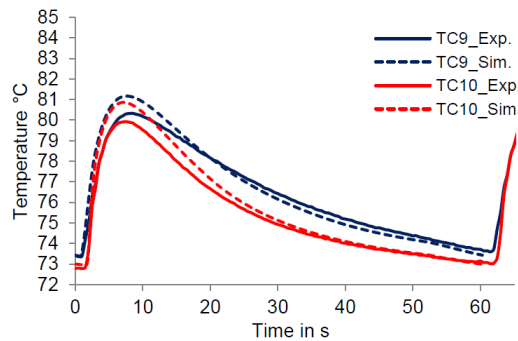
(c) Direct gated side: temperatures underneath the cavity.

Figure 5.23.: PA6 GF35: Measured and simulated temperature history for Experiment No. 2. [132]

in the early packing stage (Fig. 5.25a). The high melt pressure forces the solid but flexible layer towards the face of the pressure sensor. At this point, the measured pressure will closely correspond to the pressure of the melt core. The right side (Fig. 5.25b) depicts a probably state close to the end of the packing stage. While the gate is still open, the pressure of the melt core is in balance with the pressure applied by the now massive, rigid and shrinking solid material. The solid body has already lost contact with the sensor, which, consequently, measures ambient pressure. This complex interaction of the liquid and solid phases is not captured by the simulation model. Hence, the pressure sensor shows a faster pressure decay than the simulation. For this reason, and in this special case, the comparison of predicted and measured pressure history is only valid for the early packing stage where the solidified volume is still low.

In addition to this instance of improper pressure measurement, it was also found that the simulation tends to overpredict the gate seal time at the direct gate. Fairly good

(a) POM

(b) PA6 GF35

(c) PA6 GF45
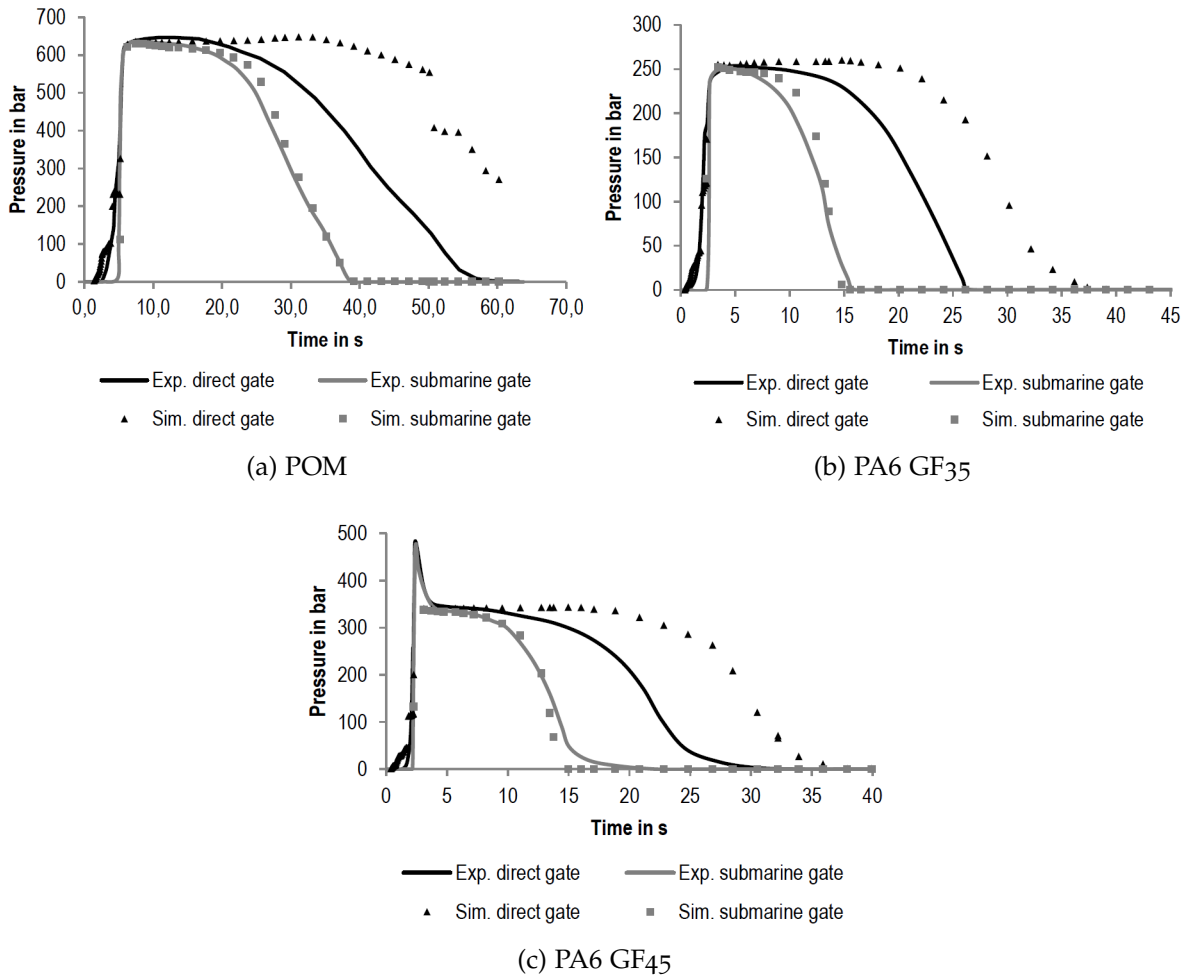
Figure 5.24.: Measured and predicted cavity pressure for Experiment No. 2. [132]

agreement was observed at the submarine gate.

Detailed model vs. simple model

The coupled simulation of polymer flow, cooling water flow, and temperature field in the mold components, when carried out with the detailed model, comes at high computational cost. Several injection cycles must be simulated until a steady-state cyclic condition is achieved. Hence, warpage predictions obtained with the detailed model were compared to predictions obtained with the simple model as described in Section 5.2.4. The results obtained with both models essentially show the impact of the thermal boundary conditions on shrinkage s and warpage Δ. The predicted values for Experiment No. 2 are given in Table 5.11

(a) Conditions at the early packing stage.

(b) Conditions before the end of the packing stage.
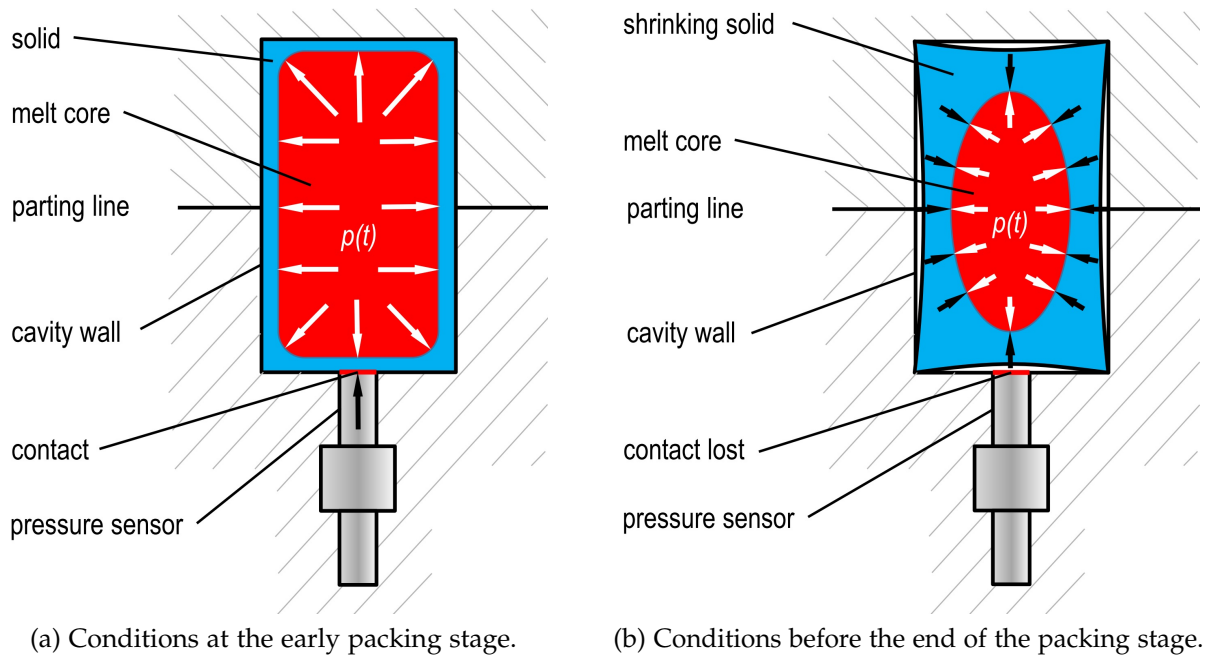
Figure 5.25.: A rough sketch of the cross section at the location of the pressure sensor. The conditions of liquid and solid phases are depicted for two points in packing time.

There are two contrary effects which influence the predicted warpage:

- The measured temperature profiles show a temperature difference between the hotter inside and the outside of the corner, which is only considered by the detailed model. This causes more shrinkage of the material on the inside of the corner, and therefore an increase in warpage.
- During the filling stage, the high shear rates at the gates generate heat due to viscous dissipation. Therefore, the temperature level of the mold is elevated in the gate regions. The result is a prolonged gate-seal time, which improves packing efficiency and leads to lower shrinkage levels throughout the part. This effect tends to reduce warpage in the present case.

Both effects balance out, and finally, the predicted shrinkage and warpage of both models differs only slightly with deviations in both directions. For this reason, warpage predictions for the other experiments were obtained using the simple model. This measure allows the simulation of several experiments in a reasonable time frame.

		detailed model		simple model	
		shrinkage s	warpage Δ	shrinkage s	warpage Δ
POM	direct gate	1.55%	0.94 mm	1.36%	0.94 mm
	submarine gate	1.93%	1.24 mm	1.82%	1.17 mm
PA6 GF35	direct gate	0.54%	1.88 mm	0.54%	1.76 mm
	submarine gate	0.80%	2.82 mm	0.82%	2.89 mm
PA6 GF45	direct gate	0.31%	1.28 mm	0.29%	1.19 mm
	submarine gate	0.59%	2.31 mm	0.59%	2.47 mm

Table 5.11.: Comparison of predicted shrinkage s and warpage Δ obtained with the detailed and the simple model for Experiment No. 2. [132]

Warpage and shrinkage results

POM

In this section, the predicted shrinkage and warpage, as defined in Section 5.2.3, are compared to the measured values. Fig. 5.26a shows the comparison for POM. In the case of direct gating, the simulation predicted a minor decrease in warpage with increased packing pressure (Experiments No. 1-3), while in reality, the warpage increased with packing pressure. Warpage was predicted almost perfectly for Experiment No. 3, but overestimated for Experiments No. 1 and 2. Considering the submarine gated parts, the simulation strongly underpredicted warpage in all experiments. Moreover, the trend of the predicted warpage was again wrong. An increase in packing pressure caused a reduction in warpage, which is in contrast to the simulation results. In Experiment No. 5 the packing pressure was released before the direct gate was sealed. This caused a massive increase in warpage of the direct gated parts. The simulation model does capture the higher volumetric shrinkage in the core properly, but it fails to predict the higher warpage correctly. Considering Fig. 5.20, a correlation between void volume and warpage can be seen.

(a) Warpage
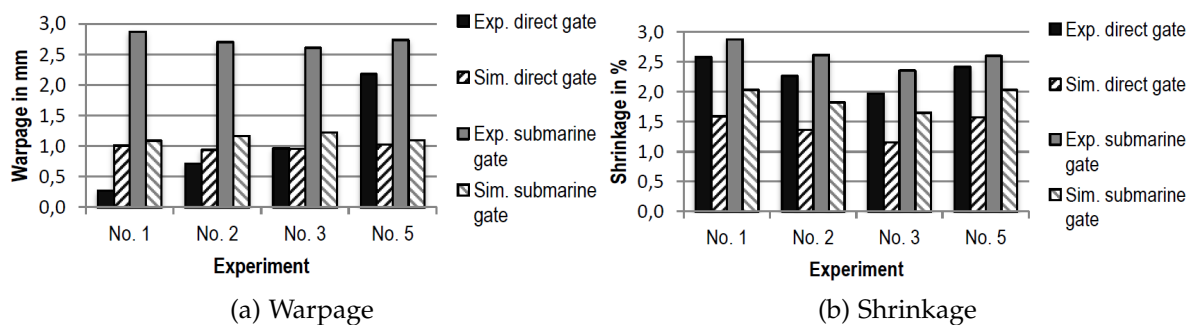
(b) Shrinkage

Figure 5.26.: Measured and predicted warpage and shrinkage for POM. [132]

Predicted and measured shrinkage values are shown in Fig. 5.26b. In all cases, the predicted shrinkage does follow the trend with respect to process conditions correctly. The simulation consistently underestimates shrinkage by around 30%. Some additional simulations (not shown here) performed using material data for Delrin 127UV resulted in a marginally better prediction of the shrinkage magnitude, while warpage predictions worsened.

It should be pointed out that the shrinkage model used for 3D simulations is generic, meaning that no correction with actual tested shrinkage values is performed. Moldflows Corrected Residual In-Mold Stress (CRIMS) model was developed to overcome limitations in material modeling. It would probably yield more accurate shrinkage results, but it is not applicable to parts which are not purely thin-shell like. More on this topic can be found in [4].

PA6 +GF

In regard to the fiber filled material grades, things are quite different. From the experiments, it is evident that varying processing conditions have little influence on shrinkage and warpage. The same is true for the numerical model, although the model's sensitivity to process parameters is somewhat higher. The fiber model, on the other hand, significantly affects the simulation result. Therefore, the prediction of the fiber orientation is a key issue, and the model parameters should be discussed in more detail.

For this reason, a number of different settings of model parameters and closure approximations were used to investigate the impact of fiber orientation on the accuracy of shrinkage and warpage prediction. Moreover, the same simulations were also performed with Autodesk Moldflow Insight 2016 and compared to the results obtained with the 2015 release. This is because of enhancements in the 3D RSC fiber model which were implemented in the 2016 release [137].

Some notes on the fiber model parameters: In the present study, it was found that warpage is affected by the reduced strain closure factor κ which must be estimated or determined experimentally (see Section 2.1.5). This parameter slows down the evolution of the orientation tensor. With the default value of 0.05, the warpage of the submarine gated part is considerably higher than that of the direct gated part. When κ is reduced to 0.025, the warpage of the submarine gated part decreases, while the direct gated part is hardly affected. This is particularly true for version 2015 and PA6 GF35, while the effect is less pronounced in the case of PA6 GF45. In the 2016 version, the influence of κ on warpage is negligible. The coefficient of interaction C_i can be estimated by the empirical equations (2.19) and (2.18) found by Phan-Thien *et al.* [62] and Bay [42], respectively (see section 2.1.5). However, based on the findings

presented in Chapter 6, these values are too high in conjunction with the RSC model, and thus, a value of 0.001 was chosen for Moldflow Insight Version 2015. With these settings, Insight 2016 predicts a considerably higher degree of orientation. When using the auto calculated C_i of 0.0162 with Insight 2016, the orientation magnitude in the first principal direction is similar to the results obtained with the 2015 version. To maintain comparability between the two releases, a C_i of 0.001 and a κ of 0.025 was used for all simulations. Variations of C_i hardly change the shrinkage and warpage results, however.

Why the closure approximation affects the warpage prediction: To predict the shrinkage and warpage of a fiber filled polymer, it is necessary to model the mechanical and thermal properties of the composite from the properties of matrix and inclusions with respect to fiber orientation. An orientation averaging step is required, in order to take the orientation distribution into account. For this step, the 2nd order orientation tensor a_{ij}, obtained during the flow simulation, and the 4th order orientation tensor a_{ijkl} are needed. Since a_{ijkl} is unknown, it must be approximated by means of a_{ij}. Moldflow offers different forms of closure approximations, where the 4 orthotropic versions [61] give similar shrinkage and warpage results. Only the hybrid closure [40] leads to significantly different results.

Taken together: Simulations were performed using the RSC fiber model, with $C_i = 0.001$, $\kappa = 0.025$, Mori-Tanaka micro-mechanics model, Rosen-Hashin thermal expansion coefficient model, hybrid and orthotropic closure approximation fitted for low C_i (ORL) as well as with the Moldflow Insight releases 2015 and 2016.

Fig. 5.27a shows the predicted and measured warpage values of the direct gated parts made of PA6 GF35. In all experiments, warpage was dramatically underpredicted with the RSC model in conjunction with the orthotropic closure approximation, while slightly better results were obtained with the 2016 release. With the hybrid closure, the warpage predictions of both releases 2015 and 2016 were dramatically different. While the results obtained with the hybrid closure and the 2015 release show very good agreement with the measurements in all cases, the same simulations performed with the 2016 release show a significant overprediction of warpage. Basically, the same is true for the warpage of the submarine gated parts shown in Fig. 5.27b. The predicted shrinkage values shown in Fig. 5.27c and Fig. 5.27d are generally too high. In particular, the hybrid closure in release 2015 yields unrealistically high shrinkage values, while the same results obtained with the 2016 release show shrinkage values, comparable to those obtained with the ORL closure.

In the case of PA6 GF45, the influence of the closure approximation on warpage is less pronounced, but still relevant in the case of the submarine gated part. The predicted warpage is heavily underestimated in the case of direct gating (Fig. 5.28a) and about 30 to 50 % too low in the case of submarine gating (Fig. 5.28b) when the ORL is used. The hybrid closure in conjunction with the 2016 release, on the other hand, gives a

(a) Warpage direct gate   (b) Warpage submarine gate

(c) Shrinkage direct gate   (d) Shrinkage submarine gate
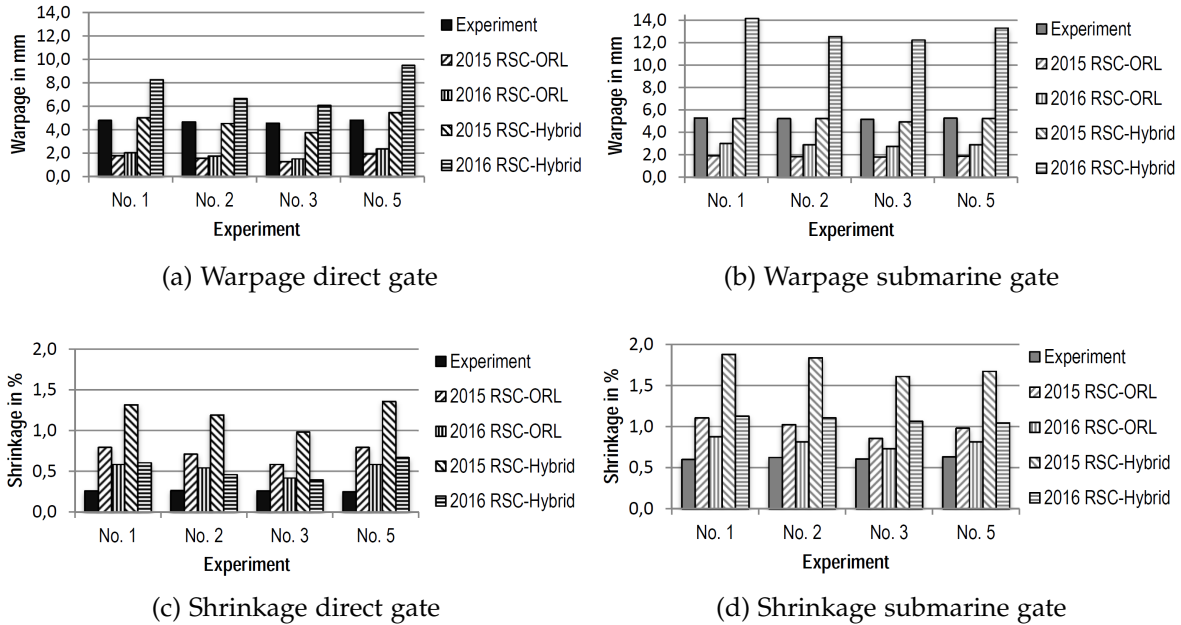
Figure 5.27.: Measured and predicted warpage and shrinkage for PA6 GF35. [132]

fairly good estimation of the warpage of the submarine gated part. Shrinkage was overestimated in all cases, while only the results obtained with the 2015 release and the hybrid closure showed a severe deviation. The same closure model with the 2016 release, on the other hand, gives the most accurate shrinkage predictions in almost all cases.

Discussion

Accurate warpage predictions predominantly call for good material data, realistic boundary conditions, and proper process parameters. In the present case, measurements of temperature and pressure were used to improve boundary conditions and process settings in order to simulate the experimental setups as accurately as possible. Only plastic grades with good material data (for instance the Moldflow Plastic Labs) were used for the investigations. This was done in order to minimize the risk of compromised simulation results due to poorly characterized material data. Hence, the best preconditions for accurate results were created.

Considering the experimental results, it is interesting to see that even with the large direct gate, it is not possible to produce parts without inner defects. In the case of POM, voids emerge in the thick walls of the part although not necessarily in the thickest sections, which are the corners. In relation to the direct gated parts, the

(a) Warpage direct gate

(b) Warpage submarine gate

(c) Shrinkage direct gate

(d) Shrinkage submarine gate
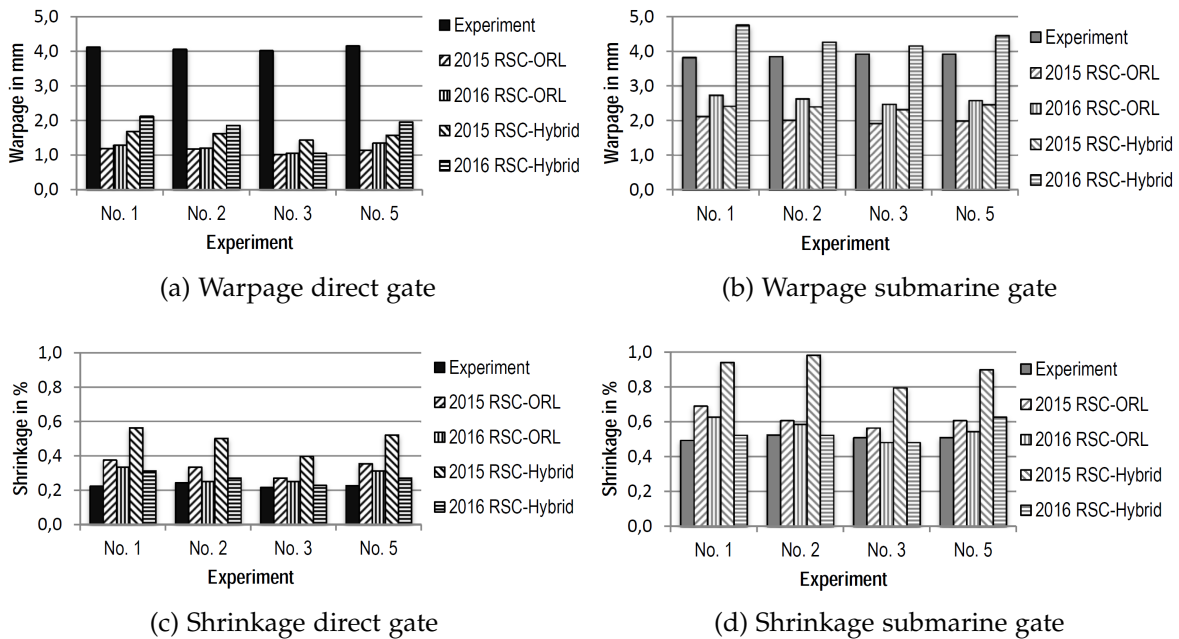
Figure 5.28.: Measured and predicted warpage and shrinkage for PA6 GF45. [132]

void volume in the submarine gated parts is considerably higher. When the packing pressure is relieved before the direct gate freezes off, void volume and warpage severely increase. From the 10 test settings, only numbers 2 and 3 are practically meaningful, since the full packing time and proper packing pressure were applied. In those cases, the simulation results for the direct gated part were in good agreement with the measurements. However, the simulation failed to quantitatively predict the warpage of the submarine gated part, and it failed when voids were generated at will in the direct gated part.

In the case of fiber filled material, process parameters hardly affect shrinkage or warpage in either experiment or numerical simulation. In contrast to the unfilled material, voids only form in areas with extremely high shrinkage. What is more commonly seen is a porous zone. In this part, however, there is no indication that these inner defects affect warpage. There is no way to significantly influence warpage by means of process parameters, neither in experiment nor numerically. The warpage of the molded parts was predominately determined by the fiber orientation. The predicted warpage is also only sensitive to the fiber models used. A way of setting up the fiber models in order to obtain consistently accurate warpage results was not found. The results presented in Chapter 6 indicate that state-of-the-art fiber models struggle to correctly predict the fiber orientation in thick walls. Therefore, the greatest potential to improve warpage predictions for fiber reinforced, chunky plastic parts certainly lies in the improvement of fiber models and closure approximations.

5.2.7. Concluding remarks

In the case of POM, it was found that warpage predictions were in reasonable agreement with the measurements as long as the void volume in the molding was low. When the void volume increases, due to gating in a thin walled section, or packing pressure is released before gate seal, warpage increases dramatically in experiment. This effect is not shown by the numerical simulation model. This finding supports the conclusions made in the preceding Section 5.1. Hence, excessively high volumetric shrinkage should be avoided by means of appropriate part and mold design. This is a major requirement for reliable warpage prediction.

In the case of a fiber reinforced polymer, it was experimentally observed that high warpage occurs in all cases and that process conditions have little influence on shrinkage and warpage. There is no indication that the amount of warpage correlates with the formation of voids or porous zones in the molding. In accordance with the experiments, the predicted warpage is primarily sensitive to the fiber orientation state, and therefore depends on the accuracy of the fiber models. The investigations presented in Chapter 6 lead to the conclusion that recent fiber models may provide inaccurate results in thick walls. In the present case, warpage originates at the thick corners of the part, and as expected, the quality of the warpage predictions is indeed compromised. Therefore, it can be concluded that warpage predictions will lack accuracy if warpage originates from a part geometry with thick walls and a 3D flow pattern.

6. Fiber orientation in a complex, chunky part[1]

Investigations into the prediction and validation of fiber orientation distribution (FOD) are commonly based on a simple geometry, such as a center-gated disk or an end-gated rectangular plaque. This makes it possible to conveniently observe the influence of shear and stretching flow on the resulting FOD. Model constants, such as the coefficient of fiber interaction C_I, are determined by means of measurements taken from moldings with simple geometry. Hardly any studies show the predicted and measured fiber orientation in moldings with a complex and thick-walled geometry. In this case, a 3D flow pattern, and, therefore, a complex superposition of shear and extensional flow occurs. The ability of recent fiber models to predict the fiber orientation in a complex 3D geometry was not adequately demonstrated so far. The accurate prediction of the FOD is a basic requirement for the precise calculation of shrinkage and warpage. One attempt to predict the fiber orientation in 3D features was made by VerWeyst *et al.* [138]. Due to a lack of computing power, only some features of the whole cavity were meshed in 3D. A standard mold filling simulation based on the Hele-Shaw approximation [1] was used to obtain the boundary conditions at the 3D zones. The predictions were then compared to measurements and showed qualitative agreement.

This case study goes one step further and investigates the FOD in the chunky part presented in Section 5.1, both numerically and experimentally. The FOD was measured at different locations using a μCT device and compared to predictions using Autodesk Moldflow Insight 2014. The aim of this study was to validate the fiber prediction capabilities of the standard Folger-Tucker- (FT) and the Reduced Strain Closure model (RSC) on a chunky part with 3D flow regimes. Furthermore, the interaction coefficient C_I and the reduced strain closure factor κ is varied and the results are compared to the experimental data.

---

[1]Parts of this chapter were published in International Polymer Processing under the title "Prediction and Validation of Short Fiber Orientation in a Complex Injection Molded Part with Chunky Geometry" [139]

143

6.1. Measurements

The geometry of the investigated part and its overall dimensions are shown in Fig. 5.1. The part is gated in a region with rather thin walls of around 1.5 mm which are connected to regions with thick walls of up to 12 mm.

For the measurement of FOD and fiber length distribution (FLD), two samples were cut out of the moldings at the locations shown in Fig. 6.1. Both samples had rectangular cross sections with a side length of 5 mm and a height according to the local wall thickness. The shape and dimensions of the samples are shown in Fig. 6.2. The relatively small dimensions of these samples were necessary in order to obtain the desired spatial resolution of the CT data. The first specimen was taken a short distance downstream from the gate, where the wall thickness increases and a 3D flow pattern exists. During the packing stage, the polymer flows through this area until the gate is sealed. Any changes in packing history or gate dimension, and its influence on the fiber orientation, will be observable in this sample. Initial scans of the whole part indicated a fiber-free layer on the inside of the two arms. Thus, the second specimen was taken from a location far downstream from the gate, where the fiber-free layer was observed. Cases A and D, as described in Section 5.1.4, were
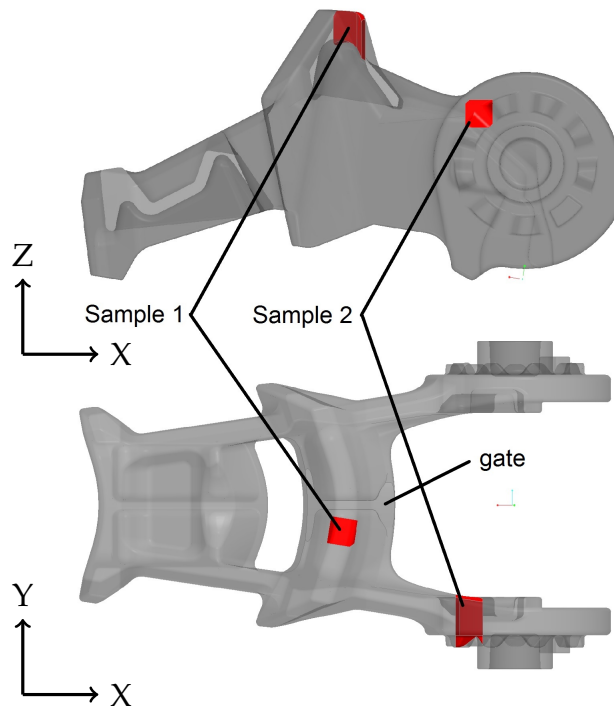
Figure 6.1.: Location of Sample 1 near the gate and Sample 2 far from the gate. [139]

chosen to investigate the influence of packing efficiency and injection velocity on
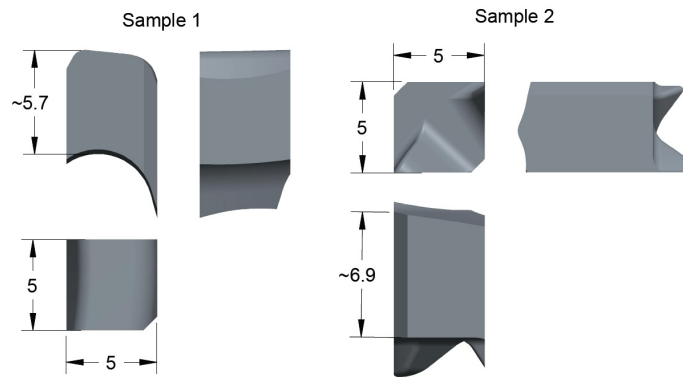
Figure 6.2.: Dimensions of Samples 1 and 2. [139]

FOD and FLD. In Case D, the diameter of the gate was increased from 1.2 mm to 1.8 mm. The injection velocity profile was changed and the injection time prolonged (refer to Fig. 5.3 and 5.4). Moreover, the constant packing pressure of Case A was replaced by a packing profile (see 5.1.2). The process settings used can be found in Section 5.2. The samples shown in Fig. 6.1 were taken from moldings produced with these settings.

X-ray computed tomography (see Section 3.2) was used to determine FOD and FLD at 2 locations on the molding. For both cases (FOD and FLD), a minimal fiber length of 30 μm was defined. Smaller structures are no longer thought of as fibers, but rather as fragments, which do not contribute to reinforcement. Therefore, these were not considered for the quantitative analyses.
The visual comparison of fiber orientation requires an overlay of CT data with simulation results. The CT orientation data, which consists of single fiber data, was mapped onto the grid of the simulation result. This was done by registering the CT data to the CAD data, and subsequently averaging the CT tensor elements for each of the grid elements. At each grid point, around 1500 fibers were used to calculate the number-average fiber orientation tensor.

6.2. Numerical model

The numerical model is described in Section 5.1.3. All of the process settings, solver settings and boundary conditions are presented there, in addition to the material used for the molding trials and simulations. For this study, Autodesk Moldflow Insight 2014[2] was used to model the filling, packing and cooling stages of the process and to determine the fiber orientation distribution in the molding. The focus of this study is

---

[2]Synergy Build - 13293-Bin395-Ins374; Insight Build - 13274-Bin394-Ins342

the prediction of the FOD. Therefore, a number of simulations using different fiber models and settings were performed. These settings are described along with the simulation results in Section 6.3.2.

In the case of the 3D simulation, Moldflow Insight 2014 only supports a random fiber orientation as boundary condition at the injection location. The model, however, contains the hot runner nozzle and the cold runner with the narrow gate of just 1.2 and 1.8 mm, respectively. It was assumed that the orientation defined at the inlet would be "washed out" before the melt enters the cavity. Hence, the predicted fiber orientation in the cavity would not be affected by the inlet boundary condition. Moldflow Insight 2016 allows the definition of arbitrary fiber orientations at the injection location, even for 3D models. Subsequent simulations with the 2016 release were performed by the author. It was found that a correct fiber orientation inlet condition is only of relevance if the runner system is either not modeled or very short. Therefore, the assumption stated above is appropriate.

6.3. Results

The components of the orientation tensor are dependent on the coordinate frame. In a part with complex geometry, however, the presentation of single components does not allow a physically meaningful interpretation of the tensor values. Hence, the visualization of the tensor in terms of its eigenvalues and the corresponding eigenvectors is preferred. Fig. 6.3 shows a general ellipsoid spanned by the three eigenvectors. The longest eigenvector points in the direction of the main fiber orientation, while its
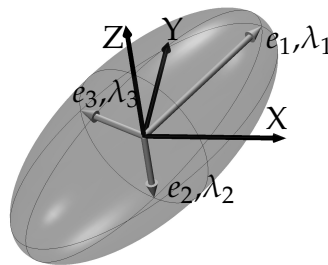
Figure 6.3.: 3D ellipsoid spanned by the eigenvectors of the orientation tensor. [139]

eigenvalue indicates the probability of finding a fiber orientated in this direction. If all the fibers are perfectly aligned, the ellipsoid degenerates to a line. A completely random orientation would generate a sphere, and a random orientation in a plane would result in a disk.

Fig. 6.4 shows a slice of the CT data and the computed fiber orientation tensor at the same location. Both figures show a skin-core structure with highly oriented fibers in

(a) Sample 1: Sliced at Z-3.5 mm from top.

(b) CT image at the location shown in (a).

(c) Orientation tensor calculated from the CT data. Color coded is the length of the first eigenvector.
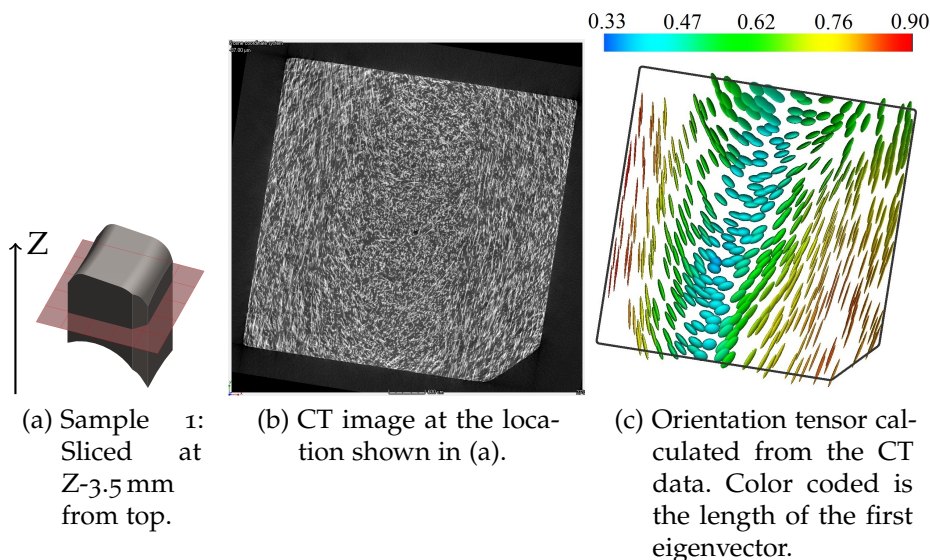
Figure 6.4.: With the single fiber data extracted form the CT data (b), the orientation tensor can be computed and visualized as ellipsoides (c). [139]

the outer layers and a region with low orientation in the core of the sample. However, the visualization of the orientation tensor as ellipsoid allows the easy interpretation of the fiber orientation state in direction and magnitude at a glance. This visualization, moreover, enables the direct comparison to the predicted FOD.

6.3.1. Influence of the processing conditions on the fiber orientation

Due to the length of Sample 2 (Fig. 6.1) and the required resolution of the CT data, not the whole volume of Sample 2 was scanned. Areas within the boundary of Sample 2 where no tensor is drawn were outside of the scanned volume. Fig. 6.5 shows the measured fiber orientation at different locations of Sample 1 (Fig. 6.1) for Case A and D. In both cases, the main orientation direction and the magnitude of the orientation is basically the same. The size of the core zone with the low fiber orientation is smaller in Case D. This is caused by the prolonged gate seal time, and the extended shear flow during the packing stage, which is a result thereof. The lower injection rate used in case two does also contribute to the higher thickness of the highly oriented skin layer. At Z-2.5 mm the principal orientation in the core layer is still pointing in flow direction while the fibers tend to align perpendicular to the flow direction at Z-3.5 mm. This skin-core structure is typically observed in moldings with high wall thickness and was shown in several studies although based on parts with simple geometry [44, 45, 49, 51].
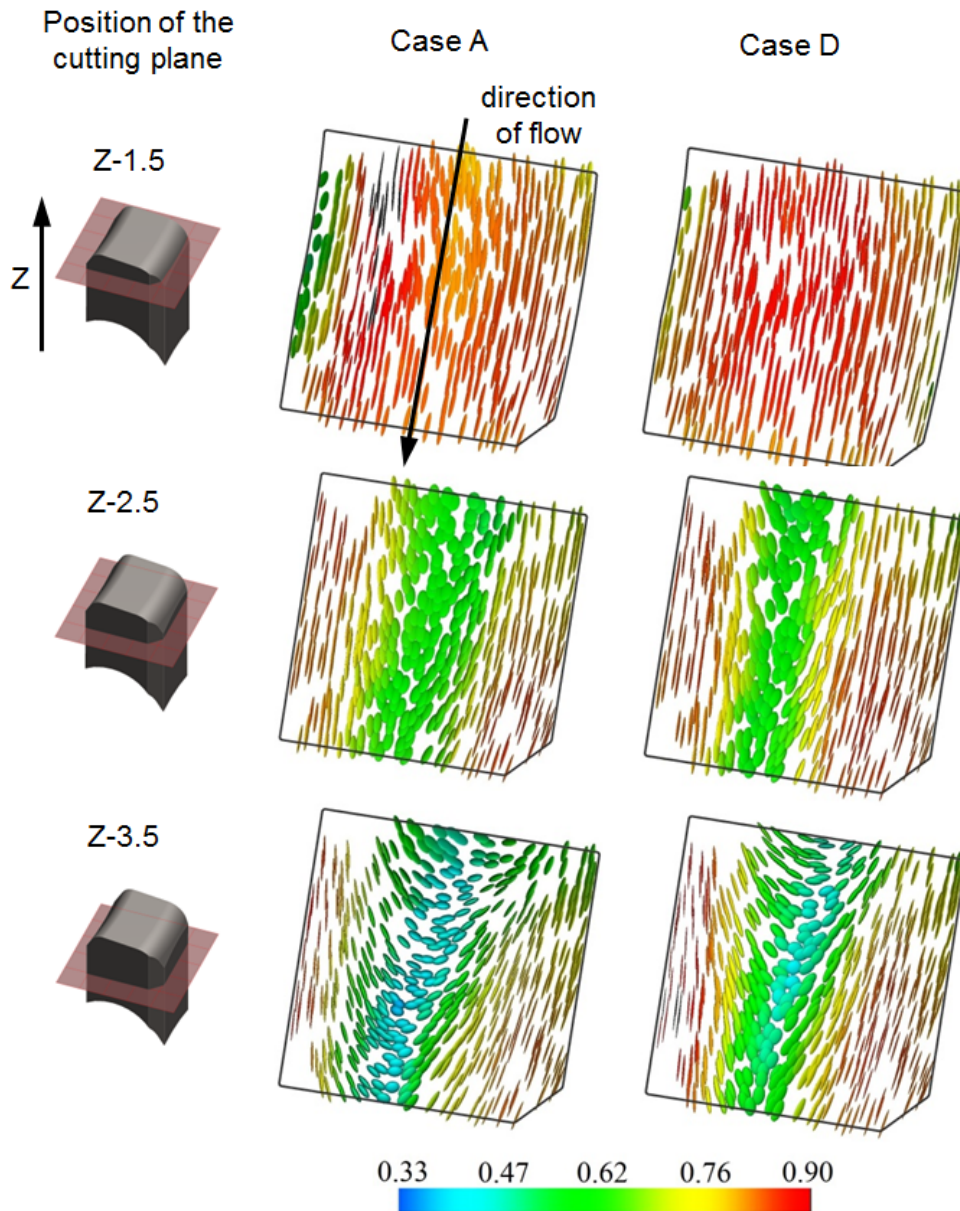
Figure 6.5.: Comparison of the measured fiber orientation for the two different process conditions at different locations of Sample 1. Color coded is the length of the first eigenvector of the orientation tensor. [139]

The fiber orientation in Sample 2, which was taken far downstream of the gate, shows a very distinct skin-core structure (Fig. 6.6). A rather thin layer of higher oriented fibers parallel to the flow direction at the wall, and a thick core where the fibers are predominately oriented perpendicular to the flow direction were both found. The fiber orientation in the core is caused by the divergent flow from the gate region to the thick walled sections of the cavity. Again, the core structure is somewhat smaller in Case D, with the larger runner and gate diameter. In proportion to the local wall thickness, however, the core structure is very large in both cases. A further alignment of the fibers during the packing stage through ongoing shear flow is not possible near the end of the cavity. Therefore, the effect of the divergent flow on the fiber orientation dominates in this section of the molding.

In addition to the fiber orientation in the molded samples, the CT scans also revealed zones with a sharply reduced fiber concentration in the first case. Fig. 6.7 shows a slice through the CT data at the inner wall of Sample 2 for both cases. In Case A, there is a small layer with a thickness in the order of 0.2 mm where the fiber concentration is close to zero. With the lower injection rate and larger gate diameter, as well as the shear rate which is reduced as an effect thereof, this anomaly vanished. CT-scans of the whole molding indicated that the fiber-free layer extends from the gate to the position of Sample 2 and a bit further. The presence of fiber-free layers was also observed in the work of Darlington & Smith [41]. It was assumed that the formation of the fiber-free layer was shear dependent. This seems to be the case in the present study as well.

With the single fiber data obtained by the CT measurements, it is straight forward to calculate the FLD at the specified volumes. The FLD was evaluated for Case A and D in both samples in order to investigate the influence of shear rate and shear stress on fiber breakage during processing. Fig. 6.8a shows the measured FLD in Sample 1 for both Cases. The weight-average fiber length (according to ISO22314 [140]) is clearly higher in Case D, where shear rate and stress were lower, due to the decreased injection rate and the larger gate diameter. A much higher difference was found in Sample 2, where most of the material was introduced in the filling phase and therefore experienced high shear rates (Fig. 6.8b). During the packing stage, a through flow of the areas near the gate takes place. Therefore, a larger amount of the material found in Sample 1 was introduced at the end of the filling stage and during the packing stage where the shear rates were low.

The absolute fiber length may lack accuracy since a large number of the fibers were cut at the boundaries of the sample, especially in regions with high alignment. The samples have the same geometry and were taken at the same location, which implies the same boundary conditions. Thus, the FLD obtained for the two cases should be at least qualitatively comparable.
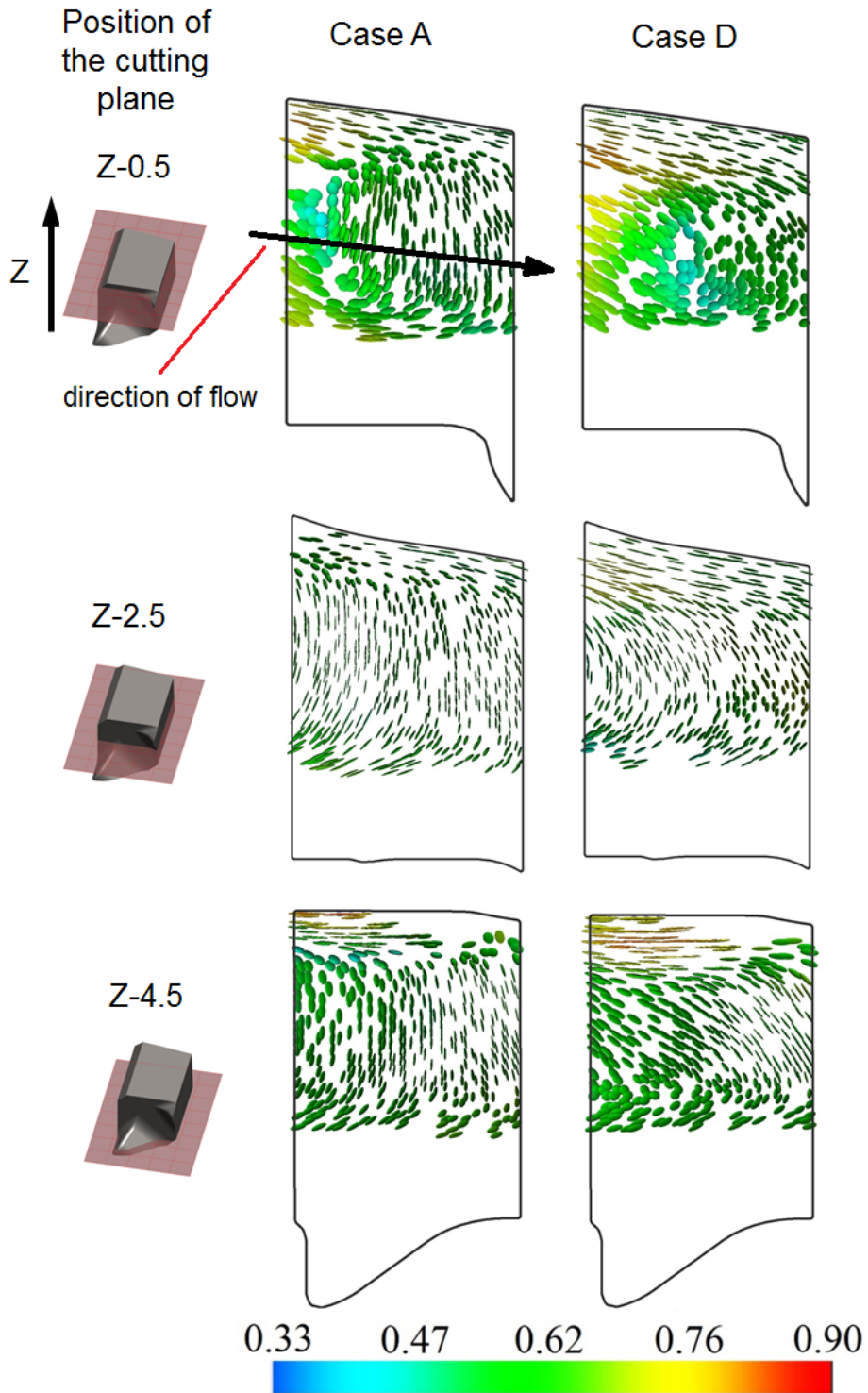
Figure 6.6.: Comparison of the measured fiber orientation for the two different process conditions at different locations of Sample 2. Color coded is the length of the first eigenvector of the orientation tensor. [139]

(a) Location of the slice at Sample 2.   (b) Case A   (c) Case D
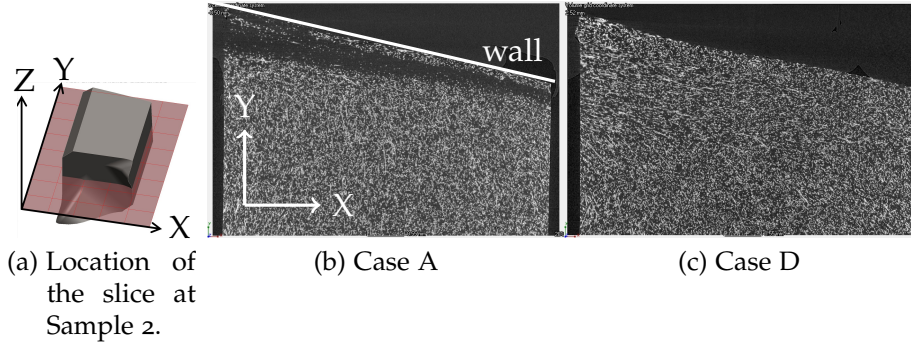
Figure 6.7.: CT slice at Sample 2 showing a layer with very low fiber concentration at the wall in Case A (a). With the larger gate diameter and the lower injection rate used in Case D, the fiber concentration becomes homogenous (b). [139]

(a) Sample 1. Case A: weight-average fiber length = 138 μm, number-average fiber length = 91 μm. Case D: weight-average fiber length = 152 μm, number-average fiber length = 99 μm. [139]

(b) Sample 2. Case A: weight-average fiber length = 120 μm, number-average fiber length = 83 μm. Case D: weight-average fiber length = 154 μm, number-average fiber length = 103 μm. [139]
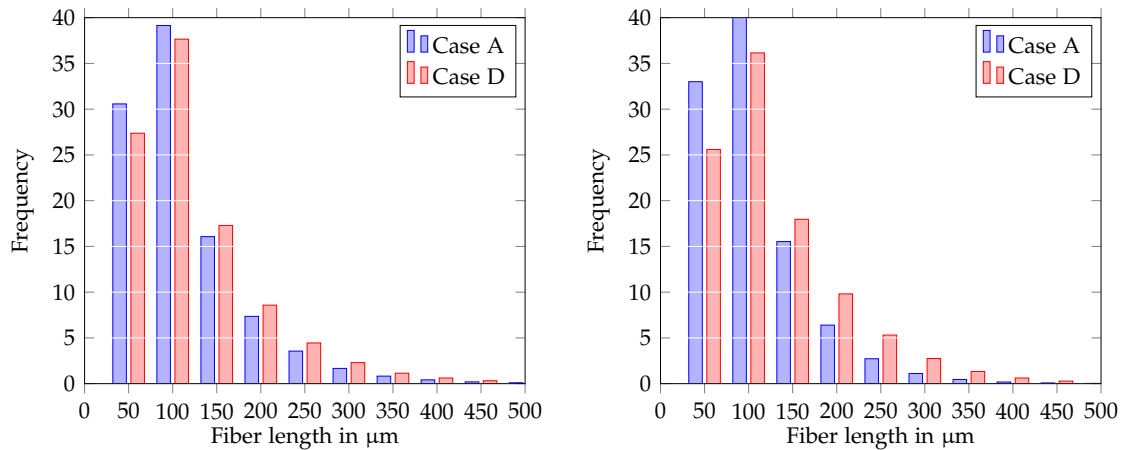
Figure 6.8.: Measured fiber length distribution in Sample 1 and 2 obtained from Cases A and D.

6.3.2. Results of the fiber orientation prediction

The quality of the fiber orientation prediction is quite similar for both cases. Therefore, only the results for Case D are shown. A large number of simulations with different combinations of orientation models, closure approximations and settings of the model parameters were performed to match the experimentally-obtained FOD. Only the settings which were the best fit with the experimental FOD data are presented here in order to summarize the findings. Fig. 6.9 shows the measured and the predicted fiber orientation tensor, visualized as ellipsoids at different locations of Sample 1. The results of Sample 2 are given in Fig. 6.10.

Evaluating equation (2.18) for the actual material with a fiber volume fraction of 23.35 % and an aspect ratio of the fibers of 20 gives a C_I of 0.00064. Equation (2.19), on the other hand, gives 0.01946. Moldflows' auto-calculated value is 0.0162 for the actual material, and this value works well with the Folgar-Tucker model and the orthotropic fitted closure approximation (ORF). However, in combination with the RSC model, the degree of fiber alignment is significantly underestimated. A good correlation was achieved with a C_I of 0.0005, a reduced strain closure factor κ of 0.05, and the orthotropic fitted closure approximation for low C_I (ORL). Similar RSC model behavior was reported by Jerabek *et al.* [114]. They performed investigations on the fiber orientation in a dumbbell shaped multipurpose specimen.

Both fiber orientation models predict the principal direction of the fiber orientation in the shear layers with reasonable accuracy. The FT model predicts the core layer to some extent, but the degree of alignment is too high. In Sample 2, even the orientation in the shear layer is significantly overestimated. The RSC model gives a better estimation of the size of the core layer, and also gives better values of the orientation in the shear layers, although the size of the core zone is still underpredicted. Both models fail to predict the principal direction of the fiber orientation in the core layer, where the fibers are aligned perpendicular to the flow direction. This is especially true in Sample 2, where the fiber models predict a principal direction parallel to flow, although with a reduced degree of orientation. Different combinations of the reduced strain closure factor and the fiber interaction coefficient C_I do not lead to further improvements in the prediction accuracy of the fiber orientation of the core zone.

6.3.3. Discussion

The fiber orientation results obtained with the F-T and the RSC model are in qualitative agreement with the measured data. The RSC model outperforms the F-T model in predicting the degree of orientation in the shell layers, as well as the thickness of the core zone. This finding is consistent with the results of previously published studies
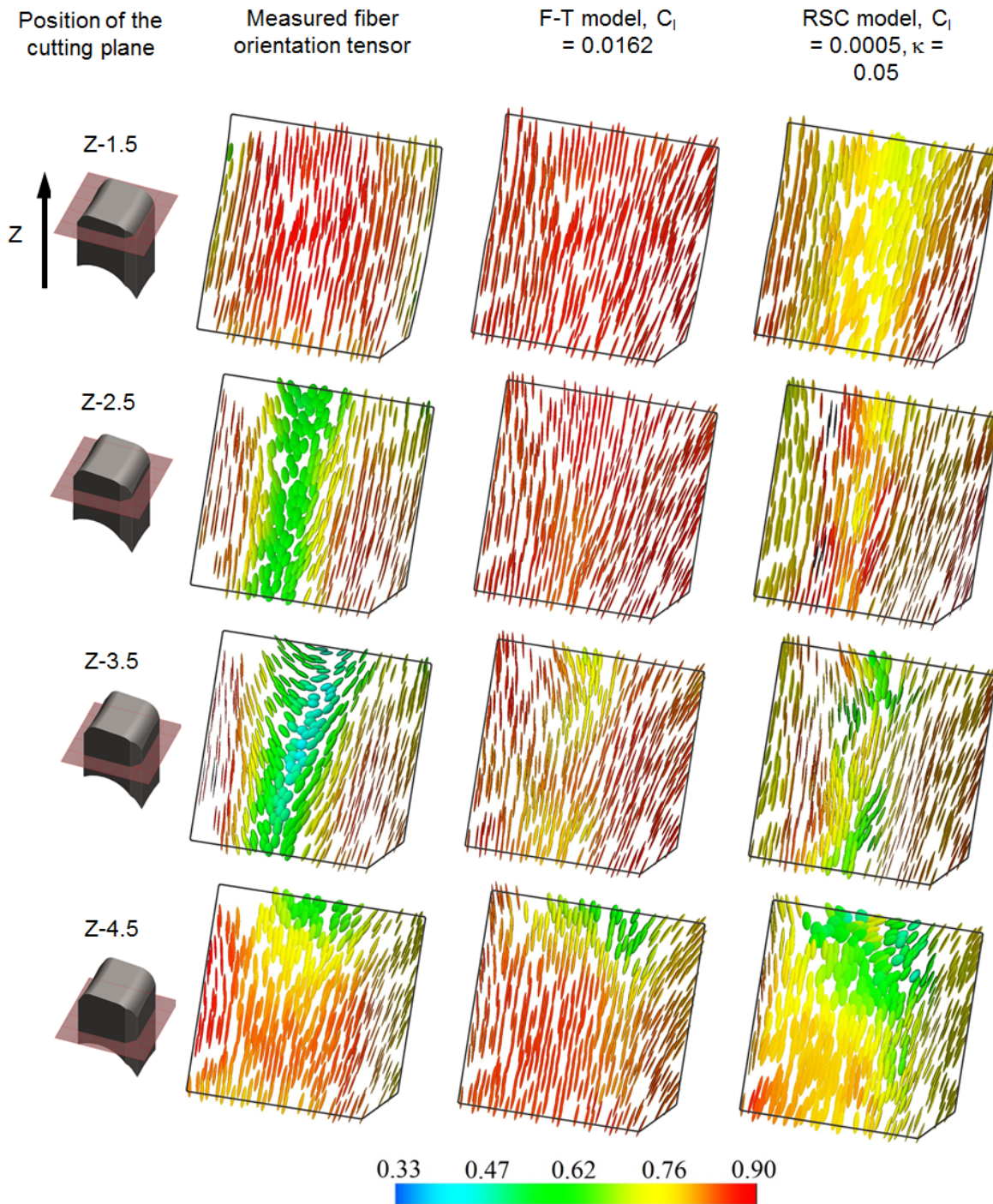
Figure 6.9.: Comparison of measured and predicted fiber orientation at different locations of Sample 1 for Case D. [139]

| Position of the cutting plane | Measured fiber orientation tensor | F-T model, C_I = 0.0162 | RSC model, C_I = 0.0005, κ = 0.05 |

Z-0.5

Z

Z-2.5

Z-4.5

0.33   0.47   0.62   0.76   0.90
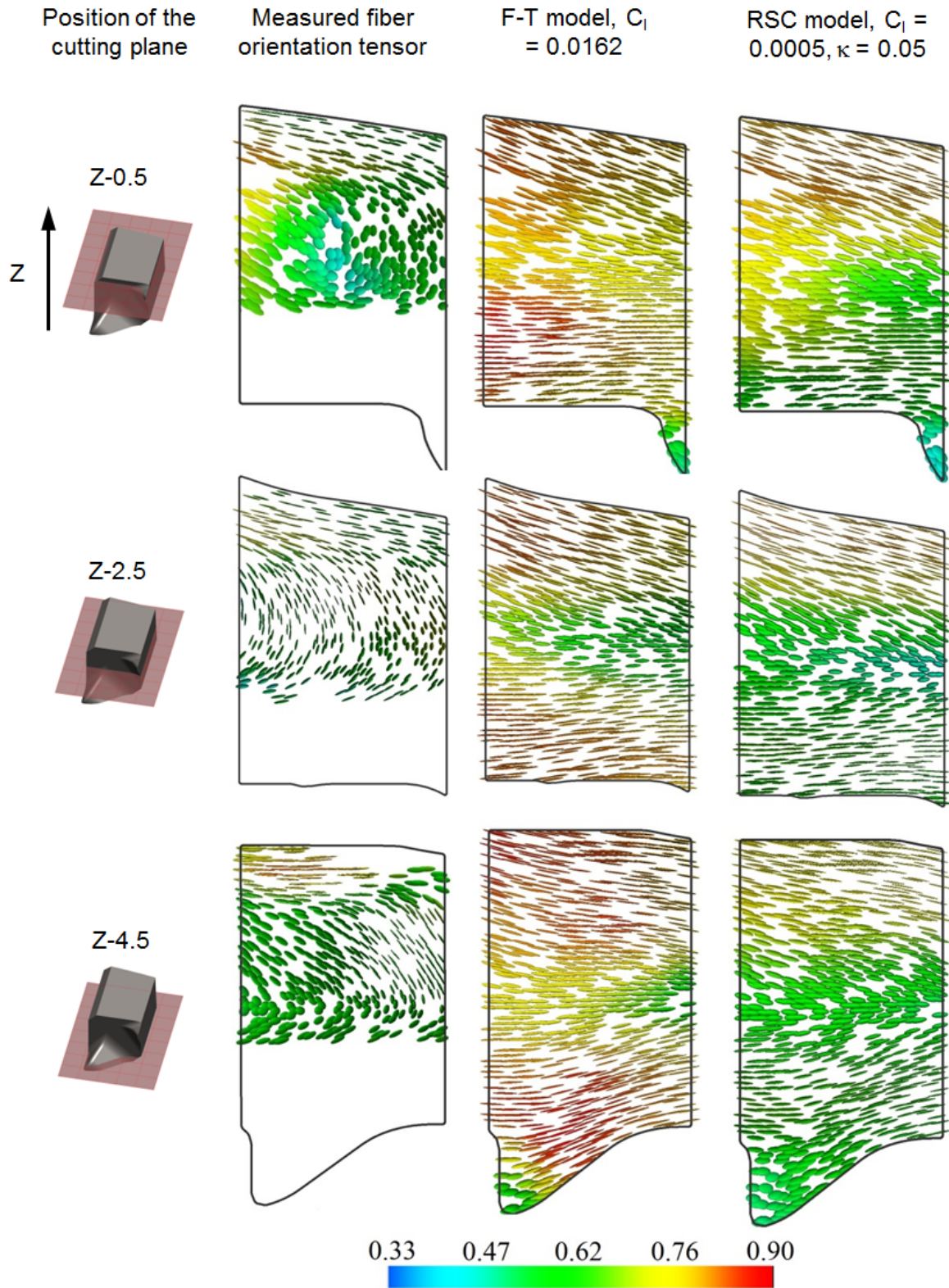
Figure 6.10.: Comparison of measured and predicted fiber orientation at different locations of Sample 2 for Case D. [139]

[50, 51, 63]. The F-T model enables a practicable estimation of the fiber orientation distribution in the molding by using only the fiber interaction coefficient C_I. This model parameter could be calculated automatically based on aspect ratio and the volume fraction of the filler. The RSC model, on the other hand, requires an additional model constant which cannot be calculated in advance and must be assumed. Due to the interaction of both model constants, their determination is no longer straight forward. Several studies on parts with simple geometry and rather thin walls have shown that it is possible to predict the fiber orientation with reasonable accuracy. ([49, 63]). However, the results in the present case indicate that there is still room for improvement when considering chunky parts with complex geometry and thick walls. Obviously the effect of the extensional flow on the fiber orientation is underestimated by state-of-the-art fiber models and software, while the effect of shear on the fiber orientation is captured very well.

The fiber orientation plays an important role in the calculation of the mechanical properties of the composite. It therefore affects shrinkage and warpage results as well as the accuracy of subsequent structural FEM simulations. The case studies presented in Chapter 3 (and many others not published) indicate that the fiber orientation prediction capability of the RSC model is (mostly) sufficient in order to determine the warpage of chunky parts with reasonable accuracy. However, the accuracy of the warpage result may be severely impaired by the quality of the FOD if the deformation originates from a thick section of the part. Moreover, the calculation of the mechanical properties with the predicted FOD would overpredict the Young's modulus in flow direction at the core zone. This may affect the accuracy of structural FEM simulations considering the anisotropy of the composite.

The question arises of whether the poor accuracy of the orientation prediction in the core zone is caused by flaws in the numerical model, the flow model, the fiber model, or within their software implementation. A number of numerical experiments were performed to investigate where the lack of accuracy may have originated. A mesh convergence study, as described in Section 3.3.5, did not lead to a significantly different fiber orientation solution. The same is true for a finer discretization in time. This was tested by enforcing smaller time steps by setting the parameter "Maximum % volume to fill per time step" to 0.5 (default = 4) and the "convergence tolerance factor" to 0.1 (default = 1). There was no significant improvement in the accuracy of the fiber orientation.

Rheological model

The Cross WLF model (see Section 2.1.4) was used in this study to model the viscosity of the melt. It is assumed that the rheological behavior of the melt is not altered

by the orientation of the fibers. This way, flow kinematics and the fiber orientation problem are decoupled and calculated in a sequential manner.

The question arises as to whether a coupled calculation could significantly improve the accuracy of the FOD prediction. Mazahir *et al.* [56] found that the effect of coupling on the fiber orientation was negligible in their case of a thin center-gated disk. This must not necessarily be true for chunky moldings with thick walls. In any case, this procedure would introduce additional model parameters which would have to be determined experimentally. Furthermore, it would lead to a drastic increase in computational effort. Moldflow does not yet support an option to model this interaction between fiber orientation and rheology.

From these observations, it can be concluded that the error arises either from the decoupled rheological model or the fiber orientation model itself.

6.4. Concluding remarks

In the present study, the fiber orientation distribution in a complex, chunky part was determined experimentally and compared to simulation results. The aim of this study was to show the performance of state-of-the-art fiber models and software in predicting the fiber orientation in a complex part with no thin-shell geometry.

The measured fiber orientation shows a small core region in the sample near the gate, and a large core region in the sample far from the gate. In the core region, the fibers are oriented perpendicular to the flow direction. The results obtained with both fiber models are in qualitative agreement with the measured orientation. Prediction of the fiber orientation in the shell layers by the RSC model is in good quantitative agreement with the measurements. The F-T model, on the other hand, overestimates the orientation in the shell layers far off the gate. Both models fail to predict the true orientation in the core zone correctly. Although they show a reduced degree of orientation in the core region, the principal direction of the fibers is still predicted to be in flow direction. The RSC model outperforms the F-T model in estimating the size of the core zone. It was found that the value of the fiber interaction coefficient C_I strongly depends on the selected fiber model. A C_I which gives reasonable agreement with the F-T model leads to a significant underprediction of the fiber orientation when using the RSC model.

Parts with chunky geometry and/or thick walls will always show a thick core region where the fibers are oriented perpendicular to the flow direction. The prediction of the thickness of the core region as well as the fiber orientation in the core region is difficult, and obviously both the F-T and the RSC model underestimate the effect of extensional flow on the fiber orientation. Several potential sources of error were

considered and investigated in this study. From the observations made in this study, it can be concluded that the error arises either from the decoupled rheological model or the fiber model itself. This study shows that the ability of state-of-the-art fiber models and software to predict the fiber orientation in a molding with thick walls is limited. This drawback could be an issue when the structural performance of the molding is investigated in a subsequent FEM analysis. It also presents a potential source of error when the shrinkage and warpage of a part with thick walls are predicted.

7. Weld lines and their effect on strength

7.1. Introduction

When a flow front is parted by an obstacle in the cavity, such as a core pin, the separated melt fronts will collide at the back of the obstacle. The interface where the two melt fronts merge again is called a weld or meld line, depending on the angle at which the fronts meet. In what follows, weld and meld lines will be treated as the same thing and no distinction will be made between them.

As its name implies, a weld line can be observed on the part surface as a visible line. This is especially the case on parts with a high gloss surface finish. In such cases, weld lines must be avoided, or if this is not possible, minimized by special processes such as rapid heating and cooling. However, weld lines do not only cause aesthetic issues. The mechanical strength of the molded part at the weld line is also adversely affected. This is mainly a result of two different effects. Weld lines always show a notch at the surface with a depth of some μm. Therefore, in case of a mechanical load, they act as locations with stress concentration. Additionally, the fibers at the weld line tend to align perpendicular to the flow direction. This thesis deals with parts for mechanically demanding applications. Aesthetic issues are not considered in this study.

From the mechanical point of view, it is not sufficient to just look at the surface, and the term "weld line" is therefore somewhat misleading. For strength considerations, one must look at the whole interface of the two merging melt fronts as well as what happens to that interface after it has formed. A term like "weld interface" or simply "weld face" is, in fact, more appropriate and is therefore preferred in this context.

Quite a number of research studies have been conducted to investigate how the strength of the weld line is affected by geometry, filler, and process conditions. Meddad & Fisa [141] performed molding trials with polystyrene, high impact polystyrene and polypropylene. They found that melt and mold temperature have the highest impact on the tensile properties of the weld line. Injection velocity and packing pressure had no effect. The first investigations into the weld line properties of fiber reinforced

polycarbonate were done by Hamada *et al.* [142], using a multi cavity mold. They found that the strength properties of the weld line are affected by re-alignment of the fibers when back flow occurs in the packing stage. Vaxman *et al.* [143] performed investigations into the tensile properties of samples with and without weld lines. They used unfilled and filled Noryl and polypropylene, and found that weld lines have little impact on tensile strength in the case of an unfilled polymer, but cause a significant reduction in tensile strength when a fiber filled material is considered. The reason for this is the alignment of the fibers at the weld line, which is mainly parallel to the weld face. A similar investigation, using PA6.6, was carried out by Meddad & Fisa [141], which also led to similar conclusions. Additional research on this topic has been conducted by Selden [144] and Kim *et al.* [145]. The work of Tomari *et al.* [146] sought methods to improve the strength of weld lines in parts molded from fiber reinforced polymers. Wu & Liang [147] expanded the problem of weld line strength to microinjection molding. Janko *et al.* [148] proposed and demonstrated a mold-based approach to moving the weld line at the time it is formed in order to improve fiber orientation. Compared to specimens with a standard weld line, the new method yielded a large rise in flexural strength and improved tensile properties.

The actual strength of the part at the weld line is strongly affected by the flow after the two melt fronts have met. If the weld face forms when the cavity is almost filled, then little or no material will flow through the weld face. The weld face is neither convected downstream the cavity, nor is it deformed by a secondary flow during the packing phase. In this study, such a type of weld face will be referred to as "sharp". When the weld face forms close to the gate, there is a high likelihood that the weld face will be instantly conveyed away with the incoming polymer flow. The weld face is "washed-out". A third possibility is that the weld face is not completely washed-out, but deformed to some extent.

The numerical simulation not only enables the prediction of weld lines as indicators of aesthetic surface defects. It is also possible to track the position of the weld face after its formation, which is essential in order to be able to draw conclusions about the mechanical strength. Fig. 7.1 shows a good example of a sharp (Fig. 7.1a) and a washed-out weld face (Fig. 7.1a). It shows the shape of the melt front when it flows around the core pin. The green volume is the already filled volume when gated from the left side (Fig. 7.1a) and the right side (Fig. 7.1b), respectively. From this plot alone, it is difficult to draw conclusions about the shape and characteristics of the weld face. Therefore, it is worthwhile to take a deeper look at this topic: Fig. 7.2 shows an overlay plot of the predicted shape of the weld face (depicted in green) and the flow front (in blue) at the moment just before they merge. The plot shows the shape of the weld face right after its formation. In other words, it represents the interface where the flow fronts meet. Depending on the processed material grade, the surface finish of the mold, and the processing conditions used, the shown weld face would be visible as a thin line on the surface of the molded part. This plot provides no information

about what happens after the merging of the flow fronts. Depending on the flow field during the filling and packing stages, the weld face may be affected or not. In order to investigate this, the material present at the weld face (the green volume shown in Fig. 7.2) may be marked and tracked during the filling and packing stages. When material is conveyed away with the plastic flow, it ends up at some other location in the cavity. This result is shown in Fig. 7.3. The green volume depicted in this plot is the material which was originally at the weld face shown in Fig. 7.2. This plot indeed provides useful information about the characteristics, and therefore, the mechanical properties of the weld face. When the part is gated on the left side, the weld face behind the core pin is almost completely removed by the in-rushing polymer flow (Fig. 7.1a). The weld face is washed-out and will have little effect on the mechanical strength of the moldings. In the second case, the part is gated on the right side, which was found to be much better with regard to fiber orientation, warpage and mold layout (Fig. 7.1a). However, a sharp weld face forms at the core pin on the left side, and the molded parts may break under impact load during service. This is one case of many where weld lines and the understanding of their influence on the mechanical properties of the part are of great importance.
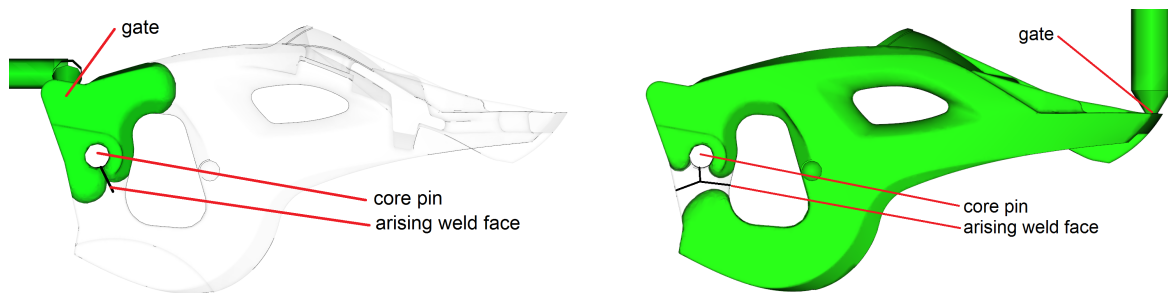
(a) Part gated from the left side. The weld face at the core pin forms at the beginning of the filling stage.

(b) Part gated from the rigth side. The weld face forms at the very end of the filling stage.

Figure 7.1.: Formation of a weld face at a core pin for two different gate locations.

The question thus arises as to how weld faces affect the mechanical performance of the molded part? Does the wash-out of the weld face improve the strength properties at that location? Moreover, how valuable is the result shown in Fig. 7.3 to evaluate the relevance of a weld face?

A two-cavity mold for dumbbell shaped specimens was built to answer these questions. One cavity is end-gated, while the other is gated from both sides. Hence, every shot, a flawless specimen is produced, along with one having a weld face in the center. Additionally, the mold design allows the distortion of the weld face. Hence, a sharp, distorted, or even washed-out weld face is obtained. Tensile tests were performed
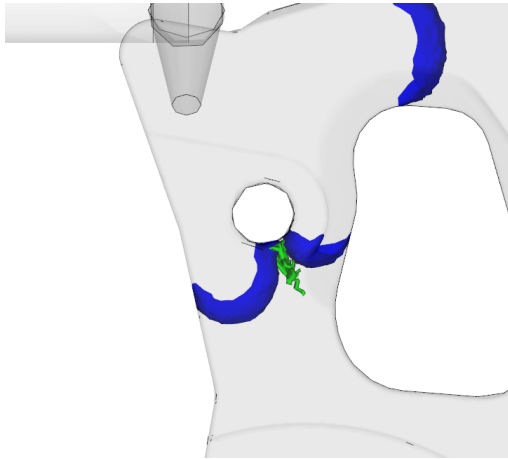
(a) Part gated from the left side.

(b) Part gated from the rigth side.

Figure 7.2.: The figure shows the predicted shape of the weld face at the time of its formation (green face) and the approaching flow front (blue face).
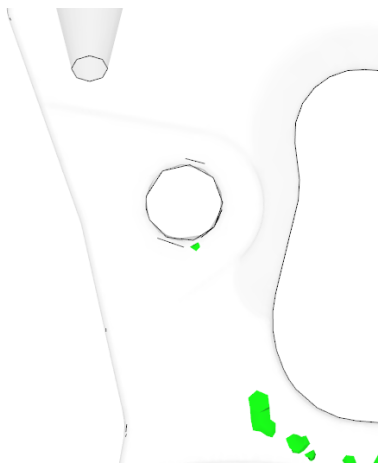
(a) Part gated from the left side. Almost the whole weld face was removed by the ongoing flow during the filling stage.

(b) Part gated from the right side. A sharp T-shaped weld face is preserved and fragments of other weld faces are present too.

Figure 7.3.: The figure shows the predicted shape of the weld face at the time of ejection.

on the specimens to investigate their strength properties for two different polymer grades and various process settings.

7.2. Test specimen and mold layout

The mold layout and the dimensions of the specimens are shown in Fig. 7.4. The mold has two cavities which are fed by a cold runner. One specimen is gated from one side and the other from both sides. Specimens with 4, 6 and 8 mm thickness can be produced with this mold.
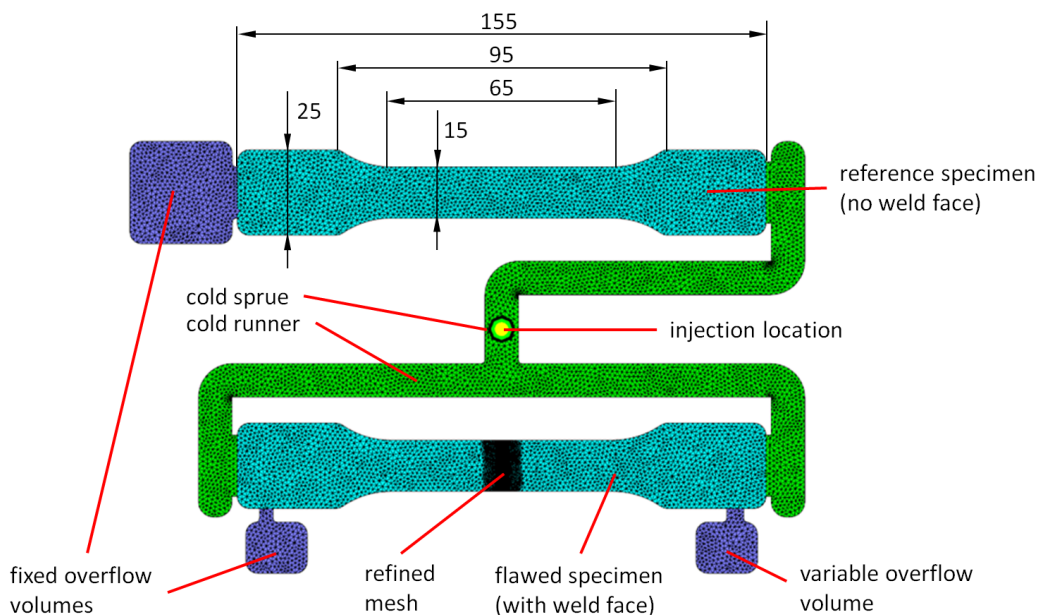
Figure 7.4.: Setup with small overflow volume causing a sharp weld face in the middle of the specimen. Dimensions are given in mm.

Three overflow volumes were placed at different locations, while the size of one volume could be changed. One overflow volume was placed at the end of the single gated specimen to prolong the shear flow through the cavity, and thereby to achieve a higher level of fiber orientation. The other two overflow volumes enable control of the weld face in the middle of the specimen. In the symmetrical case, both volumes have the same size and the weld surface is sharp. When a larger volume is chosen on one side, the weld face still forms in the middle of the specimen, but is then deformed towards the larger volume (Fig. 7.5a). With an even larger volume on one side, the weld face gets severely distorted Fig. 7.5b.

(a) Medium sized overflow volume   (b) Large overflow volume
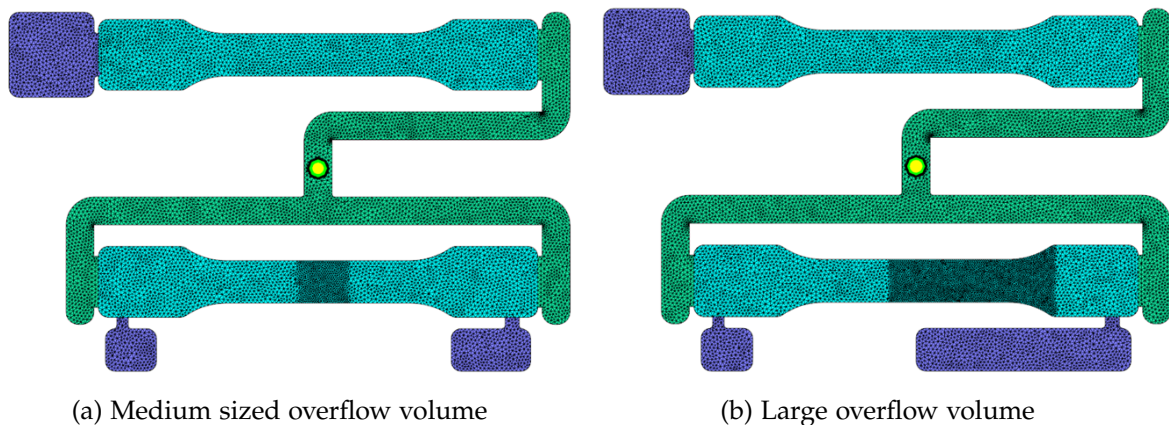
Figure 7.5.: Variants with medium and large overflow volumes to create distorted weld faces.

The sizes and locations of the overflow volumes were determined by means of numerical simulation. This enabled the prediction of the final shape of the weld face (sharp, deformed or washed-out), and supports the experimental part of this study. The final numerical models and the obtained results are therefore briefly presented.

7.2.1. Numerical model

Autodesk Moldflow Release 2016[1] was used for this study. The numerical models featuring both cavities, the cold runner and the overflow volumes, are shown in Fig. 7.4 and 7.5. Only the version with 8 mm thickness was modeled. The aim of the model is the prediction of the weld face, its movement during the filling and packing stages as well as the fiber orientation at its location. The cooling system of the mold is not important for the accuracy of these result and was therefore not considered. The geometry of the part allows the application of a midplane or dual domain analysis (see Section 2.1.1). Despite this, a 3D simulation was performed in order to obtain 3D information about the weld face and the fiber orientation.

Material data

The material data used has little influence on the filling pattern when parts with thick walls are molded. Therefore, DuPont Delrin 127UV (POM) was used to predict the filling pattern and to adjust the location and size of the overflow volumes. Additionally, simulations using UBE Nylon 1015gc9 (PA6 GF45) were performed to

---

[1]Synergy build - 20150506.1305-C760L87; Insight build - 20150506.1305-C760L80

investigate the fiber orientation near the weld face. The relevant material properties data can be found in A.5.

Process settings and boundary conditions

The process settings used for the simulation were estimated and selected from the optimal range for each polymer grade. They are summarized in Table 7.1

	Delrin 127UV	UBE Nylon 1015gc9
Fill + pack analysis		
Melt temperature	215°C	285°C
Mold surface temperature	90°C	70°C
Injection time	6 s	3 s
Velocity/pressure switch-over	at 98% of the volume filled	
Packing pressure	50 MPa	50 MPa
Packing time	60 s	40 s
Cooling time	10 s	10 s

Table 7.1.: Applied process settings and boundary conditions for Delrin 127UV and UBE Nylon 1015gc9.

Solver settings

The analysis sequence used was: Fill + Pack. No special adjustments were required for this study and all settings were left to default.

Mesh

The accuracy of the predicted filling pattern is only marginally dependent on the mesh density (see Section 3.3.5). For this task, a relatively rough mesh would be perfectly suitable. Since fiber orientation at the weld face was one aim of the numerical study, the mesh had to be sufficiently fine in this region. For this reason, part and runner were meshed (as usual in this thesis) with at least 12 elements across the wall thickness. Moreover, the mesh was refined at the location of the weld face. The three meshes are shown in Fig. 7.4 and 7.5. The element count was in the order of 7×10^5 and the maximum aspect ratio was below 30 in all three cases.

7.2.2. Results of the numerical simulation

The predicted shape of the weld face was similar for both materials. Therefore, only the results obtained with UBE Nylon 1015gc9 are shown. The simulations of the different configurations led to the weld face prediction shown in Fig. 7.6. As expected, a sharp weld face is present when the overflow volumes are the same size. Due to the symmetry, no flow across the weld face can occur (Fig. 7.6a). When a larger overflow volume is used on one side of the specimen, the following happens:

1. During the filling stage, the two melt fronts meet at the center of the specimen. Neither of the overflow volumes is completely filled at this time and they hold the same mass.
2. As filling continues, the smaller volume is filled first. Now there are two possible flow paths from the gate to the large overflow volume: the direct way through the cold runner and the way through the weld face. The greater volume flow takes the direct way with less resistance, and does not affect the weld face. The remaining volume flow passes through the weld face towards the larger overflow volume.
3. The same happens during the packing stage. There is still a volume flow from the gate which feeds the cavities and the overflow volumes while compensating for the shrinkage of the cooling polymer. However, the volume flow passing through the weld face is rather small and does not significantly contribute to the distortion of the weld face.

A somewhat larger overflow volume on one side causes a deformation of the weld face, as shown in Fig. 7.6b. When an even larger volume is used on one side, the flow through the weld face increases and it is washed-out, as shown in Fig. 7.6c.

The key to predicting the tensile strength of specimens that have a weld face is the prediction of the fiber orientation at the weld face. Fig. 7.7 shows the a_{11} component of the predicted fiber orientation tensor for the parts with and without a weld face. A value of 1 corresponds to 100% alignment in length direction of the specimen. Zero would mean that all fibers are oriented in a plane perpendicular to that direction. Fig. 7.7a shows the orientation prediction for the reference specimen at half the thickness. The fibers are highly oriented in flow direction (which is equal to the draw direction), even in the core.

Along with the sharp weld face (see Fig. 7.6a) comes a very low fiber orientation ín flow direction at its location (Fig. 7.7b). Hence, most of the fibers lay in the plane of the weld face. It must be noted that the predicted "sharpness" of the weld face is limited by the mesh density. The coarser the mesh, the more "blurred" the fiber orientation at the weld line becomes.

(a) Small overflow volume on both sides. A sharp weld face is obtained.

(b) Medium overflow volume on the right side: The weld face is destorted.

(c) Large overflow volume on the right side: The weld face is washed-out.

Figure 7.6.: Predicted shape of the weld face at ejection for the three different overflow volumes.

(a) reference specimen

(b) sharp weld face

(c) deformed weld face

(d) washed-out weld face
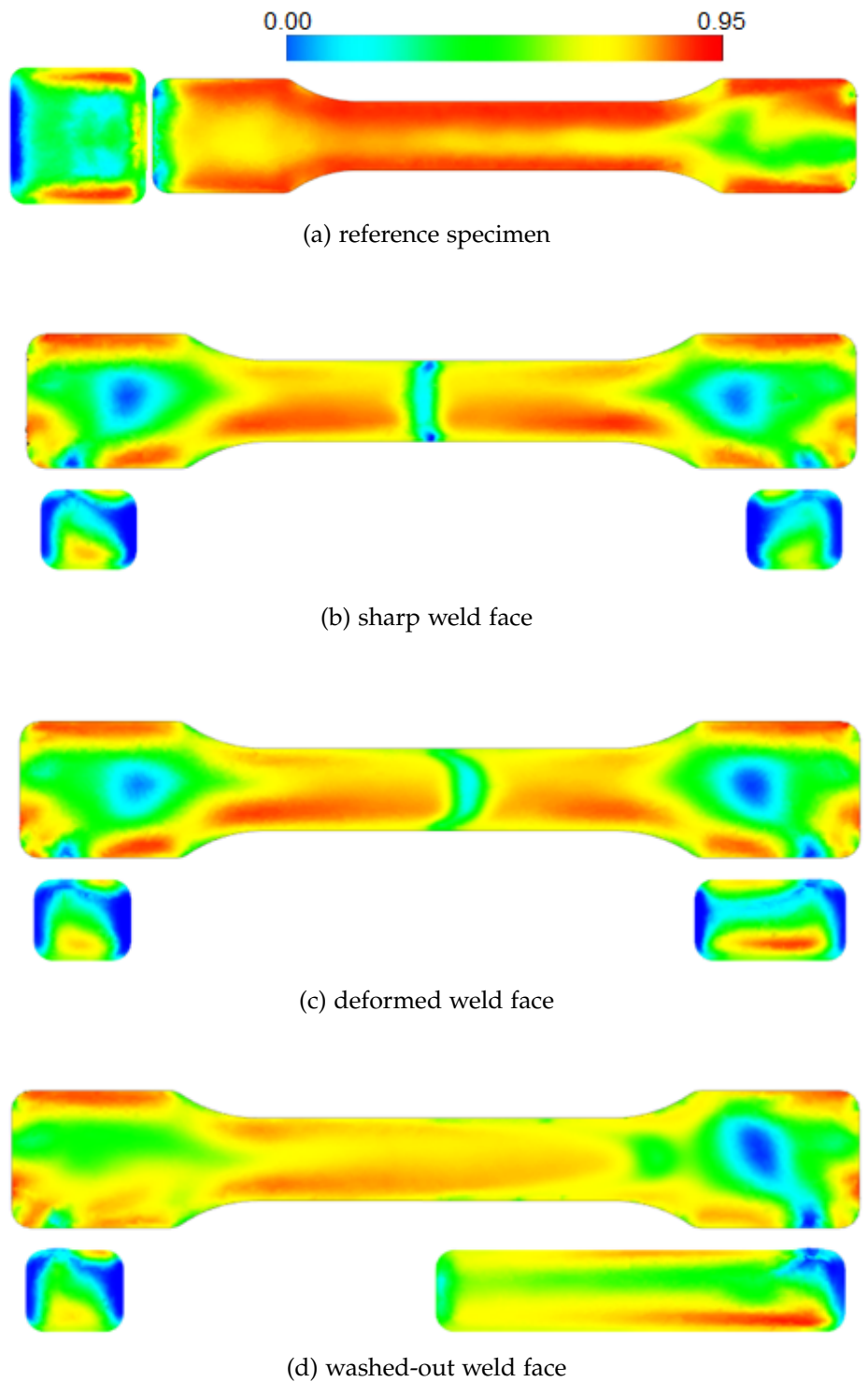
Figure 7.7.: Predicted fiber orientation at half the thickness of the 8 mm specimen molded from PA6 GF45. Color coded is the a_{11} component of the orientation tensor.

A moderate distortion of the weld face (see Fig. 7.6b) does not significantly improve the fiber alignment at the weld face (Fig. 7.7c).

The large overflow volume causes a flow through the weld face, which realigns the fibers. Hence, a high degree of alignment is achieved at the center of the specimen (7.7d). However, the overflow volume is too small to completely remove the weld face from the specimen. The a_{11} component drops from around 0.8 to 0.5 at the boundary of the weld face (the right end of the parallel section).

7.3. Experimental setup

The high viscosity POM DuPont Delrin 127UV and the PA6 G45 grade DuPont Zytel 73GF45[2] were used for the molding trials.

7.3.1. Process settings: POM

For the POM grade, a set of process conditions was chosen to investigate their influence on the strength properties of the specimens. Mold and melt temperature, packing pressure, and injection velocity were varied as summarized in Table 7.2 (p_{cav} is the peak cavity pressure measured right downstream of the gate). The packing pressure was varied in a range where no visible sink marks appeared (low pressure) and no ejection issues emerged (high pressure). The mold temperature was varied in four steps from 50°C up to 120°C. The optimal mold temperature for this material is between 80 and 100°C and the optimal melt temperature between 210°C and 220°C. Due to the small usable melt temperature range, it was varied in only two steps from 200°C to 220°C. In addition to the molding trials with the well suitable injection time of 6 s, some shots were also made with a very short and a very long injection time. The first setup was performed with different overflow volumes in order to investigate whether or not distortion of the weld face affects the strength of the specimens in the case of unfilled material. Only the specimens with 4 mm thickness were produced from this material and tested. For each experiment, at least 10 shots under stable conditions were produced.

---

[2]Although the same material grade was used initially for the simulation, this one is from another manufacturer.

exp. No.	p_{cav} in MPa	T_{mold} in °C	T_{melt} in °C	t_{inj} in s	overflow vol.
1	60	80	200	6	small
2	24	80	200	6	small
3	80	80	200	6	small
4	80	80	220	6	small
5	60	80	220	6	small
6	60	50	200	6	small
7	60	120	200	6	small
8	60	80	200	6	medium
9	60	80	200	6	large
10	60	80	200	1.6	small
11	55	80	200	16.8	small
12	60	100	200	6	small
13	60	100	220	6	small

Table 7.2.: Experimental setup for Delrin 127UV.

7.3.2. Process settings: PA6 GF45

In the case of the fiber filled material, the processing conditions were not varied. What is of interest in this case is the difference in strength between both specimens (with and without weld face). It is believed that the strength properties of the specimens are essentially dependent on the fiber orientation, which is hardly affected by the processing conditions (see Chapter 6). Instead, all geometry combinations were tested (thickness of the specimen s and overflow volumes). The mold and melt temperatures were kept at 80°C and 285°C, respectively. Packing pressure and injection time were also adapted to the thickness of the specimens. The experimental setup is given in Table 7.3 For each experiment, at least 10 shots under stable conditions were produced.

exp. No.	p_{cav} in MPa	t_{inj} in s	overflow vol.	s in mm
1	45	2.6	large	4
2	45	2.6	medium	4
3	45	2.6	small	4
4	55	2.6	small	6
5	55	2.6	medium	6
6	55	2.6	large	6
7	65	3.9	small	8
8	65	3.9	mid	8
9	65	3.9	large	8

Table 7.3.: Experimental setup for DuPont Zytel 73G45.

7.4. Measurements

A Zwick universal testing machine was used to perform tensile tests on the molded specimens. A draw speed of 250 mm/min was used for all tests at a temperature of 25°C. All stresses and strains results given are engineering stresses[3] and strains, respectively. Moreover, it should be noted that the strain was not directly measured and was therefore merely calculated from the measured distance of the jaws. Hence, the strain values presented should not be compared to values of other sources and only act as a relative measure within this study. Ten specimens from each cavity and from all experiments were tested. The stress at break σ_{break} and strain at break ϵ_{break} was evaluated for each drawing test and averaged over the 10 specimens from the same experiment and cavity. The standard deviation was calculated for the stress ($SD_{\sigma_{break}}$) and strain ($SD_{\epsilon_{break}}$) results to indicate the stability of the process. The specimens were stored at normal room temperature and humidity for about one week before testing.

7.5. Results and discussion

7.5.1. POM

Tab. 7.4 shows the results of the tensile tests performed on the specimens made of POM. The results show one dominating factor for the mechanical properties of the specimens: the mold temperature. Except for those from Experiments 6 and 7, all specimens were produced using a mold temperature between 80°C and 100°C, which is the optimal range for this material. In this case, the weld face causes just a marginal decrease in the tensile strength of around 3%. In contrast, the weld face has a severe impact on the strain the sample can sustain before breaking (compare ϵ_{break}), which is reduced by around 40%. A distortion of the weld face neither affects the strength nor the ductility of the sample (compare No. 1, 8, 9). Packing pressure (compare No. 1-3), melt temperature (compare No. 1 and 5) and injection velocity (compare No. 1, 10 and 11) have no significant impact on σ_{break} or ϵ_{break}. The standard deviations are very low and indicate a stable process. The samples produced at 100°C mold temperature (compare No. 1 and 12) have a better ductility.

A mold temperature of 50°C (No. 6) causes a decrease of σ_{break} of around 20% and of ϵ_{break} of 50%, in case of a weld face. Moreover, the standard deviation shows a high degree of scattering of the mechanical properties. The reference specimen shows a

---

[3]the calculation of the stress is based on the nominal, undeformed cross section of the specimen

	reference specimen				specimen with weld face			
No.	σ_{break}	$SD_{\sigma_{break}}$	ϵ_{break} %	$SD_{\epsilon_{break}}$	σ_{break}	$SD_{\sigma_{break}}$	ϵ_{break}	$SD_{\epsilon_{break}}$
1	68	0.17	44	0.51	67	0.26	27	0.91
2	68	0.36	45	0.32	66	0.38	26	0.73
3	70	0.43	42	0.66	68	0.45	26	0.49
4	70	0.17	41	0.34	68	0.47	28	0.76
5	69	0.14	43	0.30	68	0.38	27	1.9
6	67	0.31	36	0.14	53	13.74	13	8.07
7	69	0.52	38	4.44	63	4.54	18	8.79
8	70	0.30	43	0.73	68	0.32	25	0.56
9	69	0.18	43	0.30	68	0.35	25	0.87
10	67	0.39	37	5.40	66	0.53	25	1.43
11	68	0.19	41	0.33	66	0.41	25	1.96
12	69	0.31	51	0.54	67	0.26	31	0.40
13	69	0.41	49	2.31	67	0.25	36	0.74

Table 7.4.: Measured fracture stress σ_{break} in MPa and strain at break (ϵ_{break}) in % of the POM specimens. Averaged over 10 shots. SD is the standard deviation.

decrease in ductility of around 20%. Increasing the mold temperature to 120°C has basically the same effects (No. 7).

In summary:

- A weld line causes just a small drop in the fracture strength of the specimen.
- The ductility of the specimen at the weld face is significantly reduced.
- The mechanical properties are independent of the inner structure of the weld face (e.g sharp or washed-out)
- The mechanical properties are mostly affected by the mold temperature.

From these findings, one can conclude that in the case of POM, surface defects at the weld line are the prime reason for the decrease in ductility. These defects can be reduced by increasing the mold and melt temperatures in order to decrease viscosity and slow down the formation of the frozen layer when the flow fronts merge. In this way, the notch at the surface of the weld face is reduced.

Perfect venting around the weld face would probably further improve its mechanical properties. However, this is hardly feasible without introducing even more surface defects at the vents.

7.5.2. PA6 GF45

The results of the tensile tests performed on the specimens made of PA6 GF45 are shown in Table 7.5.

	reference specimen				specimen with weld face			
No.	σ_{break}	$SD_{\sigma_{break}}$	ϵ_{break} %	$SD_{\epsilon_{break}}$	σ_{break}	$SD_{\sigma_{break}}$	ϵ_{break}	$SD_{\epsilon_{break}}$
1	210	1.39	10	0.19	188	2.04	9	0.20
2	210	2.04	10	0.23	123	2.55	6	0.13
3	212	1.18	9	0.30	90	0.76	5	0.20
4	217	1.11	11	0.13	91	1.24	5	0.17
5	216	1.49	11	0.38	109	2.09	6	0.11
6	216	0.55	11	0.37	188	1.27	10	0.2
7	218	1.08	14	0.67	93	0.70	7	0.40
8	221	0.91	14	0.28	110	0.70	7	0.11
9	222	1.51	13	0.13	181	1.51	12	0.18

Table 7.5.: Measured fracture stress σ_{break} in MPa and strain at break (ϵ_{break}) in % of the PA6 GF45 specimens. Averaged over 10 shots. SD is the standard deviation.

In the case of fiber reinforced material, the strength of the specimen is strongly affected by the inner structure of the weld face. A sharp weld face (No. 3, 4 and 7) causes a decrease in fracture strength to about 40% of the reference specimen. There is no dependency on the thickness of the samples. A slight distortion of the weld face increases the strength by around 25% (No. 2, 5 and 8). In the case of the washed-out weld face, around 80% to 90% of the reference strength is achieved (No. 1, 6 and 9). Fig. 7.8 shows the stress and strain at break results of the flawed samples in relation to the reference specimens in order to highlight the significance of the weld face characteristic. The effect of weld face distortion on strength decreases with the increasing thickness of the samples. The stress-strain relationship is quite linear in the case of the fiber filled material. Hence, the same decrease in fracture stress caused by the weld face is also seen at the fracture strain.

These findings are in good agreement with the predicted fiber orientation shown in Fig. 7.7. Assuming that all fibers lay in the plane of the sharp weld face (no reinforcing effect of the fibers), the strength of the sample would be entirely determined by the strength of the polymer matrix. In the case of PA6, the fracture strength is in the order of 60 MPa. In theory, that would be around 36% of the strength obtained with the flawless specimens, compared to the 42% determined experimentally. The distortion of the weld face has a randomizing effect on the fiber orientation at the weld face and leads to improved mechanical properties. When the weld face is washed-out, the flow through the weld face causes the realignment of the fibers and the strength of the sample significantly increases. The experiments show that this effect is more pronounced in thinner samples. An explanation for this could be that the lower thickness of the samples imposes a higher shear rate in the flow through the weld face. The consequence of a higher shear rate is the stronger alignment of the fibers.

(a) Relative fracture strength   (b) Relative strain at break
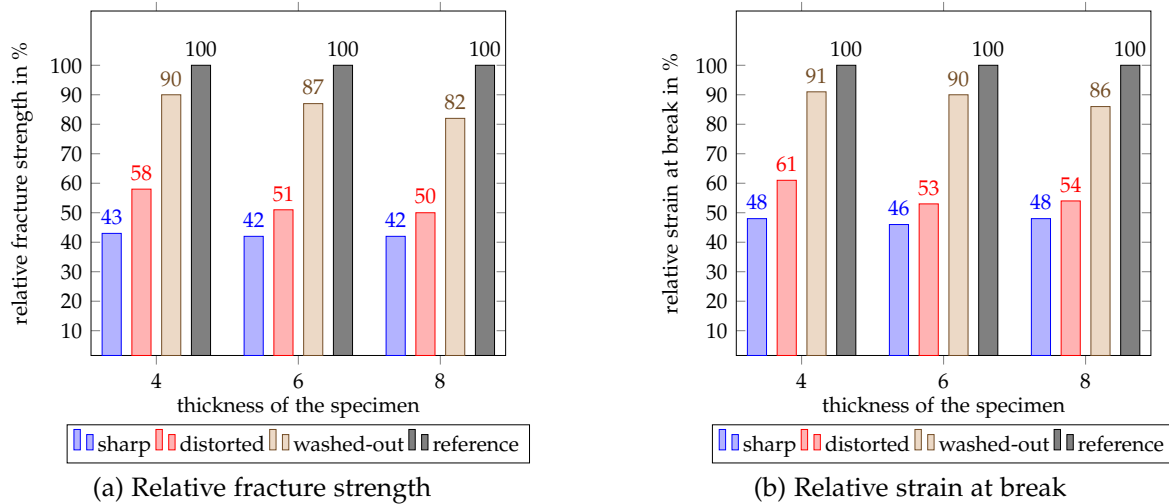
Figure 7.8.: Relative stress and strain values of the specimens made of PA6 GF45.

7.6. Concluding remarks

The significance of weld faces on the mechanical performance of a molded part depends on the processed material.

POM

The molding trials with POM basically support the findings of other studies, as for instance, the work of Meddad & Fisa [141]. The fracture strength of the part is not severely affected by a weld line, but the ductility is. Mold and melt temperature were found to be the most influential process parameters on the ductility of the weld line. Packing pressure and injection speed had no significant effect. Additionally, the geometry was varied to generate a through-flow of the weld face. In the case of the unfilled material, no effect on the tensile strength properties of the specimen was observed. From this investigation, one can conclude that the presence of weld faces in the molding is irrelevant when:

- mold and melt temperature were chosen from the optimal range and no air is trapped at the weld face.
- the part is not used for applications in which it has to undergo extreme deformation before failure (as, for instance, in safety critical applications).

It must be noted that this conclusion is not generally valid. Regarding POM, the weld face may affect the mechanical performance of the part at low or elevated temperatures, at impact loads and/or more dimensional stress states. It may also

affect its chemical resistance and fatigue behavior. Although similar findings were obtained with other polymer grades (see [143]) one can not conclude that this is true for all unfilled polymer grades.

PA6 GF45

Considering fiber filled materials, a through-flow of the weld face has a severe impact on the tensile properties. It is known that the fiber orientation in a sharp weld face is predominately parallel to the weld face [143]. Hence, the tensile strength at the weld face is just at the level of the base polymer. When through-flow is achieved, the fiber orientation is affected, and the strength increases. This is the only way to achieve a significant improvement in the strength properties of parts with weld faces. The prediction of the movement of the weld face (Fig. 7.2 and 7.3) turned out to be very valuable when it came to characterizing the significance of weld faces. Moreover, it was shown that the predicted fiber orientation at the weld face correlates well with the mechanical properties of the sample. This is a major prerequisite for the consideration of the weld face in a subsequent structural FEM simulation of the molded part.

8. Summary and conclusions

The initial questions which this thesis seeks to answer were: "Is a commercial injection molding simulation software capable of accurately predicting the warpage of chunky parts?" and "If yes, where are the limits?" These are actually very important questions. Severe warpage may render the molded parts useless and extensive reworking of the injection mold would be required to eliminate warpage. This is a very costly and time-consuming task which can be avoided by the accurate prediction of warpage and corrective action before the mold is built.

Methods and models for the simulation of the injection molding process have been developed and verified for plastic parts with the classic thin-shell structure. Most published research studies focus on simple geometries, such as flat plates, center gated disks or boxes. Some studies have presented results based on more complex parts, which, however, still have the thin-shell structure. Thus, these studies do not provide any insight into the applicability of injection molding simulation tools to chunky parts.

This thesis is based upon numerical and experimental studies of different plastic parts already in production, a newly developed part without experimental data, and a specifically designed research part. The parts investigated in this thesis were designed for specific applications with high demands on stiffness and strength. They all have a complex and chunky geometry with varying wall thickness. Within this thesis, numerous case studies have been conducted on these industrial plastic parts. The aim was to gain insight into the value and limitations of injection molding simulation applied to chunky parts. The state-of-the-art software Autodesk Moldflow Insight was used throughout this thesis.

All simulation results were supported by experiments and measurements[1]. Several case studies are presented in detail in Chapter 3, with the intention to highlight certain aspects of modeling the injection molding process. Each study has a different focus, in order to illustrate the impact of modeling, discretization in space and time, material data, sub-models, and solver settings on the solution. The dominant influencing

---

[1]Since production molds were used, process related measurements like cavity pressure or mold temperature were only obtained in certain cases. Warpage results were always compared to measurements.

factors were determined for each case and suggestions for proper modeling were derived.

The opportunities provided by injection molding simulation

Chunky parts usually have a high mechanical stiffness in comparison to thin-shell parts. In the course of this research, it was found that uniform mold cooling does not generally mean zero warpage, and that non-uniform mold cooling does not generally lead to warpage. This is basically true for unfilled and fiber reinforced material grades. The contribution of non-uniform mold cooling conditions to warpage was generally in the order of up to 50% in the case of POM, and up to 20% in the case of PA6+GF45. Injection molding simulation is a valuable tool to investigate the effectiveness of the mold cooling system and its impact on cycle time and warpage. In all cases shown, it would have been impossible to avoid warpage by simply improving the mold's cooling system. Considering complex, chunky parts, there is no point in designing a highly sophisticated and expensive mold cooling system if the cycle time is not of prime importance.

One noteworthy exception is presented in Section 3.6, where warpage was essentially caused by inappropriate mold design. This led to a very high temperature difference between core and cavity. A detailed 3D representation of the hot runner nozzle was introduced to investigate its impact on the mold temperature distribution, and, consequently, on part warpage. The nozzle only touches the mold insert at its very tip, where pure heat conduction occurs. On its whole length, it is insulated by an air gap. Radiation, conduction, or natural convection (depending on the size of the gap) must be considered to calculate the total heat flux into the mold. A proper way to simulate this heat flux (by circumventing the software's limited modeling capabilities in heat transfer) is outlined in this thesis.

The case studies have shown that mold cooling and runner systems must be considered in order to obtain accurate warpage predictions. High quality material properties data is also a crucial requirement. The impact of processing settings on warpage was generally found to be rather low (with few exceptions). A reasonable estimation of process settings and boundary conditions is sufficient for the purpose of true warpage predictions (before cutting the mold) and generally causes little error. Good to very good accordance of simulation and experiment was finally achieved in all of the case studies presented in Chapter 3. Warpage was always slightly underpredicted, with deviations to the measurements in the order of 10% to 30%. One case study dealt with the true prediction and compensation of warpage. Simulation results were used to optimize the part design and to compensate for warpage before the mold was built. The first molding trials produced high quality parts without warpage. Hence, the

objective of this study was accomplished. This part of the thesis is of high practical relevance to all those who deal with similar plastic parts.

The answer to the primary question stated above is certainly yes. State-of-the-art commercial injection molding simulation software is indeed capable of predicting the warpage of chunky parts with reasonable accuracy. Additionally, the prediction of other results such as filling pattern, weld lines, air traps, cavity pressure, mold temperature distribution, etc. is not compromised by a chunky part geometry and succeeds with high precision[2].

The limits of injection molding simulation

Nonetheless, severe deviations of the predictions from the measurements were observed in two case studies. These results led to further research activities.

Chapter 4 presents a case where the predicted filling pattern did not match experimental short shots. Several influencing factors were considered, and their contribution to the prediction accuracy was determined by means of numerical experiments. It turned out that the simulated filling pattern is hardly affected by the mold temperature distribution, discretization in space and time, material data, or even poor venting conditions. In this case, it was found that the deformation of the mold under melt pressure was the root cause of the poor simulation results. Increasing the stiffness of the mold led to a significantly different filling pattern, which was in good agreement with the simulation result. A simple way to model and predict mold deflection under pressure is also outlined in this thesis. A standard mold filling simulation using reasonable process settings is perfectly suitable to obtain fairly accurate prediction results. This approach is, however, only valid if the assumption of a rigid mold is indeed feasible.

Chapter 5 dealt with the influence of voids on warpage. In one case, the simulation model failed to predict warpage even qualitatively. The molded parts were severely distorted, while almost no warpage was predicted. Experiments and µCT measurements showed that a reduction of volumetric shrinkage in the thick walls (which was characterized by a lower void volume) caused a significant decrease in warpage. This relationship was not shown by the simulation model.

The same part was used to investigate the accuracy of the fiber model in predicting the fiber orientation in the sections with thick walls (see Chapter 6). Small samples were cut out of the molded part and scanned by a µCT device in order to determine the length and orientation of all fibers in the sample volume. The discrete fiber data was used to calculate the orientation tensor, which was then compared to the

---

[2]If the case is properly modeled and the dominant influencing factors are considered.

predicted fiber orientation obtained with various settings of the Moldflow solver. A good quantitative prediction of the fiber orientation state was observed in the shear layer. Both the predicted thickness of the core layer and the fiber orientation in the core layer were only in qualitative agreement with the measurement. It was supposed that this weakness may have severe consequences when warpage occurs in the thick sections of a fiber reinforced part. To the authors knowledge, the suitability of recent fiber models and software to accurately predict the fiber orientation in a chunky 3D geometry has not yet been proven.

As a result of these findings, a simple U-shaped test part was especially designed to further investigate the impact of voids and fiber orientation on warpage. This part has all the properties found to be very problematic (see Section 5.2). It has a thin-walled geometry with thick walls in both corners. Hence, high volumetric shrinkage occurs in the thick corners and the 3D flow regime challenges the accuracy of the fiber model. In other words, the part was designed to expose the limits of state-of-the-art injection molding software. Experiments with POM showed that warpage predictions were in good agreement if high packing efficiency, and therefore low volumetric shrinkage was achieved. Otherwise, the measured warpage was significantly higher than predicted. In the case of PA6+GF, it was generally not possible to predict shrinkage and warpage with reasonable precision. The predicted warpage was only sensitive to the settings in the fiber model. This fact indicates that the goal of accurate warpage prediction is closely related to the accuracy of fiber models.

Suggestions

When working with unfilled polymer grades, gate location as well as runner and gate dimensions must be chosen in order to achieve a high packing efficiency of the thick-walled sections of the part. Adding flow leaders from the gate to the thick regions is a proper way of achieving better pressure propagation and extended packing time. If the predicted warpage originates from a thick section with very high volumetric shrinkage, the simulated results may lack reliability.

Experiments and simulations indicate that anisotropic shrinkage due to the orientation effect of the fibers is the dominant cause of warpage if a fiber reinforced material is processed. Apart from the case presented in Chapter 5, the processing conditions generally had little impact on warpage. The packing efficiency does significantly affect shrinkage, but only slightly affects warpage. The key to accurate warpage predictions seems to be the accurate prediction of the fiber orientation. State-of-the-art fiber models and software are not yet able to correctly calculate the fiber orientation state in thick walls. This may severely compromise the accuracy of the warpage prediction if the warpage originates from a section with thick walls. If possible, those areas should be cored out to improve the quality of the simulation results.

8. Summary and conclusions

This thesis shows that injection molding simulation is a very powerful and valuable tool. In many cases, it is applicable to complex three-dimensional and chunky parts without restrictions. However, care must be taken if warpage occurs in thick walled sections of the part.

References

1. Hieber, C. A. & Shen, S. F. A finite-element/finite-difference simulation of the injection-molding filling process. *Journal of Non-Newtonian Fluid Mechanics* **7**, 1–32 (1980).

2. Autodesk. *Choosing a mesh type* `https://knowledge.autodesk.com/support/ moldflow-insight/learn-explore/caas/CloudHelp/cloudhelp/2016/ENU/ MoldflowInsight/files/GUID-4B1EA908-C18E-44E3-9BD9-14FE7F160291- htm.html`. Accessed: 2015-12-05. 2015.

3. Yu, H. G. & Thomas, R. *Method for modelling three dimension objects and simulation of fluid flow* US Patent 6,096,088. 2000.

4. Kennedy, P. *Practical and scientific aspects of injection molding simulation* PhD thesis (Technische Universiteit Eindhoven, 2008).

5. Zhou, H. *Computer Modeling for Injection Molding: Simulation, Optimization and Control* (Wiley, New Jersey, 2013).

6. Zheng, R., Tanner, R. I. & Fan, X. J. *Injection Molding: Integration of Theory and modeling Methods* (Springer Verlag, Berlin, Heidelberg, 2011).

7. Costa, F. S., Ray, S., Friedl, S., Cook, P. S. & Xu, S. *The Effect of Inertia on Fill Pattern in Injection Molding* in *Society of Plastics Engineers Annual Technical Conference–ANTEC* (2001).

8. Autodesk. *3D flow derivation* `https://knowledge.autodesk.com/support/ moldflow-flex/learn-explore/caas/CloudHelp/cloudhelp/2016/ENU/ MoldflowInsight360/files/GUID-C94D0362-421F-4EC1-89A6-931BB8D6D365- htm.html`. Accessed: 2015-12-05. 2015.

9. Kee, R. J., Coltrin, M. E. & Glarborg, P. in *Chemically Reacting Flow* 67–149 (John Wiley & Sons, Inc., 2005).

10. Autodesk. *Generate Mesh tool* `https://knowledge.autodesk.com/support/ moldflow-insight/learn-explore/caas/CloudHelp/cloudhelp/2014/ENU/ MoldflowInsight/files/GUID-E2A8493F-9767-4A74-8E45-9872D3FC6639- htm.html`. Accessed: 2015-12-05. 2015.

11. Autodesk. *High aspect ratio (3D)* `https://knowledge.autodesk.com/support/moldflow-insight/learn-explore/caas/CloudHelp/cloudhelp/2015/ENU/MoldflowInsight/files/GUID-20F60325-7022-47F1-889E-AE0AA9D76F61-htm.html`. Accessed: 2015-12-05. 2015.

12. Cardozo, D. Three Models of the 3D Filling Simulation for Injection Molding: A Brief Review. en. *Journal of Reinforced Plastics and Composites* **27,** 1963–1974 (2008).

13. Bajaj, M., Bhat, P. P., Prakash, J. R. & Pasquali, M. Multiscale simulation of viscoelastic free surface flows. *Journal of non-newtonian fluid mechanics* **140,** 87–107 (2006).

14. Gaston, L., Kamara, A. & Bellet, M. An arbitrary Lagrangian-Eulerian finite element approach to non-steady state turbulent fluid flow with application to mould filling in casting. *International journal for numerical methods in fluids* **34,** 341–369 (2000).

15. Lewis, R. W., Navti, S. E. & Taylor, C. A mixed Lagrangian-Eulerian approach to modelling fluid flow during mould filling. *International Journal for Numerical Methods in Fluids* **25,** 931–952 (1997).

16. Tezduyar, T. E. Interface-tracking and interface-capturing techniques for finite element computation of moving boundaries and interfaces. *Computer Methods in Applied Mechanics and Engineering* **195,** 2983–3000 (2006).

17. Hirt, C. & Nichols, B. Volume of fluid (VOF) method for the dynamics of free boundaries. *Journal of Computational Physics* **39,** 201–225 (1981).

18. Ubbink, O. & Issa, R. A Method for Capturing Sharp Fluid Interfaces on Arbitrary Meshes. *Journal of Computational Physics* **153,** 26–50 (1999).

19. Adalsteinsson, D. & Sethian, J. A. A fast level set method for propagating interfaces. *Journal of Computational Physics* **118,** 269–277 (1995).

20. Osher, S. & Sethian, J. A. Fronts propagating with curvature dependent speed: Algorithms based on Hamilton–Jacobi formulation. *Journal of Computational Physics* **79,** 12–49 (1988).

21. Autodesk. *Autodesk Moldflow Insight 2011: Flow Front Advancement in the 3D Flow Solver* `http://images.autodesk.com/apac_japan_main/files/autodesk_moldflow_2011_3dflow_flowfront_advancement_validation_en.pdf`. Accessed: 2015-12-05. 2010.

22. Kamal, M. R., Isayev, A. I. & Liun, S. J. *Injection Molding: Technology and Fundamentals* (Hanser, Munich, 2009).

23. Han, C. D. Polymer melt rheology - a guide for industrial practice. *Journal of Polymer Science: Polymer Letters Edition* **20,** 198–199 (1982).

24. Bird, R., Armstrong, R. & Hassager, O. *Dynamics of polymeric liquids. Vol. 1, 2nd Ed.: Fluid mechanics* (John Wiley and Sons Inc.,New York, NY, 1987).

25. Carreau, P. J. Rheological equations from molecular network theories. *Transactions of The Society of Rheology (1957-1977)* **16,** 99–127 (1972).

26. Cross, M. M. Rheology of non-Newtonian fluids: A new flow equation for pseudoplastic systems. *Journal of Colloid Science* **20,** 417–437 (1965).

27. Williams, M. L., Landel, R. F. & Ferry, J. D. The temperature dependence of relaxation mechanisms in amorphous polymers and other glass-forming liquids. *Journal of the American Chemical society* **77,** 3701–3707 (1955).

28. Hieber, C. A. & Chiang, H. H. Shear-rate-dependence modeling of polymer melt viscosity. *Polymer Engineering & Science* **32,** 931–938 (1992).

29. Luyé, J.-F., Régnier, G., Le Bot, P., Delaunay, D. & Fulchiron, R. PVT measurement methodology for semicrystalline polymers to simulate injection-molding process. *Journal of Applied Polymer Science* **79,** 302–311 (2001).

30. Chiu, C.-P., Liu, K.-A. & Wei, J.-H. A method for measuring PVT relationships of thermoplastics using an injection molding machine. *Polymer Engineering & Science* **35,** 1505–1510 (1995).

31. Zuidema, H., Peters, G. W. M. & Meijer, H. E. H. Influence of cooling rate on pVT-data of semicrystalline polymers. *Journal of Applied Polymer Science* **82,** 1170–1186 (2001).

32. Wang, J., Xie, P., Yang, W. & Ding, Y. Online pressure-volume-temperature measurements of polypropylene using a testing mold to simulate the injection-molding process. *Journal of Applied Polymer Science* **118,** 200–208 (2010).

33. Wang, J. *PVT Properties of Polymers for Injection Molding* (INTECH Open Access Publisher, 2012).

34. Lucyshyn, T., Duretek, I., Langecker, G. & Fischer, K. in *Program and Abstracts of the 22nd Annual Meeting of the Polymer Processing Society, Yamagata, Japan 2006* 237–237 (2006).

35. Van Krevelen, D. W. & Te Nijenhuis, K. *Properties of polymers: their correlation with chemical structure; their numerical estimation and prediction from additive group contributions* (Elsevier, 2009).

36. Zoller, P., Kehl, T. A., Starkweather, H. W. & Jones, G. A. The equation of state and heat of fusion of poly(ether ether ketone). *Journal of Polymer Science Part B: Polymer Physics* **27,** 993–1007 (1989).

37. Zoller, P. & Fakhreddine, Y. A. Pressure–volume–temperature studies of semicrystalline polymers. *Thermochimica Acta* **238,** 397–415 (1994).

38. Folgar, F. & Tucker III, C. L. Orientation Behavior of Fibers in Concentrated Suspensions. en. *Journal of Reinforced Plastics and Composites* **3,** 98–119 (1984).

39. Jeffery, G. B. The Motion of Ellipsoidal Particles Immersed in a Viscous Fluid. *Proceedings of the Royal Society of London. Series A, Containing Papers of a Mathematical and Physical Character* **102,** 161–179 (1922).

40. Advani, S. G. & Tucker III, C. L. The Use of Tensors to Describe and Predict Fiber Orientation in Short Fiber Composites. *Journal of Rheology (1978-present)* **31,** 751–784 (1987).

41. Darlington, M. W. & Smith, A. C. Some features of the injection molding of short fiber reinforced thermoplastics in center sprue-gated cavities. en. *Polymer Composites* **8,** 16–21 (1987).

42. Bay, R. S. *Fiber orientation in injection-molded composites: a comparison of theory and experiment* PhD thesis (University of Illinois at Urbana-Champaign, 1991).

43. Bay, R. S. & Tucker III, C. L. Fiber orientation in simple injection moldings. Part I: Theory and numerical methods. *Polymer Composites* **13,** 317–331 (1992).

44. Bay, R. S. & Tucker III, C. L. Fiber orientation in simple injection moldings. Part II: Experimental results. *Polymer Composites* **13,** 332–341 (2004).

45. Gupta, M. & Wang, K. K. Fiber orientation and mechanical properties of short-fiber-reinforced injection-molded composites: Simulated and experimental results. en. *Polymer Composites* **14,** 367–382 (1993).

46. Lee, S. C., Yang, D. Y., Ko, J. & Youn, J. R. Effect of compressibility on flow field and fiber orientation during the filling stage of injection molding. *Journal of Materials Processing Technology* **70,** 83–92 (1997).

47. Zheng, R., Kennedy, P., Phan-Thien, N. & Fan, X.-J. Thermoviscoelastic simulation of thermally and pressure-induced stresses in injection moulding for the prediction of shrinkage and warpage for fibre-reinforced thermoplastics. *Journal of Non-Newtonian Fluid Mechanics* **84,** 159–190 (1999).

48. Guo, R., Azaiez, J. & Bellehumeur, C. Rheology of fiber filled polymer melts: Role of fiber-fiber interactions and polymer-fiber coupling. en. *Polymer Engineering & Science* **45,** 385–399 (2005).

49. Vincent, M., Giroud, T., Clarke, A. & Eberhardt, C. Description and modeling of fiber orientation in injection molding of fiber reinforced thermoplastics. *Polymer. Polymer Blends, Composites and Hybrid Polymeric Materials IUPAC MACRO 2004* **46,** 6719–6725 (2005).

50. Wang, J., O'Gara, J. F. & Tucker III, C. L. An objective model for slow orientation kinetics in concentrated fiber suspensions: Theory and rheological evidence. *Journal of Rheology* **52,** 1179–1200 (2008).

51. Phelps, J. H. & Tucker III, C. L. An anisotropic rotary diffusion model for fiber orientation in short- and long-fiber thermoplastics. *Journal of Non-Newtonian Fluid Mechanics* **156,** 165–176 (2009).

52. Shokri, P. & Bhatnagar, N. Effect of the Post-Filling Stage on Fiber Orientation at the Mid-Plane in Injection Molding of Reinforced Thermoplastics. *Physics Procedia. International Conference on Solid State Devices and Materials Science, April 1-2, 2012, Macao* **25,** 79–85 (2012).

53. Oumer, A. N. & Mamat, O. A study of fiber orientation in short fiber-reinforced composites with simultaneous mold filling and phase change effects. *Composites Part B: Engineering* **43,** 1087–1094 (2012).

54. Yashiro, S., Sasaki, H. & Sakaida, Y. Particle simulation for predicting fiber motion in injection molding of short-fiber-reinforced composites. *Composites Part A: Applied Science and Manufacturing. CompTest 2011* **43,** 1754–1764 (2012).

55. Agboola, B. O., Jack, D. A. & Montgomery-Smith, S. Effectiveness of recent fiber-interaction diffusion models for orientation and the part stiffness predictions in injection molded short-fiber reinforced composites. *Composites Part A: Applied Science and Manufacturing* **43,** 1959–1970 (2012).

56. Mazahir, S. M., Vélez-Garcia, G. M., Wapperom, P. & Baird, D. Evolution of fibre orientation in radial direction in a center-gated disk: Experiments and simulation. *Composites Part A: Applied Science and Manufacturing* **51,** 108–117 (2013).

57. Phelps, J. H., Abd El-Rahman, A. I., Kunc, V. & Tucker III, C. L. A model for fiber length attrition in injection-molded long-fiber composites. *Composites Part A: Applied Science and Manufacturing* **51,** 11–21 (2013).

58. Sepehr, M., Ausias, G. & Carreau, P. J. Rheological properties of short fiber filled polypropylene in transient shear flow. *Journal of Non-Newtonian Fluid Mechanics* **123,** 19–32 (2004).

59. Wang, J. *Improved fiber orientation predictions for injection molded composites* PhD thesis (University of Illinois at Urbana-Champaign, 2007). (Visited on 07/01/2014).

60. Autodesk. *Fiber orientation prediction theory references* https://knowledge.autodesk.com/support/moldflow-flex/learn-explore/caas/CloudHelp/cloudhelp/2016/ENU/MoldflowInsight360/files/GUID-BD0CFAC8-D8A9-42E7-8838-7DD2E67829B1-htm.html. Accessed: 2015-12-05. 2015.

61. Cintra, J. S. J. & Tucker III, C. L. Orthotropic closure approximations for flow-induced fiber orientation. *Journal of Rheology (1978-present)* **39,** 1095–1122 (1995).

62. Phan-Thien, N., Fan, X. .-.-J., Tanner, R. I. & Zheng, R. Folgar-Tucker constant for a fibre suspension in a Newtonian fluid. *Journal of Non-Newtonian Fluid Mechanics* **103,** 251–260 (2002).

63. Wang, J. & Jin, X. *Comparison of recent fiber orientation models in autodesk moldflow insight simulations with measured fiber orientation data* in *Proceedings of the Polymer Processing Society 26th Annual Meeting* (2010), 4–8.

64. Rees, H. *Mold Engineering* 2nd ed. (Carl Hanser Verlag, Munich, 2009).

65. Kelly, A., Mulvaney-Johnson, L., Beechey, R. & Coates, P. The effect of copper alloy mold tooling on the performance of the injection molding process. *Polymer Engineering & Science* **51,** 1837–1847 (2011).

66. Xu, X., Sachs, E., Allen, S. & Cima, M. *Designing conformal cooling channels for tooling* in *Solid Freeform Fabrication Proceedings* (1998), 131–146.

67. Levy, G. N., Schindel, R. & Kruth, J.-P. Rapid manufacturing and rapid tooling with layer manufacturing (LM) technologies, state of the art and future perspectives. *CIRP Annals-Manufacturing Technology* **52,** 589–609 (2003).

68. Saifullah, A. & Masood, S. *Finite element thermal analysis of conformal cooling channels in injection moulding* in *5th Australasian Congress on Applied Mechanics (ACAM 2007)* **1** (2007), 337–341.

69. Beaumont, J. P., Sherman, R. & Nagel, R. F. *Successful Injection Molding: Process, Design, and Simulation* (Hanser Gardner Publications, 2002).

70. Fischer, J. *Handbook of Molded Part Shrinkage and Warpage* Second Edition (William Andrew Publishing, Boston, 2013).

71. Shoemaker, J. *Moldflow Design Guide: A Resource for Plastics Engineers* (Carl Hanser Verlag GmbH & Co. KG, 2006).

72. Jacques, M. S. An analysis of thermal warpage in injection molded flat parts due to unbalanced cooling. *Polymer Engineering & Science* **22,** 241–247 (1982).

73. Shen, C.-Y. & Li, H.-M. Numerical simulation for effects of injection mold cooling on warpage and residual stresses. *Polymer-Plastics Technology and Engineering* **42,** 971–982 (2003).

74. Delaunay, D., Le Bot, P., Fulchiron, R., Luye, J. F. & Régnier, G. Nature of contact between polymer and mold in injection molding. Part II: Influence of mold deflection on pressure history and shrinkage. *Polymer Engineering & Science* **40,** 1692–1700 (2000).

75. Yu, C. J., Sunderland, J. E. & Poli, C. Thermal contact resistance in injection moulding. *Polymer Engineering & Science* **30,** 1599–1606 (1990).

76. Urquhart, J. M. & Brown, C. S. *The effect of uncertainty in heat transfer data on the simulation of polymer processing* tech. rep. NPL Report DEPC MPR 001 (London, 2004).

77. Dawson, A., Rides, M., Allen, C. R. G. & Urquhart, J. M. Polymer-mould interface heat transfer coefficient measurements for polymer processing. *Polymer Testing* **27,** 555–565 (2008).

78. Nylund, C. & Meinander, K. The influence of heat transfer coefficient on cooling time in injection Molding. *Heat and Mass Transfer* **41,** 428–431 (2005).

79. Banerjee, P. K. & Butterfield, R. *Boundary element methods in engineering science* (McGraw-Hill London, 1981).

80. Zienkiewicz, O. C. & Taylor, R. L. *The finite element method: solid mechanics* (Butterworth-heinemann, 2000).

81. Kwon, T. Mold cooling system design using boundary element method. *Journal of Manufacturing Science and Engineering* **110,** 384–394 (1988).

82. Autodesk. *Cool analysis for transient mold temperature investigations* https://knowledge.autodesk.com/support/moldflow-insight/learn-explore/caas/CloudHelp/cloudhelp/2015/ENU/MoldflowInsight/files/GUID-4DB0EDB1-8DB3-4EDE-B385-64AA09EA6192-htm.html. Accessed: 2015-12-05. 2014.

83. Huang, M.-C. & Tai, C.-C. The effective factors in the warpage problem of an injection-molded part with a thin shell feature. *Journal of Materials Processing Technology* **110,** 1–9 (2001).

84. Subramanian, N. R., Tingyu, L. & Seng, Y. A. Optimizing warpage analysis for an optical housing. *Mechatronics* **15,** 111–127 (2005).

85. Kurtaran, H., Ozcelik, B. & Erzurumlu, T. Warpage optimization of a bus ceiling lamp base using neural network model and genetic algorithm. *Journal of Materials Processing Technology* **169,** 314–319 (2005).

86. Ozcelik, B. & Erzurumlu, T. Comparison of the warpage optimization in the plastic injection molding using ANOVA, neural network model and genetic algorithm. *Journal of Materials Processing Technology* **171,** 437–445 (2006).

87. Ozcelik, B. & Sonat, I. Warpage and structural analysis of thin shell plastic in the plastic injection molding. *Materials and Design* **30,** 367–375 (2009).

88. Chen, C.-P., Chuang, M.-T., Hsiao, Y.-H., Yang, Y.-K. & Tsa, C.-H. Simulation and experimental study in determining injection molding process parameters for thin-shell plastic parts via design of experiments analysis. *Expert Systems with Applications* **36,** 10752–10759 (2009).

89. Ahn, D. G., Kim, D. W. & Yoon, Y. U. Optimal injection molding conditions considering the core shift for a plastic battery case with thin and deep walls. *Journal of Mechanical Science and Technology* **24,** 145–148 (2010).

90. Deng, Y.-M., Zhang, Y. & Lam, Y. C. A hybrid of mode-pursuing sampling method and genetic algorithm for minimization of injection molding warpage. *Materials and Design* **31,** 2118–2123 (2010).

References

91. Guo, W., Hua, L., Mao, H. & Meng, Z. Prediction of warpage in plastic injection molding based on design of experiments. *Journal of Mechanical Science and Technology* **26,** 1133–1139 (2012).

92. Wang, X., Zhao, G. & Wang, G. Research on the reduction of sink mark and warpage of the molded part in rapid heat cycle molding process. *Materials and Design* **47,** 779–792 (2013).

93. Liu, F., Zeng, S., Zhou, H. & Li, J. A study on the distinguishing responses of shrinkage and warpage to processing conditions in injection molding. *Journal of Applied Polymer Science* **125,** 731–744 (2012).

94. Guo, X. *Crystallization, Microstructure, Residual Stresses and Birefringence in Injection Molding of Semicrystalline Polymer: Simulation and Experiment* PhD thesis (University of Akron, Dept. of Polymer Engineering, 1999).

95. Titomanlio, G., Drucato, V. & Kamal, M. Mechanism of Cooling Stress Build-Up in Injection Molding of Thermoplastic Polymers. *International Polymer Processing* **1,** 55–59 (1987).

96. Jansen, K. Residual stresses in quenched and injection moulded products. *International Polymer Processing* **9,** 82–89 (1994).

97. Boitout, F., Agassant, J. F. & Vincent, M. Elastic Calculation of Residual Stresses in Injection Molding. *International Polymer Processing* **10,** 237–242 (1995).

98. Baaijens, F. Calculation of residual stresses in injection molded products. *Rheologica Acta* **30,** 284–299 (1991).

99. Santhanam, N., Chiang, H., Himasekhar, K., Tuschak, P. & Wang, K. Postmolding and load-induced deformation analysis of plastic parts in the injection molding process. *Advances in Polymer Technology* **11,** 77–89 (1991).

100. Rezayat, M. & Stafford, R. O. A thermoviscoelastic model for residual stress in injection molded thermoplastics. *Polymer Engineering & Science* **31,** 393–398 (1991).

101. Kabanemi, K. & Crochet, M. Thermoviscoelastic Calculation of Residual Stresses and Residual Shapes of Injection Molded Parts. *International Polymer Processing* **7,** 60–70 (1992).

102. Schwarzl, F. & Staverman, A. Time-temperature dependence of linear viscoelastic behavior. *Journal of Applied Physics* **23,** 838–843 (1952).

103. Dutta, N. K. & Edward, G. H. Generic relaxation spectra of solid polymers. I. Development of spectral distribution model and its application to stress relaxation of polypropylene. *Journal of applied polymer science* **66,** 1101–1115 (1997).

104. Lucyshyn, T., Knapp, G., Kipperer, M. & Holzer, C. Determination of the transition temperature at different cooling rates and its influence on prediction of shrinkage and warpage in injection molding simulation. *Journal of Applied Polymer Science* **123,** 1162–1168 (2012).

105. Kamal, M., Lai-Fook, R. & Hernandez-Arguilar, J. Residual thermal stresses in injection moldings of thermoplastics: A theoretical and experimental study. *Polymer Engineering and Science* **42,** 1098–1114 (2002).

106. Zoetelief, W., Douven, L. & Housz, A. I. Residual thermal stresses in injection molded products. *Polymer Engineering and Science* **36,** 1886–1896 (1996).

107. Tucker III, C. L. & Liang, E. Stiffness predictions for unidirectional short-fiber composites: review and evaluation. *Composites science and technology* **59,** 655–671 (1999).

108. Mori, T. & Tanaka, K. Average Stress in Matrix and Average Elastic Energy of Materials with Misfitting Inclusion. *Acta Metallurgica* **21,** 571–574 (1973).

109. Rosen, B. W. & Hashin, Z. Effective thermal expansion coefficients and specific heats of composite materials. *International Journal of Engineering Science* **8,** 157–173 (1970).

110. http://www.geomagic.com/en/products-landing-pages/inspection. Accessed June 1, 2016.

111. Hine, P., Davidson, N., Duckett, R. A. & Ward, I. M. Measuring the fibre orientation and modelling the elasitc properties of injection-moulded long-glass-fibre-reinforced nylon. *Composites Science and Technology* **53,** 125–131 (1995).

112. Eberhardt, C., Clarke, A., Vincent, M., Giroud, T. & Flouret, S. Fibre-orientation measurements in short-glass-fibre composites – II : a quantitative error estimate of the 2D image analysis technique. *Composites Science and Technology* **61,** 1961–1974 (2001).

113. Salaberger, D., Kannappan, K., Kastner, J., Reussner, J. & Auinger, T. Evaluation of computed tomography data from fibre reinforced polymers to determine fibre length distribution. *International Polymer Processing* **26,** 283–291 (2011).

114. Jerabek, M. *et al. Characterization of short fiber reinforced polypropylene composites* in *Conference on Industrial Computed Tomography (iCT2012)* (Wels, Austria, 2012), 55–58.

115. Köpplmayr, T. *et al.* Influence of fiber orientation and length distribution on the rheological characterization of glass-fiber-filled polypropylene. *Journal of Polymer Testing* **32,** 535–544 (2013).

116. Chang, Y. *et al. Dynamic property of the frozen-layer and its effects on warpage in injection molded parts* in *Annual Technical Conference - ANTEC* **5** (2009).

References

117.   *SIGMASOFT®: 15 Years of Simulation Milestones* `http://www.sigmasoft.de/` `press_release/sigmasoft-15-years-of-simulation-milestones/`. Accessed: 2015-12-11. 2013.

118.   Autodesk. *Warp Settings dialog-3D Warp advanced options* `https://knowledge.` `autodesk.com/support/moldflow-insight/learn-explore/caas/CloudHelp/` `cloudhelp/2016/ENU/MoldflowInsight/files/GUID-82DF114A-EE6E-4E8F-` `BD65-2886BE9B45C9-htm.html`. Accessed: 2015-12-12. 2015.

119.   Autodesk. *Mesh aggregation for 3D Warp analysis (Concept)* `https://knowledge.` `autodesk.com/support/moldflow-insight/learn-explore/caas/CloudHelp/` `cloudhelp/2015/ENU/MoldflowInsight/files/GUID-CF7B24D2-7199-4341-` `9A12-240F24DEE70F-htm.html`. Accessed: 2015-12-12. 2014.

120.   Leo, V. & Cuvelliez, C. The effect of the packing parameters, gate geometry, and mold elasticity on the final dimensions of a molded part. *Polymer Engineering & Science* **36,** 1961–1971 (1996).

121.   Tucker, C. L. Flow regimes for fiber suspensions in narrow gaps. *Journal of Non-Newtonian Fluid Mechanics* **39,** 239–268 (1991).

122.   Pantani, R., Speranza, V. & Titomanlio, G. Relevance of mold-induced thermal boundary conditions and cavity deformation in the simulation of injection molding. *Polymer Engineering & Science* **41,** 2022–2035 (2001).

123.   Giacomin, A. *et al.* Core deflection in injection molding. *Journal of Non-Newtonian Fluid Mechanics* **166,** 908–914 (2011).

124.   Bakharev, A., Zhiliang, F. & Costa, F. *Prediction of core shift effects using mold filling simulation* in *ANTEC... conference proceedings* **1** (2004), 621–625.

125.   Kleindel, S., Eder, R., Schretter, H. & Hochenauer, C. The Elastic Mold Deformation during the Filling and Packing Stage of the Injection Molding Process. *Smart Science* **2,** 44–53 (2014).

126.   Kleindel, S., Salaberger, D., Eder, R., Schretter, H. & Hochenauer, C. Measurement and Numerical Simulation of Void and Warpage in Glass Fiber Reinforced Molded Chunky Parts. *International Polymer Processing* **30,** 100–112 (2015).

127.   Leo, V. *Design and Processing for Lowest Warpage* `http://www.solvay.com/` `en/binaries/Ixef-PARA-Design-and-Processing-for-Lowest-Warpage_EN-` `227830.pdf`. Accessed June 28, 2016.

128.   Udell, K. S. Heat transfer in porous media considering phase change and capillarity - the heat pipe effect. *International Journal of Heat and Mass Transfer* **28,** 485–495 (1985).

129.   Wang, J., Xie, P., Yang, W. & Ding, Y. Online pressure–volume–temperature measurements of polypropylene using a testing mold to simulate the injection-molding process. *Journal of Applied Polymer Science* **118,** 200–208 (2010).

130. Mannella, G. A., Carrubba, V. L., Brucato, V., Zoetelief, W. & Haagh, G. No-flow temperature in injection molding simulation. *Journal of Applied Polymer Science* **119,** 3382–3392 (2011).

131. Autodesk. *Autodesk Knowledge Network* 2015.

132. Kleindel, S., Eder, R., Schretter, H. & Hochenauer, C. Experimental and Numerical Investigation of Shrinkage and Warpage of a U-Shaped Injection Molded Part. *International Polymer Processing* **31,** 68–81 (2016).

133. Ammar, A., Leo, V. & Régnier, G. Corner Deformation of Injected Thermoplastic Parts. *International Journal of Forming Processes* **6,** 53–70 (2003).

134. Akkerman, R., Wiersma, H. & Peeters, L. Spring-forward in continuous fibre reinforced thermosets. *Simulation of Materials Processing: Theory, Methods and Applications: Numiform98,* 471–476 (1998).

135. Albert, C. & Fernlund, G. Spring-in and warpage of angled composite laminates. *Composites Science and Technology* **62,** 1895–1912 (2002).

136. Bakharev, A. *et al. Corner Effect in Warpage Simulation* in *Society of Plastics Engineers Annual Technical Conference–ANTEC* (Boston, Massachusetts, 2005), 511–515.

137. Autodesk. *What's new in the Moldflow 2016 release. 3D fiber accuracy improvements* <http://help.autodesk.com/view/MFIA/2016/ENU/?guid=GUID-0585DEAA-35F8-4B18-AF47-0D0AE4C3B2E1> (2015).

138. VerWeyst, B. E., Tucker III, C. L., Foss, P. H. & O'Gara, J. F. Fiber orientation in 3-D injection molded features: prediction and experiment. *International Polymer Processing* **14** (1999).

139. Kleindel, S., Salaberger, D., Eder, R., Schretter, H. & Hochenauer, C. Prediction and validation of short fiber orientation in a complex injection molded part with chunky geometry. *International Polymer Processing* **30,** 366–380 (2015).

140. *Plastics – Glass-fibre-reinforced products – Determination of fiber length* Standard (International Organization for Standardization, Geneva, Switzerland, 2006).

141. Meddad, A. & Fisa, B. Weldline strength in glass fiber reinforced polyamide 66. *Polymer Engineering & Science* **35,** 893–901 (1995).

142. Hamada, H., Maekawa, Z., Horino, T., Lee, K. & Tomari, K. Improvement of Weld Line Strength in Injection Molded FRTP Articles. *International Polymer Processing* **2,** 131–136 (1988).

143. Vaxman, A., Narkis, M., Siegmann, A. & Kenig, S. Weld-line characteristics in short fiber reinforced thermoplastics. *Polymer Composites* **12,** 161–168 (1991).

144. Selden, R. Effect of processing on weld line strength in five thermoplastics. *Polymer Engineering and Science* **37,** 205–218 (1997).

145. Kim, J. K., Song, J. H., Chung, S. T. & Kwon, T. H. Morphology and mechanical properties of injection molded articles with weld-lines. *Polymer Engineering & Science* **37,** 228–241 (1997).

146. Tomari, K., Takashima, H. & Hamada, H. Improvement of weldline strength of fiber reinforced polycarbonate injection molded articles using simultaneous composite injection molding. *Advances in Polymer Technology* **14,** 25–34 (1995).

147. Wu, C.-H. & Liang, W.-J. Effects of geometry and injection-molding parameters on weld-line strength. *Polymer Engineering & Science* **45,** 1021–1030 (2005).

148. Janko, M., Spiegl, B., Kaufmann, A., Lucyshyn, T. & Holzer, C. Weld line improvement of short fiber reinforced thermoplastics with a movable flow obstacle. *Journal of Applied Polymer Science* **132** (2015).

List of abbreviations and symbols

Abbreviations

BEM	boundary element method
CAD	computer aided design
CAE	computer aided engineering
CFD	computational fluid dynamics
CTE	coefficient of thermal expansion
DOE	design of experiments
DSC	differential scanning calorimetry
GF	glass fiber
FEM	finite element method
FLD	fiber length distribution
FT	Folgar-Tucker
FOD	fiber orientation distribution
HTC	heat transfer coefficient
μCT	micro-computed tomography
ORF	orthotropic fitted closure approximation
ORL	orthotropic closure approximation fitted for low C_I
PA	Polyamide
POM	Polyoxymethylene
PP	Polypropylene
pvT	pressure-volume-temperature
RHCM	rapid heat cycle molding
RSC	reduced strain closure
SD	standard deviation
TC	thermocouple
UV	ultraviolet
v/p	velocity/pressure
VOF	volume of fluid

Symbols

$\mathbf{A}$	second-order orientation tensor
$\mathbb{A}$	fourth-order orientation tensor
a	thermal diffusivity
A	area
A_1	Cross model parameter
A_2	Cross model parameter
A_3	Cross model parameter
a_{ij}	second-order orientation tensor
a_{ijkl}	fourth-order orientation tensor
a_r	aspect ratio of the fibers
a_T	time temperature shift factor
b_{1m}	Tait model parameter
b_{2m}	Tait model parameter
b_{3m}	Tait model parameter
b_{4m}	Tait model parameter
b_{1s}	Tait model parameter
b_{2s}	Tait model parameter
b_{3s}	Tait model parameter
b_{4s}	Tait model parameter
b_5	Tait model parameter
b_6	Tait model parameter
b_7	Tait model parameter
b_8	Tait model parameter
b_9	Tait model parameter
C	Tait model constant
C_{12}	view factor
C_I	fiber interaction coefficient
C_{ijkl}	fourth-order stiffness tensor
c_p	specific heat at constant pressure
d	distance
$\mathbf{D}$	rate of deformation tensor
D_1	Cross model parameter
D_2	Cross model parameter
D_3	Cross model parameter
$\mathbf{e}_i$	eigenvector
E	Young's modulus
g	gravitational acceleration
G	shear modulus
Gr	Grashof number

h_c	heat transfer coefficient
$\boldsymbol{I}$	identity tensor
k	thermal conductivity
l	length
L	length
m	mass
n	Cross model parameter
$\boldsymbol{n}$	normal vector
Nu	Nusselt number
p	pressure
p_{cav}	cavity pressure
Pr	Prandtl number
q	specific heat flux
Q	specific heat flux
r	radius
Ra	Rayleigh number
Re	Reynolds number
s	length scale
s	shrinkage
t	time
t_i	injection time
t_{inj}	injection time
t_p	packing time
t_c	cooling time
T	temperature
T^*	Cross model parameter
T_g	glass transition temperature
T_t	transition temperature
T_w	cavity wall temperature
$\boldsymbol{u}$	velocity vector
v	specific volume
v_0	Tait model parameter
$\mathbf{W}$	vorticity tensor
$\boldsymbol{x}$	position vector
α_{kl}	tensor of thermal coefficients of expansion
α	coefficient of thermal expansion
α_1	coefficient of thermal expansion in the flow direction
α_2	coefficient of thermal expansion in the transverse direction
β	polymer expansivity
$\dot{\gamma}$	shear rate
Δ	warpage

ϵ	strain
ϵ	emissivity
ϵ_{kl}	total strain tensor
$\dot{\epsilon}$	rate of strain tensor
η	dynamic viscosity
η_0	Cross model parameter
κ	RSC model parameter
λ_i	eigenvalue
ν	kinematic viscosity
λ	dilatational viscosity
ν	Poissons ratio
ξ	particle shape factor
$\xi(t)$	pseudo-time scale
ρ	density
σ	Stefan-Boltzmann constant
σ	stress tensor
σ_{ij}	stress tensor
$\boldsymbol{\tau}$	extra stress tensor
τ^*	Cross model parameter
ϕ	level set distance function
ϕ	volume fraction of the fibers

Appendix A.

Material data

The model coefficients, the material properties, and the test information given here, came form the Moldflow Insight material database. Only the material properties data which is relevant for the simulations presented in this thesis is presented. A detailed description of the models and their coefficients is given in Chapter 2.

A.1. DuPont Delrin 127UV

A.1.1. Moldflow quality indicators

Filling quality indicator	silver
Packing quality indicator	silver
Warpage quality indicator	silver

A.1.2. Delrin 127UV: Rheological material properties

Cross-WLF model coefficients

Model coefficients

n	0.194
τ^*	402956 Pa
D_1	2511.11 Pa·s
D_2	488 K
D_3	0 K/Pa
A_1	36.455
A_2	2000 K

Test information

Source	Manufacturer
Date last modified	17-MAR-2003
Date tested	N/A
Method	Capillary rheometer, ISO 11443

Viscosity over shear rate plot
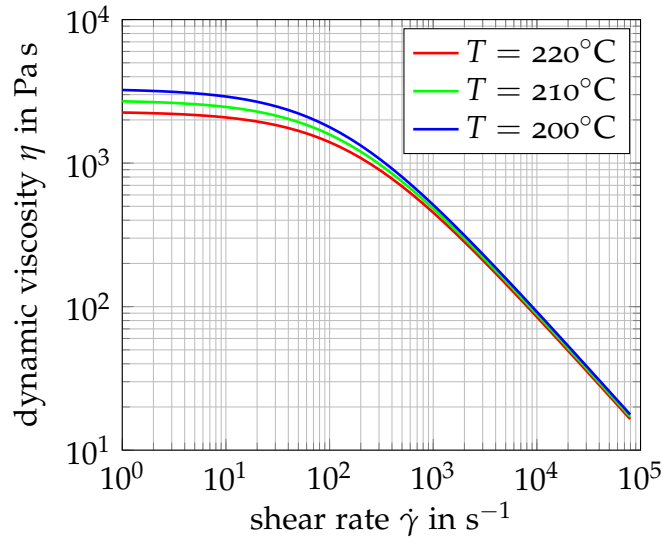
Transition temperature

T_t 144 °C

Test information

Source	Manufacturer
Date last modified	27-FEB-2003
Date tested	N/A
Method	T_c onset ISO11357-3 at -10°C/min

A.1.3. Delrin 127UV: Thermal properties

Specific heat data

Temperature (T) in °C	Specific heat (c_p) in J/kg·K	Heating/cooling rate in K/s
215	3000	N/A

Test information

Source	Manufacturer
Date last modified	17-MAR-2003
Date tested	N/A
Method	DSC: ISO 11357-3

Thermal conductivity data

Temperature (T) in °C	Thermal conductivity (k) in W/m·K	Heating/cooling rate in K/s
215	0.22	N/A

Test information

Source	Manufacturer
Date last modified	27-OCT-2008
Date tested	N/A
Method	not specified
Comments	Measured by different institutes, no standard

A.1.4. Delrin 127UV: pvT properties

2-domain modified Tait pvT model coefficients

Melt density	$1.16\,\text{g/cm}^3$
Solid density	$1.4172\,\text{g/cm}^3$

Model coefficients

b_5	$417\,\text{K}$
b_6	$8.667\text{e-}08\,\text{K/Pa}$
b_{1m}	$0.0008276\,\text{m}^3/\text{kg}$
b_{2m}	$4.849\text{e-}07\,\text{m}^3/\text{kg}\cdot\text{K}$
b_{3m}	$1.855\text{e+}08\,\text{Pa}$
b_{4m}	$0.00464\,\text{1/K}$
b_{1s}	$0.000737\,\text{m}^3/\text{kg}$
b_{2s}	$2.641\text{e-}07\,\text{m}^3/\text{kg}\cdot\text{K}$
b_{3s}	$2.17959\text{e+}08\,\text{Pa}$
b_{4s}	$0.004875\,\text{1/K}$
b_7	$9.067\text{e-}05\,\text{m}^3/\text{kg}$
b_8	$0.04032\,\text{1/K}$
b_9	$4.105\text{e-}09\,\text{1/Pa}$

Test information

Source	Manufacturer
Date last modified	27-FEB-2003
Date tested	N/A
Method	calculated
Comments	Analytical from solid/melt densities, compressibilities, CLTEs and transition temperature

Specific volume vs temperature plot
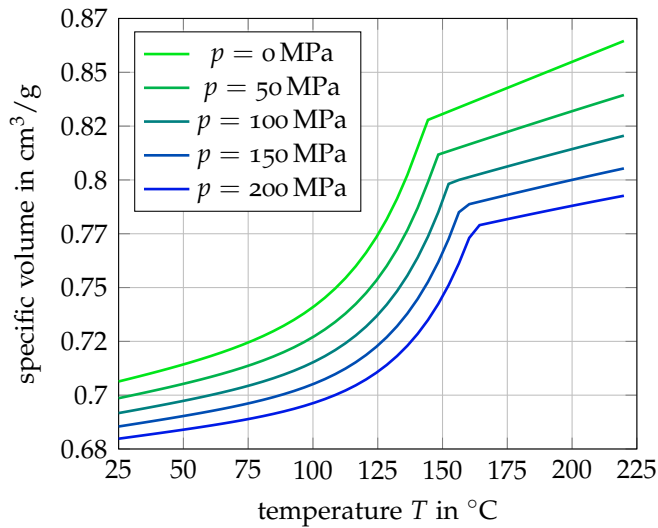
A.1.5. Delrin 127UV: Mechanical properties

Properties

Elastic modulus, 1st principal direction ($E1$)	3000 MPa
Elastic modulus, 2nd principal direction ($E2$)	3000 MPa
Poissons ratio (ν_{12})	0.35
Poissons ratio (ν_{23})	0.35
Shear modulus (G_{12})	1111.11 MPa
Transversely isotropic coefficient of thermal expansion (CTE) data	
α_1	0.000135 1/K
α_2	0.000135 1/K

Test information

Source	Manufacturer
Date last modified	27-FEB-2003
Date tested	N/A
Method	Tensile modulus test-bars: ISO 527-1/2

A.2. DuPont Delrin 100

A.2.1. Moldflow quality indicators

Filling quality indicator   gold
Packing quality indicator   gold
Warpage quality indicator   gold

A.2.2. Delrin 100: Rheological material properties

Cross-WLF model coefficients

Model coefficients

n	0.1608
τ^*	398000 Pa
D_1	5.55e+13 Pa·s
D_2	223.15 K
D_3	7.63e-08 K/Pa
A_1	28.89
A_2	51.6 K

Test information

Source	Autodesk Moldflow Plastics Labs
Date last modified	28-FEB-13
Date tested	28-FEB-13
Method	Moldflow Injection Molding Rheometer

Viscosity over shear rate plot
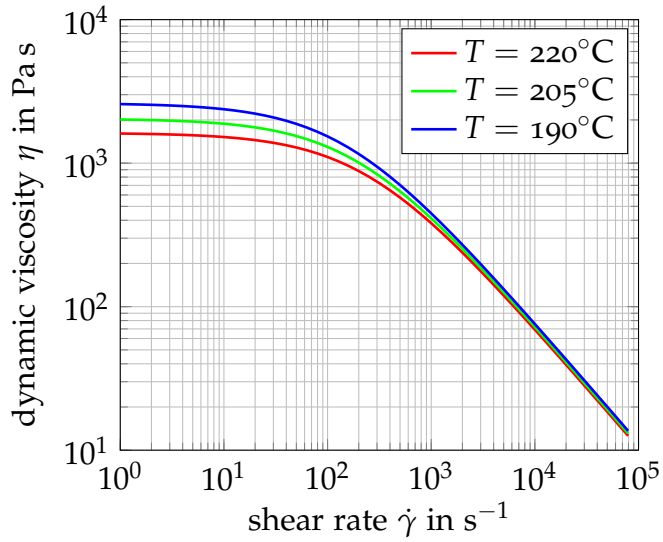
Transition temperature

T_t	149 °C

Test information

Source	Autodesk Moldflow Plastics Labs
Date last modified	23-JAN-13
Date tested	23-JAN-13
Method	DSC: T_c onset (ASTM D 3418) at -20°C/min

A.2.3. Delrin 100: Thermal properties

Specific heat data

Temperature (T) in °C	Specific heat (c_p) in J/kg·K	Heating/cooling rate in K/s
32	1286	-0.333
57	1479	-0.333
80	1779	-0.333
90	2129	-0.333
112	2167	-0.333
125	2415	-0.333
132	2878	-0.333
136	4566	-0.333
139	12532	-0.333
143	20900	-0.333
146	14184	-0.333
149	2981	-0.333
150	2227	-0.333
157	1972	-0.333
220	1932	-0.333

Test information

Source	Autodesk Moldflow Plastics Labs
Date last modified	23-JAN-13
Date tested	23-JAN-13
Method	DSC Cooling Scan -20°C/min (ASTM E 1269)

Thermal conductivity data

Temperature (T) in °C	Thermal conductivity (k) in W/m·K	Heating/cooling rate in K/s
25.4	0.2853	0
35.4	0.2836	0
55.2	0.2934	0
74.9	0.2906	0
94.8	0.2856	0
114.5	0.2799	0
134.7	0.2773	0
155.4	0.2489	0
172.9	0.2274	0
192.8	0.2285	0
212.8	0.232	0

Test information

Source	Autodesk Moldflow Plastics Labs
Date last modified	23-JAN-13
Date tested	23-JAN-13
Method	Line Source Method (ASTM D 5930)

A.2.4. Delrin 100: pvT properties

2-domain modified Tait pvT model coefficients

Melt density	$1.1523\,\text{g/cm}^3$
Solid density	$1.4277\,\text{g/cm}^3$

Model coefficients

b_5	$448.15\,\text{K}$
b_6	$3.10\text{e-}08\,\text{K/Pa}$
b_{1m}	$0.0008452\,\text{m}^3\text{/kg}$
b_{2m}	$5.65\text{e-}07\,\text{m}^3\text{/kg·K}$
b_{3m}	$1.57079\text{e+}08\,\text{Pa}$
b_{4m}	$0.007667\,1\text{/K}$
b_{1s}	$0.0007446\,\text{m}^3\text{/kg}$
b_{2s}	$2.944\text{e-}07\,\text{m}^3\text{/kg·K}$
b_{3s}	$2.87663\text{e+}08\,\text{Pa}$
b_{4s}	$0.004784\,1\text{/K}$
b_7	$0.0001006\,\text{m}^3\text{/kg}$
b_8	$0.08434\,1\text{/K}$
b_9	$4.469\text{e-}09\,1\text{/Pa}$

Test information

Source	Autodesk Moldflow Plastics Labs
Date last modified	25-JAN-13
Date tested	25-JAN-13
Method	Indirect Dilatometry

Specific volume vs temperature plot
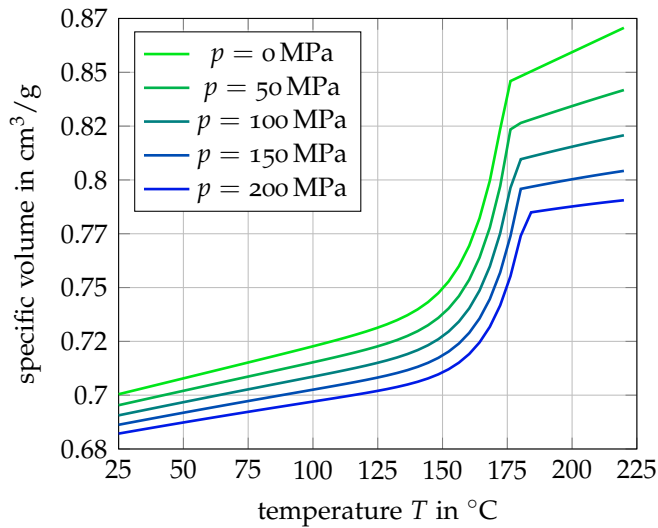
A.2.5. Delrin 100: Mechanical properties

Properties

Elastic modulus, 1st principal direction ($E1$)	3100 MPa
Elastic modulus, 2nd principal direction ($E2$)	3100 MPa
Poissons ratio (ν_{12})	0.35
Poissons ratio (ν_{23})	0.35
Shear modulus (G_{12})	1050 MPa
Transversely isotropic coefficient of thermal expansion (CTE) data	
α_1	0.00011 1/K
α_2	0.00011 1/K

Test information

Source	Manufacturer
Date last modified	06-FEB-13
Date tested	06-FEB-13
Method	Not Specified

A.3. DuPont Zytel 73G45

A.3.1. Moldflow quality indicators

Filling quality indicator	silver
Packing quality indicator	silver
Warpage quality indicator	bronze

A.3.2. Zytel 73G45: Rheological material properties

Cross-WLF model coefficients

Model coefficients

n	0.4299
τ^*	62054.4 Pa
D_1	4.38423e+21 Pa·s
D_2	323.15 K
D_3	0 K/Pa
A_1	52.34
A_2	51.6 K

Test information

Source	Manufacturer
Date last modified	13-JAN-00
Date tested	N/A
Method	Not Specified

Viscosity over shear rate plot
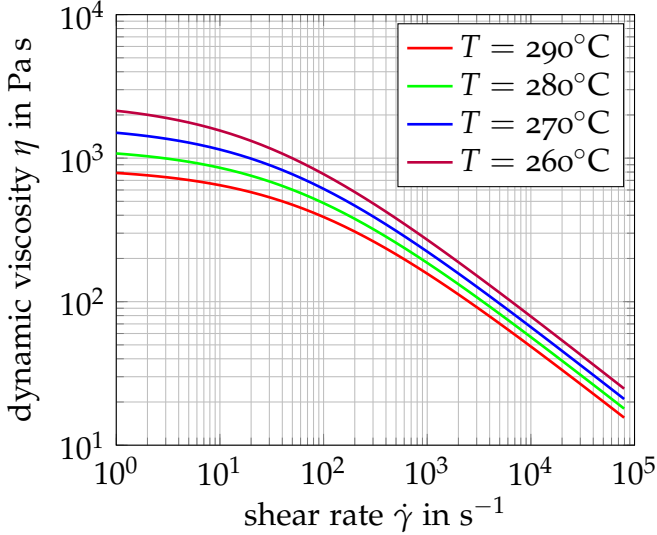
Transition temperature

T_t 171 °C

Test information

Source	Manufacturer
Date last modified	13-JAN-00
Date tested	N/A
Method	Not Specified

A.3.3. Zytel 73G45: Thermal properties

Specific heat data

Temperature (T) in °C	Specific heat (c_p) in J/kg·K	Heating/cooling rate in K/s
275	2200	N/A

Test information

Source	Manufacturer
Date last modified	13-JAN-00
Date tested	N/A
Method	Not Specified

Thermal conductivity data

Temperature (T) in °C	Thermal conductivity (k) in W/m·K	Heating/cooling rate in K/s
275	0.24	N/A

Test information

Source	Manufacturer
Date last modified	13-JAN-00
Date tested	N/A
Method	Not Specified

A.3.4. Zytel 73G45: pvT properties

2-domain modified Tait pvT model coefficients

Melt density	$1.3411\,\text{g/cm}^3$
Solid density	$1.5291\,\text{g/cm}^3$

Model coefficients

b_5	$454.15\,\text{K}$
b_6	$8.3\text{e-}08\,\text{K/Pa}$
b_{1m}	$0.0007353\,\text{m}^3/\text{kg}$
b_{2m}	$1.101\text{e-}07\,\text{m}^3/\text{kg·K}$
b_{3m}	$1.32627\text{e+}08\,\text{Pa}$
b_{4m}	$0.001275\,1/\text{K}$
b_{1s}	$0.0006555\,\text{m}^3/\text{kg}$
b_{2s}	$1\text{e-}08\,\text{m}^3/\text{kg·K}$
b_{3s}	$3.40107\text{e+}08\,\text{Pa}$
b_{4s}	$0.002782\,1/\text{K}$
b_7	$7.935\text{e-}05\,\text{m}^3/\text{kg}$
b_8	$0.01484\,1/\text{K}$
b_9	$4.067\text{e-}09\,1/\text{Pa}$

Test information

Source	Manufacturer
Date last modified	13-JAN-00
Date tested	N/A
Method	Not Specified

Specific volume vs temperature plot
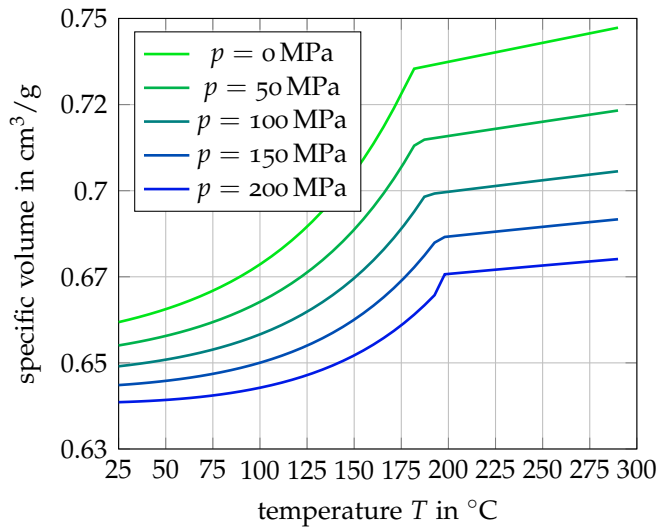
A.3.5. Zytel 73G45: Mechanical properties

Properties

Elastic modulus, 1st principal direction ($E1$)	13354 MPa
Elastic modulus, 2nd principal direction ($E2$)	7460.1 MPa
Poissons ratio (ν_{12})	0.3989
Poissons ratio (ν_{23})	0.4635
Shear modulus (G_{12})	3332.43 MPa
Transversely isotropic coefficient of thermal expansion (CTE) data	
α_1	1.797e-05 1/K
α_2	4.214e-05 1/K

Test information

Source	Supplemental
Date last modified	09-MAY-11
Date tested	N/A
Method	References

A.4. EMS-Grivory Grilon BG-35

A.4.1. Moldflow quality indicators

Filling quality indicator	gold
Packing quality indicator	gold
Warpage quality indicator	gold

A.4.2. Grilon BG-35: Rheological material properties

Cross-WLF model coefficients

Model coefficients	
n	0.31
τ^*	225000 Pa
D_1	7.5e+18 Pa·s
D_2	318.15 K
D_3	0 K/Pa
A_1	45.25
A_2	51.6 K

Test information	
Source	Moldflow Plastics Labs
Date last modified	27-OCT-08
Date tested	10-AUG-04
Method	Moldflow Injection Molding Rheometer; FST FlowSpiralTest
Comments	Fit to FST data

Viscosity over shear rate plot
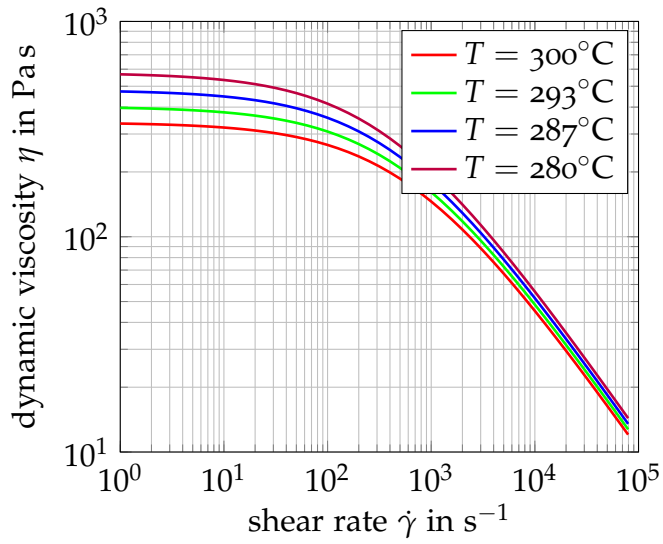
Transition temperature

T_t 200 °C

Test information

Source	Moldflow Plastics Labs
Date last modified	15-NOV-07
Date tested	10-AUG-04
Method	DSC: T_c onset (ASTM D 3418) at -20°C/min

A.4.3. Grilon BG-35: Thermal properties

Specific heat data

Temperature (T) in °C	Specific heat (c_p) in J/kg·K	Heating/cooling rate in K/s
50	1900	-0.333
90	2179	-0.333
197	2487	-0.333
204	2696	-0.333
206	3089	-0.333
208	4601	-0.333
210	6846	-0.333
216	4437	-0.333
219	2563	-0.333
222	2406	-0.333
228	2305	-0.333
310	2334	-0.333

Test information

Source	Moldflow Plastics Labs
Date last modified	09-JAN-08
Date tested	10-AUG-04
Method	DSC Cooling Scan -20°C/min (ASTM E 1269)

Thermal conductivity data

Temperature (T) in °C	Thermal conductivity (k) in W/m·K	Heating/cooling rate in K/s
290	0.26	0

Test information

Source	Manufacturer
Date last modified	03-NOV-08
Date tested	01-MAR-03
Method	Line Source Method (ISO 8894)

A.4.4. Grilon BG-35: pvT properties

2-domain modified Tait pvT model coefficients

Melt density	$1.237\,\text{g/cm}^3$
Solid density	$1.4148\,\text{g/cm}^3$

Model coefficients

b_5	$497.15\,\text{K}$
b_6	$9\text{e-}08\,\text{K/Pa}$
b_{1m}	$0.000787\,\text{m}^3/\text{kg}$
b_{2m}	$3.244\text{e-}07\,\text{m}^3/\text{kg·K}$
b_{3m}	$2.19594\text{e+}08\,\text{Pa}$
b_{4m}	$0.003339\,\text{1/K}$
b_{1s}	$0.0007568\,\text{m}^3/\text{kg}$
b_{2s}	$2.512\text{e-}07\,\text{m}^3/\text{kg·K}$
b_{3s}	$2.67313\text{e+}08\,\text{Pa}$
b_{4s}	$0.003464\,\text{1/K}$
b_7	$3.02\text{e-}05\,\text{m}^3/\text{kg}$
b_8	$0.06208\,\text{1/K}$
b_9	$8\text{e-}09\,\text{1/Pa}$

Test information

Source	Manufacturer
Date last modified	27-OCT-09
Date tested	01-MAR-03
Method	Indirect Dilatometry; ISO 1183

Grilon BG-35: Specific volume vs temperature plot
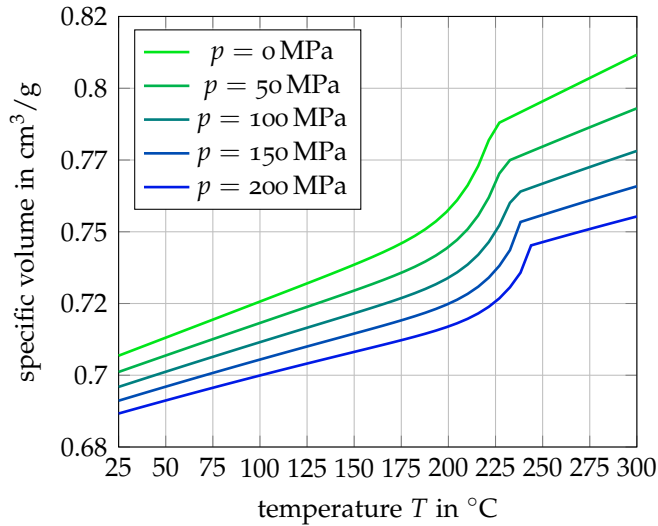
A.4.5. Grilon BG-35: Mechanical properties

Properties

Elastic modulus, 1st principal direction ($E1$)	11970.2 MPa
Elastic modulus, 2nd principal direction ($E2$)	4570.43 MPa
Poissons ratio (ν_{12})	0.375
Poissons ratio (ν_{23})	0.577
Shear modulus (G_{12})	1643.7 MPa
Transversely isotropic coefficient of thermal expansion (CTE) data	
α_1	2.35e-05 1/K
α_2	10.5e-05 1/K

Test information

Source	Manufacturer
Date last modified	27-OCT-09
Date tested	01-MAR-03
Method	Universal Testing Machine; ISO 527
Comments	ISO 11359; DIN 53752

A.5. Ube Industries Limited Nylon 1015gc9

A.5.1. Moldflow quality indicators

Filling quality indicator   gold
Packing quality indicator   gold
Warpage quality indicator   gold

A.5.2. UBE Nylon 1015gc9: Rheological material properties

Cross-WLF model coefficients

Model coefficients	
n	0.2326
τ^*	262244 Pa
D_1	2.80497e+15 Pa·s
D_2	323.15 K
D_3	0 K/Pa
A_1	35.93
A_2	51.6 K

Test information	
Source	Moldflow Plastics Labs
Date last modified	07-JUL-06
Date tested	07-JUL-06
Method	Moldflow Injection Molding Rheometer

Viscosity over shear rate plot
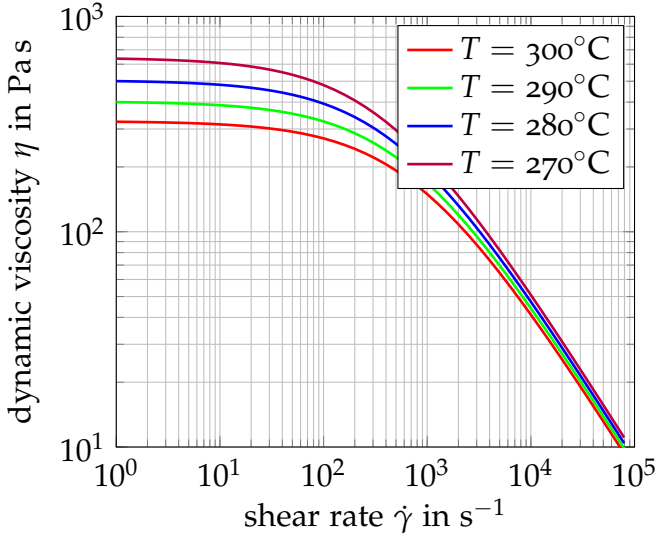
Transition temperature

T_t	184 °C

Test information

Source	Moldflow Plastics Labs
Date last modified	07-JUL-06
Date tested	07-JUL-06
Method	DSC: T_c onset (ASTM D 3418) at -20°C/min

A.5.3. UBE Nylon 1015gc9: Thermal properties

Specific heat data

Temperature (T) in °C	Specific heat (c_p) in J/kg·K	Heating/cooling rate in K/s
50	843	-0.333
59	1279	-0.333
115	1676	-0.333
158	1979	-0.333
167	2048	-0.333
171	2281	-0.333
174	3655	-0.333
178	6094	-0.333
182	3569	-0.333
186	2105	-0.333
191	1882	-0.333
300	1970	-0.333

Test information	
Source	Moldflow Plastics Labs
Date last modified	07-JUL-06
Date tested	07-JUL-06
Method	DSC Cooling Scan -20°C/min (ASTM E 1269)

Thermal conductivity data

Temperature (T) in °C	Thermal conductivity (k) in W/m·K	Heating/cooling rate in K/s
38.2	0.2952	0
58.2	0.3084	0
77.8	0.2917	0
97.4	0.2978	0
137.3	0.2928	0
157.6	0.2983	0
178.7	0.3102	0
199.2	0.3147	0
238.5	0.3081	0
259.2	0.3135	0
280.3	0.3264	0
301.1	0.3266	0

Test information

Source	Moldflow Plastics Labs
Date last modified	07-JUL-06
Date tested	07-JUL-06
Method	Line Source Method (ASTM D 5930)

A.5.4. UBE Nylon 1015gc9: pvT properties

2-domain modified Tait pvT model coefficients

Melt density	$1.3066\,\text{g/cm}^3$
Solid density	$1.5156\,\text{g/cm}^3$

Model coefficients

b_5	$498.15\,\text{K}$
b_6	$4\text{e-}08\,\text{K/Pa}$
b_{1m}	$0.0007475\,\text{m}^3/\text{kg}$
b_{2m}	$2.977\text{e-}07\,\text{m}^3/\text{kg}{\cdot}\text{K}$
b_{3m}	$1.91414\text{e+}08\,\text{Pa}$
b_{4m}	$0.003125\,\text{1/K}$
b_{1s}	$0.000698\,\text{m}^3/\text{kg}$
b_{2s}	$1.909\text{e-}07\,\text{m}^3/\text{kg}{\cdot}\text{K}$
b_{3s}	$3.3702\text{e+}08\,\text{Pa}$
b_{4s}	$0.002295\,\text{1/K}$
b_7	$4.951\text{e-}05\,\text{m}^3/\text{kg}$
b_8	$0.03353\,\text{1/K}$
b_9	$4.259\text{e-}09\,\text{1/Pa}$

Test information

Source	Moldflow Plastics Labs
Date last modified	18-JUL-06
Date tested	18-JUL-06
Method	Indirect Dilatometry

Specific volume vs temperature plot
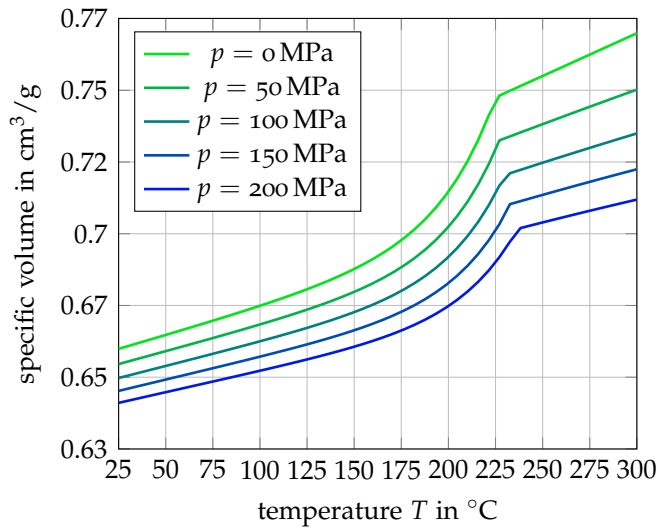
A.5.5. UBE Nylon 1015gc9: Mechanical properties

Properties

Elastic modulus, 1st principal direction ($E1$)	13248.2 MPa
Elastic modulus, 2nd principal direction ($E2$)	7409.22 MPa
Poissons ratio (ν_{12})	0.3991
Poissons ratio (ν_{23})	0.4633
Shear modulus (G_{12})	3307.32 MPa
Transversely isotropic coefficient of thermal expansion (CTE) data	
α_1	1.812e-05 1/K
α_2	4.243e-05 1/K

Test information

Source	Supplemental
Date last modified	03-FEB-15
Date tested	
Method	References